Morphology Control of Porous Materials and Molecular Sieve Membrane Applications

A DISSERTATION
SUBMITTED TO THE FACULTY OF THE GRADUATE SCHOOL
OF THE UNIVERSITY OF MINNESOTA
BY

Won Cheol Yoo

IN PARTIAL FULFILLMENT OF THE REQUIREMENTS
FOR THE DEGREE OF
DOCTOR OF PHILOSOPHY

Andreas Stein, Advisor

December 2010

Acknowledgments

During my graduate studies, I cannot imagine where I would be right now without the help from the following people.

Prof. Andreas Stein who has been supporting and guiding me as an advisor as well as a mentor with patience and belief in me.

The Stein group alumni, current members and collaborators; Dr. Zhiyong Wang, Dr. Nick Denny, Dr. Fan Li, Dr. Sandeep Kumar, Mr. Pyung-Soo Lee, Mr. Jared A. Stoeger, Ms. Melissa Fierke, Mr. Matthew Dubay, Mr. David Josephson, Mr. Anh Vu, Mr. Nicholas Petkovich, Mr. Yuqiang Qian and Mr. Stephen Rudisill.

Korean friends in Minnesota; Mr. Han Yong Eom, Dr. Joong Hoon Kwon, Dr. Sung Ho Choi, Mr. Hyun Chul Jang, Mr. Yoon Sang Park and Korean friends in the Department of Chemistry.

I want to share the thesis with my family in Korea; my brother Young Jin Yoo, my sister Ji Sook Yoo and their adorable kids, my nephew Tae Kwon Yoo and niece Seo Yoon Kim who just got born.

And, thanks to my mother, Jeong Ae Kang and my father, Yoon Ho Yoo who endlessly support and love me. I never doubt that I cannot do anything without your care and love. I would like to say I love you and want to dedicate this thesis to my parents.

Last, thank God. I have been happy within you. Please guide me where I am supposed to go.

Abstract

For advanced applications of porous materials, morphology control of porous materials is desired. Simultaneous dissolution and surfactant-induced re-assembly via micelle formation with dissolved species were performed to introduce mesoporosity in the amorphous silica spheres and zeolite crystals. Textural features of mesoporous silica spheres were controlled from corrugated to smooth. Mesoporous zeolite catalysts were synthesized via surfactant-induced re-assembly with dissolved crystal fragments of zeolite crystals. In addition, the concept of confined synthesis was used for control of morphologies of zeolite crystals. Using 3-D ordered macroporous (3DOM) carbon as a template, growth patterns and shape development of zeolite crystals were studied. Various shaped zeolite crystals, e.g., hollow interior (geode-like structure), corrugated/smooth surface of polycrystalline crystals, needle-shaped crystals and 3DOM imprinted single crystals, were produced by careful choice of reaction parameters during the confined synthesis. Polycrystalline aggregates produced by the confined synthesis were used as seed particles for zeolite membrane fabrication. Novel seeding techniques, rubbing and leveling methods, were applied to deposit the confinement product directly on the surface of porous alumina supports, and zeolite membranes were grown by secondary hydrothermal growth. Moreover, rapid thermal processing and conventional calcination were used to investigate the effect of thermal treatments on the overall membrane quality. To evaluate the membrane quality, permeation measurements to separate *p-/o*-xylene isomers based on the zeolite's intrinsic capability of size-selective molecular separations were conducted. A high separation factor and high permeance were observed. (232 words)

Table of Contents

Acknowledgments……..... i

Abstract……..…ii

Table of Contents……..….iii

List of Tables……ix

List of Figures…….…...x

Chapter 1

An Introduction to Porous Materials…….…..1

1.1 Motivation for Morphology Control of Porous Materials……..…..1

1.2 Overview of Porous Materials…….....2

1.3 Microporous Materials ……...….3

1.3.1 Mechanisms of zeolite crystallization…….…..….4

1.3.2 Morphology control of microporous materials……...…6

1.3.2.1 Direct synthesis of meso-zeolite materials…….…..…6

1.3.2.2 Template-assisted method……..….8

1.3.2.3 Post-synthesis treatment to form meso-zeolite materials……..11

1.4 An Introduction to Zeolite Films……....12

1.4.1 Seed deposition…….....14

1.4.2 Oriented MFI zeolite films…….…...18

1.4.3 Rapid thermal processing (RTP): grain boundary defect elimination……..21

1.5 Mesoporous Materials…….…24

1.5.1 Synthetic mechanism of mesoporous materials……...24

1.5.2 Morphology control of mesoporous silica…….…..27

1.5.2.1 Direct synthesis of mesoporous silica sphres……....28

1.5.2.2 Post synthesis of mesoporous silica spheres…….29

1.6 Conclusions……....31

1.7 References…….….32

Chapter 2

Morphology Control of Mesoporous Silica Spheres via Pseudomorphic Transformations

2.1 Introduction……....41

2.2 Experimental Section…….…42

2.2.1 Reagents…….….42

2.2.2 Preparation of silica spheres……42

2.2.3 Hydrothermal reactions……....43

2.2.4 Preparation of hollow-core@mesoporous-shell carbon spheres by nanocasting……...43

2.2.5 Characterization……....44

2.3. Results……....44

2.3.1 Pseudomorphic transformation of amorphous silica spheres……44

2.3.2 Carbon nanocasting of mesoporous silica spheres……50

2.4 Discussion……...54

2.5 Conclusion……..…57

2.6 References……..…58

Chapter 3

Fabrication of Mesoporous Zeolites through Desilication and Re-assembly Processes

3.1 Introduction……...61

3.2 Experimental Section……64

3.2.1 Reagents……..64

3.2.2 Synthesis of ZSM-5……64

3.2.3 Synthesis of meso-zeolites……..64

3.3.4 Synthesis of H-form of zeolites……..65

3.3.5 Characterization……..65

3.3 Results……...66

3.3.1 HZ_100 series……66

3.3.2 HZ_50 series……...75

3.3.3 HZ_30 series……...84

3.4 Discussion……85

3.4.1 Textural characteristics of meso-zeolites……85

3.4.2 Surfactant induced re-assembly of dissolved species……..87

3.4 Conclusions……...88

3.5 References……89

Chapter 4

Growth Patterns and Shape Development of Zeolite Nanocrystals in Confined Syntheses

4.1 Introduction……...92

4.2 Experimental Section……97

4.2.1 Reagents……..97

4.2.2 Preparation of 3DOM carbon and polyelectrolyte coatings……97

4.2.3 Hydrothermal reactions……...98

4.2.4 Recovery of zeolite spheres and thin film preparation……....98

4.2.5 Characterization…….…..99

4.3 Results and Discussion…….….99

4.3.1 Growth of polycrystalline spheres…….…..99

4.3.1.1 Polycrystalline spheres with corrugated surface…….…..99

4.3.1.2 Polycrystalline spheres with hollow interior……106

4.3.2 Growth of imprinted single crystals……107

4.3.3 Shape development of discrete zeolite particles…….114

4.3.4 Secondary population growth……..117

4.4 Conclusions……...118

4.5 References…….……119

Chapter 5

High Performance Randomly Oriented Zeolite Membranes Using Brittle Seeds and Rapid Thermal Processing

5.1 Introduction……..123

5.2 Experimental Section……125

5.2.1 Reagents……..125

5.2.2 Preparation of seed particles……...125

5.2.3 Seed deposition (rubbing and leveling methods)……126

5.2.4 Zeolite membrane growth (secondary hydrothermal growth)……126

5.2.5 Permeation test……127

5.2.6 Characterization……..128

5.3 Results and Discussion……129

5.3.1 Zeolite membranes on α-alumina supports (100 °C for 12 h)……129

5.3.2 Zeolite membranes on α-alumina supports (175 °C for 1 h)……..141

5.3.3 Zeolite membranes on stainless steel tube supports……...144

5.4 Conclusions……...149

5.5 References……149

Chapter 6

Summary and Outlook

6.1 Summary……...153

6.1.1 Surfactant-induced re-assembly of dissolved species……153

6.1.2 Morphology control of zeolite nanocrystals using confined synthesis…...153

6.1.3 Fabrication of high performance zeolite membranes using brittle seed particles……..154

6.2 Outlook……155

6.2.1 Design of dual/multi-component catalysts……155

6.2.2 Metal ion impregnated meso-zeolite catalysts……156

6.2.3 Thin *b*-oriented MFI membranes……157

6.3 References……158

Bibliography……159

List of Tables

Table 2.1 Textural characteristics of pseudomorphic silica products and nanocast carbon spheres……. 50

Table 3.1 Textural characteristics of ZSM-5 crystals and meso-zeolite materials……..73

Table 3.2 Characteristic data for selected zeolites…….. 84

Table 5.1 Comparison of xylene isomer separation factors, permeation data and membrane structure for MFI-zeolite membranes from the present work and from select references…….139

List of Figures

Figure 1.1 MFI zeolite. The framework is viewed along the [010] direction..……..4

Figure 1.2 Schematic illustration for the crystallization mechanism of pure silica MFI…5

Figure 1.3 Structure directing agent (SDA) for a two dimensional zeolite. Two positively charged nitrogen atoms in the SDA control the assembly of the inorganic framework, while a long hydrocarbon group prevents growth of the zeolite in the direction in which that group extends……..7

Figure 1.4 MFI nanosheets with a multilamellar structure. SEM image (a) and TEM images (b, c, e) present structural features. X-ray diffraction (XRD) patterns (d) confirm the crystallinity, and nitrogen isotherm and pore size distribution (f) the mesoporosity of this method……...7

Figure 1.5 SEM images (a and b) of mesoporous zeolite LTA synthesized using $(CH_3O)_3SiC_3H_6N(CH_3)_2C_{16}H_{33}$ as a porogen……..8

Figure 1.6 Growth of zeolite crystals around carbon particles. TEM image (right) shows an isolated single ZSM-5crystal and the electron diffraction patterns (inset)…….9

Figure 1.7 Three-dimensionally ordered mesoporous (3DOm) carbon templates with SEM images (a-c) represent different pore sizes, 10 nm, 20 nm, 40 nm, respectively. Small angle x-ray scattering (SAXS) data (d), nitrogen isotherms (e) and BJH pore size distribution obtained by nitrogen sorption measurements…….10

Figure 1.8 TEM images of zeolite crystals produced inside 3DOm carbon as a template. (a) and (b) show MFI crystals inside templates, and (c) and (d) present isolated MFI crystals……...11

Figure 1.9 The schematic illustration of the desilication method with different Si/Al ratio and the corresponding nitrogen isotherms……12

Figure 1.10 Schematic illustration of zeolite film processing (secondary growth method) using molecular sieve particles (MFI, left) as building blocks to form crystal monolayers (middle) and oriented, intergrown films (right)……14

Figure 1.11 Various types of molecular linkages…….15

Figure 1.12 SEM images of a 2-D array of closely packed, uniformly aligned silicalite-1 crystals grown on the polymer coated glass slide. (A) Crystals grown in high coverage. (B) The orientation of the crystals with their *c* axes perpendicular to the glass plane…..16

Figure 1.13 Photographic images showing the process (a-c) of monolayer assembly of silicalite-1 microcrystals on glass.[89] (a) A Certain amount of zeolite particles is located on the furctionalized glass slide. (b) Zeolite particles are rubbed by a gloved finger. (c) After rubbing, the glass color is changed from transparent to milky color……17

Figure 1.14 Scenarios of microstructure control by crystal-shape design, deposition, and growth using crystal-shape modifiers including tetrapropylammonium (monomer-TPA: TPA) (for example, top left) and bis-N,N-(tripropylammoniumhexamethylene)-di-N,N-propylammonium trihydroxide (trimer-TPA: tC6) (top right)…….20

Figure 1.15 Performance of *c*-[82,83,104] *b*-[84,98] *h0h*-[83] oriented, and thin and randomly oriented (*t*)[96] silicalite-1 membranes for separating the indicated components at temperatures ranging from room temperature to as high as 400°C (light gray: RT–100°C, gray: 100–200°C, black: 200–400°C)……..20

Figure 1.16 LSCM images of a) c-oriented and b) b-oriented MFI films. The right parts of (a) and (b) are partially transparent SEM images of the membrane surface to simultaneously view the fluorescing polycrystalline features……..22

Figure 1.17 Cross-sectional LSCM images of RTP-untreated (A) and RTP-treated *c*-oriented MFI membrane. A1, A2 and B1, B2 represent the cross-sectional views from the top surfaces of RTP-untreated (A) and RTP-treated (B) membranes, respectively. The arrows in the B indicate limited propagation of crack formation from the bottom to the top surface…….23

Figure 1.18 Two synthetic strategies of mesoporous materials through soft templating method: (A) cooperative self-assembly and (B) liquid-crystal templating process……...26

Figure 1.19 Schematic illustration of fabrication of mesoporous materials via hard templating process…….27

Figure 1.20 Transmission electron microscopy (TEM) images of the electrodeposited surfactant-templated mesoporous silica film. (a) Top view and (b) cross-sectional view of the sample. The inset in (a) is an electron diffraction pattern of the mesostructured film. The scale bars are 50 nm (a) and 20 nm (b)……..27

Figure 1.21 TEM images (a-d, left) show mesoporous silica spheres with different alkyl chains of quaternary ammonium as a surfactant, C12, C14, C16, C18, respectively. Small angle X-ray scattering (SAXS) patterns (right) present characteristic features of ordered mesopores from the samples prepared under different surfactant conditions. The scale bar corresponds to 20 nm. The arrows indicate the size of mesopores corresponding the different chain lengths of the surfactants used in the reaction……..29

Figure 1.22 TEM images and schematic representation of double pseudomorphic transformation of amorphorous silica into mesoporous silica spheres (MCM-41 and MCM-48)……..30

Figure 1.23 The schematic illustration of the concept of surface-protected etching for transforming solid structures into hollow structures with permeable shells……..31

Figure 2.1 SEM images of amorphous parent silica spheres: (A) SiO_2-EtOH, (B) SiO_2-*i*PrOH and (C) SiO_2-BuOH……....46

Figure 2.2 Nitrogen sorption isotherms, BET surface areas and pore volumes (inset) of parent silica spheres prepared under different solvent conditions. (a) SiO_2-EtOH, (b) SiO_2-*i*PrOH and (c) SiO_2-BuOH……46

Figure 2.3 SEM images of parent silica and hydrothermal silica spheres: (A) parent silica spheres produced in EtOH (SiO_2-EtOH), (B) hydrothermal product HT-SiO_2-EtOH, (C) magnified image of HT-SiO_2-EtOH, (D) hydrothermal product HT-SiO_2-*i*PrOH, (E)

broken structures of HT-SiO_2-*i*PrOH, (F) magnified image of HT-SiO_2-*i*PrOH, (G) hydrothermal product HT-SiO_2-BuOH, (H) broken structures of HT-SiO_2-BuOH, (I) magnified image of HT-SiO_2-BuOH…….47

Figure 2.4 TEM images of hydrothermal reaction products (A) HT-SiO_2-EtOH, (B) HT-SiO_2-*i*PrOH and (C) HT-SiO_2-BuOH. The inset in (B) shows an enlargement of the circled region with a scale bar of 100 nm. (D) shows a higher magnification image of HT-SiO_2-*i*PrOH. ……48

Figure 2.5 SAXS patterns of hydrothermal products and nanocast carbon spheres: (a) HT-SiO_2-EtOH, (b) HT-SiO_2-*i*PrOH, (c) HT-SiO_2-BuOH and (D) PFC- *i*PrOH…….49

Figure 2.6 Schematic illustration of the preparation of hollow carbon spheres by nanocasting…….……..….51

Figure 2.7 SEM (A and B) and TEM (C and D) images of nanocast hollow carbon spheres after HF etching (PFC-*i*PrOH)…….52

Figure 2.8 TEM images of nanocast carbon spheres after HF etching. HT-SiO_2-EtOH was used as a preform……..…..53

Figure 2.9 (A) Nitrogen sorption isotherms and (B) pore size distributions calculated from the adsorption branches by the BJH (Barrett-Joyner-Halenda) method. (a) HT-SiO_2-EtOH, (b) HT-SiO_2-*i*PrOH, (c) HT-SiO_2-BuOH and (D) PFC-*i*PrOH……..54

Figure 2.10 ^{29}Si solid-state MAS NMR spectra of the parent silica spheres: (A) SiO_2-EtOH, (B) SiO_2-*i*PrOH and (C) SiO_2-BuOH. ……...56

Figure 2.11 SEM images of HT-SiO_2-*i*PrOH mesoporous silica spheres produced using (A) half the regular NaOH concentration and (B) twice the regular NaOH concentration…….……57

Figure 3.1 A schematic illustration showing the preparation of meso-zeolite materials via desilication (upper right) and desilication/re-assembly processes (bottom right). ……...63

Figure 3.2 SEM images of (a) HZ_100_OH1.5_NS, (b) HZ_100_OH1.5_S, (c) HZ _100_OH2_NS, (d) HZ_100_OH2_S, (e) HZ_100_OH3_NS, and (f) HZ_100_OH3_S. ……68

Figure 3.3 TEM images of (a and b) HZ_100_OH2_S, (c) HZ_100_OH3_NS, and (d) HZ_100_OH3_S. The images in (a) and (d) correspond to the marked regions in the insets that present a lower magnification image……69

Figure 3.4 Nitrogen sorption isotherms for samples prepared using different concentrations of base (A for HZ_100_OH1.5_NS/S, B for HZ_100_OH2_NS/S, and C for HZ_100_OH3_NS/S). The parent zeolite crystal ZSM-5_100, desilication products and desilication/re-assembly products are denoted as a, b and c in all graphs, respectively……70

Figure 3.5 (A and B) BJH pore size distributions of samples prepared using different concentrations of base: (A) for HZ_100_OH1.5_NS (a) and HZ_100_OH1.5_S (b), and (B) for HZ_100_OH2_NS (a) and HZ_100_OH2_S (b). (C) Comparison of the pore size distributions for desilication products HZ_100_OH1.5_NS (a) and HZ_100_OH2_NS (b). (D) Comparison of the pore size distributions for desilication/re-assembly products HZ_100_OH1.5_S (a) and HZ_100_OH2_S (b). ……71

Figure 3.6 Influence of the hydroxide ion concentration and the presence of CTAB on (A) the surface area related to pores > 2 nm ("external surface area") and (B) the micropore volume. Data for the desilication products (HZ_100_OH(1.5, 2, 3)_NS) (a) and desilication/re-assembly products (HZ_100_OH(1.5, 2, 3)_S) (b) are shown in both graphs. The dashed lines represent values for the parent sample. The numbers on the concentration-axes refer to the conditions listed in the experimental section……..74

Figure 3.7 XRD patterns of (a) ZSM-5_100, (b) HZ_100_OH1.5_NS, (C) HZ_100_OH1.5_S, (d) HZ_100_OH2_NS, (e) HZ_100_OH2_S, (f) HZ_100_OH3_NS, and (g) HZ_100_OH3_S. The reflection peak marked with an asterisk (*) originates from the α-alumina used as an internal standard. ……75

Figure 3.8 SEM images of (a) HZ_50_OH1_NS, (b) HZ_50_OH1_S, (c) HZ _50_OH2_NS, (d) HZ_50_OH2_S, (e) enlarged image of HZ _50_OH2_NS, (f) enlarged image of HZ _50_OH2_S, (g) HZ_50_OH3_NS, and (h) HZ_50_OH3_S. ……77

Figure 3.9 TEM images of (a) HZ_50_OH2_NS, (b) enlarged image of HZ_50_OH2_NS, (c) HZ_50_OH2_S, and (d) enlarged image of HZ_50_OH2_S. Enlargements of the squares in panels (a) and (c) are shown in (b) and (d), respectively……78

Figure 3.10 Nitrogen sorption isotherms for parent samples and samples prepared using different concentrations of base (A for HZ_50_OH1_NS/S, B for HZ_50_OH2_NS/S, and C for HZ_50_OH3_NS/S). In all graphs, the parent zeolite crystal ZSM-5_50, desilication products and desilication/re-assembly products are denoted as a, b, and c, respectively……79

Figure 3.11 (A–C) BJH pore size distributions of samples prepared using different concentrations of base: (A) HZ_50_OH1_NS (a) and HZ_50_OH1_S (b), (B) HZ_50_OH2_NS (a) and HZ_50_OH2_S (b), (C) HZ_50_OH3_NS (a) and HZ_50_OH3_S (b). (D) Comparison of pore size distributions for desilication products HZ_50_OH1_NS (a), HZ_50_OH2_NS (b), and HZ_50_OH3_NS (c). (E) Comparison of pore size distributions for desilication/re-assembly products HZ_50_OH1_S (a), HZ_50_OH2_S (b), and HZ_50_OH3_S (c). (F) The development of the dual-pore system of HZ_50_OH2_S after reaction times of (a) 4 h, (b) 13 h, and (c) 24 h……. 80

Figure 3.12 Influence of the hydroxide ion concentration and the presence of CTAB on (A) the surface area related to pores > 2 nm ("external surface area") and (B) the micropore volume. Data for the desilication products (HZ_50_OH(1, 2, 3)_NS) (a) and desilication/re-assembly products (HZ_50_OH(1, 2, 3)_S) (b) are shown in both graphs. The dashed lines represent values for the parent sample. The numbers on the concentration-axes refer to the conditions listed in the experimental section……...81

Figure 3.13 XRD patterns of (a) ZSM-5_50, (b) HZ_50_OH1_NS, (c) HZ_50_OH1_S, (d) HZ_50_OH2_NS, (e) HZ_50_OH2_S, (f) HZ_50_OH3_NS, and (g) HZ_50_OH3_S. The reflection peak marked with an asterisk (*) originates from the α-alumina used as an internal standard…… 82

Figure 3.14 ^{27}Al (left) and ^{29}Si (right) solid-state MAS NMR spectra for (a) ZSM-5_50, (b) HZ_50_OH2_NS, and (c) HZ_50_OH2_S……. 83

Figure 3.15 SEM (a) and TEM (b) images of the collapsed zeolite crystals after treatment in a high concentration of base (HZ_100_OH6_S)……...87

Figure 4.1 Illustration of different zeolite growth patterns obtained by programming sequences of IHT cycles with selected nutrient concentrations in the precursor that penetrates the 3DOM carbon reactor (L = low nutrient concentration, H = high nutrient concentration). (A) Growth of polycrystalline spheres in a sequence where nucleation dominates during each step. (B) Single crystal growth in a system where the low nutrient concentration favors slow growth. The circles represent single crystal domains spanning multiple macropores and the dashed black arrows indicate regions of merging domains. (C) Shape development from discrete, irregular seeds precipitated during an H step to faceted, coffin-shaped zeolite particles after changing to L steps to switch from nucleation to growth dominant conditions. (D) A secondary population of smaller zeolite particles results from a change of solutions that switch from growth to nucleation dominant conditions. The size of the templating macropores is the same in all cases…. 96

Figure 4.2 SEM images illustrating the different morphologies of silicalite products obtained after HT syntheses in 3DOM nanoreactors for varying processing conditions ……..101

Figure 4.3 SEM images of carbon-silicalite composites after the indicated number of IHTn cycles and after calcination (calc.)…… 102

Figure 4.4 Powder X-ray diffraction (XRD) patterns of carbon-silicalite composites after the indicated number of infiltration/hydrothermal reaction (IHTn) cycles (n = cycle number) and after calcination (calc.) ……..103

Figure 4.5 TEM images of IHT_2 (a) and IHT_5 (b)……..103

Figure 4.6 SEM images and photographs of the 3DOM carbon/silicalite composite after one and two IHT cycles (high silica concentration, outermost anionic polyelectrolyte layer). The SEM images show cross-sectional regions near the edge or near the center of

the monolith. Each monolith was fractured for SEM analysis after reaction and drying of the sample……....104

Figure 4.7 Photograph (top left) and SEM image (top right) of the calcined product consisting of a 3D array of close-packed silicalite spheres. Bottom: SEM images at different magnifications of a layer of spheres assembled on a flat silicon substrate after dispersion of the spheres in ethanol……105

Figure 4.8 SEM image of silicalite prepared inside 3DOM C with smaller, 110 nm diameter pores (high silica concentration, outermost anionic polyelectrolyte layer). Although the nanoporous reactor is less ordered, the product morphology is similar to that obtained in the larger macropores. Some spheres with smooth surfaces and some more corrugated particle agglomerates are observed after the 3rd IHT cycle…….106

Figure 4.9 SEM image of geode-like polycrystalline zeolites (a) and photograph image of the geode structure of an amethyst (b), a larger analogue for the much smaller hollow spheres shown in panel (a)……...107

Figure 4.10 SEM images illustrating sequential single crystal growth using precursor L: (A) to (D) crystal domain growth in sequential IHT reactions after cycles L_2, L_3, L_5 and L_7, respectively, (E) different region after L_7, (F) after L_{11}, (G) calcined sample after L_{13}, (H) after L_{15}, (I) enlarged image of (H)……..109

Figure 4.11 (A) SEM and (B) TEM images of the sample formed after L_5 and subsequent calcination. An SAED pattern of the particle shown in (B) is provided in the inset of (B)……...110

Figure 4.12 TEM images of various shaped zeolite crystals after cycle L_{11}: (A) A sphere templated by one macropore. The inset shows the corresponding selected area electron diffraction (SAED) pattern, confirming that the sphere is a single silicalite-1 crystal. (B) A representative crystal showing the influence of confinement on the characteristic coffin-like morphology of silicalite-1. The crystal is faceted along the *a*-planes. The facet marked by the white arrowhead is enlarged in the high resolution TEM image. (C) Three spheres with outgrowths. (D) High resolution image of the area marked by the white

arrowhead in panel (C). The outgrowth follows the *c*-direction and its width is close to the size of windows in 3DOM carbon. The inset shows the corresponding SAED pattern. A similar particle can be seen in the center of the SEM image shown in Figure 1F….113

Figure 4.13 SEM images illustrating the shape development of zeolite particles during programmed growth with multiple concentration schedules: (A) Product obtained after H_1. (B) Product obtained after a H_1L_1. (C) Product after H_1L_2, clearly showing faceted, coffin-like crystals. The white arrows point at twinned crystals. (D) Product after H_1L_3 and (E) product after H_1L_4. At these stages, crystals aggregate and growth becomes limited by confinement inside the 3DOM carbon monolith. (F) A secondary population of irregular zeolite particles is produced after applying precursor H following six L cycles (L_6H_1). ……..115

Figure 4.14 TEM images illustrating the shapes, pore structures and crystallinity of the faceted, coffin-like products shown in Figures 4B and 4C: (A) and (B) low magnification images of the products obtained after cycles H_1L_1 and H_1L_2, respectively, (C) and (D) higher magnification images of crystals obtained after cycle H_1L_1. The black arrows in (B) indicate twinned structures and the white arrow in the (C) indicates the *c*-orientation. FFT patterns of the TEM images in (C) and (D) are presented in the insets……...116

Figure 4.15 SEM image showing that a secondary population of irregular zeolite particles is produced after cycle L_6H_1. This is the same image as Figure 4.13F……118

Figure 5.1 Permeation setup for xylene isomer separation…… 128

Figure 5.2 Fabricating the high-performance zeolite membrane. Polycrystalline spherical aggregates of silicalite-1 (300 nm in diameter) were prepared by confined synthesis in 3DOM carbon[31]. These aggregates were broken down into single crystal grains (50–100 nm) by rubbing them directly onto a home-made α-alumina support to form a seed layer. Any remaining aggregates were either pushed down deeper into pores of the support or broken down further by a leveling process. The high-quality seed layer was used to prepare well-intergrown and very thin (400–500 nm) zeolite membranes with appropriate secondary growth conditions. The thin zeolite membranes were thermally treated to

remove SDA molecules by conventional calcination (CC) or a rapid thermal processing (RTP) step……130

Figure 5.3 SEM image of polycrystalline spherical aggregates produced by five IHT cycles (a) and XRD patterns of a seed layer prepared by the rubbing and leveling methods on the porous alumina disc after removal of a PEI layer (b). The two indexed peaks in the right image (b) are characteristic for silicalite-1. The scale bar in (a) is 500 nm and the reflection peak marked with an asterisk (*) originates from the α-alumina support (b)……...131

Figure 5.4 Development of the membrane. a-e, SEM images of seed layers and silicalite-1 seeded membranes on a porous α-alumina support at various stages of the fabrication process. **a,** Top view of a seed layer after the rubbing step and **b,** after rubbing and leveling. After secondary hydrothermal growth, intergrown MFI-zeolite layers are formed. **c,** In membranes prepared without leveling (denoted as R-membranes), several protrusions remain after secondary growth, but **d,** they are not prominent in membranes grown from the leveled seed layers shown in **b** (denoted as RL-membranes). **e,** The cross-sectional view of the RL-membrane after secondary growth shows an ultrathin MFI-zeolite layer on top of the α-alumina support. All scale bars correspond to 500 nm. **f,** X-ray diffraction patterns of zeolite films treated by conventional calcination (CC) and rapid thermal processing (RTP). The reflection peak marked with an asterisk (*) originates from the α-alumina support……133

Figure 5.5 Development of the membrane. Low magnification SEM images of seed layers (**a** and **b**) and zeolite membranes after secondary growth (**c** and **d**). **a,** The seed layer prepared by the rubbing process. **b,** The seed layer after rubbing and leveling processes. **c,** The zeolite membrane (R-membrane) prepared from **a** via secondary growth shows numerous protrusions. **d,** Most of these are absent in the zeolite membrane prepared from **b** after secondary growth (RL-membrane). The scale bar corresponds to 5 μm in all images……...134

Figure 5.6 MFI-zeolite membrane prepared by extended secondary hydrothermal growth (100 ˚C for 20 h). **a,** An SEM image showing a top view of the membrane after

calcination. The scale bar corresponds to 1 μm. **b,** The XRD pattern shows features characteristic for preferred *hoh*-out-of-plane orientation of the crystallites. The asterisk marks a reflection originating from the α-alumina support. ……..136

Figure 5.7 Permeation data and *p-/o*-xylene separation factors for nanocrystal-seeded membranes thermally-treated by conventional calcination or rapid thermal processing. Graphs **a** and **b** correspond to R-membranes prepared without a leveling step and thermally treated by CC and RTP, respectively. Graphs **c** and **d** correspond to RL-membranes from preparations in which a leveling step was used and membranes were thermally treated by CC and RTP, respectively. Data points and error bars in graph **d** correspond to the three RL-membranes with separation factors in the range from 123 to 139……138

Figure 5.8 Thermal stability test of RTP-treated RL-membrane. The zeolite membrane was maintained at 100 °C for 12 h to fully adsorb xylene vapor. The stability test was profiled at 175 °C. The x-axis presents the permeation test time at 175 °C after staying at 100 °C for 12 h…….140

Figure 5.9 X-ray photoelectron spectra. Al on the surface of the RTP treated RL-membrane was identified……..... 141

Figure 5.10 SEM images of the RL-membrane prepared at 175 °C for 1h hydrothermal reaction and after conventional calcination to remove SDAs: (a) The plain view of the zeolite membrane. (b) The cross-sectional view of the zeolite membrane. ……142

Figure 5.11 XRD patterns of the RL-membrane prepared at 175 °C for 1h hydrothermal reaction: (a) after RTP treatment (b) after RTP and conventional calcination (CC) treatment. ……143

Figure 5.12 Permeation data and *p-/o*-xylene separation factors for CC-treated RL-membrane (a) and RTP-CC-treated RL-membrane (b)……...144

Figure 5.13 Schematic illustration of zeolite membrane fabrication on the stainless steel tube. After two times of seed deposition of polycrystalline aggregates (right top),

secondary hydrothermal growth was performed and the zeolite membrane was calcined by conventional calcination (right bottom)…….145

Figure 5.14 Two different strategies to fabricate zeolite membranes on the stainless steel tube support: (a) multiple-seeding of polycrystalline aggregates by the rubbing and leveling methods, and secondary growth for filling in the spaces between seed particles, and (b) deposition of big MFI crystals on the support and subsequent seeding of polycrystalline aggregates on the first seed layer, and secondary growth followed for zeolite membrane fabrication……..…….146

Figure 5.15 SEM images of the surface of the stainless steel tube (a), a seed layer after multiple-seeding of polycrystalline aggregates by the rubbing and leveling methods (b), the surface of zeolite membrane after CC treatment (c), and the zeolite membrane after RTP treatment (d). PEI polymer layer was removed by calcination (450 °C for 3 h) after each deposition process. SEM measurements were accomplished without coating for all samples…….……...147

Figure 5.16 SEM images of the surface of the big MFI seed layer (a), a seed layer after multiple-seeding of polycrystalline aggregates (b), the surface of the zeolite membrane after CC treatment (c), and the zeolite membrane after RTP treatment (d). Big MFI seeding and polycrystalline aggregate seeding were accomplished by the rubbing and leveling methods. The PEI polymer layer was removed by calcination (450 °C for 3 h) after each deposition process. SEM images were obtained without coating for all samples..……148

Figure 6.1 An illustration for fabrication of dual/multi-component polycrystalline catalysts via nucleation dominant conditions..…….... 155

Figure 6.2 An illustration for 3DOM imprinted dual/multi-component catalysts. ……155

Figure 6.3 An illustration of a metal-nanoparticle/zeolite composite catalyst……...156

Figure 6.4 SEM images of Au nanoparticles inside 3DOM carbon: (a) the plain view and (b) the cross sectional view. The negatively charged Au nanoparticles were located inside

positively charged 3DOM carbon by vacuum infiltration of an Au nanoparticle solution ……156

Figure 6.5 An illustration of impregnation of metal ions into zeolite frameworks through the surfactant-induced re-assembly process. ……..157

Figure 6.6 Nanosized and coffin-shaped MFI zeolites after several infiltration hydrothermal reaction cycles of H_1L_2. SEM image (a) of MFI nanocrystals after calcination and the corresponding TEM image (b)…….158

Chapter 1
An Introduction to Porous Materials

1.1 Motivation for Morphology Control of Porous Materials

Whenever I am asked what I am doing in the graduate study from people in other fields, the answer is always the same: "I am making some porous materials like a sponge, and use them for separation of smaller ones from mixtures with larger ones". Surprisingly, everyone can understand it very easily because they know what a sponge is, at least. This generality of porous materials attracted me to this area and guided me forward to study more practical and advanced applications of porous materials.

Porous materials have high surface areas and wide ranges of pore sizes.[1-3] Via functionalization, the utility of porous materials can be improved further.[4,5] Therefore, porous materials have been used in various applications from purification of water by ion exchange to catalysts for the petroleum industry and medical diagnostics.[1,2,6] In particular for applications, control over the morphology of porous materials is desired, including control over shape, size, texture and phase distribution of components. For example, sphere-shaped mesoporous materials are suitable for drug/gene delivery vehicles because of relatively short diffusion lengths for loaded guest molecules, which can be released by various methods.[7-9] For packing materials used in chromatography, the size and monodispersity of packing materials should be well controlled.[10-12]

This thesis will focus on methods for controlling the morphology (size, shape and texture) of porous materials with silica and aluminosilicate compositions. It describes methods for controlling textures of mesoporous silica spheres and introducing mesopores into zeolite crystals by re-precipitation of dissolved species via surfactant-induced micelle formation under hydrothermal reaction conditions.[13,14] In addition, the use of three-dimensionally ordered macroporous (3DOM) carbon materials as a massively parallel reactor for growth and shape development of zeolite crystals is illustrated.[15,16] Furthermore, techniques for using zeolite crystals with controlled shapes as seed particles for fabrication of molecular sieve zeolite membranes are outlined. A novel method was developed to create zeolite membranes and the performance was tested.[17]

In this chapter, general background information and concepts of morphology control of porous materials will be addressed. In addition, applications of porous materials, especially zeolite film fabrication, will be introduced. In the following chapters, the experimental details and results will be described.

1.2 Overview of Porous Materials

Porous materials can be classified in terms of pore sizes by the definition of the Internation Union of Pure and Applied Chemists (IUPAC): microporous materials have pore sizes less than 2 nm, mesoporous materials have pore sizes in the 2–50 nm range and macroporous materials have pore sizes larger than 50 nm.[18] Porous materials have been of significant interest due to their intrinsic properties of defined pore structure and high surface area that can allow interactions with ions, atoms and molecules.[1-3] Therefore, porous materials have been widely applied to catalysis, ion exchange, adsorption, separation, etc.[1,2,6,19,20] Furthermore, incorporation of functional groups can be accomplished via various chemical methods, which makes porous materials more attractive for advanced applications.[4,5]

As examples of microporous materials, activated carbon materials and zeolites are well known.[2,21] Activated carbon materials present less defined pore sizes and disordered pore alignment.[21] On the other hand, zeolites, which are commonly aluminosilicate crystalline materials, exhibit well defined pore sizes and 2-D or 3-D networks. The sizes of pores in zeolite materials are well matched to molecular sizes so that these materials can be used as molecular sieve separation membranes.[2,19] In addition, aluminosilicate zeolite materials have an intrinsic negative framework charge that can be compensated by various metal cations. Furthermore, the negatively charged networks can incorporate protons, which then render the framework acidic. Therefore, zeolites have been widely used as acid catalysts in industrial processes.[1,6]

Recently, microporous metal organic frameworks (MOFs) have generated much interest. Metal ions act like “joints” for connecting "strut"-like organic ligands to form microporous frameworks.[22,23] The flexibility of the choice of metal ions and organic ligands has been of great interest in gas molecule adsorption, catalysis and molecular sieve membrane separation.[24-26]

For mesoporous materials, the size and the alignment of mesopores can be controlled via various synthetic conditions.[3] Furthermore, incorporation of functionalities can be accomplished via chemical methods.[4,5] Numerous advantages of mesoporous materials have made these attractive for various applications including not only adsorption and catalysis but also composite materials for advanced applications, such as electrodes of batteries materials, drug delivery vehicles and chemical sensors.[4,5]

For macroporous materials, the size of pores is larger than 50 nm. These materials can be prepared by various methods. For example, well ordered macroporous materials can be fabricated by infiltration of matter into colloidal crystal templates that consist of spheres larger than 50 nm in size.[27,28] After removal of the colloidal crystal templates, the inverse structures with well-ordered macroporous features are obtained.

1.3 Microporous Materials

Zeolites have been found in nature as volcanic rocks and ash layers.[29] Through long time crystallization in these environments, natural zeolites have been formed. However, due to the impurities involved in natural zeolites and the more practical aims, artificial zeolites have been designed and synthesized. So far, around 150 zeolite types (Figure 1.1 for MFI framework type zeolite) have been synthesized and 48 types of natural zeolites are known.[29]

Zeolites have well defined pore structure and intrinsic acidity, so that zeolites have been widely used in catalysis, ion exchange and separation. For advanced applications, it is desirable to control the morphology of zeolites. In the following sections, the crystallization mechanism and morphology control of zeolites will be discussed.

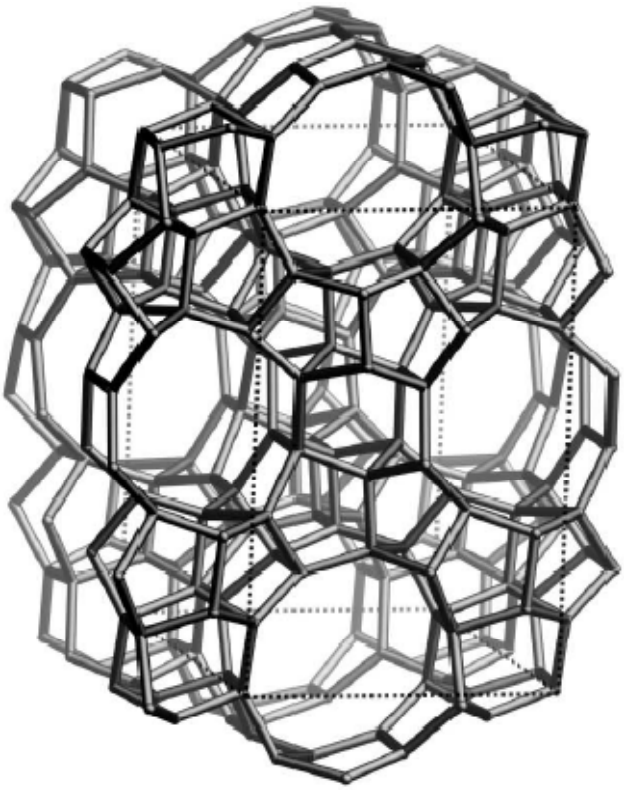

Figure 1.1 MFI zeolite. The framework is viewed along the [010] direction.[30]

1.3.1 Mechanisms of zeolite crystallization

Microporous crystalline materials (zeolites) consist of corner-shared TO_4 tetrahedra (T = Si^{4+}, Al^{3+}, P^{5+}, Ge^{4+} etc.).[31-33] The tetrahedral framework forms well defined pore structures with unique geometry. Aluminosilicates are the most well known zeolite materials. The synthetic precursors for zeolites contain sources of T atoms, a mineralizing agent (OH^- or F^-), structure directing agents (SDAs, soluble quaternary ammonium ions and alkali metal ions such as Na^+ or K^+) and water.[31] The precursor mixtures usually undergo hydrothermal reactions, and then as-made products usually are calcined to open up the pores filled by SDAs. The thermal and chemical stability of zeolite materials are superior to those of mesoporous materials so that zeolites have been used widely in industry as catalysts.

According to Davis and co-workers, in the initial step, water molecules assemble around hydrophobic silicates and organic SDAs, called hydrophobic hydration.[31,34,35]

When the hydrophobic spheres of SDAs and silicates overlap (enthalpy driving force) through weak van der Waals forces, trapped or ordered water molecules are released from the assembly to the bulk water phase, causing an entropy gain in the system. The primary units of assembled species are adsorbed into big crystals through an Ostwald ripening process, or more aggregated to reduce the surface energy. The aggregates are then nucleated via cross-linking of silicates around SDAs that imply microscale pores. Finally, big crystals are produced through aggregation of nuclei or adsorbing the primary units by an Ostwald ripening process. These postulates were studied by solid-state NMR. Even though the tetrapropylammonium (TPA) ion was used as a representative SDA for this reaction, it has been generally accepted as a model system to understand the crystallization mechanism of zeolite materials in general (Figure 1.2).

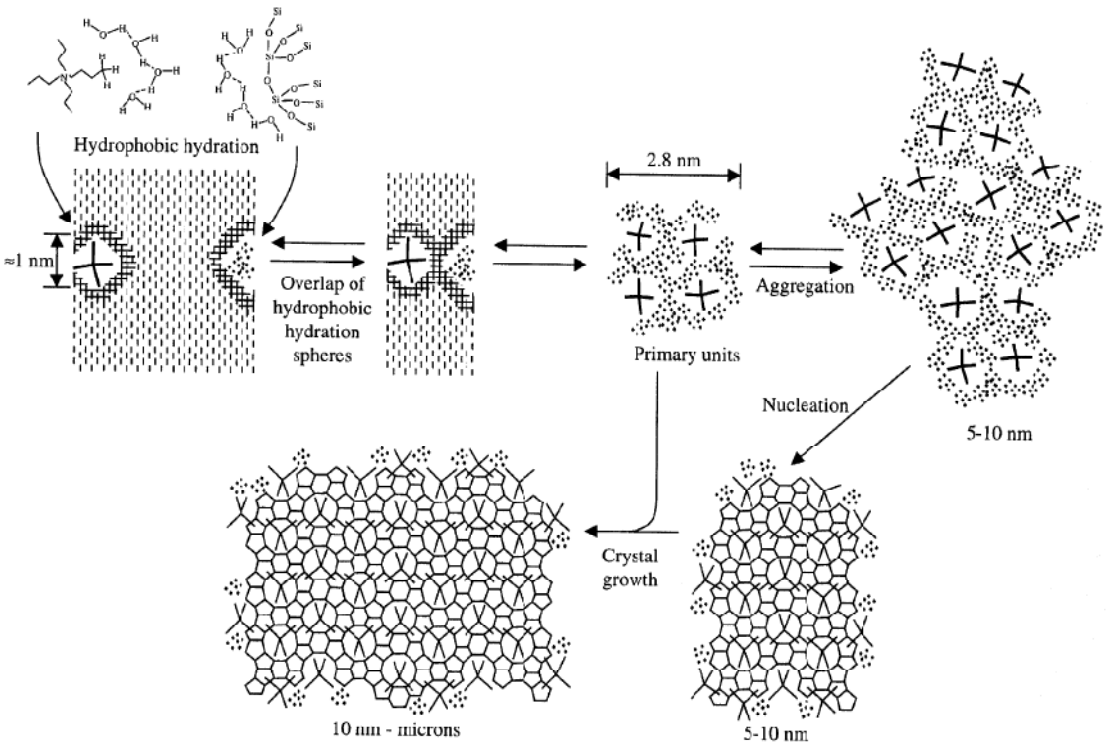

Figure 1.2 Schematic illustration for the crystallization mechanism of pure silica MFI.[34]

1.3.2 Morphology control of microporous materials

Morphology control of zeolite materials is important for advanced applications. For example, zeolite membranes prepared by secondary growth methods need seed particles with uniform size and shape.[19] In addition, zeolite catalysts need to have a more open structure to facilitate diffusion of guest molecules to active catalytic sites.[36-41] Fabrication of zeolites with extra mesoporosity called meso-zeolite materials will be the focus of this section.

1.3.2.1 Direct synthesis of meso-zeolite materials

Limited diffusion of guest molecules to active sites of zeolite materials has been a major obstacle for using zeolites most effectively as catalysts. Much effort has been devoted to solve this problem through the following approaches: fabrication of extra large pore zeolites (more than 12-membered rings of T-atoms) with various compositions[31-33], preparation of layered structures[42,43], use of dual-templating for creation of combined meso-/micro-pores[44], use of an additive in conjunction with SDAs to introduce mesoporosity,[36,45,46] and a template-assisted method to produce nanosized zeolite crystals.[15,16,37-39,47,48] My focus in this thesis is on creating extra porosity with mesopore sizes (> 2 nm) in the zeolite materials, so extra large pore zeolites and layered structures will not be discussed.

Recently, Ryoo and co-workers synthesized a dual-template with di-quaternary ammonium moieties connected with a C6 alkyl linker and a long alkyl chain (C22) at the tail, which can serve as both a SDA and for mesoscale micelle formation (Figure 1.3).[44,49] This dual-template can generate zeolite frameworks by its hydrophilic head groups while limiting growth in certain directions (here, *b*-axis of MFI type zeolite) to create mesoscale voids (Figure 1.4). MFI nanosheets show a very high surface area (> 700 m^2 g^{-1}) with relatively tunable mesopore size from ca. 3 to 15 nm inside MFI zeolites. Furthermore, they can present not only increased external surface area for more access of large molecules, but also reduced coke formation during catalytic reactions. More durable catalytic reactions were achieved by MFI nanosheet catalysts compared to conventional MFI zeolites because coke formation mainly occurred in the mesoporous part rather than

on the micropores. However, the need to design a dual-template for other types of zeolites still remains.

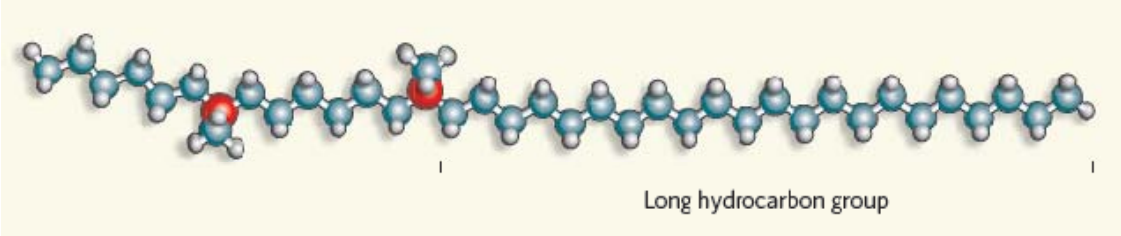

Figure 1.3 Structure directing agent (SDA) for a two-dimensional zeolite. Two positively charged nitrogen atoms in the SDA control the assembly of the inorganic framework, while a long hydrocarbon group prevents growth of the zeolite in the direction in which that group extends.[49]

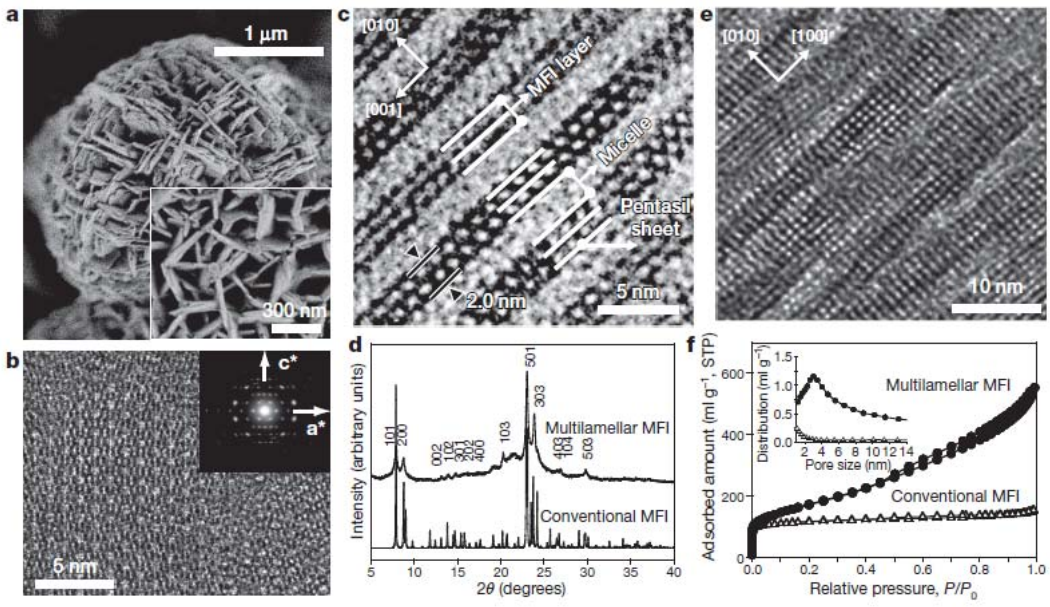

Figure 1.4 MFI nanosheets with a multilamellar structure. SEM image (a) and TEM images (b, c, e) present structural features. X-ray diffraction (XRD) patterns (d) confirm the crystallinity, and nitrogen isotherm and pore size distribution (f) the mesoporosity of this method.[44]

On the other hand, use of an additive with SDAs can also produce meso-zeolite materials. The additive should be well accommodated not only with SDAs but also with precursor compositions and high pH conditions. The main concept is incorporation of SDAs with hydrophobic moieties modified with silicon alkoxides for co-condensation with zeolite frameworks. Polymers (i.e., polyethyleneimine, PEI) or long alkyl chains of a quaternary ammonium backbone are functionalized with silicon alkoxides. The additives can be miscible with the combination of SDAs and precursor solutions to form a mesoscale porogen that can be removed by calcination (Figure 1.5).[36,45,46,50] Relatively good fine-tuning of mesopore sizes was achieved by altering the molecular weight of the polymer or the alkyl chain length.

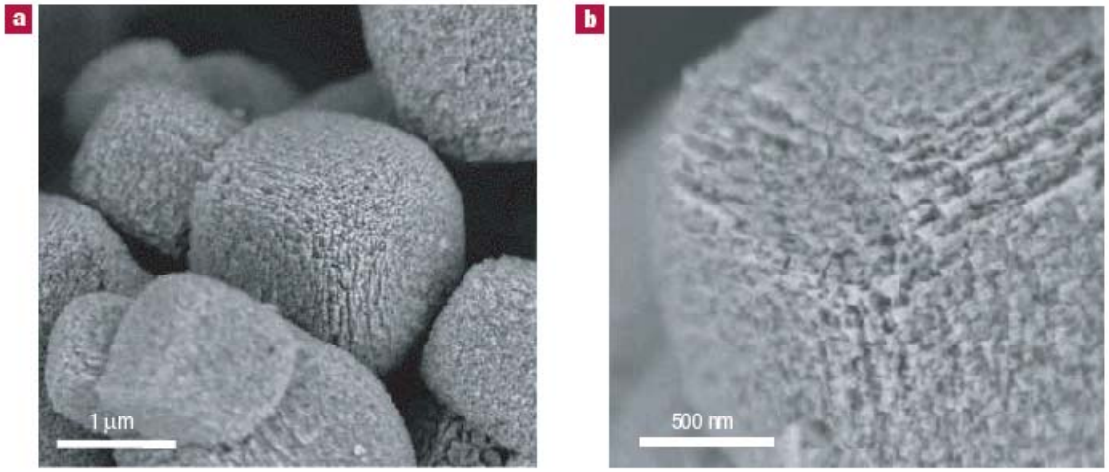

Figure 1.5 SEM images (a and b) of meso-zeolite LTA synthesized using $(CH_3O)_3SiC_3H_6N(CH_3)_2C_{16}H_{33}$ as a porogen.[46]

1.3.2.2 Template-assisted method

Well-defined porosity can be achieved by a template-assisted method. This concept could be considered as a type of nanocasting[51,52] that generates molded materials dictated by a preform that could include not only porous frameworks but also an object to make porosity in the final products. For example, nanosized carbon particles (ca. 10 nm) can be employed to create mesoporosity in zeolite materials (Figure 1.6).[37,47,53,54] Conventional zeolite syntheses were carried out in a reaction vessel that contained carbon

particles. The final products presented mesoporosity in the single crystal zeolite materials, by which the inert carbon particles were incorporated in the crystal growth to create mesoscale pores. In addition, colloidal crystal templates ordered with face-centered cubic (FCC) symmetry and inverse structures of colloidal crystal templates can be used as a preform for fabrication of extra porous zeolite materials. For example, small silica spheres (ca. 10-40 nm in diameter) were assembled with FCC symmetry. The voids in between silica particles were infiltrated with a carbon precursor. After carbonization and removal of silica spheres, the inverse FCC structures called three-dimensionally ordered mesoporous (3DOm) materials were obtained (Figure 1.7).[38,55] This 3DOm template showed very well ordered symmetry and tunable porosity, resulting from the use of colloidal crystals of monodisperse silica spheres. This 3DOm template was employed for growing zeolite materials. After calcination to remove the template, the 3DOm-imprinted zeolite materials showed size tunable mesoporosity with 10-40 nm pores inside zeolite frameworks.

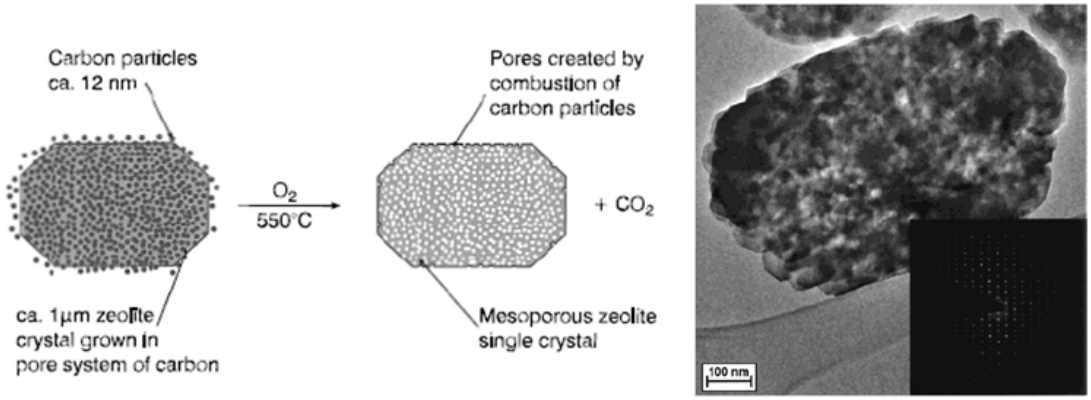

Figure 1.6 Growth of zeolite crystals around carbon particles. TEM image (right) shows an isolated single ZSM-5crystal and the electron diffraction patterns (inset).[47]

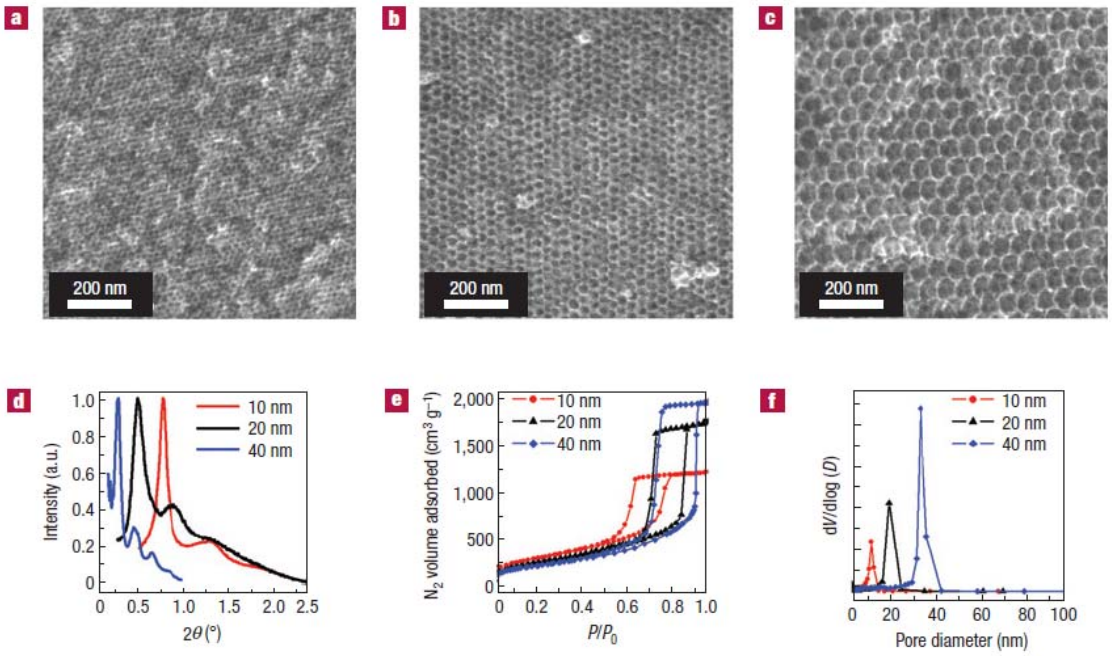

Figure 1.7 Three-dimensionally ordered mesoporous (3DOm) carbon templates with SEM images (a-c) representing different pore sizes, 10 nm, 20 nm and 40 nm, respectively. Small angle X-ray scattering (SAXS) data (d), nitrogen sorption isotherms (e) and BJH pore size distribution obtained by nitrogen sorption measurements (f).[55]

In addition, very small zeolite particles can be obtained through the template-assisted method. According to a report by Fan et al., isolated zeolite particles with sizes of 10-40 nm in diameter can be obtained by disconnection of 3DOm zeolite crystals (Figure 1.8).[55] By conventional hydrothermal reactions, it is much more difficult to produce small zeolite particles with diameters less than 50 nm and requires very long reaction times on the order of months.[55,56,63,105] The monodisperse and small zeolite particles (< 50 nm) could be useful as seed particles for secondary-growth-assisted zeolite film fabrication.

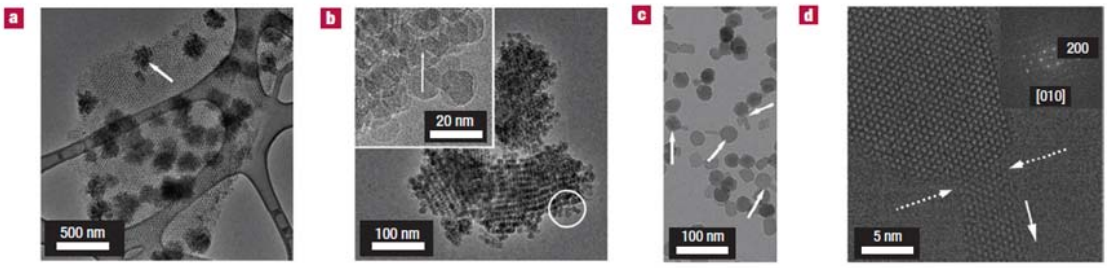

Figure 1.8 TEM images of zeolite crystals produced inside 3DOm carbon as a template. (a) and (b) show MFI crystals inside templates, and (c) and (d) present isolated MFI crystals.[55]

1.3.2.3 Post-synthesis treatment to form meso-zeolite materials

Two different (or maybe opposite) approaches — dealumination and desilication — have been used to create mesoporosity in zeolite crystals. First, dealumination by thermal treatment (e.g., steam treatment) or acid treatment has been a well known post-synthetic method to create mesoporosity in zeolite crystals.[57,58] Selective removal of Al from the zeolite frameworks generates extra pores. However, it increases the ratio of Si/Al (lower Al content) compared to the parent zeolites and decreases the intrinsic Brønsted acidity, which usually reduces the overall acidity of the zeolite catalysts.

The aforementioned drawbacks could be compensated by use of a desilication method as a post synthetic approach.[40,59-61] Under basic conditions, selective removal of Si atoms produces extra pores throughout the zeolite framework (Figure 1.9). It extracts Si from the framework, so that the Si/Al ration decreases (higher Al content) and the external surface area easily increases up to 250 $m^2 g^{-1}$ with relatively well preserved micropore volumes (ca. 70 %) compared to the parent zeolites. In addition, the intrinsic acidity (the Brønsted acidity) is still maintained. Moreover, the Si/Al ratio can control the mesoporosity of the zeolite structures: lower Si/Al ratios (e.g., Si/Al = 15) of zeolites generate less open structures because the higher Al content preserves the frameworks more against attack under basic conditions. On the other hand, higher Si/Al ratio (e.g., Si/Al = 200) zeolites are more readily dissolved by base due to the lower Al content of the zeolite crystals.

One of the advantages of the desilication method is the ease of the process and the generality of this method for most types of zeolites. According to papers by Pérez-Ramírez and co-workers, mild synthetic conditions (i.e., treatment with 0.2 M NaOH for 30 min at 338 K) can generate mesoporosity in various types of zeolites (i.e., MFI, BEA, FER and MOR).[60,61] The mesopore size distribution (ca. 10 nm measured by BJH method) can be controlled by different Si/Al ratios, reaction temperatures, base concentrations and reaction times. In addition, the produced mesopore sizes are smaller than those (ca. 20-30 nm) obtained from dealumination methods.[60]

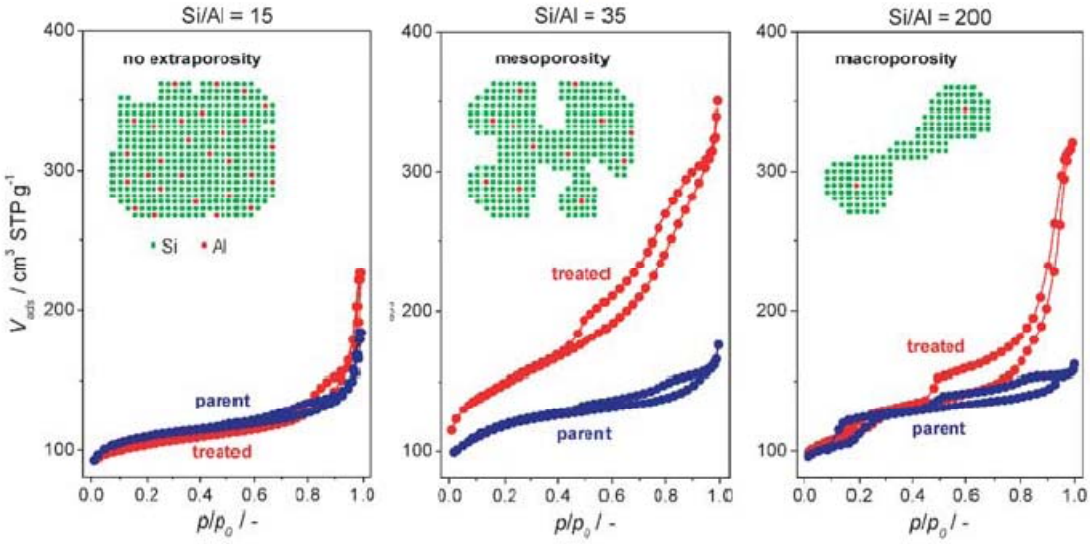

Figure 1.9 The schematic illustration of the desilication method with different Si/Al ratio and the corresponding nitrogen sorption isotherms.[40]

1.4 An Introduction to Zeolite Films

The crystalline nature of zeolites gives rise to chemical and physical robustness for high temperature and pressure catalytic reactions that are of much interest in industrial processes. In addition, the tunable and well defined pore structures of zeolites can be utilized for "molecular sieving": separation of molecules whose sizes are similar to each other. Zeolite films for separation have been of interest as alternatives to conventional industrial separation processes, i.e., distillation and crystallization.[62-72]

Moreover, size-selective separation and catalytic performance of zeolite films utilized in catalytic membrane reactors could be implemented for simultaneous separation and catalysis.[66,73-75] Furthermore, chemical sensors[76,77] and low-k dielectric materials[77,78] for microelectronics in the semiconductor industry could also be accomplished through fabrication of zeolite films.

Polycrystalline zeolite films with the intrinsic capability of size-selective molecular separations have been intensively studied.[62,65] Many types of zeolite films have been employed for separation of different molecular mixtures, depending on the size of the pores.[63,66,69,72,79,80] Among those, silicalite-1 or siliceous ZSM-5 zeolite (MFI framework type) films have been widely investigated as model membranes for manufacturing processes. MFI zeolites have been widely studied and the target separations (i.e., hydrocarbon isomers, organic/water or alcohol/water) are related to industrially important raw materials (Figure 1.10).[62,65,67,81-83] For example, xylene isomer separation using MFI zeolite films has been reported because MFI has the proper pore size (ca. 6 Å) that can allow *p*-xylene (kinetic diameter ca. 5.8 Å) to pass through the membranes but not for bulkier *o*-/*m*-xylene (kinetic diameter ca. 6.8 Å). Xylene is one of the important raw materials in the petrochemical industry as precursors and solvents with an annual production of 22 million tons.[84] Xylene can be produced by various catalytic chemical reactions of other raw materials (e.g., toluene or naphtha) and as a byproduct from steam cracking of hydrocarbon feeds (pyrolysis of gasoline).[85,86] However, the thermodynamic equilibrium of *p*-xylene (24.8 %), *m*-xylene (53.4 %) and *o*-xylene (21.8 %) at 377 °C has limited the production of high purity of *p*-xylene from catalytic isomerization.[87] The separation has been achieved by energy-intensive fractional crystallization or distillation. Therefore, the opportunity for MFI membrane reactors to selectively separate *p*-xylene during the reaction could be an alternative less energy-intensive process.

Among various synthetic methods to fabricate zeolite membranes, such as steam assisted crystallization,[88,89] electrochemical methods,[90] microwave assisted methods[91,92] etc.,[93-97] seeded growth or secondary hydrothermal growth methods for zeolite membrane fabrication have received much attention due to their reproducibility in forming well developed continuous films.[62,64,76,82,83,98]

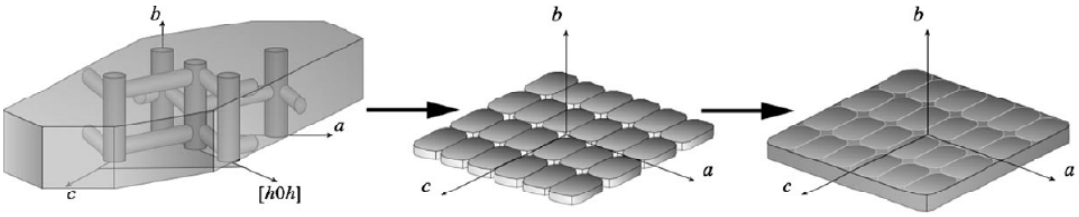

Figure 1.10 Schematic illustration of zeolite film processing (secondary growth method) using molecular sieve particles (MFI, left) as building blocks to form crystal monolayers (middle) and oriented, intergrown films (right).[19,62]

1.4.1 Seed deposition

The general synthetic procedure involves the following steps: zeolite particles deposited on a support are immersed in the precursor solution, and then zeolite growth occurs from the seed particles during the hydrothermal reaction, and eventually intergrown zeolite films are fabricated. Therefore, effective seed deposition is a crucial step to producing high quality zeolite films.

Prof. Yoon has developed seed deposition methods involving various interactions between seeds and supports.[99] Chemical or physical interactions, i.e., covalent linkage, H-bonding and ionic bonding (Figure 1.11), can be achieved via surface modification of the seeds and the supports, which can generate a high quality monolayer of seed particles over centimeter-scale supports. The concept is that only the seed and the support interact, but not the seeds amongst themselves. The general synthetic process takes place in a non-humid environment using an organic solvent (e.g., toluene). The functionalized support is located in between glass slides in the organic solution containing functionalized zeolite particles. The reaction vessel is then transferred to a sonication bath where sonic power causes the glass to vibrate. During sonication that also generates heat into the system, limited amounts of seed particles are introduced into the gap between the glass and the support. Chemical or physical interaction is achieved to produce a monolayer of seeds. Generally, the face that has a higher surface area is favorably deposited on the support when anisotropic zeolite particles are used. However, it is also possible to control the orientation of seed deposition when a uniformly aligned polymer layer is used as a template for aligning zeolite particles (Figure 1.12).[100]

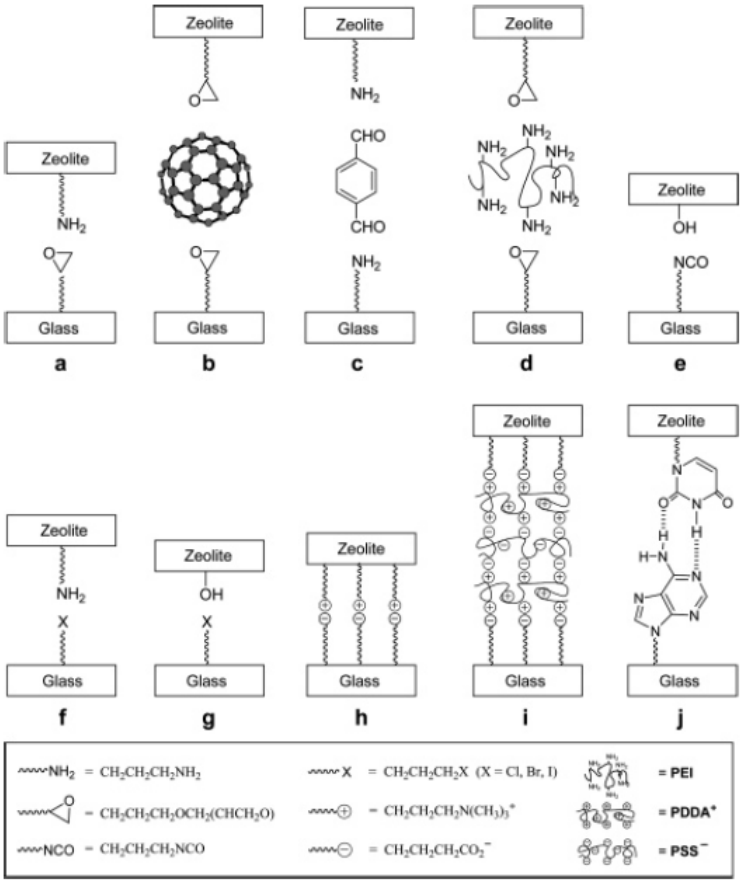

Figure 1.11 Various types of molecular linkages.[99]

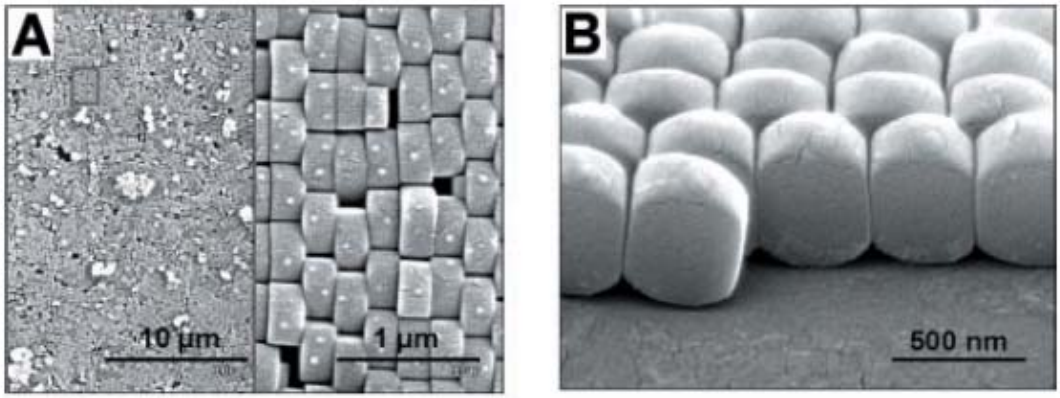

Figure 1.12 SEM images of a 2-D array of closely packed, uniformly aligned silicalite-1 crystals grown on the polymer coated glass slide. (A) Crystals grown in high coverage. (B) The orientation of the crystals with their *c* axes perpendicular to the glass plane.[100]

Recently, dry manual assembly by the so called the "rubbing method", was developed by Yoon and co-workers.[101,102] Gently rubbing zeolite particles on the functionalized support can generate monolayer quality seed deposition. During rubbing, zeolite particles above the first layer on the support are removed due to relatively weaker interactions between particles, compared to stronger interactions between the first layer and the support (Figure 1.13). The whole process time depends on the size of particle and the support, but it usually takes several minutes. Compared to the sonication-assisted method, the rubbing method can reduce the processing time greatly while maintaining the quality of seed deposition.[98,99,101,102] Recently, an evaporation-assisted deposition method was reported, in which a zeolite (MFI) suspension in the solvent mixture (*sec*-butanol and a trace amount of linoleic acid) was gently dropped on the water-covered porous substrate.[76,103] Controlled evaporation allowed the larger surface area face (*a*-*c* plane of MFI) of anisotropic MFI crystals to settle down on to the support and produced a monolayer quality of *b*-oriented MFI zeolites on the various porous supports.

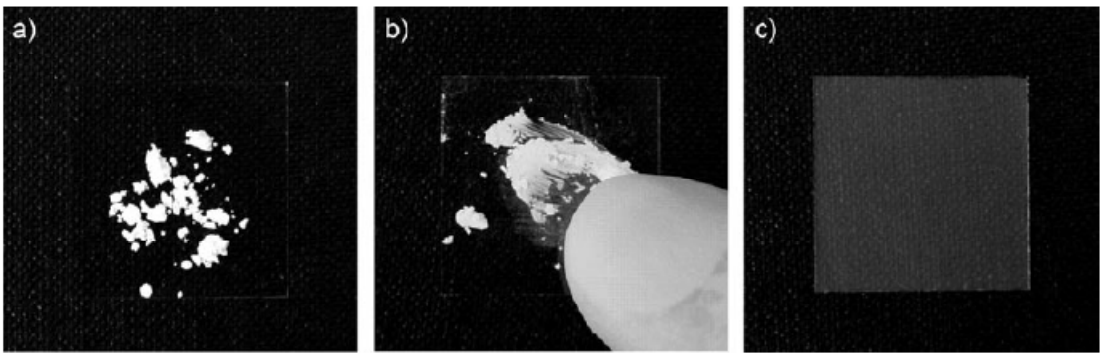

Figure 1.13 Photographic images showing the process (a-c) of monolayer assembly of silicalite-1 microcrystals on glass.[101] (a) A certain amount of zeolite particles is located on the functionalized glass slide. (b) Zeolite particles are rubbed by a gloved finger. (c) After rubbing, the appearance of the glass changes from transparent to milky.

On the other hand, for size-selective separation using zeolite films, the seed deposition should be done on porous supports (e.g., porous alumina or porous stainless steel tube). Preparing a high quality seed layer on the porous support demands that the surface of the support is smooth. Therefore, a very thin mesoporous silica layer or a waxing method have been widely used.[62,83,104-106] For use of mesoporous silica, the mosoporous silica layer (ca. 2 nm pores) is first covered by slip casting on the porous support, which can provide a continuous and smooth surface on the support. This silica layer can be decorated with a tethering molecule that can have an interaction with a functional group on zeolite particles to produce a seed layer. When a mesoporous silica layer covers the support, the flux decrease of xylene isomer is around 5 %.[107] In addition, it was noted that this interlayer could prevent the aluminum leaching from the alumina disc, in which it causes coking and eventually, blocking of the pores of the zeolite films.[107]

In the waxing method, wax is imbedded inside porous support to provide a smooth surface for seed deposition and prohibiting zeolite growth inside the support during secondary growth.[104,105] After secondary growth to fabricate zeolite films, the wax is removed by calcination or dissolution with a solvent.

1.4.2 Oriented MFI zeolite films

The MFI zeolite has a multidimensional pore system (see the Figure 1.10 left for the multidimensional pore system of MFI): the *b*-axis has intersecting straight channels and the *a*-axis has sinusoidal or zig-zag channels. Adsorption and diffusion of molecules are different depending on the molecular pathway through these pore directions.[62,83,108] For size-selective separation of xylene isomers, for instance, the straight channel direction of zeolite membranes presents faster *p*-xylene flux that does not pass through interconnection of other directions.[83] Manipulation of zeolite membranes with certain orientation could thus be addressed by microstructure design, high quality seed deposition techniques and control of crystal growth during secondary growth.

First, for morphology control of the microstructure of MFI, the spherical and the signature coffin-type structures can be produced when the tetrapropylammonium (TPA) cation is used as a structure-directing agent (SDA). In addition, tailor-made SDAs called crystal-shape modifiers can produce different morphologies of MFI. When a tri-quaternary cation, bis-N,N-(tripropylammoniumhexamethylene)-di-N,N-propylammonium trihydroxide (trimer-TPA: tC6) is used, the main difference in the morphology of MFI is a platelike leaf-shaped structure. The product is thin along the *a*-axis rather than the *b*-axis that is mainly observed in coffin-like structure of MFI when TPA is used (Figure 1.14).[62,83,109,110]

For design of high performance membranes, i.e., high separation factors (SF) and fast fluxes, it is not enough to consider only the orientation of the seed layer. Complicated situations should be considered, such as preferred growth orientation during secondary growth, controlled in-plane growth to fill the gaps between the seeds, minimizing mismatched grain development and stress-induced crack formation from the calcination step for removing SDAs.[62] For instance, *c*- or *hoh*-oriented MFI membranes can kinetically be fabricated from a randomly oriented seed layer under different temperature conditions; at a relatively lower temperature (i.e., 100 °C) *hoh*-oriented membranes are preferred and at relatively high temperature (i.e., 175 °C) *c*-oriented membranes are preferred.[64,82,111,112]

For *b*-oriented membranes, first, a *b*-oriented seed layer should be deposited on the porous supports. However, when monomer TPA is used as a SDA for growing zeolite membranes using a *b*-oriented seed layer, in the initial step, an *a*-oriented twin structure is easily developed. Furthermore, a *c*-oriented membrane is eventually formed according to the van der Drift's theory of dominant growth in the faster growth direction (*c*-axis for MFI) when enough secondary growth time is applied.[64] Therefore, minimizing out-of-plane growth for developing in-plane growth should be performed, which can be established by using a crystal-shape modifier (trimer TPA (tC6)).[83,107] Promotion of in-plane growth to fill the gaps of seeds was generated from use of trimer TPA SDAs during the secondary growth reaction, and continuous *b*-oriented MFI films were fabricated (Figure 1.14).

The advantages of using *b*-oriented MFI membranes for separation of specific isomers (i.e., xylene isomers) are many: *p*-xylene can pass through the straight channels rather than the tortuous pathways, the large in-plane area and thin thickness of seed layer can generate lower density of grains, and one expects to have fast flux, and less stress-induced crack formation between the zeolite film and the support during calcination compared to other types of orientation.[113] According to a report by Lai et al., *b*-oriented membranes presented the best SF up to ca. 480 with a flux of ca. 2.0×10^{-9} mol s^{-1} Pa^{-1} for xylene isomer separation.[83] For a membrane with mixed orientations (*a*- and *b*-orientations) and *a*-oriented membrane were fabricated, but very low SF with less than 10 and no permeation test were reported for xylene isomer separation, respectively.[83,107,114]

Unfortunately, none of the specific polycrystalline zeolite membranes show superior performance for all different types of separations. For example, even the *b*-oriented MFI membrane that presented the best performance for xylene isomer separation had a worse performance than *c*-oriented MFI membranes for the separation of branched/linear hydrocarbon isomers (i.e., butane isomer separation, Figure 1.15). It seems that more complex mechanisms are involved with different types of separations, so more theoretical and experimental developments are still needed.

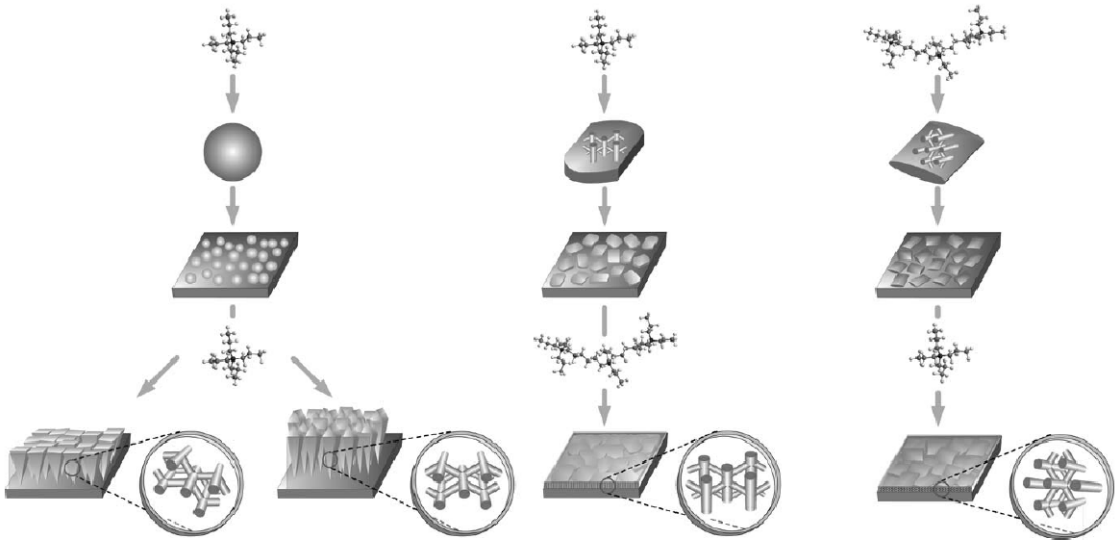

Figure 1.14 Scenarios of microstructure control by crystal-shape design, deposition, and growth using crystal-shape modifiers including tetrapropylammonium (monomer-TPA: TPA) (for example, top left) and bis-N,N-(tripropylammoniumhexamethylene)-di-N,N-propylammonium trihydroxide (trimer-TPA: tC6) (top right). The preferred orientations of the zeolite membranes are *hoh*-, *c*-, *b*- and *a*-orientations from bottom left to right in the schematic illustration.[62]

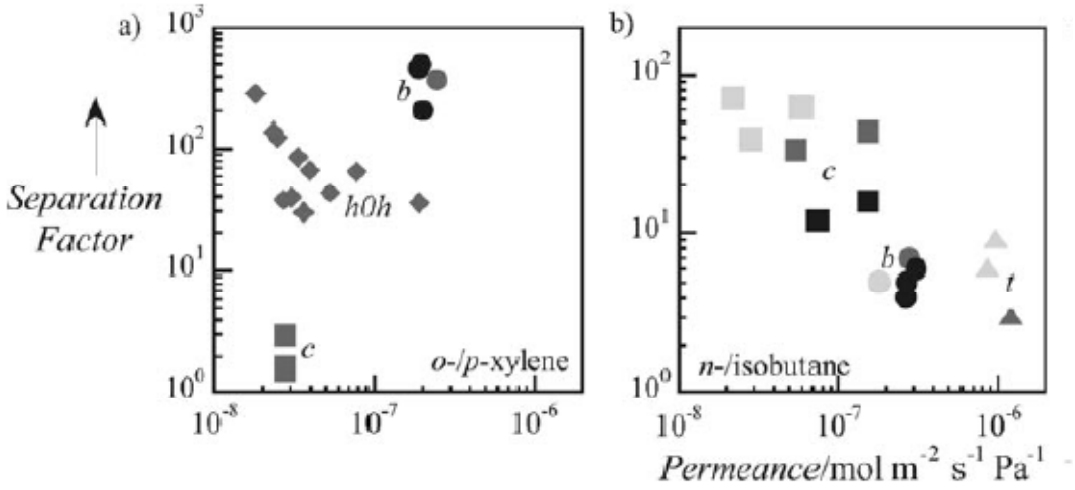

Figure 1.15 Performance of *c*-[81,82,115] *b*-[83,107] *h0h*-[82] oriented, and thin and randomly oriented (*t*)[105] silicalite-1 membranes for separating the indicated components at temperatures ranging from room temperature to as high as 400°C (light gray: RT–100°C, gray: 100–200°C, black: 200–400°C).[62]

1.4.3 Rapid thermal processing (RTP): grain boundary defect elimination

Regions around grain boundary defects are non-zeolitic, providing non-selective pathways for molecules to be separated.[62,83,115-117] The endeavor to reduce the density of grain boundary defects of polycrystalline zeolite films has been of much attention for realization of high performance zeolite films. However, such defects are difficult to detect visually by commonly used electron microscopy techniques, i.e., scanning electron microscopy (SEM) and transmission electron microscopy (TEM): the size of defects is very small, so SEM cannot detect such a defect and TEM is not applicable due to the film's thickness (usually in the micrometer range). For visualizing grain boundary defects, recently, laser scanning confocal microscopy (LSCM) has been employed by incorporation of dye molecules (ca. 1 nm) that are bigger than the zeolitic pore size.[62,118-120] Diffused dye molecules can be placed between grain boundary defects, but not into zeolitic pores. Thus, it is possible to detect the grain boundary defects that mainly originate from the calcination process used to remove SDAs, which causes tensile stresses by the abrupt contraction of the zeolite unit cell contraction and the mismatch of thermal coefficients between the support and the zeolite film.[62,83] For example, a *c*-oriented MFI membrane has a higher density of grain boundary defects than a *b*-oriented MFI zeolite membrane under LSCM investigation (Figure 1.16).[62,119] This implies that the *b*-oriented MFI zeolite membrane has more intergrown features compared to a *c*-oriented membrane. In addition, zeolite films are transparent. Therefore, depth profiling is possible, allowing one to obtain information about the development or difference of formation of defects or cracks along the vertical direction of zeolite films.

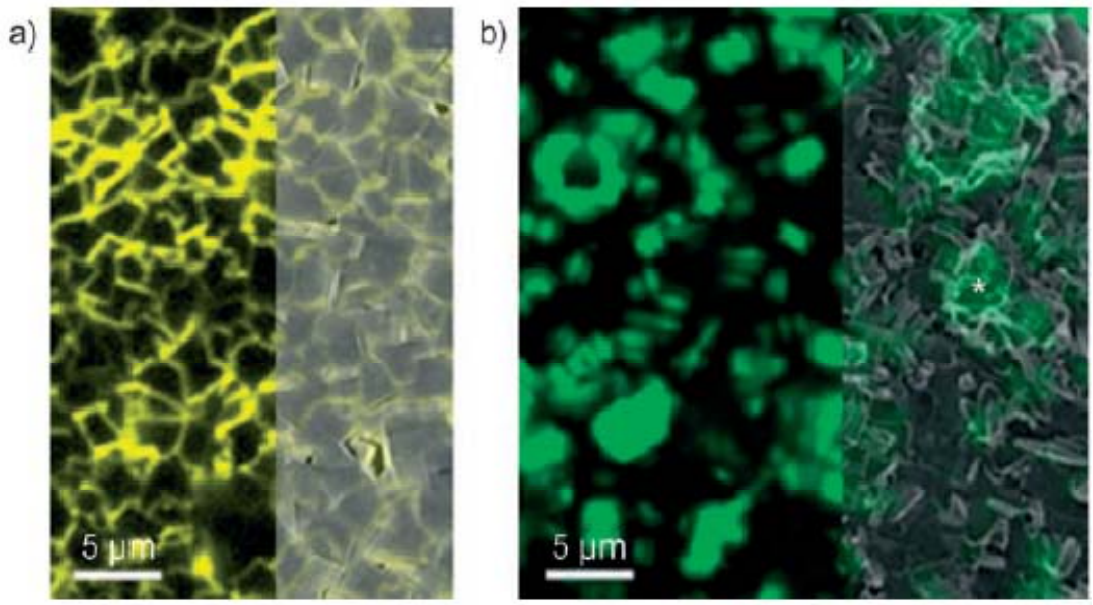

Figure 1.16 LSCM images of (a) c-oriented and (b) b-oriented MFI films. The right parts of (a) and (b) are partially transparent SEM images of the membrane surface to simultaneously view the fluorescing polycrystalline features.[62,119]

The grain boundary possesses Si-OH dangling groups on the surface. For reducing the grain boundary defect, recently, Choi et al. reported that rapid thermal processing (RTP) could strengthen grain bonding at the boundaries.[117] Simple heat treatment causes the condensation of dangling bonds on the boundaries to strengthen the grains of thick columnar MFI zeolite membranes (*c*-oriented membrane). Such a hypothesis was proved by using LSCM to show that fewer grain boundary defects were detected for the RTP-treated *c*-oriented MFI membrane compared to the non RTP-treated sample. In addition, according to the depth profile measurements, the grain boundary development was changed to laterally circular patterns on the in-plane for the RTP-treated zeolite film from the vertical development for the non RTP-treated sample (not shown here).[121] The stronger grain boundary bonding by RTP changed the pattern of grain boundary propagation and furthermore, crack development from the bottom of the zeolite film to the top surface was limited (Figure 1.17).

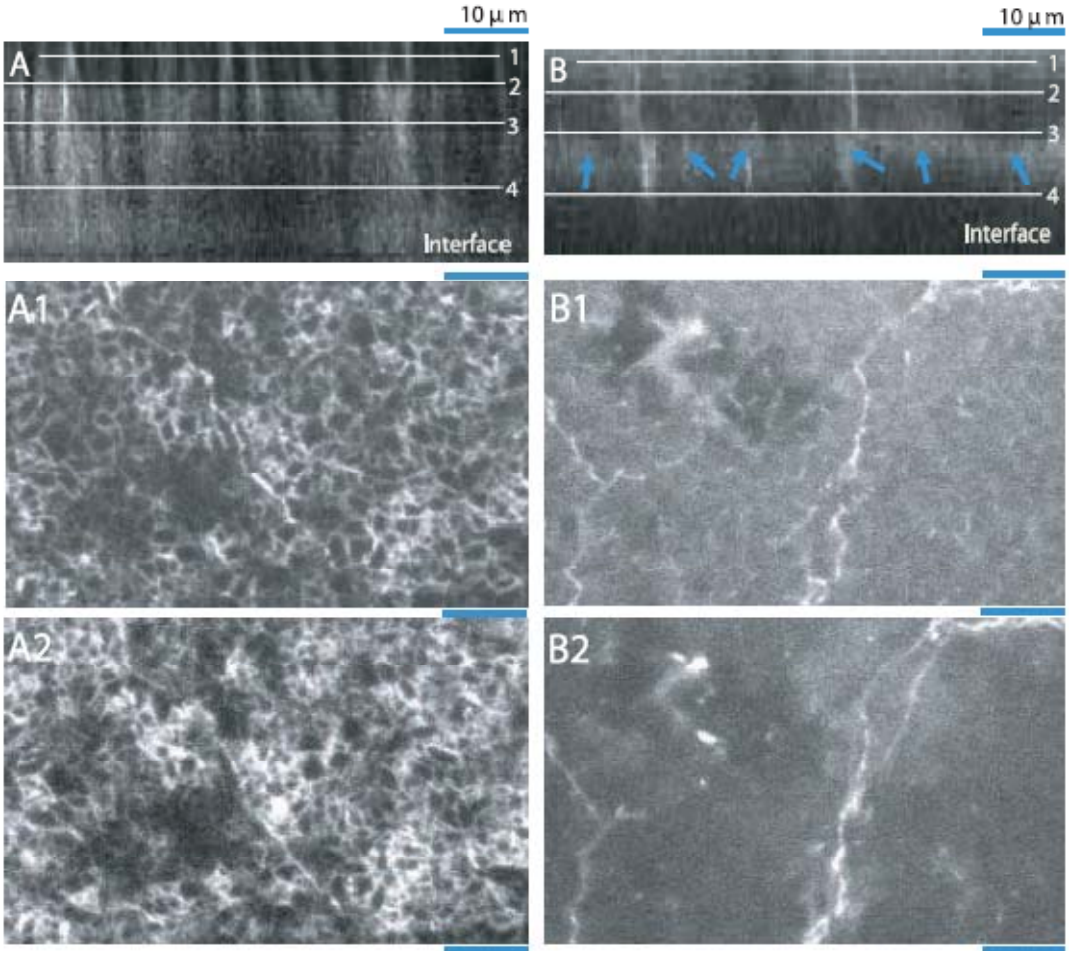

Figure 1.17 Cross-sectional LSCM images of RTP-untreated (A) and RTP-treated *c*-oriented MFI membrane (B). A1, A2 and B1, B2 represent the cross-sectional views from the top surfaces of RTP-untreated (A) and RTP-treated (B) membranes, respectively. The arrows in the B indicate limited propagation of crack formation from the bottom to the top surface.[117]

As mentioned above, one cannot expect to obtain one specific polycrystalline zeolite membrane with superior performance for all different types of separations. However, the strategy to eliminate grain boundary defects could reduce non-selective pathways of separating molecules through non-zeolitic pores. Therefore, the RTP-treated *c*-oriented MFI membrane presented very high SF of 128 for xyleme isomer separation, compared to conventionally calcined *c*-oriented MFI zeolite films presenting usually less

than 4 as a SF.[64,82] Furthermore, RTP-treated *c*-oriented MFI zeolite films showed a high SF of 34 insensitive to the operating temperature for butane isomer separation (not shown here).[121] It should be noted that combining selectivity on both separations of xylene isomers (SF=128) and butane isomers (SF=34) is not easily accomplished with a single membrane.[117] For instance, a *b*-oriented MFI membrane showed SF of 480 for xylene isomer separation but SF of 6 for butane isomer separation.[83,122] Therefore, this methodological development for improving the quality of zeolite films by eliminating grain boundary defects through simple heat treatment provides an opportunity for large-scale fabrication of different types of zeolite membranes.

1.5 Mesoporous Materials

Templated mesoporous materials have been investigated since the late 1980s when it was discovered that pillared clays presented mesoscale pores.[1,3] However, a tremendous amount of research began when scientists at Mobil Corporation reported ordered and tailored mesoporous aluminosilicate materials using alkylquarternary ammonium as a surfactant to create mesopores in 1992.[123,124] Much effort has been devoted to synthesizing mesoporous materials with various compositions (metal oxide,[1,3,123,124] metal,[125-127] metal sulfide,[128] carbon[5,129] and polymer[130,131] etc.) and different mesoporous structures with 2-D or 3-D framework symmetry.[3,124,132,133] The rational design of mesoporous materials is important for various applications. In the following sections, the synthetic mechanism for forming template-assisted mesoporous materials will be discussed. In addition, for advanced applications, morphology control of mesoporous silica will be introduced.

1.5.1 Synthetic mechanism of mesoporous materials

Template-assisted preparations of mesoporous materials have been of great interest due to the ability to fine tune the mesopore sizes and to develop different mesoporous structures. Two different methods, soft templating and hard templating, have been implemented for design of mesoporous materials for suitable applications

For the soft templating method, the interaction between organic surfactants and inorganic species via coulombic forces, hydrogen bonding and van der Waals forces

gives rise to assembly of micelles.[3,123,124,133-135] The soft templating method can be generally categorized into two main pathways: cooperative self-assembly and liquid-crystal templating.

The cooperative self-assembly pathway is established on the basis of interactions between surfactants and inorganic species (Figure 1.18A).[3,134,136] Silicate polyanions interact with positively charged surfactants via an electrostatic attraction force. The silicates are polymerized on the interface of the organic surfactants. Further reactions proceed while the charge density between inorganic species and surfactants are matched to each other. Then, assembly of the inorganic-organic material forms the final mesophase, which is further assembled to produce a 3-D arrangement with the lowest interfacial energy. In addition, non-ionic surfactants, e.g., amphiphilic triblock copolymer P123 ($EO_{20}PO_{70}EO_{20}$), can be incorporated with charged inorganic species through electrostatic forces assisted by double layer hydrogen bonding.[133,135] Dissolved nonionic surfactants in strong acidic conditions are hydrated on the hydrophilic head groups of surfactants, exhibiting positive charge via double layer hydrogen bonding. Then, cationic silica species in acidic conditions are associated with anions in the solution (e.g., Cl^-, Br^- and SO_4^{2-}), which presents negatively charged species. Therefore, electrostatic attraction via hydrogen bonding between hydrated nonionic surfactants and negatively charged silica species produces assembly of inorganic-organic materials.

For the liquid-crystal templating method, surfactants first assemble to form micelles above a critical micelle concentration (Figure 1.18B).[3,123,124] Then, these micelles self-assemble into an ordered mesophase. Inorganic species are introduced in between the micelles to fill out the pores. This liquid-crystal templating method is related to the mechanism of the evaporation-induced self-assembly (EISA) method that has been widely used for mesoporous silica films.[3,106,137] During solvent evaporation, the assembly of surfactants forms liquid-crystal phases while inorganic precursors in volatile polar solvent are further polymerized. According to papers by Zhao and co-workers, the synthesis of polymer resin and carbon materials was carried out under EISA strategy.[130,132] The preferential evaporation of ethanol improved phenolic resin assembly within the ordered liquid-crystal mesophases of block copolymer surfactants. It was

determined that the cross-linking and polymerizing processes of the phenolic resin frameworks separated from the assembly with surfactants.

On the other hand, the hard templating method is associated with the replication of precursors infiltrated into a hard template (Figure 1.19).[51,132,137,138] A replica with the topological features of the hard template can be obtained. This hard templating method, also called nanocasting, has been widely used for replication of mesoporous carbon materials from a silica hard template. Ideally, any precursors could be used for replication of the hard template, however, it has been limited due to partial loading of precursors inside the hard templates and faster growth of guest precursors outside the hard template.[137]

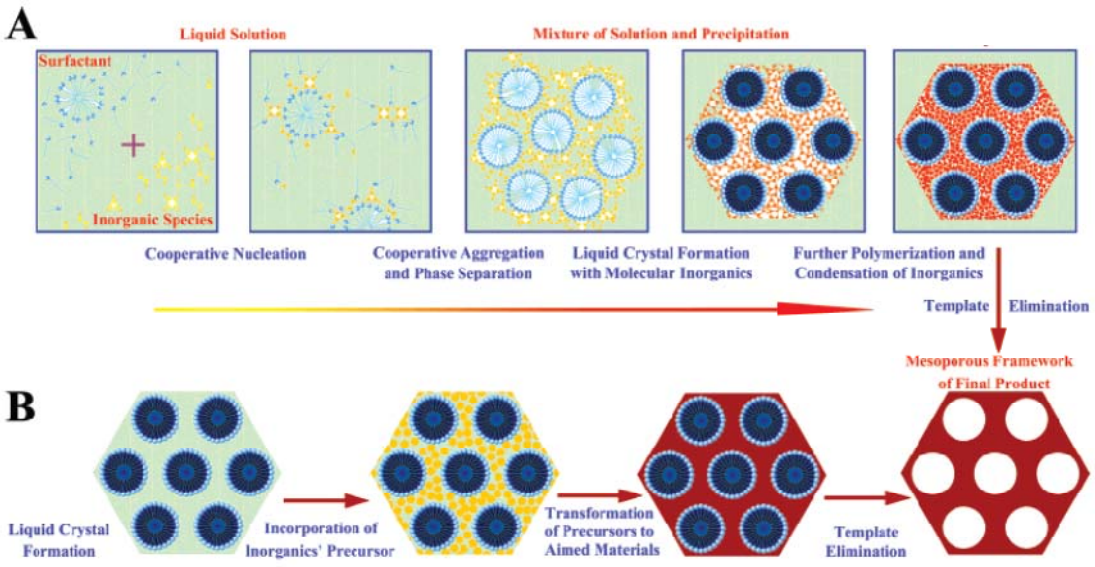

Figure 1.18 Two synthetic strategies of mesoporous materials through soft templating method: (A) cooperative self-assembly and (B) liquid-crystal templating process.[3]

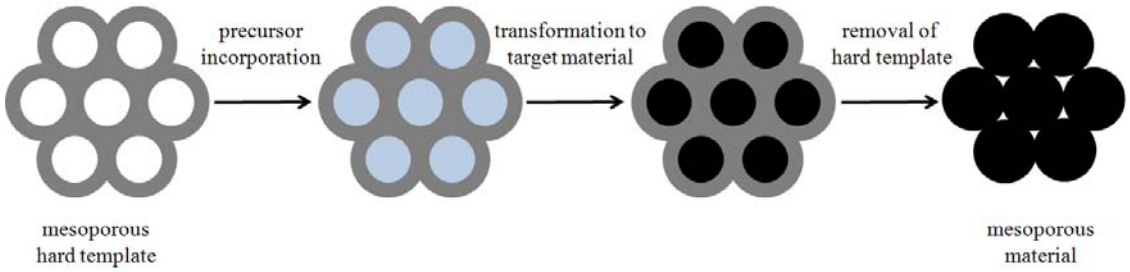

Figure 1.19 Schematic illustration of fabrication of mesoporous materials via hard templating process.

1.5.2 Morphology control of mesoporous silica

Morphology control of mesoporous materials is important for desired applications. For example, mesoporous films can be used for membrane-based separations and sensors; they were initially prepared by sol-gel dip-coatings and recently by electrochemically assisted self-assembly (Figure 1.20).[106,139] In addition, mesoporous silica spheres can be used as a drug/gene delivery vehicle because of controlled-release of loaded molecules by various methods.[7-9] Fabrication of spherical mesoporous silica materials will be discussed in the following sections.

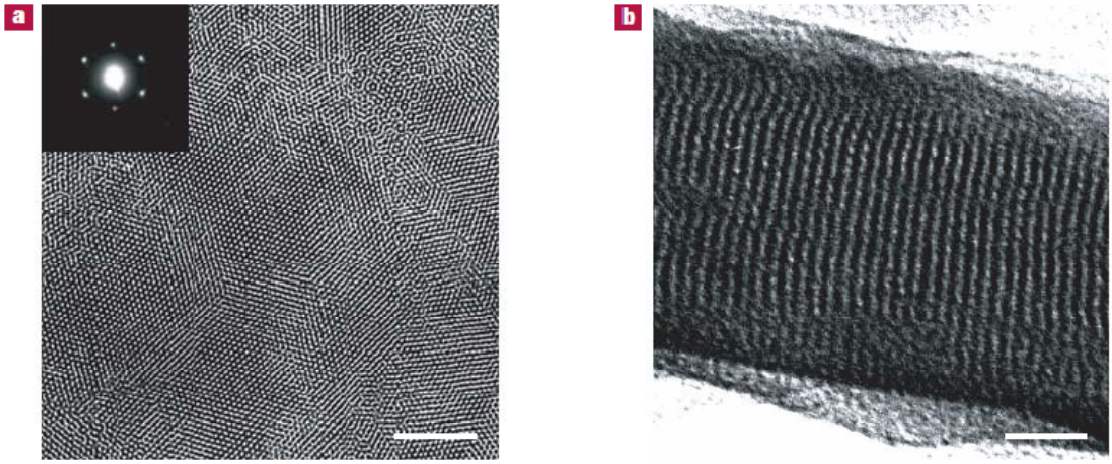

Figure 1.20 Transmission electron microscopy (TEM) images of the electrodeposited surfactant-templated mesoporous silica film. (a) Top view and (b) cross-sectional view of the sample. The inset in (a) is an electron diffraction pattern of the mesostructured film. The scale bars are 50 nm (a) and 20 nm (b).[139]

1.5.2.1 Direct synthesis of mesoporous silica sphres

The Stöber method has been widely used to produce monodisperse amorphous silica spheres. [140] Hydrolysis and condensation of silicon alkoxide in a mixture of water, short alkyl chain alcohol and ammonia as a catalyst are accomplished under ambient conditions. Inspired by the Stöber method, much effort has been devoted to fabricate mesoporous silica spheres via hydrolysis and condensation of the silica source with addition of a surfactant. Because of the morphological benefit of spherical shapes with tunable porosity, mesoporous silica spheres are attractive for advanced applications, i.e., drug delivery, catalysis, packing material of chromatography.[7-12,141-145]

As a direct synthesis of mesoporous silica spheres, the modified Stöber method was used with a quaternary ammonium surfactant (CTAB) as a cationic surfactant[146-151] or with alkyltrialkoxysilane as a porogen or supramolecule[152] to create mesopores. In the case of a cationic surfactant, hydrolyzed and condensed silicate oligomers are assembled with the cationic surfactant to form mesoscale micelles. Depending on the alkyl chain length of the surfactant, the pore size can be controlled (Figure 1.21), and an additive called a swelling agent can also control the pore size and the texture, producing more corrugated features on the surface.[153] On the other hand, when a porogen is used, alkyltrialkoxysilane is co-condensed. Mesopores can be formed after removal of the porogen by calcination. Other templates, i.e., a neutral template and fluorinated cationic surfactants, could also be used for creating mesopores in the silica spheres.[154,155]

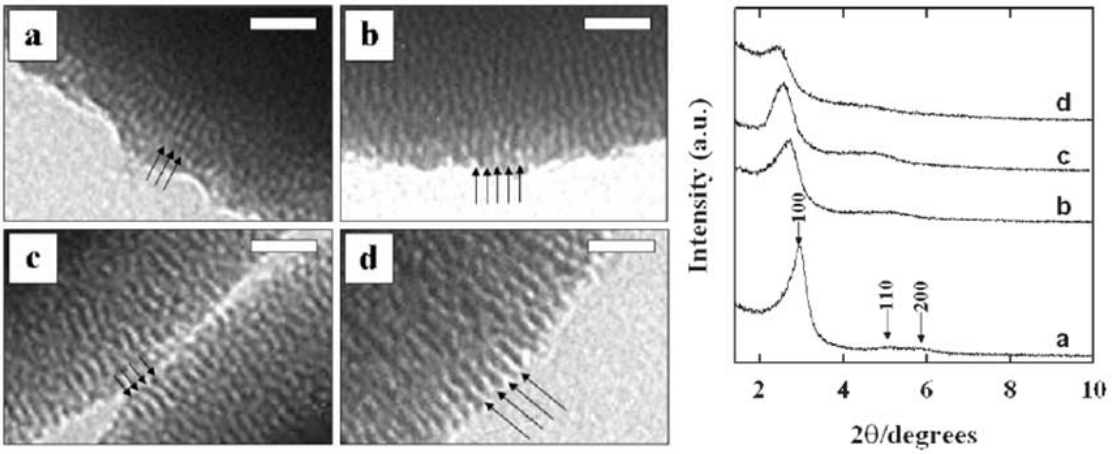

Figure 1.21 TEM images (a-d, left) show mesoporous silica spheres with different alkyl chains of quaternary ammonium as a surfactant, C12, C14, C16, C18, respectively. Small angle X-ray scattering (SAXS) patterns (right) present characteristic features of ordered mesopores from the samples prepared under different surfactant conditions. The scale bar corresponds to 20 nm. The arrows indicate the size of mesopores corresponding to the different chain lengths of the surfactants used in the reaction.[148]

1.5.2.2 Post synthesis of mesoporous silica spheres

For advanced applications of mesoporous silica spheres, for instance, packing materials for chromatography, the size and monodispersity should be well controlled.[10-12] However, there are still challenges with particle aggregation, relatively poor monodispersity and less size control in the direct synthesis approaches. Recently, the concept of pseudomorphic transformations, in which chemical compositions change while maintaining the outer morphology of objects, was employed to introduce meosporosity into the amorphous silica spheres that are made from the Stöber method.[12,156-160] Monodisperse amorphous silica spheres from Stöber syntheses are partially dissolved by base and the dissolved silicates are simultaneously re-precipitated with a cationic surfactant (CTAB) to form surfactant templating micelles. Dissolution and re-precipitation of silicate oligomers with a surfactant should occur at equilibrium with the specific molar ranges of compositions to generate mesoporosity into the amorphous silica spheres. According to papers by Galarneau and co-workers,[12,156,157] it is possible to transform amorphous to mesoporous silica spheres with 2-D hexagonal (*p6mm*)

symmetry and furthermore, the cubic (*Ia3d*) symmetry can be achieved to minimize the interfacial energy through intermediate mixed phases (Figure 1.22).

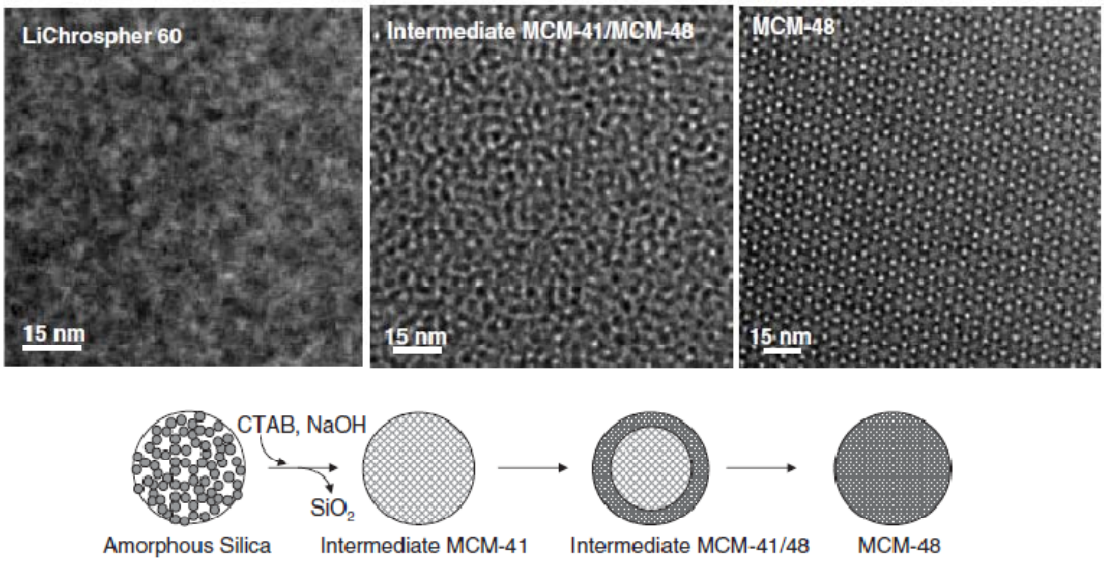

Figure 1.22 TEM images and schematic representation of double pseudomorphic transformation of amorphorous silica into mesoporous silica spheres (MCM-41 and MCM-48).[156]

In addition, Yin and co-workers reported that surface-protected etching can generate mesoporosity inside the amorphous silica spheres.[141] The concept of the surface-protected etching is to use an amphiphilic polymer, i.e., polyvinylpyrrolidone (PVP), to cover the surface of silica spheres for protecting against attack under basic conditions. Under basic conditions, the amorphous silica spheres are usually dissolved evenly, but after protection with a polymer on the surface, limited etching occurs at the surface. Once the etchant (OH^-) penetrates the silica spheres, the etching rate increases, generating hollow-core and mesoporous shell silica spheres (Figure 1.23). Because the initial silica spheres from Stöber syntheses have a very good monodispersity, etched hollow@meso-shell silica spheres also have good monodispersity. Both the pseudomorphic transformation and the surface-protected etching can also be applied for introducing mesoporosity on the surface of composite materials comprising functional nanocrystal core and amorphous silica shell for protection of core materials.

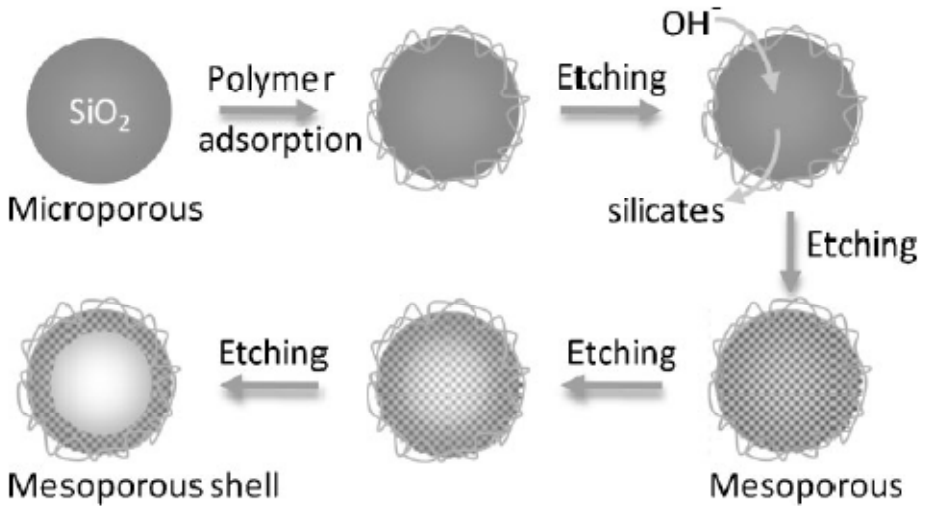

Figure 1.23 The schematic illustration of the concept of surface-protected etching for transforming solid structures into hollow structures with permeable shells.[141]

1.6. Conclusions

So far, general background material and methods for controlling the morphology of porous materials have been addressed. It is noted that controlling morphology of porous materials is essential for advanced applications. In the later chapters, approaches to introducing mesoporosity into the amorphous silica spheres and zeolite crystals will be discussed. Simultaneous dissolution and surfactant-induced re-assembly of dissolved species via micelle formation will be employed to create mesoporosity in the amorphous silica spheres and zeolite crystals. In addition, using a 3DOM carbon template as a massively parallel nanoreactor, growth patterns and shape development of zeolite crystals in confined synthesis will be described. Depending on reaction parameters, various shapes and different growth mechanisms of zeolite crystals will be introduced. Furthermore, a facile technique for fabricating zeolite membranes will be addressed. Novel seeding methods will be applied to deposit seed particles that are produced by confined synthesis. The permeation test of zeolite membranes will emphasize that our synthetic approaches can be generalized to other types of zeolite films.

1.6 References

(1) Corma, A. *Chem. Rev.* **1997**, *97*, 2373-2419.

(2) Davis, M. E. *Nature* **2002**, *417*, 813-821.

(3) Wan, Y.; Zhao, D. *Chem. Rev.* **2007**, *107*, 2821-2860.

(4) Stein, A.; Melde, B. J.; Schroden, R. C. *Adv. Mater.* **2000**, *12*, 1403-1419.

(5) Stein, A.; Wang, Z.; Fierke, M. A. *Adv. Mater.* **2009**, *21*, 265-293.

(6) Corma, A. *J. Cat.* **2003**, *216*, 298-312.

(7) Zhu, Y.; Shi, J.; Shen, W.; Dong, X.; Feng, J.; Ruan, M.; Li, Y. *Angew. Chem. Int. Ed.* **2005**, *44*, 5083-5087.

(8) Lai, C.-Y.; Trewyn, B. G.; Jeftinija, D. M.; Jeftinija, K.; Xu, S.; Jeftinija, S.; Lin, V. S.-Y. *J. Am. Chem. Soc.* **2003**, *125*, 4451-4459.

(9) Lu, J.; Liong, M.; Zink, J. I.; Tamanoi, F. *Small* **2007**, *3*, 1341-1346.

(10) Han, Y.; Lee, S. S.; Ying, J. Y. *Chem. Mater.* **2007**, *19*, 2292-2298.

(11) Kirkland, J. J.; Truszkowski, F. A.; Dilks, C. H.; Engel, G. S. *J. Chromatogr. A* **2000**, *890*, 3-13.

(12) Martin, T.; Galarneau, A.; Renzo, F. D.; Brunel, D.; Fajula, F.; Heinisch, S.; Crétier, G.; Rocca, J.-L. *Chem. Mater.* **2004**, *16*, 1725-1731.

(13) Yoo, W. C.; Stein, A. *Chem. Mater.* **2010**, *submitted*.

(14) Yoo, W. C.; Zhang, X.; Tsapatsis, M.; Stein, A. *manuscript in preparation.* **2010**.

(15) Yoo, W. C.; Kumar, S.; Penn, R. L.; Tsapatsis, M.; Stein, A. *J. Am. Chem. Soc.* **2009**, *131*, 12377-12383.

(16) Yoo, W. C.; Kumar, S.; Wang, Z.; Ergang, N. S.; Fan, W.; Karanikolos, G. N.; McCormick, A. V.; Penn, R. L.; Tsapatsis, M.; Stein, A. *Angew. Chem. Int. Ed.* **2008**, *47*, 9096-9099.

(17) Yoo, W. C.; Stoeger, J. A.; Lee, P.-S.; Tsapatsis, M.; Stein, A. *Angew. Chem. Int. Ed.* **2010**, *49*, 8699-8703.

(18) *IUPAC Mannual of Symbols and Terminology, Appendix 2, Part 1, Colloidal and Surface Chemistry Pure Appl. Chem. 1972, 31, 578.*

(19) Snyder, M. A.; Tsapatsis, M. *Angew. Chem. Int. Ed.* **2007**, *46*, 7560-7573.

(20) Moliner, M.; Román-Leshkov, Y.; Davis, M. E. *Proc. Natl. Acad. Sci. USA* **2010**, *107*, 6144-6168.

(21) Bansal, R. C.; Goyal, M. *Activated Carbon Adsorption.*, CRC Press:Boca Raton, 2005; p 497.

(22) Long, J. R.; Yaghi, O. M. *Chem. Soc. Rev.* **2009**, *38*, 1213-1214.

(23) Tranchemontagne, D. J.; Mendoza-Cortés, J. L.; O'Keeffe, M.; Yaghi, O. M. *Chem. Soc. Rev.* **2009**, *2009*, 1257-1283.

(24) Huang, A.; Bux, H.; Steinbach, F.; Caro, J. *Angew. Chem. Int. Ed.* **2010**, *49*.

(25) Lee, J. Y.; Farha, O. K.; Roberts, J.; Scheidt, K. A.; Nguyen, S. T.; Hupp, J. T. *Chem. Soc. Rev.* **2009**, *38*, 1450-1459.

(26) Murray, L. J.; Dincă, M.; Long, J. R. *Chem. Soc. Rev.* **2009**, *38*, 1294-1314.

(27) Stein, A.; Li, F.; Denny, N. R. *Chem. Mater.* **2008**, *20*, 649-666.

(28) Holland, B. T.; Blanford, C. F.; Stein, A. *Science* **1998**, *281*, 538-540.

(29) http://en.wikipedia.org/wiki/Zeolite.

(30) Baerlocher, C.; Meier, W. M.; Olson, D. H., Atlas of Zeolite Framework Types, 5th Ed. 2001, The Structure Commission of the International Zeolite Associaiton, Elsevier.

(31) Corma, A.; Davis, M. E. *ChemPhysChem* **2004**, *5*, 304-313.

(32) Sun, J.; Bonneau, C.; Cantim, A.; Corma, A.; Diaz-Cabanas, M. J.; Moliner, M.; Zhang, D.; Li, M.; Zou, X. *Nature* **2009**, *458*, 1154-1158.

(33) Davis, M. E.; Saldarriaga, C.; Montes, C.; Garces, J.; Crowder, C. *Nature* **1998**, *331*, 698-699.

(34) de Moor, P.-P. E. A.; Beelen, T. P. M.; Komanschek, B. U.; Beck, L. W.; Wagner, P.; Davis, M. E.; van Santen, R. A. *Chem. Eur. J.* **1999**, *5*, 2083-2088.

(35) Burkett, S. L.; Davis, M. E. *Chem. Mater.* **1995**, *7*, 1453-1463.

(36) Wang, H.; Pinnavaia, T. J. *Angew. Chem. Int. Ed.* **2006**, *45*, 7603-7606.

(37) Madsen, C.; Jacobsen, C. J. H. *Chem. Commun.* **1999**, 673-674.

(38) Kim, S.-S.; Shah, J.; Pinnavaia, T. J. *Chem. Mater.* **2003**, *15*, 1664-1668.

(39) Tao, Y.; Kanoh, H.; Abrams, L.; Kaneko, K. *Chem. Rev.* **2006**, *106*, 896-910.

(40) Pérez-Ramírez, J.; Christensen, C. H.; Egeblad, K.; Christensen, C. H.; Groen, J. E. *Chem. Soc. Rev.* **2008**, *37*, 2530-2542.

(41) Holland, B. T.; Abrams, L.; Stein, A. *J. Am. Chem. Soc.* **1999**, *121*, 4308-4309.

(42) Maheshwari, S.; Jordan, E.; Kumar, S.; Bates, F. S.; Penn, R. L.; Shantz, D. F.; Tsapatsis, M. *J. Am. Chem. Soc.* **2008**, *130*, 1507-1516.

(43) Corma, A.; Fornes, V.; Pergher, S. B.; Maesen, T. L. M.; Buglass, J. G. *Nature* **1998**, *396*, 353-356.

(44) Choi, M.; Na, K.; Kim, J.; Sakamoto, Y.; Terasaki, O.; Ryoo, R. *Nature* **2009**, *461*, 246-250.

(45) Park, D. H.; Kim, S. S.; Wang, H.; Pinnavaia, T. J.; Papapetrou, M. C.; Lappas, A. A.; Triantafyllidis, K. S. *Angew. Chem. Int. Ed.* **2009**, *48*, 7645-7648.

(46) Choi, M.; Cho, H. S.; Srivastava, R.; Venkatesan, C.; Choi, D.-H.; Ryoo, R. *Nat. Mater.* **2006**, *5*, 718-723.

(47) Jacobsen, C. J. H.; Madsen, C.; Houzvicka, J.; Schmidt, I.; Carlsson, A. *J. Am. Chem. Soc.* **2000**, *122*, 7116-7117.

(48) Fan, W.; Snyder, M. A.; Kumar, S.; Lee, P.-S.; Yoo, W. C.; McCormick, A. V.; Penn, R. L.; Stein, A.; Tsapatsis, M. *Nat. Mater.* **2008**, *7*, 984-991.

(49) Corma, A. *Nature* **2009**, *461*, 182-183.

(50) Lee, D.-H.; Choi, M.; Yu, B.-W.; Ryoo, R. *Chem. Commun.* **2009**, 74-76.

(51) Lu, A.-H.; Schüth, F. *C. R. Chimie* **2005**, *8*, 609-620.

(52) Yang, H.; Zhao, D. *J. Mater. Chem.* **2005**, *15*, 1217-1231.

(53) Schmidt, I.; Madsen, C.; Jacobsen, C. J. H. *Inorg. Chem.* **2000**, *39*, 2279-2283.

(54) Kustova, M.; Egeblad, K.; Zhu, K.; Christensen, C. H. *Chem. Mater.* **2007**, *19*, 2915-2917.

(55) Fan, W.; Snyder, M. A.; Kumar, S.; Lee, P.-S.; Yoo, W. C.; McCormick, A. V.; Penn, R. L.; Stein, A.; Tsapatsis, M. *Nat. Mater.* **2008**, *7*, 984-991.

(56) Yamamura, M.; Chaki, K.; Wakatsuki, T.; Okado, H. *Zeolites* **1994**, *14*, 643-649.

(57) Müller, M.; Harvey, G.; Prins, P. *Microporous Mesoporous Mater.* **2000**, *34*, 135-147.

(58) Groen, J. C.; Moulijn, J. A.; Pérez-Ramírez, J. *Microporous Mesoporous Mater.* **2005**, *87*, 153-161.

(59) Groen, J. C.; Bach, T.; Ziese, U.; Paulaime-van Donk, A. M.; de Jong, K. P.; Moulijn, J. A.; Pérez-Ramírez, J. *J. Am. Chem. Soc.* **2005**, *127*, 10792-10793.

(60) Groen, J. C.; Moulijn, J. A.; Pérez-Ramírez, J. *J. Mater. Chem.* **2006**, *16*, 2121-2131.

(61) Groen, J. C.; Jansen, J. C.; Moulijn, J. A.; Pérez-Ramírez, J. *J. Phys. Chem. B* **2004**, *108*, 13062-13065.

(62) Snyder, M. A.; Tsapatsis, M. *Angew. Chem. Int. Ed.* **2007**, *46*, 7560-7573.

(63) Bein, T. *Chem. Mater.* **1996**, *8*, 1636-1653.

(64) Gouzinis, A.; Tsapatsis, M. *Chem. Mater.* **1998**, *10*, 2497-2504.

(65) Yan, Y.; Davis, M. E.; Gavalas, G. R. *Ind. Eng. Chem. Res.* **1995**, *34*, 1652-1661.

(66) Tarditi, A. M.; Irusta, S.; Lombardo, E. A. *Chem. Eng. J.* **2006**, *122*, 167-174.

(67) Gump, C. J.; Tuan, V. A.; Noble, R. D.; Falconer, J. L. *Ind. Eng. Chem. Res.* **2001**, *40*, 565-577.

(68) Yuan, W.; Lin, Y. S.; Yang, W. *J. Am. Chem. Soc.* **2004**, *126*, 4776-4777.

(69) Wang, Z.; Ge, Q.; Shao, J.; Yan, Y. *J. Am. Chem. Soc.* **2009**, *131*, 6910-6911.

(70) Choi, J.; Tsapatsis, M. *J. Am. Chem. Soc.* **2010**, *132*, 448-449.

(71) Miachon, S.; Ciavarella, P.; van Dyk, L.; Kumakiri, I.; Fiaty, K.; Schuurman, Y.; Dalmon, J.-A. *J. Membr. Sci.* **2007**, *298*, 71-79.

(72) Bárcia, P. S.; Ferreira, A.; Gascon, J.; Aguado, S.; Silva, J. A. C.; Rodrigues, A. E.; Kapteijn, F. *Micro. Meso. Mater* **2010**, *128*, 194-202.

(73) Coronas, J. *Chem. Eng. J.* **2010**, *156*, 236-242.

(74) McLeary, E. E.; Jansen, J. C.; Kapteijn, F. *Microporous Mesoporous Mater.* **2006**, *90*, 198-220.

(75) Caro, J.; Noack, M. *Microporous Mesoporous Mater.* **2008**, *115*, 215-233.

(76) Liu, Y.; Li, Y.; Yang, W. *J. Am. Chem. Soc.* **2010**, *132*, 1768-1769.

(77) Davis, M. E. *Nature* **2002**, *417*, 813-821.

(78) Lew, C. M.; Cai, R.; Yan, Y. *Acc. Chem. Res.* **2010**, *43*, 210-219.

(79) Snyder, M. A.; Tsapatsis, M. *Angew. Chem. Int. Ed.* **2007**, *46*, 7560-7573.

(80) Caro, J.; Noack, M. *Microporous Mesoporous Mater.* **2008**, *115*, 215-233.

(81) Choi, J.; Ghosh, S.; King, L.; Tsapatsis, M. *Adsorption* **2006**, *12*, 339-160.

(82) Xomeritakis, G.; Lai, Z.; Tsapatsis, M. *Ind. Eng. Chem. Res.* **2001**, *40*, 544-552.

(83) Lai, Z.; Bonilla, G.; Diaz, I.; Nery, J. G.; Sujaoti, K.; Amat, M. A.; Kokkoli, E.; Terasaki, O.; Thompson, R. W.; Tsapatsis, M.; Vlachos, D. G. *Science* **2003**, *300*, 456-460.

(84) Graph, G. *Purchasing Magazine* **2003**, June 19.

(85) Tullo, A. H. *Chem. Eng. News* **2001**, *79(35)*, 28.

(86) Kroschwitz, J. I.; in *Kirk-Othmer Encyclopedia of Chemical Technology, Wiley, New York,* **1998**, p.831.

(87) Chirico, R. D.; Steele, W. V. *J. Chem. Eng. Data* **1997**, *42*, 784.

(88) Chaikittisilp, W.; Davis, M. E.; Okubo, T. *Chem. Mater.* **2007**, *19*, 4120-4122.

(89) Hunt, H. K.; Lew, C. M.; Sun, M.; Yan, Y.; Davis, M. E. *Microporous Mesoporous Mater.* **2010**, *128*, 12-18.

(90) Berenguer-Murcia, Á.; Morallón, E.; Cazorla-Amorós, E.; Linares-Solano, Á. *Microporous Mesoporous Mater.* **2003**, *66*, 331-340.

(91) Mintova, S.; Mo, S.; Bein, T. *Chem. Mater.* **1998**, *10*, 4030-4036.

(92) Li, X.; Yan, Y.; Wang, Z. *Ind. Eng. Chem. Res.* **2010**, *49*, 5933-5938.

(93) Huang, A.; Caro, J. *Chem. Mater.* **2010**, *22*, 4353-4355.

(94) Liu, X.; Liu, W.; Li, J.; Zhang, Y.; Lang, L.; Ma, L.; Zhang, B. *Ind. Eng. Chem. Res.* **2010**, *49*, 8826-8831.

(95) Jeong, H.-K.; Krohn, J.; Sujaoti, K.; Tsapatsis, M. *J. Am. Chem. Soc.* **2001**, *124*, 12966-12968.

(96) Wang, Z.; Ge, Q.; Shao, J.; Yan, Y. *J. Am. Chem. Soc.* **2009**, *131*, 6910-6911.

(97) Jiang, Y.-B.; Xomeritakis, G.; Chen, Z.; Dunphy, D.; Kissel, D. J.; Cecchi, J. L.; Brinker, C. J. *J. Am. Chem. Soc.* **2007**, *129*, 15446-15447.

(98) Lee, I.; Buday, J. L.; Jeong, H.-K. *Microporous Mesoporous Mater.* **2009**, *122*, 288-293.

(99) Yoon, K. B. *Acc. Chem. Res.* **2007**, *40*, 29-40.

(100) Lee, J. S.; Lee, Y.-J.; Tae, E. L.; Park, Y. S.; Yoon, K. B. *Science* **2003**, *301*, 818-821.

(101) Lee, J. S.; Kim, J. H.; Lee, Y. J.; Jeong, N. C.; Yoon, K. B. *Angew. Chem. Int. Ed.* **2007**, *46*, 3087-3090.

(102) Khanh, N. N.; Yoon, K. B. *J. Am. Chem. Soc.* **2009**, *131*, 14228-14230.

(103) Liu, Y.; Li, Y.; Yang, W. *Chem. Commun.* **2009**, 1520-1522.

(104) Hedlund, J.; Jareman, F.; Bons, A.-J.; Anthonis, M. *J. Mem. Sci.* **2003**, *222*, 163-179.

(105) Hedlund, J.; Sterte, J.; Anthonis, M.; Bons, A.-J.; Carstensen, B.; Corcoran, N.; Cox, D.; Deckman, H.; Gijnst, W. D.; de Moor, P.-P.; Lai, F.; McHenry, J.; Mortier, W.; Reinoso, J.; Peters, J. *Microporous Mesoporous Mater.* **2002**, *52*, 179-189.

(106) Lu, Y.; Ganguli, R.; Drewien, C. A.; Anderson, M. T.; Brinker, C. J.; Gong, W.; Guo, Y.; Soyes, H.; Dunn, B.; Huang, M. H.; Zink, J. I. *Nature* **1997**, *389*, 364-368.

(107) Lai, Z.; Tsapatsis, M.; Nicolich, J. P. *Adv. Funct. Mater.* **2004**, *14*, 716-729.

(108) Gavalas, G. R. *Ind. Eng. Chem. Res.* **2008**, *47*, 5797-5811.

(109) Bonilla, G.; Díaz, I.; Tsapatsis, M.; Jeong, H.-K.; Lee, Y.; Vlachos, D. G. *Chem. Mater.* **2004**, *16*, 5697-5705.

(110) Díaz, I.; Kokkoli, E.; Terasaki, O.; Tsapatsis, M. *Chem. Mater.* **2004**, *16*, 5226-5232.

(111) Bonilla, G.; Vlachos, D. G.; Tsapatsis, M. *Microporous Mesoporous Mater.* **2001**, *42*, 191-203.

(112) Bons, A.-J.; Bons, P. D. *Microporous Mesoporous Mater.* **2003**, *62*, 9-16.

(113) Lai, Z.; Bonilla, G.; Diaz, I.; Nery, J. G.; Sujaoti, K.; Amat, M. A.; Kokkoli, E.; Terasaki, O.; Thompson, R. W.; Tsapatsis, M.; Vlachos, D. G. *Science* **2003**, *300*, 456-460.

(114) Choi, J.; Ghosh, S.; Lai, Z.; Tsapatsis, M. *Angew. Chem. Int. Ed.* **2006**, *45*, 1154-1158.

(115) Xomeritakis, G.; Gouzinis, A.; Nair, S.; Okubo, T.; He, M.; Overney, R. M.; Tsapatsis, M. *Chem. Eng. Sci.* **1999**, *54*, 3521-3531.

(116) Jeong, H.-K.; Lai, Z.; Tsapatsis, M.; Hanson, J. C. *Microporous Mesoporous Mater.* **2005**, *84*, 332-337.

(117) Choi, J.; Jeong, H.-K.; Snyder, M. A.; Stoeger, J. A.; Masel, R. I.; Tsapatsis, M. *Science* **2009**, *325*, 590-593.

(118) Snyder, M. A.; Vlachos, D. G.; Nikolakis, V. *J. Membr. Sci.* **2007**, *290*, 1-18.

(119) Snyder, M. A.; Lai, Z.; Tsapatsis, M.; Vlachos, D. G. *Microporous Mesoporous Mater.* **2004**, *76*, 29-33.

(120) Bonilla, G.; Tsapatsis, M.; Vlachos, D. G.; Xomeritakis, G. *J. Membr. Sci.* **2001**, *182*, 103-109.

(121) Choi, J.; Jeong, H.-K.; Snyder, M. A.; Stoeger, J. A.; Masel, R. I.; Tsapatsis, M. *Science* **2009**, *325*, 590-593.

(122) Lai, Z.; Tsapatsis, M. *Ind. Eng. Chem. Res.* **2004**, *43*, 3000-3007.

(123) Kresge, C. T.; Leonowicz, M. E.; Roth, W. J.; Vartuli, J. C.; Beck, J. S. *Nature* **1992**, *359*, 710-712.

(124) Beck, J. S.; Vartuli, J. C.; Roth, W. J.; Leonowicz, M. E.; Kresge, C. T.; Schmitt, K. D.; Chu, C. T.-W.; Olson, D. H.; Sheppard, E. W.; McCullen, S. B.; Higgins, J. B.; Schlenker, J. L. *J. Am. Chem. Soc.* **1992**, *114*, 10834-10843.

(125) Armatas, G. S.; Kanatzidis, M. G. *Natue* **2006**, *441*, 1122-1125.

(126) Sun, D.; Riley, A. E.; Cadby, A. J.; Richman, E. K.; Korlann, S. D.; Tolbert, S. H. *Nature* **2006**, *441*, 1126-1130.

(127) Attard, G. S.; Bartlett, P. N.; Coleman, N. R. B.; Elliott, J. M.; Owen, J. R.; Wang, J. H. *Science* **1997**, *278*, 838-840.

(128) Braun, P. V.; Osenar, P.; Stupp, S. I. *Nature* **1996**, *380*, 325-328.

(129) Ryoo, R.; Joo, S. H.; Jun, S. *J. Phys. Chem. B* **1999**, *103*, 7743-7746.

(130) Meng, Y.; Gu, D.; Zhang, F.; Shi, Y.; Cheng, L.; Feng, D.; Wu, Z.; Chen, Z.; Wan, Y.; Stein, A.; Zhao, D. *Chem. Mater.* **2006**, *18*, 4447-4464.

(131) Zalusky, A. S.; Olayo-Valles, R.; Wolf, J. H.; Hillmyer, M. A. *J. Am. Chem. Soc.* **2002**, *124*, 12761-12773.

(132) Wan, Y.; Yang, H.; Zhao, D. *Acc. Chem. Res.* **2006**, *39*, 423-432.

(133) Zhao, D.; Huo, Q.; Feng, J.; Chmelka, B. F.; Stucky, G. D. *J. Am. Chem. Soc.* **1998**, *120*, 6024-6036.

(134) Huo, Q.; Margolese, D. I.; Ciesla, U.; Feng, P.; Gier, T. E.; Sieger, P.; Leon, R.; Petroff, P. M.; Schüth, F.; Stucky, G. D. *Nature* **1994**, *368*, 317-321.

(135) Zhao, D.; Feng, J.; Huo, Q.; Melosh, N.; Fredrickson, G. H.; Chmelka, B. F.; Stucky, G. D. *Science* **1998**, *279*, 548-552.

(136) Firouzi, A.; Kumar, D.; Bull, L. M.; Besier, T.; Sieger, P.; Huo, Q.; Walker, S. A.; Zasadzinski, J. A.; Glinka, C.; Nicol, J.; Margolese, D.; Stucky, G. D.; Chmelka, B. F. *Science* **1995**, *267*, 1138-1143.

(137) Yang, H.; Zhao, D. *J. Mater. Chem.* **2005**, *15*, 1217-1231.

(138) Al-Muhtaseb, S. A.; Ritter, J. A. *Adv. Mater.* **2003**, *15*, 101-114.

(139) Walcarius, A.; Sibottier, E.; Etienne, M.; Ghanbaja, J. *Nat. Mater.* **2007**, *6*, 602-608.

(140) Stöber, W.; Fink, A.; Bohn, E. *J. Colloid Interface Sci.* **1968**, *26*, 62-69.

(141) Zhang, Q.; Lee, I.; Ge, J.; Zaera, F.; Yin, Y. *Adv. Funct. Mater.* **2010**, *20*, 2201-2214.

(142) Wang, Y.; Yu, A.; Caruso, F. *Angew. Chem. Int. Ed.* **2005**, *44*, 2888-2892.

(143) Shokouhimehr, M.; Piao, Y.; Kim, J.; Jang, Y.; Hyeon, T. *Angew. Chem. Int. Ed.* **2007**, *46*, 7039-7043.

(144) Chen, H.-T.; Huh, S.; Wiench, J. W.; Pruski, M.; Lin, V. S.-Y. *J. Am. Chem. Soc.* **2005**, *127*, 13305-13311.

(145) Wang, Y.; Caruso, F. *Chem. Mater.* **2005**, *17*, 953-961.

(146) Pauwels, B.; Tendeloo, G. V.; Thoelen, C.; Rhijn, W. V.; Jacobs, P. A. *Adv. Mater.* **2001**, *13*, 1317-1320.

(147) Grün, M.; Lauer, I.; Unger, K. K. *Adv. Mater.* **1997**, *9*, 254-257.

(148) Yoon, S. B.; Kim, J.-Y.; Kim, J. H.; Park, Y. J.; Yoon, K. R.; Park, S.-K.; Yu, J.-S. *J. Mater. Chem.* **2007**, *17*, 1758-1761.

(149) Tan, B.; Rankin, S. E. *J. Phys. Chem. B* **2004**, *108*, 20122-20129.

(150) Tendeloo, G. V.; Lebedev, O. I.; Collart, O.; Cool, P.; Vansant, E. F. *J. Phys.:Condens. Matter* **2003**, *15*, S3037-S3046.

(151) Grün, M.; Unger, K. K.; Matsumoto, A.; Tsutsumi, K. *Microporous Mesoporous Mater.* **1999**, *27*, 207-216.

(152) Büchel, G.; Unger, K. K.; Matsumoto, A.; Tsutsumi, K. *Adv. Mater.* **1998**, *10*, 1036-1038.

(153) Kim, J. H.; Yoon, S. B.; Kim, J.-Y.; Chae, Y. B.; Yu, J.-S. *Colloids and Surfaces A: Physicochem. Eng. Aspects* **2008**, *313-314*, 77-81.

(154) Tan, B.; Lehmler, H.-J.; Vyas, S. M.; Knutson, B. L.; Rankin, S. E. *Adv. Mater.* **2005**, *17*, 2368-2371.

(155) Nooney, R. I.; Thirunavukkarasu, D.; Chem, Y.; Josephs, R.; Ostafin, A. E. *Chem. Mater.* **2002**, *14*, 4721-4728.

(156) Galarneau, A.; Iapichella, J.; Bonhomme, K.; Renzo, F. D.; Kooyman, P.; Terasaki, O.; Fajula, F. *Adv. Funct. Mater.* **2006**, *16*, 1657-1667.

(157) Martin, T.; Galarneau, A.; Renzo, F. D.; Fajula, F.; Plee, D. *Angew. Chem. Int. Ed.* **2002**, *41*, 2590-2592.

(158) Botella, P.; Corma, A.; Navarro, M. T. *Chem. Mater.* **2007**, *19*, 1979-1983.

(159) Kim, T.-W.; Chung, P.-W.; Lin, V. S.-Y. *Chem. Mater.* **2010**, *22*, 5093-5104.

(160) Lim, S.; Ranade, A.; Du, G.; Pfefferle, L. D.; Haller, G. L. *Chem. Mater.* **2006**, *18*, 5584-5590.

Chapter 2

Morphology Control of Mesoporous Silica Spheres via Pseudomorphic Transformations

2.1 Introduction

Mesoporous silica spheres with controllable pore sizes, narrow pore size distributions and high surface areas are of interest for various applications including catalysis,[1-3] drug delivery,[4-6] packing materials for chromatography[7-9] and other applications.[10-15] Several direct methods have been developed to synthesize mesoporous silica spheres using surfactants as templates for mesopores during sphere formation.[10-12,16-22] Some of these approaches produce uniform spheres with well ordered mesopores, but often it is challenging to avoid sphere aggregation and maintain good size control and monodispersity. In the case of amorphous, dense silica spheres, the well-established Stöber method yields products with controllable size, smooth surfaces and high monodispersity.[23] To build on these structural advantages and also introduce mesoporosity into Stöber spheres, surfactant-induced pseudomorphic transformations have been developed.[24] Pseudomorphic transformations are reactions in which chemical components change, for example, through dissolution and reprecipitation, while the shape of a solid material is preserved. Pseudomorphic transformations involving hydrothermal treatment of dense, amorphous silica spheres provide an alternative method to direct syntheses of mesoporous silica spheres, retaining the sizes and monodispersity of the original silica spheres.[8,24-27]

Here, we investigate the influence of the solvent used in syntheses of dense silica spheres (EtOH, *i*PrOH or BuOH) on the morphology and texture of mesoporous products obtained after pseudomorphic transformations. Different solvent environments result in slightly different degrees of condensation of amorphous, nonporous silica spheres. However, these small differences produce significant changes in surface morphologies

following hydrothermal reactions under specific conditions. After hydrothermal transformations employing a long-chain alkylammonium surfactant, pseudomorphic products of parent silica spheres synthesized in EtOH possess smooth surfaces, whereas products from spheres synthesized in *i*PrOH or BuOH possess highly corrugated surfaces. In addition, by using the silica spheres with corrugated surfaces as templates for nanocasting (gas-phase polymerization and carbonization of phenol-formaldehyde inside mesoporous silica spheres and subsequent removal of silica with hydrofluoric acid), mesoporous carbon spheres with hollow cores and surface morphologies resembling those of the mesoporous silica spheres are formed. These core-shell structures provide indirect information about the diffusion depth of surfactant molecules into the parent silica spheres during the pseudomorphic transformation and reveal that the cores of the mesoporous silica spheres with corrugated surfaces must have remained solid. Hence, these processes provide new ways to synthesize silica spheres with dense cores and mesoporous shells and hollow carbon spheres with mesoporous shells.

2.2 Experimental Section

2.2.1 Reagents

The following chemicals were used without further purification: tetraethyl orthosilicate (TEOS, Aldrich, 98%), ammonium hydroxide (Fisher Scientific, 29.36 %), EtOH (Pharmco-AAPER, 99.98 %), *i*PrOH (Mallinckrodt, 99.5 %), *n*-BuOH (Fisher Scientific, 99.8 %), sodium hydroxide (Mallinckrodt, 99 %), CTAB (Aldrich), phenol (Fisher Scientific, 99 %), paraformaldehyde (Aldrich, 95 %), hydrofluoric acid (Mallinckrodt, 48 %). Milipore water with a resistivity 18.2 MΩ-cm was used for all reactions.

2.2.2 Preparation of silica spheres

Silica spheres were synthesized by the Stöber method.[23] Mixtures of 180 mL EtOH, *i*PrOH or BuOH with 10 mL ammonium hydroxide and 7 g TEOS were stirred at room temperature in a stoppered 500-mL round-bottom flask for 20 h. The silica spheres

were recovered and purified by multiple cycles of centrifugation and washing with EtOH. They were dried at 70–80 °C overnight before being used for hydrothermal reactions. The products were denoted SiO_2-EtOH, SiO_2-*i*PrOH and SiO_2-BuOH, depending on the solvent used.

2.2.3 Hydrothermal reactions

The amorphous parent silica spheres were transformed to mesoporous silica spheres using pseudomorphic transformation reactions. Amorphous silica spheres (0.044 g) dispersed in EtOH (2.53 mL) were added to a mixture of CTAB (0.05 g), water (10 mL) and NaOH (0.013 g) and stirred at room temperature for 30 min. The molar ratio of all components was 1 SiO_2 : 0.18 CTAB : 0.44 NaOH : 750 H_2O : 75 EtOH. The hydrothermal reaction was carried out in a Teflon-lined autoclave at 100 °C for 24 h. The products were recovered and purified by multiple cycles of centrifugation and washing with EtOH. The surfactant was removed from the mesoporous silica spheres by calcination in air at 550 °C for 6 h (heating rate 1 °C/min). The final products were denoted HT-SiO_2-EtOH, HT-SiO_2-*i*PrOH and HT-SiO_2-BuOH, depending on the solvent used in the Stöber synthesis of the parent spheres.

2.2.4 Preparation of hollow-core@mesoporous-shell carbon spheres by nanocasting

Mesoporous silica spheres (HT-SiO_2-*i*PrOH) were used as templates for nanocasting carbon spheres, following a published procedure based on phenol-formaldehyde gas-phase polymerization.[28,29] Calcined mesoporous silica spheres (0.044 g HT-SiO_2-*i*PrOH or HT-SiO_2-EtOH) were stirred for 1 h in a mixture containing 5 mL EtOH, 5 mL water and 0.03 g of $AlCl_3 \cdot H_2O$ to introduce Al into the structure as a polymerization catalyst. The Al-loaded spheres were washed with EtOH, dried at 70-80 °C overnight and calcined for 4 h at 550 °C (heating rate 1 °C/min). A flask containing phenol (0.05 g), paraformaldehyde (0.035 g) and calcined Al-mesoporous silica spheres (0.044 g) was evacuated under static vacuum (- 70 kPa) for 4 h and then heated at 100 °C for 24 h in a closed system. The color of the material changed from white to dark-red. The phenolic resin inside Al-mesoporous silica spheres was carbonized by heating the sample in nitrogen at 160 °C for 5 h (heating rate 1 °C/min) and then at

850 °C for 7 h (heating rate 5 °C/min). Silica was removed by extraction with hydrofluoric acid (10 wt%) for 24 h. *Caution: HF is highly corrosive and toxic and must be handled according to procedures specified by the Materials Safety Data Sheet for HF.* The product spheres were labeled PFC-*i*PrOH or PFC-EtOH, depending on the parent spheres.

2.2.5 Characterization

Scanning electron microscopy (SEM) images were obtained using a JEOL 6700 microscope with an accelerating voltage of 5 kV and an applied current of 20 mA. All siliceous samples were coated with 5 nm of Pt. Transmission electron microscopy (TEM) images were obtained using a JEOL 1210 microscope with an accelerating voltage of 120 kV. Samples were prepared on TEM Cu grids covered with Formvar carbon film. Nitrogen sorption measurements were carried out at 77 K on a Quantachrome Instruments Autosorb-1 system. Samples were degassed for 24 h at 150 °C. The Brunauer-Emmett-Teller (BET) method was applied to estimate specific surface areas. Pore sizes and volumes were calculated from pore size distribution curves in the adsorption branches of the isotherms. Small-angle X-ray scattering (SAXS) data were obtained using a Rigaku RU-200BVH 2-D SAXS instrument with a 12 kW rotating anode with a Cu source and a Siemens Hi-Star multi-wire area detector. The distance between the sample and the detector was 54 cm, the exposure time was 300 s and the step interval 0.01° 2θ. ^{29}Si NMR spectra were acquired using a Varian VNMRS spectrometer operating at a ^{1}H Larmor frequency of 700 MHz and a temperature of 25 ˚C. Samples were packed into a 3.2 mm rotor and spun at the magic angle (15 kHz) in a BioMAS Varian triple resonance probe. A single 90˚ pulse of 5.5 μs duration was applied to the ^{29}Si channel followed by ^{1}H decoupling (75 kHz) during acquisition. A recycle delay of 45 s was used between scans.

2.3. Results

2.3.1 Pseudomorphic transformation of amorphous silica spheres

The surfaces of the parent silica spheres prepared by Stöber syntheses in different solvents (SiO_2-EtOH, SiO_2-*i*PrOH and SiO_2-BuOH) were smooth on the SEM scale (Figure 2.1 and Figure 2.3A) and the spheres were virtually nonporous (Figure 2.2). After pseudomorphic transformation reactions, the average diameters of the mesoporous product spheres all increased {SiO_2-EtOH (436±18 nm), HT-SiO_2-EtOH (527±20 nm); SiO_2-*i*PrOH (623±37 nm), HT-SiO_2-*i*PrOH (730±45 nm); SiO_2-BuOH (494±23 nm), HT-SiO_2-BuOH (733±40 nm)}. The product spheres were more aggregated than the parent spheres. The surface morphologies of the products differed significantly after hydrothermal treatment, depending on the solvent used to synthesize the parent spheres. Smooth surfaces were maintained for HT-SiO_2-EtOH silica spheres (Figure 2.3B and C), which possessed mesoporous channels directed toward the outside surface. These can be observed by TEM in sufficiently thin, near-surface regions (Figure 2.4A). However, the products from parent silica spheres prepared in *i*PrOH (HT-SiO_2-*i*PrOH) or BuOH (HT-SiO_2-BuOH) exhibited extensive corrugation with deep cavities at the surface (Figure 2.3D-I). Such corrugation has been observed before when mesoporous silica was deposited on denser silica spheres if trimethylbenzene/decane was added to the surfactant system as a co-solvent to expand pores.[30] No such co-solvent was used here. TEM images of HT-SiO_2-*i*PrOH and HT-SiO_2-BuOH spheres reveal features resembling a mane on the outer part of the spheres (Figure 2.4B–D). Mesopores in the hydrothermal products HT-SiO_2-*i*PrOH and HT-SiO_2-BuOH were generally directed radially from the core to the outside, at least near the sphere surfaces. This directionality may result from the combined effects of individual surfactant molecules aligning on the solid sphere surface to reduce the surface energy and their tendency to assemble into micelles.[31,32] In modified Stöber syntheses of mesoporous silica spheres[33] and in syntheses of silica spheres with solid cores and mesoporous shells,[11,17,30] similar radial orientation of mesopores is also observed and has been attributed to preferred alignment of CTAB micelles normal to a growth interface.[34] The cores of HT-SiO_2-*i*PrOH and HT-SiO_2-BuOH spheres appear denser in the TEM images (Figure 2.4B and C), and SEM images of broken spheres reveal a solid-core, corrugated-shell structure (Figure 2.3E and H). In the HT-SiO_2-*i*PrOH sample, aggregates of smaller particles were observed (Figure 2.4B inset) in addition to the larger spheres. These side products are believed to have formed during the

hydrothermal transformation by direct surfactant templating of dissolved silica, and they could be removed by multiple centrifugation.

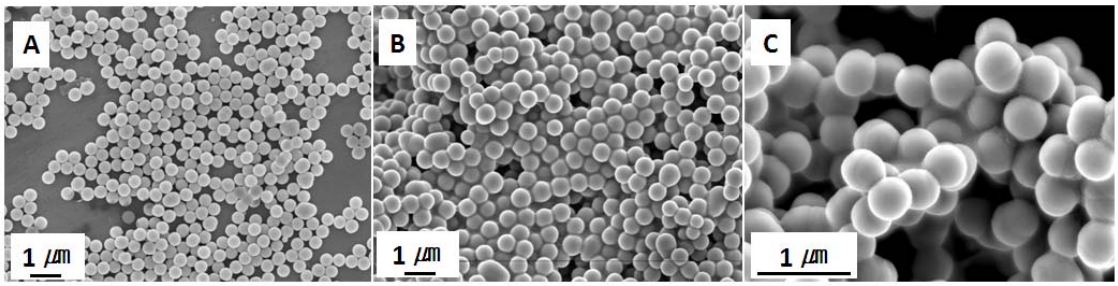

Figure 2.1 SEM images of amorphous parent silica spheres: (A) SiO_2-EtOH, (B) SiO_2-*i*PrOH and (C) SiO_2-BuOH.

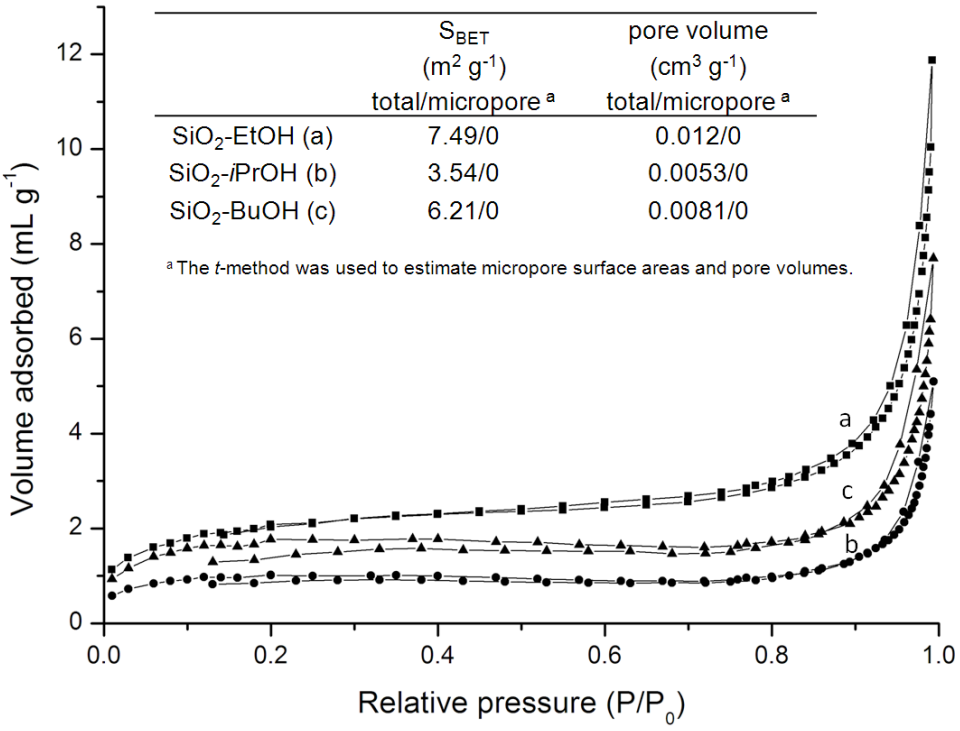

	S_{BET} ($m^2\ g^{-1}$) total/micropore [a]	pore volume ($cm^3\ g^{-1}$) total/micropore [a]
SiO_2-EtOH (a)	7.49/0	0.012/0
SiO_2-*i*PrOH (b)	3.54/0	0.0053/0
SiO_2-BuOH (c)	6.21/0	0.0081/0

[a] The *t*-method was used to estimate micropore surface areas and pore volumes.

Figure 2.2 Nitrogen sorption isotherms, BET surface areas and pore volumes (inset) of parent silica spheres prepared under different solvent conditions. (a) SiO_2-EtOH, (b) SiO_2-*i*PrOH and (c) SiO_2-BuOH.

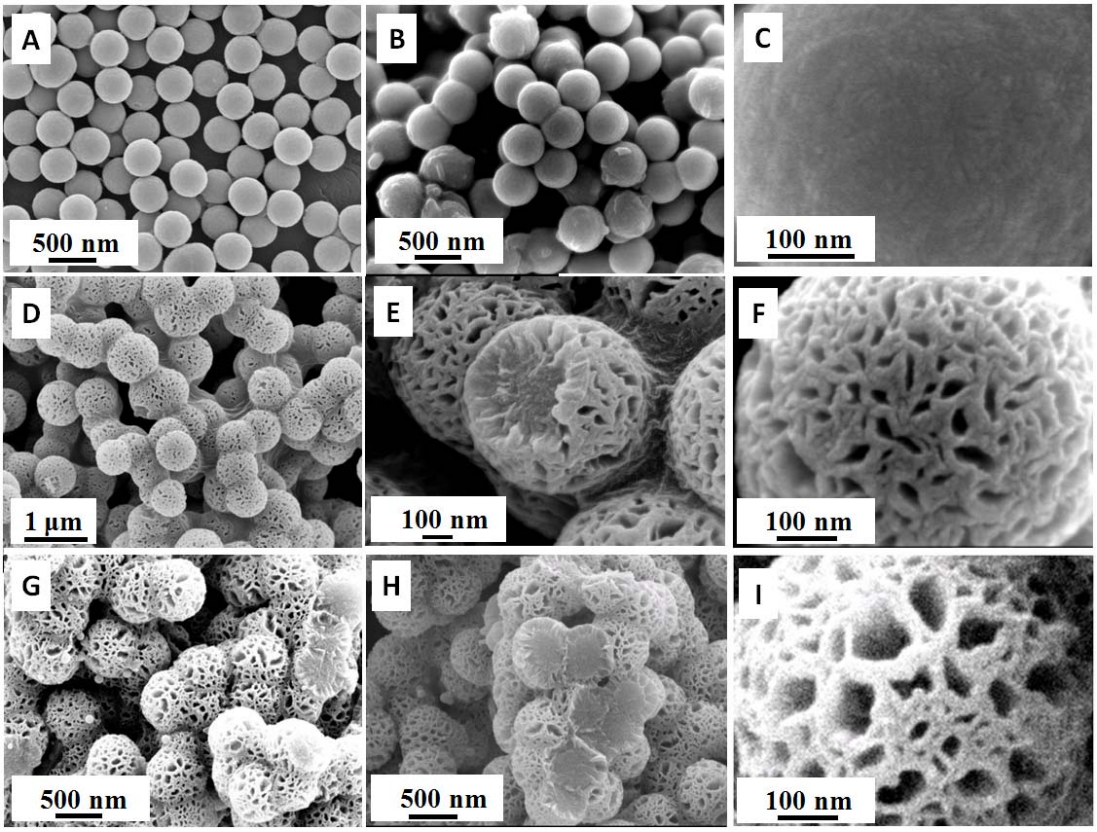

Figure 2.3 SEM images of parent silica and hydrothermal silica spheres: (A) parent silica spheres produced in EtOH (SiO_2-EtOH), (B) hydrothermal product HT-SiO_2-EtOH, (C) magnified image of HT-SiO_2-EtOH, (D) hydrothermal product HT-SiO_2-*i*PrOH, (E) broken structures of HT-SiO_2-*i*PrOH, (F) magnified image of HT-SiO_2-*i*PrOH, (G) hydrothermal product HT-SiO_2-BuOH, (H) broken structures of HT-SiO_2-BuOH, (I) magnified image of HT-SiO_2-BuOH.

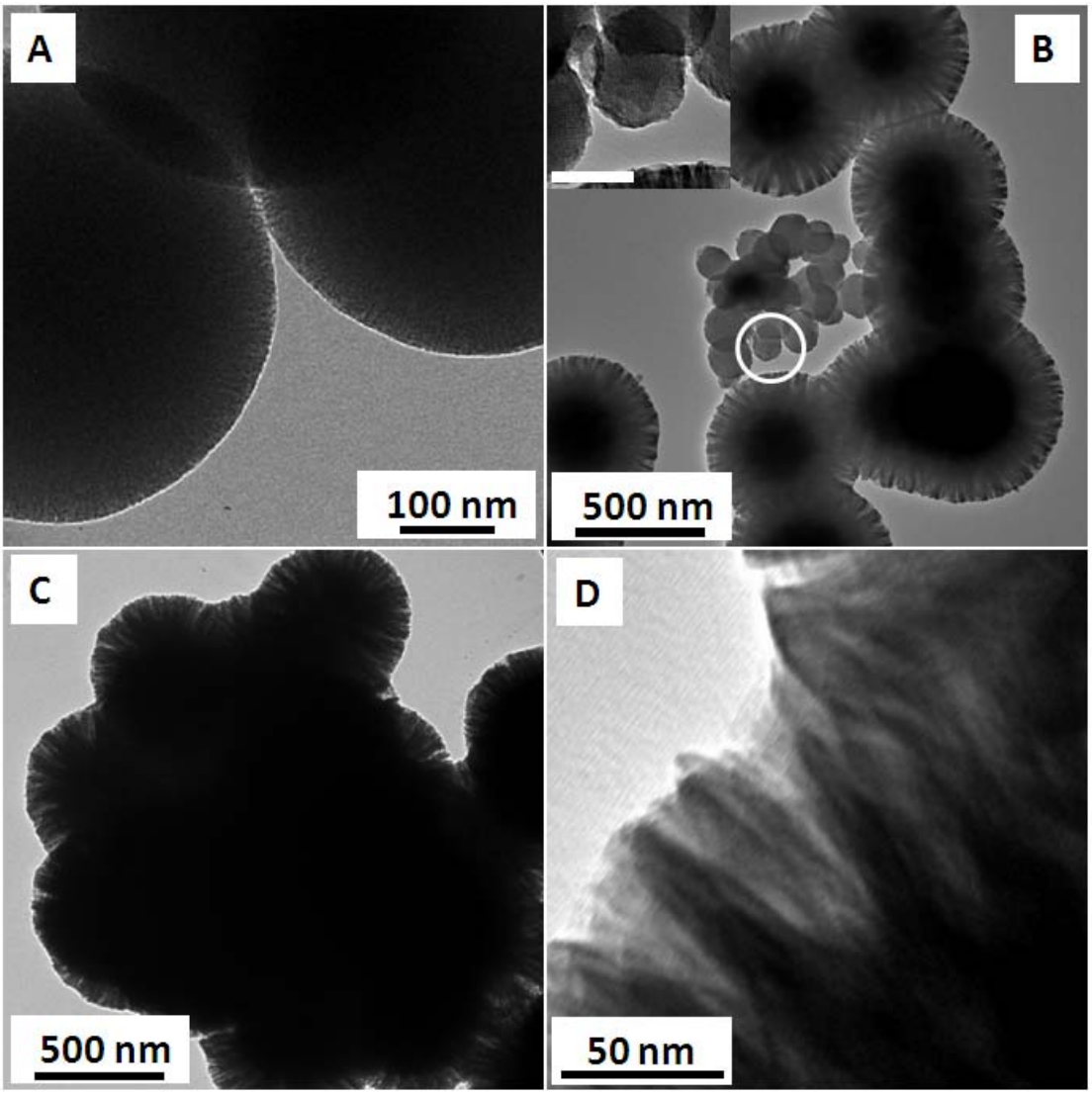

Figure 2.4 TEM images of hydrothermal reaction products (A) HT-SiO_2-EtOH, (B) HT-SiO_2-*i*PrOH and (C) HT-SiO_2-BuOH. The inset in (B) shows an enlargement of the circled region with a scale bar of 100 nm. (D) shows a higher magnification image of HT-SiO_2-*i*PrOH.

A published diffraction pattern of spherical MCM-41 particles that were synthesized by incorporating CTAB directly in a Stöber synthesis showed a major reflection indexed as (100) and lower-intensity, overlapping (110) and (200) peaks of a hexagonal pore system.[35] Those data were interpreted in terms of local hexagonal symmetry around individual mesopores with less long-range order and an overall

spherically symmetric pore distribution. The SAXS pattern of HT-SiO_2-EtOH resembles this pattern (Figure 2.5). The (100) and higher order peaks are relatively broad as a result of limited long-range order.[25,36] For HT-SiO_2-*i*PrOH the intensity of the (100) peak is significantly reduced and in case of HT-SiO_2-BuOH, a (100) peak is missing completely. Due to the corrugated shell of these spheres, mesopores are confined to smaller regions, causing extensive line broadening. In addition, surface corrugation may have perturbed the assembly of surfactant molecules near the surface, reducing the mesopore order. The *d*-spacing values corresponding to the (100) reflections of the hydrothermally treated spheres are listed in Table 2.1.

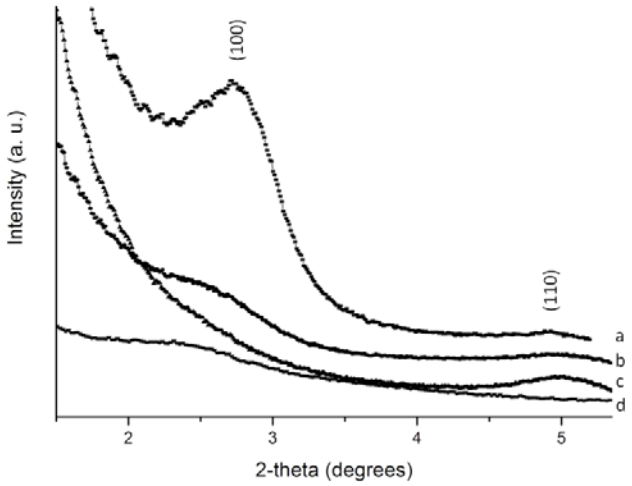

Figure 2.5 SAXS patterns of hydrothermal products and nanocast carbon spheres: (a) HT-SiO_2-EtOH, (b) HT-SiO_2-*i*PrOH, (c) HT-SiO_2-BuOH and (D) PFC- *i*PrOH.

Table 2.1 Textural characteristics of pseudomorphic silica products and nanocast carbon spheres.

Sample	S_{BET} (m^2 g^{-1}) total/micropore[a]	pore volume (cm^3 g^{-1}) total/micropore[a]	pore diameter (nm)[b]	wall thickness (nm)[c]	*d*-spacing (nm)[d]	diameter (nm)[e]	shell thickness (nm)[f]
HT-SiO_2-EtOH	729/0	0.50/0	2.1	1.2–1.7	3.3	91	NA[g]
HT-SiO_2-*i*PrOH	124/0	0.17/0	2.2	1.3–1.9	3.6	107	113 ± 29
HT-SiO_2-BuOH	219/0	0.50/0	2.4	ND[h]	ND[h]	239	151 ± 20
PFC-*i*PrOH[i]	2100/105	2.04/0.05	2.3	1.3–1.9	3.6	-182	50–120

[a] The *t*-method was used to estimate micropore surface areas and pore volumes. [b] Pore diameters were estimated from peaks in the pore size distribution curves that were derived from adsorption branches. [c] Wall thicknesses were estimated assuming either worm-like (low values) or 2-D hexagonal mesopore geometries (high values). [d] *d*-spacings of the (100) reflection. [e] This refers to the change in average diameter of product spheres compared to parent spheres. [f] Estimated from SEM or TEM images. [g] Not applicable. [h] Not determined due to the disordered mesoporous structure. [i] Nanocast carbon spheres from HT-SiO_2-*i*PrOH mesoporous silica spheres.

2.3.2 Carbon nanocasting of mesoporous silica spheres

To further investigate the density and porosity gradients across the spheres, we synthesized carbon replica structures of HT-SiO_2-*i*PrOH and HT-SiO_2-EtOH spheres by nanocasting. Nanocasting is an efficient method for producing inverse replica structures of porous materials.[37,38] Structural analysis of the products can be employed to deduce the structure of the template used for nanocasting. After introduction of aluminum into the spheres as a catalyst for polymerization, the spheres were exposed to a gas-phase phenol-formaldehyde mixture, which was polymerized and carbonized (Figure 2.6). Following removal of silica by extraction with hydrofluoric acid, an irregular network of interconnected carbon spheres was recovered from the HT-SiO_2-*i*PrOH preforms (Figure

2.7A and B). The average diameter of the carbon spheres (548 ± 27 nm) was lower than that of the silica preform, most likely due to radial contraction during the carbonization process. Some of the spheres were broken, revealing a hollow core, surrounded by ca. 50–120 nm-thick porous shells, i.e., a little thinner than the mesoporous shells in the preforms. In TEM images (Figure 2.7C and D) the shell has a mane-like appearance, similar to that observed for the silica preforms. The SAXS pattern for the hollow carbon spheres is also similar to that of the preforms with nearly identical peak positions and widths, albeit lower intensities (Figure 2.5). The hollow core confirms that polymer could penetrate the preforms only to a limited depth, providing further support for the dense core in the mesoporous silica spheres. In case of the carbon replica from HT-SiO_2-EtOH (PFC-EtOH), no hollow spheres were observed and, therefore, mesopores must have extended deeper in HT-SiO_2-EtOH, similar to the products from pseudomorphic transformations reported by Martin et al.[24] A TEM image of the surface region of the carbon replica PFC-EtOH revealed worm-like mesopores (Figure 2.8).

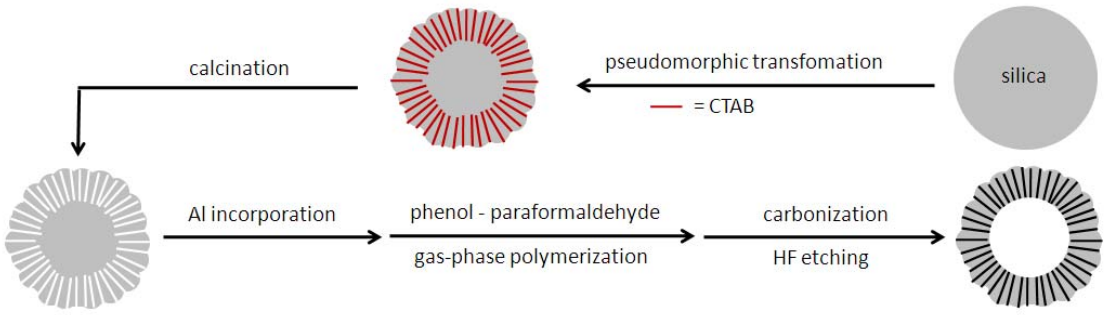

Figure 2.6 Schematic illustration of the preparation of hollow carbon spheres by nanocasting.

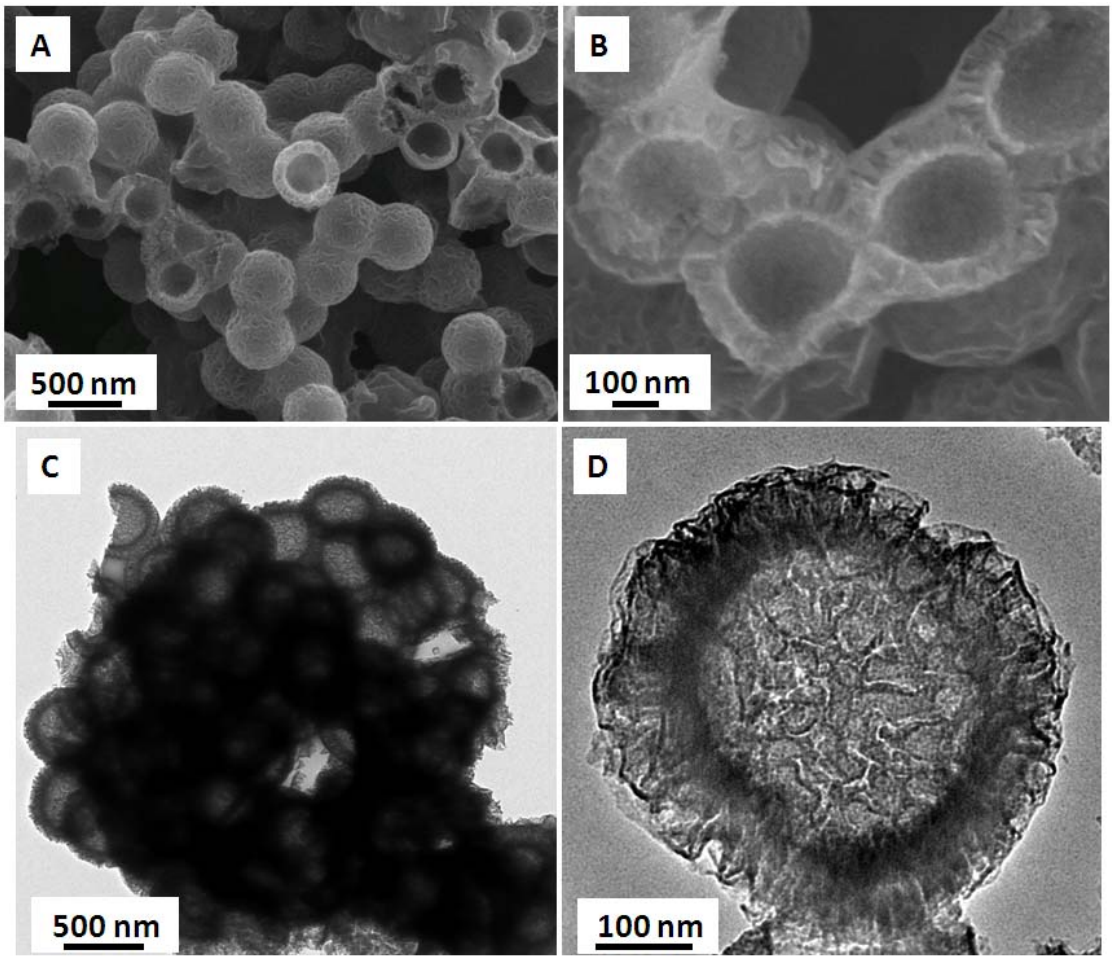

Figure 2.7 SEM (A and B) and TEM (C and D) images of nanocast hollow carbon spheres after HF etching (PFC-*i*PrOH).

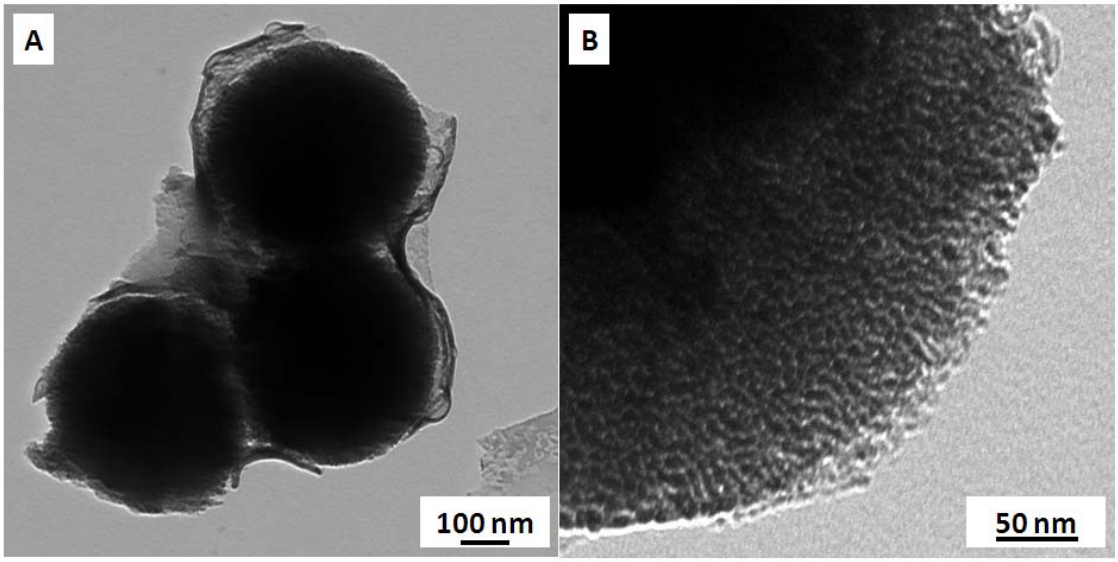

Figure 2.8 TEM images of nanocast carbon spheres after HF etching. HT-SiO_2-EtOH was used as a preform.

All three hydrothermal silica products and the carbon replica material (PFC-*i*PrOH) exhibited type IV nitrogen sorption isotherms, typical for capillary condensation in mesopores of MCM-41 type materials (Figure 2.9). While mesopore diameters and wall thicknesses were similar for all four samples, the specific BET surface areas and pore volumes differed widely (Table 2.1). The two silica samples with corrugated surfaces (HT-SiO_2-*i*PrOH and HT-SiO_2-BuOH) had significantly lower specific surface areas than HT-SiO_2-EtOH, likely resulting from the denser cores in the former samples. The very high surface area, large pore volume and presence of additional micropores of PFC-*i*PrOH are often seen in mesoporous carbons prepared by nanocasting methods.

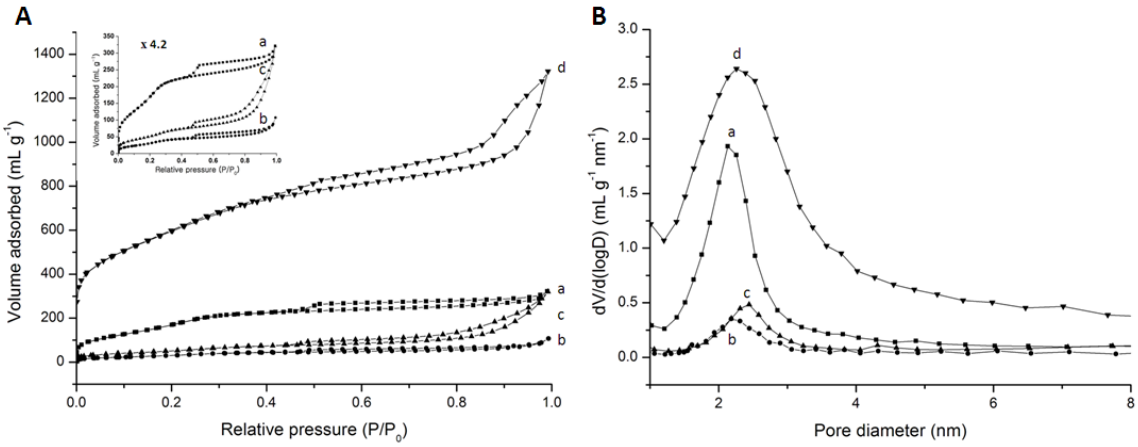

Figure 2.9 (A) Nitrogen sorption isotherms and (B) pore size distributions calculated from the adsorption branches by the BJH (Barrett-Joyner-Halenda) method. (a) HT-SiO_2-EtOH, (b) HT-SiO_2-*i*PrOH, (c) HT-SiO_2-BuOH and (D) PFC-*i*PrOH.

2.4 Discussion

What causes these drastic differences in surface morphologies and pore textures? In a study by Kim et al.,[30] some surface corrugation was introduced by employing trimethylbenzene/decane co-solvents as swelling agents during deposition of mesoporous silica on nonporous silica cores. No swelling agents were present in the hydrothermal reaction mixtures used for the transformations studied here. Tan and Rankin noted that in syntheses of mesoporous silica spheres, variations in the dielectric constant of the solvent alter the micelle organization and particle morphology.[34] However, in our study, the procedures and reaction conditions were identical during hydrothermal treatment of all three sets of silica spheres. Furthermore, micelle formation was decoupled from the solvent used during the synthesis of the amorphous parent silica spheres. It is therefore reasonable to propose that the solvent employed during the Stöber sphere synthesis influenced the final morphology, most likely by controlling the extent of silica condensation. In their original report, Stöber and co-workers found that the condensation rates and sphere sizes depended on the type of alcohol used in the synthesis.[23] Reaction rates were fastest with methanol and slowest with *n*-butanol and final particle sizes varied

inversely with the rates. Artaki et al. investigated the role of non-alcoholic solvents during condensation of sol-gel silica, pointing out that a reduction in the rate of hydrolysis and condensation causes the formation of branched gel networks with increased porosity and reduced density.[39]

We employed ^{29}Si solid-state MAS NMR spectroscopy of the parent silica spheres to investigate the degree of silica condensation in spheres prepared in the three different alcohols. The spectra of all parent silica spheres show two major peaks at -108 ppm and -98 ppm with small shoulders at -89 ppm (Figure 2.10). These correspond to Q^4, Q^3 and Q^2 resonances, respectively, i.e., a central Si with 4, 3 or 2 adjacent –O–Si– bridges and 0, 1 or 2 hydroxyl groups. The extent of condensation was estimated from the integrated peak areas by curve resolution of the Q^3 and Q^4 resonances. The amount of cross-linking was highest for SiO_2-EtOH spheres (Q^3 = 39.0 %, Q^4 = 61.0 %) and nearly identical for SiO_2-*i*PrOH (Q^3 = 44.6 %, Q^4 = 55.4 %) and SiO_2-BuOH spheres (Q^3 = 45.2 %, Q^4 = 54.8 %). Many factors may be responsible for the different degrees of condensation in different solvents, but in general, higher molecular weight alcohols retard the rate of hydrolysis and condensation of silica spheres.[23] Our NMR data show that this effect is small for the solvents used here, but the diverse surface morphologies reveal that such small differences in the silica connectivity can significantly affect the reactivity of the spheres under specific conditions.

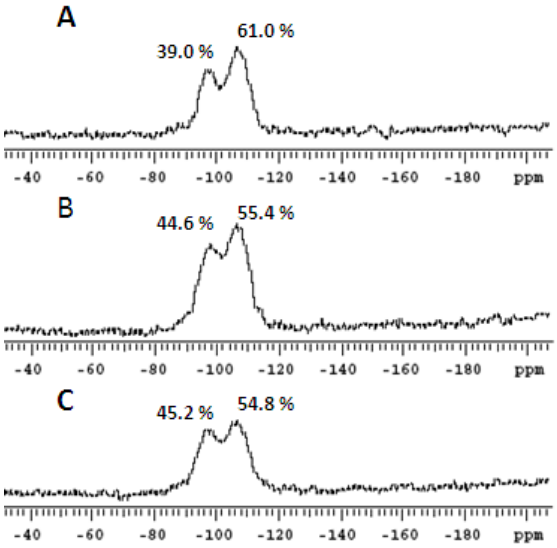

Figure 2.10 ^{29}Si solid-state MAS NMR spectra of the parent silica spheres: (A) SiO_2-EtOH, (B) SiO_2-*i*PrOH and (C) SiO_2-BuOH.

During the pseudomorphic transformation reaction, partial dissolution of silica by the alkaline solution occurs simultaneously with the assembly of the surfactant. The small differences in the extent of silica sphere condensation caused by the original solvents thus could result in different dissolution rates of silica structures during the hydrothermal reaction, which would alter the ratio between reactive silica oligomers and surfactant molecules. The more highly condensed SiO_2-EtOH spheres dissolved to a lesser extent. Therefore, less dissolved silica was available for redeposition, resulting in the smallest increase in average sphere diameter. For these spheres, the transformation to mesoporous spheres was largely pseudomorphic as described in previous studies.[24] Relatively less condensed and more reactive silica spheres (SiO_2-*i*PrOH and SiO_2-BuOH) produced more pitted mesoporous shells that surrounded nonporous cores. In these cases it appears that silica had dissolved to a greater degree and then redeposited on nondissolved spheres. Surfactant molecules were associated more strongly with the shell structure and were not readily available to penetrate the core. Hence, for these two sphere systems, the hydrothermal transformation was not truly pseudomorphic. The core-shell morphology was most pronounced with the following optimized molar ratio of reagents: 1 SiO_2 : 0.18 CTAB : 0.44 NaOH : 750 H_2O : 75 EtOH. When only half this sodium hydroxide

concentration was used to decrease the rate of dissolution, no significant morphological changes were observed for HT-SiO_2-*i*PrOH and HT-SiO_2-BuOH. On the other hand, when twice the concentration of sodium hydroxide was used, corrugated surfaces were also observed, but spheres tended to coalesce into irregular aggregates (Figure 2.11). We therefore conclude that the solvent used in the original sphere synthesis determines the degree of silica condensation, which affects the silica dissolution rate that determines the precursor:template ratio, the reaction depth relative to the sphere surface, and the redeposition processes during the pseudomorphic transformation.

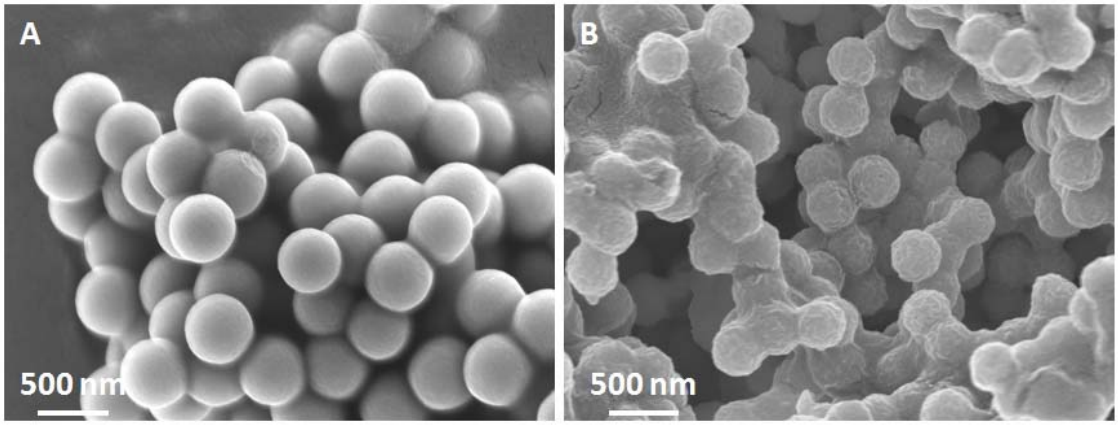

Figure 2.11 SEM images of HT-SiO_2-*i*PrOH mesoporous silica spheres produced using (A) half the regular NaOH concentration and (B) twice the regular NaOH concentration.

2.5 Conclusions

This study showed that the solvent used to prepare submicrometer silica spheres by Stöber syntheses affects the reactivity of the spheres in hydrothermal transformations that target mesoporous products. ^{29}Si solid-state MAS spectroscopy revealed small differences in the extent of silica of condensation, depending on the solvent used for the preparation of amorphous silica spheres (SiO_2-EtOH, SiO_2-*i*PrOH or SiO_2-BuOH). These small differences caused significant morphological changes on the surface after hydrothermal reactions within a specific range of conditions. Spheres prepared in EtOH produced relatively smooth spheres with mesopores penetrating relatively deep into the

bulk of the spheres. In this case the transformation can be considered largely pseudomorphic. Spheres synthesized in *i*PrOH or BuOH, solvents that retard condensation of silica, possessed slightly less interconnected silica networks. After hydrothermal transformations, the amorphous silica spheres were converted to solid core-mesoporous shell structures with narrow mesopore size distributions (diameters between 2.1–2.4 nm) but visible surface texture on the length scale of tens of nanometers. The kinetically controlled dissolution and reassembly phenomena that influence the hydrothermal transformation provide approaches for synthesizing mesoporous structures with porous shells and dense cores from monodisperse amorphous silica spheres with well-controlled size. Such spheres with density gradients can be used as templates for nanocasting of hollow carbon spheres with mesoporous shells and surface features similar to those of the hydrothermal mesoporous silica products. An understanding of factors influencing the texture and surface morphology of uniform silica spheres and hollow carbon spheres is important in the development of these materials for chromatography, controlled release and other applications.

2.6 References

(1) Chen, H.-T.; Huh, S.; Wiench, J. W.; Pruski, M.; Lin, V. S.-Y. *J. Am. Chem. Soc.* **2005**, *127*, 13305-13311.

(2) Shokouhimehr, M.; Piao, Y.; Kim, J.; Jang, Y.; Hyeon, T. *Angew. Chem. Int. Ed.* **2007**, *46*, 7039-7043.

(3) Zhang, Q.; Lee, I.; Ge, J.; Zaera, F.; Yin, Y. *Adv. Funct. Mater.* **2010**, *20*, 2201-2214.

(4) Lai, C.-Y.; Trewyn, B. G.; Jeftinija, D. M.; Jeftinija, K.; Xu, S.; Jeftinija, S.; Lin, V. S.-Y. *J. Am. Chem. Soc.* **2003**, *125*, 4451-4459.

(5) Lu, J.; Liong, M.; Zink, J. I.; Tamanoi, F. *Small* **2007**, *3*, 1341-1346.

(6) Zhu, Y.; Shi, J.; Shen, W.; Dong, X.; Feng, J.; Ruan, M.; Li, Y. *Angew. Chem. Int. Ed.* **2005**, *44*, 5083-5087.

(7) Kirkland, J. J.; Truszkowski, F. A.; Dilks, C. H.; Engel, G. S. *J. Chromatogr. A* **2000**, *890*, 3-13.

(8) Martin, T.; Galarneau, A.; Renzo, F. D.; Brunel, D.; Fajula, F.; Heinisch, S.; Crétier, G.; Rocca, J.-L. *Chem. Mater.* **2004**, *16*, 1725-1731.

(9) Han, Y.; Lee, S. S.; Ying, J. Y. *Chem. Mater.* **2007**, *19*, 2292-2298.

(10) Grün, M.; Lauer, I.; Unger, K. K. *Adv. Mater.* **1997**, *9*, 254-257.

(11) Büchel, G.; Unger, K. K.; Matsumoto, A.; Tsutsumi, K. *Adv. Mater.* **1998**, *10*, 1036-1038.

(12) Nooney, R. I.; Thirunavukkarasu, D.; Chen, Y.; Josephs, R.; Ostafin, A. E. *Chem. Mater.* **2002**, *14*, 4721-4728.

(13) Wang, Y.; Caruso, F. *Chem. Mater.* **2005**, *17*, 953-961.

(14) Wang, Y.; Caruso, F. *Adv. Mater.* **2006**, *18*, 795-800.

(15) Wang, Y.; Yu, A.; Caruso, F. *Angew. Chem. Int. Ed.* **2005**, *44*, 2888-2892.

(16) Lu, Y.; Fan, H.; Stump, A.; Ward, T. L.; Rieker, T.; Brinker, C. J. *Nature* **1999**, *398*, 223-226.

(17) Grün, M.; Unger, K. K.; Matsumoto, A.; Tsutsumi, K. *Microporous Mesoporous Mater.* **1999**, *27*, 207-216.

(18) Yoon, S. B.; Sohn, K.; Kim, J. Y.; Shin, C.-H.; Yu, J.-S.; Hyeon, T. *Adv. Mater.* **2002**, *14*, 19-21.

(19) Tan, B.; Lehmler, H.-J.; Vyas, S. M.; Knutson, B. L.; Rankin, S. E. *Adv. Mater.* **2005**, *17*, 2368-2371.

(20) Chen, H.; Hu, T.; Zhang, X.; Huo, K.; Chu, P. K.; He, J. *Langmuir* **2010**, *26*, 13556-13563.

(21) Ganguly, A.; Ahmad, T.; Ganguli, A. K. *Langmuir* **2010**, *26*, 14901-14908.

(22) Kim, T.-W.; Chung, P.-W.; Lin, V. S.-Y. *Chem. Mater.* **2010**, *22*, 5093-5104.

(23) Stöber, W.; Fink, A.; Bohn, E. *J. Colloid Interface Sci.* **1968**, *26*, 62-69.

(24) Martin, T.; Galarneau, A.; Renzo, F. D.; Fajula, F.; Plee, D. *Angew. Chem. Int. Ed.* **2002**, *41*, 2590-2592.

(25) Botella, P.; Corma, A.; Navarro, M. T. *Chem. Mater.* **2007**, *19*, 1979-1983.

(26) Galarneau, A.; Iapichella, J.; Bonhomme, K.; Renzo, F. D.; Kooyman, P.; Terasaki, O.; Fajula, F. *Adv. Funct. Mater.* **2006**, *16*, 1657-1667.

(27) Lim, S.; Ranade, A.; Du, G.; Pfefferle, L. D.; Haller, G. L. *Chem. Mater.* **2006**, *18*, 5584-5590.

(28) Lee, J.; Sohn, K.; Hyeon, T. *J. Am. Chem. Soc.* **2001**, *123*, 5146-5147.

(29) Wang, Z.; Li, F.; Ergang, N. S.; Stein, A. *Chem. Mater.* **2006**, *18*, 5543-5553.

(30) Kim, J. H.; Yoon, S. B.; Kim, J.-Y.; Chae, Y. B.; Yu, J.-S. *Colloids and Surfaces A: Physicochem. Eng. Aspects* **2008**, *313-314*, 77-81.

(31) Yoon, S. B.; Kim, J.-Y.; Kim, J. H.; Park, Y. J.; Yoon, K. R.; Park, S.-K.; Yu, J.-S. *J. Mater. Chem.* **2007**, *17*, 1758-1761.

(32) Deng, Y.; Qi, D.; Deng, C.; Zhang, X.; Zhao, D. *J. Am. Chem. Soc.* **2008**, *130*, 28-29.

(33) Tendeloo, G. V.; Lebedev, O. I.; Collart, O.; Cool, P.; Vansant, E. F. *J. Phys.:Condens. Matter* **2003**, *15*, S3037-S3046.

(34) Tan, B.; Rankin, S. E. *J. Phys. Chem. B* **2004**, *108*, 20122-20129.

(35) Pauwels, B.; Tendeloo, G. V.; Thoelen, C.; Rhijn, W. V.; Jacobs, P. A. *Adv. Mater.* **2001**, *13*, 1317-1320.

(36) Möller, K.; Kobler, J.; Bein, T. *Adv. Funct. Mater.* **2007**, *17*, 605-612.

(37) Lu, A.-H.; Schüth, F. *C. R. Chimie* **2005**, *8*, 609-620.

(38) Yang, H.; Zhao, D. *J. Mater. Chem.* **2005**, *15*, 1217-1231.

(39) Artaki, I.; Zerda, T. W.; Jonas, J. *J. Non-Cryst. Solids* **1986**, *81*, 381-395.

Chapter 3

Fabrication of Mesoporous Zeolites through Desilication and Re-assembly Processes

3.1 Introduction

Zeolites are crystalline, microporous aluminosilicate materials with well-defined pore structures and compositions, which can accomplish ion-exchange, catalysis and separation.[1-6] Zeolites have been used widely as catalysts, for example, because of their intrinsic acidity and size-selective catalytic performance. However, the diffusion limitations imposed by small pore apertures (usually less than 1 nm) for transport of large guest molecules to the active sites inside zeolites have restricted the catalytic activity of zeolites for various catalytic reactions.[2-4,7] In order to overcome these diffusion limitations, much effort has focused on decreasing the size or thickness of zeolite crystals so that more active sites are exposed to guest molecules. For instance, exfoliation of layered zeolite structures,[8,9] dual-templating approaches for creation of mesoporous zeolite crystals,[10] addition of porogens or supramolecules with SDAs[11-14] for introducing mesopores in zeolites, and template-assisted synthesis of nano-sized zeolite crystals[15-23] have been employed to create extra surface area or to reduce the size/thickness of zeolite catalysts. These methods have shown promising results; however, their synthetic processes are generally complex.

Desilication methods have recently received significant attention because they are relatively straight-forward to carry out (e.g., treatment of the zeolite with 0.2 M NaOH for 30 min at 338 K), and they can be applied to various types of zeolites (e.g., MFI, BEA, FER and MOR).[7,24-27] In an alkaline medium, less reactive Al sites maintain the zeolite framework while Si atoms are dissolved to render open structures. When compared with dealumination, a well-known post-treatment method for creating extra porosity in zeolite structures, desilication provides more controllable mesoporosity and preserves Brønsted acidity.[28,29] Generally, tailored mesoporosity by desilication can be achieved by altering

the Si/Al ratio of the parent zeolites, the reaction temperature, reaction time and concentration of the base. However, the process leads to reduced crystallinity (ca. 30 % determined by XRD and nitrogen sorption measurements) and the increase in external surface area is mainly associated with mesopores larger than 10 nm.[7,24-27]

Another approach involves simultaneous dissolution and re-deposition of dissolved species on the surface of the parent amorphous silica in the presence of long-chain alkylammonium surfactants (e.g., cetyltrimethylammonium bromide: CTAB).[30-32] Under basic conditions, the dissolved silicates assemble with surfactant molecules to form micelles and reprecipitate onto the surface of the parent spheres during the hydrothermal reaction to transform amorphous silica into mesoporous silica. These transformations of nonporous silica to porous silica can be performed without changing the shape of the parent materials in a reaction known as a pseudomorphic transformation:[30] a reaction in which chemical components change through dissolution and reprecipitation, while the shape of the solid material is preserved. Within certain compositional ranges (i.e., 1 SiO_2 : 0.1–0.18 CTAB : 0.1–0.44 NaOH : 50–750 H_2O), mesopores with 2-D hexagonal symmetry (*p6mm*) were usually developed, which originated from the formation of homogeneous micelles containing the dissolved species and the surfactant molecules.[30-33]

Here, we introduce a method for preparing mesoporous zeolite (meso-zeolite) materials by a combination of desilication and re-assembly processes, adopted from the concept of pseudomorphic transformations (Figure 3.1). Dissolved species containing silicates, aluminosilicates and fragments of the ZSM-5 crystals can be re-deposited on the parent zeolite structure by a surfactant molecule (here, CTAB) via micelle formation under hydrothermal conditions. Physicochemical properties of the meso-zeolite materials prepared by desilication and re-assembly (desilication/re-assembly) processes were characterized by solid-state ^{27}Al and ^{29}Si magic-angle-spinning (MAS) NMR, scanning and transmission electron microscopy (SEM and TEM), nitrogen sorption measurements, temperature-programmed ammonia desorption (TPD) measurements, X-ray diffraction (XRD) measurements, and elemental analysis by inductively coupled plasma spectroscopy (ICP). Final products prepared under specific alkaline conditions exhibit a dual-pore size distribution (ca. 3 and 10–30 nm), increased external surface areas (up to

327 m^2 g^{-1}) and well preserved crystallinity (ca. 83 % of the parent zeolite structure, determined by micropore pore volumes calculated from nitrogen sorption measurements, and 77 % estimated from XRD measurements). The product texture suggests that desilication and re-assembly occur simultaneously to create a dual-pore system. Re-assembly of the dissolved species by micellization of a surfactant produces small mesopores (ca. 3 nm), while the desilication process generates larger mesopores (10–30 nm) in the zeolite crystals under the specific conditions.

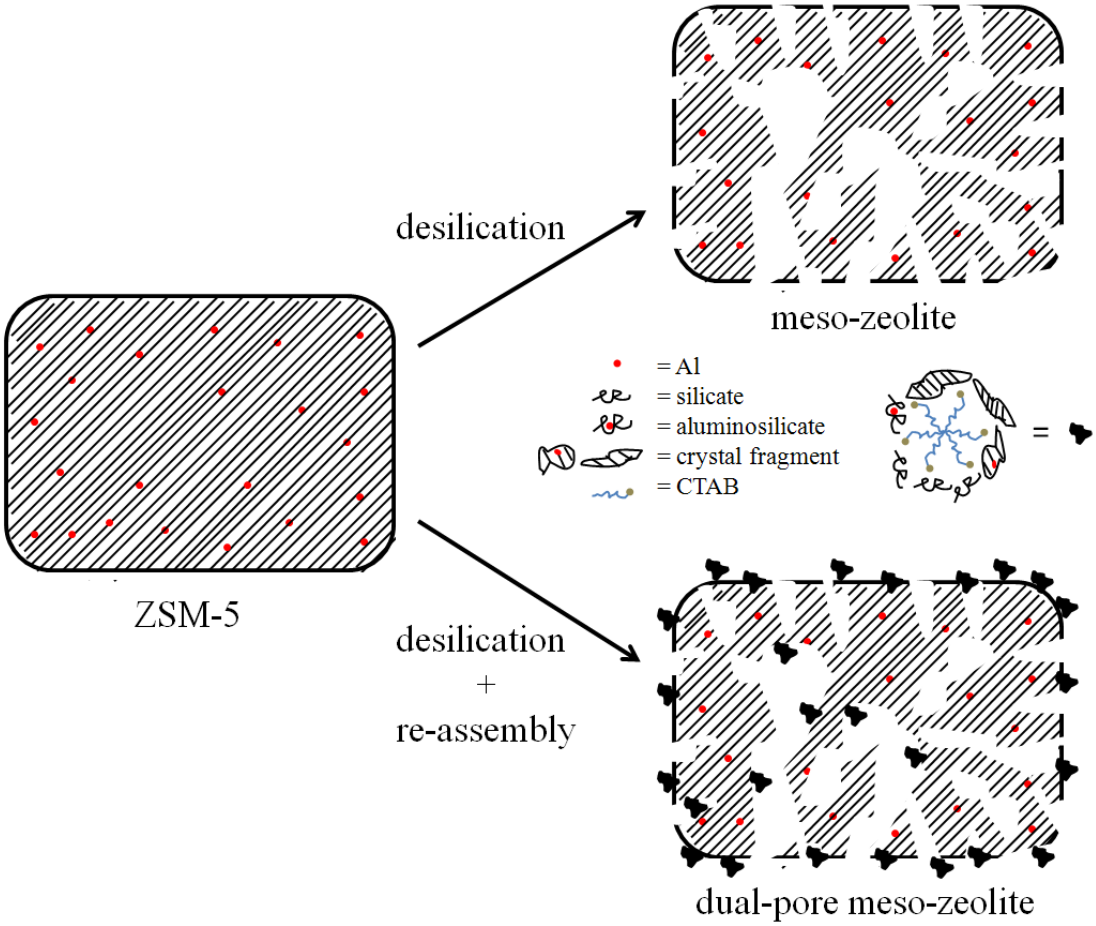

Figure 3.1 A schematic illustration showing the preparation of meso-zeolite materials via desilication (upper right) and desilication/re-assembly processes (bottom right).

3.2 Experimental Section

3.2.1 Reagents

The following chemicals were used without further purification. Tetrapropylammonium hydroxide (TPAOH, 1.0 M in H_2O), tetraethyl orthosilicate (TEOS, 98%) and cetyltrimethylammonium bromide (CTAB) were purchased from Aldrich, aluminum isopropoxide from Alfa Aesar, sodium hydroxide from Mallinckrodt Chemicals, ammonium nitrate from Fisher Scientific Company and ethanol (200 proof) from Pharmco-Aaper. Deionized water with a resistivity of 18.2 MΩ·cm was used for all reactions.

3.2.2 Synthesis of ZSM-5

Aluminum isopropoxide (0.074 g for Si/Al = 100, 0.148 for Si/Al = 50 and 0.248 for Si/Al = 30) was dissolved in a mixture of water (74.4 g) and 1.0 M aqueous TPAOH (16.56 g), and then TEOS (7.6 g) was added to the mixture. The mixtures of the following molar compositions (71.4 SiO_2 : 32 TPAOH : 9500 H_2O : 1.42 (for Si/Al = 100) / 2.85 (for Si/Al = 50) / 4.76 (for Si/Al = 30) Al_2O_3) were hydrolyzed with vigorous stirring for 24 h at room temperature. The filtered solutions were transferred into Teflon-lined autoclaves, and hydrothermal reactions were performed for 2 days (Si/Al =100), 4 days (Si/Al = 50) and 8 days (Si/Al = 30) at 100 °C. The final products were washed with water and centrifuged several times, then dried at 100 °C overnight. All samples were calcined to remove structure directing agents (SDAs) under an oxygen atmosphere with a heating rate of 1 °C/min up to 550 °C. They were maintained at 550 ˚C for 6 h and then cooled down to room temperature. The samples with Si/Al = 100, 50 and 30 were denoted as ZSM-5_100, ZSM-5_50, and ZSM-5_30, respectively.

3.2.3 Synthesis of meso-zeolites

ZSM-5_100, 50, and 30 (0.176 g) samples were dispersed in mixtures of water (20 g) and ethanol (10 g). Separately, CTAB (0.2 g) was dissolved in an alkaline solution containing 0.052 g (n = 1), 0.078 g (n = 1.5), 0.104 g (n = 2), 0.156 g (n = 3), or 0.312 g (n = 6) of NaOH and 20 g of water. Alternatively, similar alkaline solutions were

prepared without any CTAB. The alkaline solutions were combined with the zeolite dispersion to obtain mixtures with molar compositions (1 ZSM-5 : (0 or 0.18) CTAB : (n = 1, 1.5, 2, 3 or 6) NaOH : 750 H_2O : 75 EtOH). These were placed in Teflon-lined autoclaves. Hydrothermal reactions were performed for 24 h at 100 °C. The final products were washed with water and ethanol and centrifuged several times. They were dried at 80 °C overnight. All samples were calcined to remove the surfactant under an oxygen atmosphere using a heating rate of 1 °C/min up to 550 °C. They were maintained at 550 ˚C for 6 h and then cooled down to room temperature. As an example of the sample notation, samples prepared from ZSM-5_50, NaOH (n = 2) and with CTAB or without CTAB were denoted as HZ_50_OH2_S or HZ_50_OH2_NS, respectively.

3.3.4 Synthesis of H-form of zeolites

ZSM-5_50, HT_50_OH2_S, and HT_50_OH2_NS samples (ca. 50–70 mg) were sonicated in 0.1 M NH_4NO_3 solution for 1 h in a sonication bath. The samples were washed with water, centrifuged, and dried at 100 °C overnight. Then, the samples were calcined in air at 550 °C for 6 h. These samples are denoted as ZSM-5_50_H, HZ_50_OH2_S_H, and HZ_50_OH2_NS_H, respectively.

3.3.5 Characterization

Transmission electron microscopy (TEM) images were obtained using a JEOL 1210 microscope operating at 120 kV for low magnification images and a FEI Tecnai G2 F30 TEM operating at 300 kV for high resolution images collected using a CCD camera. Samples were crushed and supported on a holey carbon-coated copper grid (Ted Pella, Inc.) for the TEM investigation. Scanning electron microscopy (SEM) images were obtained with a JEOL 6700 microscope with an accelerating voltage of 5 kV and an applied current of 20 mA. All images were obtained with samples coated with 5 nm Pt. Nitrogen sorption measurements were carried out at 77 K on a Quantachrome Instruments Autosorb-1 system. Samples were degassed for 24 h at 150 °C. The Brunauer-Emmett-Teller (BET) method was applied to estimate specific surface areas. Pore sizes and volumes were calculated from pore size distribution curves in the adsorption branches of the isotherms. Elemental analyses were carried out on a Thermo

Scientific iCAP 6500 duo view ICP-OES (inductively coupled plasma optical emission spectrometer). NH_3 temperature-programmed desorption (TPD) was performed by Micromeritics to measure the acid sites on the zeolite materials, using a Micromeritics AutoChem II 2920 instrument equipped with a thermal conductivity detector (TCD). For these measurements, 50 mg of sample was placed in a quartz tube and heated to 120 °C under flowing He. A mixture of 10 % NH_3 in He was then introduced to be adsorbed onto the sample for 30 min. The sample was heated to 550 °C at 10 °C/min to release NH_3, and the desorption profile was measured by TCD. X-ray diffraction (XRD) patterns were acquired using a PANalytical X-Pert PRO MPD X-ray diffractometer equipped with a Co source (Co Kα, λ= 1.790 Å) and an X-Celerator detector. α-Alumina was used as an internal standard for evaluating the relative intensity of XRD patterns of the samples. Solid-state ^{27}Al and ^{29}Si magic-angle-spinning (MAS) NMR spectra were acquired using a Varian VNMRS spectrometer operating at a ^{1}H Larmor frequency of 600 MHz and a temperature of 25 °C. Samples were packed into a 3.2 mm rotor and spun at the magic angle at 8 kHz using a BioMAS Varian triple resonance probe. A single 16° pulse of 1 μs duration was applied for ^{27}Al NMR with a recycle delay of 1 s. A single 90° pulse of 5.5 μs duration was applied for ^{29}Si NMR with ^{1}H decoupling (71 kHz) during acquisition and a recycle delay of 45 s.

3.3 Results

3.3.1 HZ_100 series

Products in the HZ_100 series were synthesized hydrothermally at 100 °C for 24 h from precursors with molar compositions of 1 ZSM-5_100 : 0 or 0.18 CTAB : (n = 1.5, 2 or 3) NaOH : 750 H_2O : 75 EtOH. SEM images of the products show that the typical external shape of the ZSM-5 particles is approximately maintained for all samples (Figure 3.2). However, in samples treated without using CTAB (hereafter called the desilication products), voids with sizes ranging from tens to hundreds of nanometers are present (Figure 3.2a, c, and e). Some of these voids continue throughout whole particles. On the other hand, when CTAB was incorporated in the hydrothermal reactions, the

products (hereafter called desilication/re-assembly products) contained similar void spaces only in rare instances. Instead, they exhibited surfaces with more corrugated or "bumpy" textural features (Figure 3.2b, d, and f).

The particle morphology and interior of selected desilication and desilication/re-assembly products were further examined by TEM (Figure 3). In images of the desilication/reassembly product (HZ_100_OH2_S), the surface corrugation is also apparent and fringes corresponding to crystalline MFI zeolite are visible (Figure 3.3a and b). Lower magnification images of both desilication (HZ_100_OH3_NS) and (HZ_100_OH3_S) desilication/re-assembly products show dark rims around the particles, suggesting that the interior is hollow in both cases, even though the SEM image for the latter product showed only very few particles with visible voids. Apparently, most of the desilication/re-assembly particles are covered with a thin coating that hides the large voids.

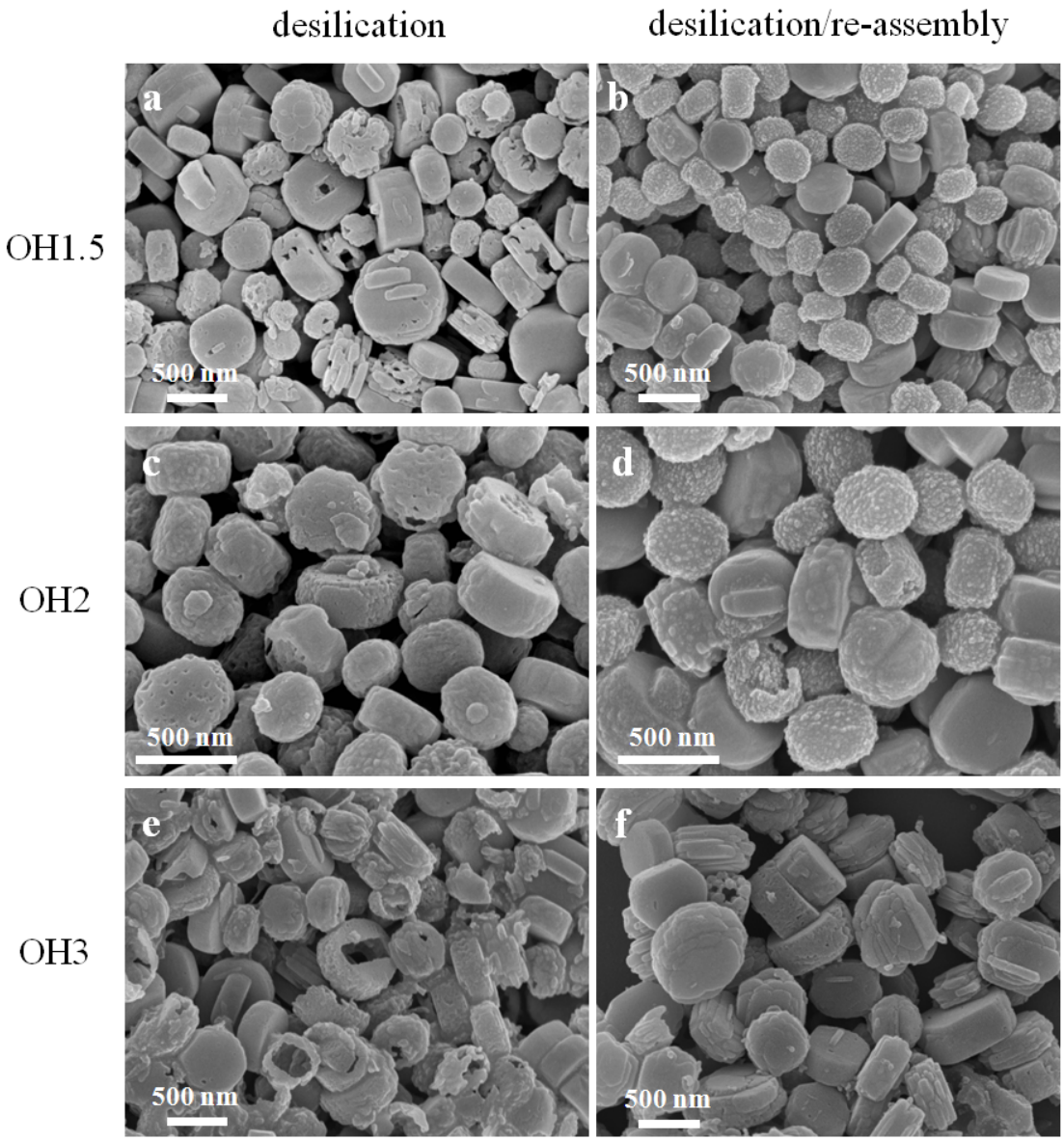

Figure 3.2 SEM images of (a) HZ_100_OH1.5_NS, (b) HZ_100_OH1.5_S, (c) HZ _100_OH2_NS, (d) HZ_100_OH2_S, (e) HZ_100_OH3_NS, and (f) HZ_100_OH3_S.

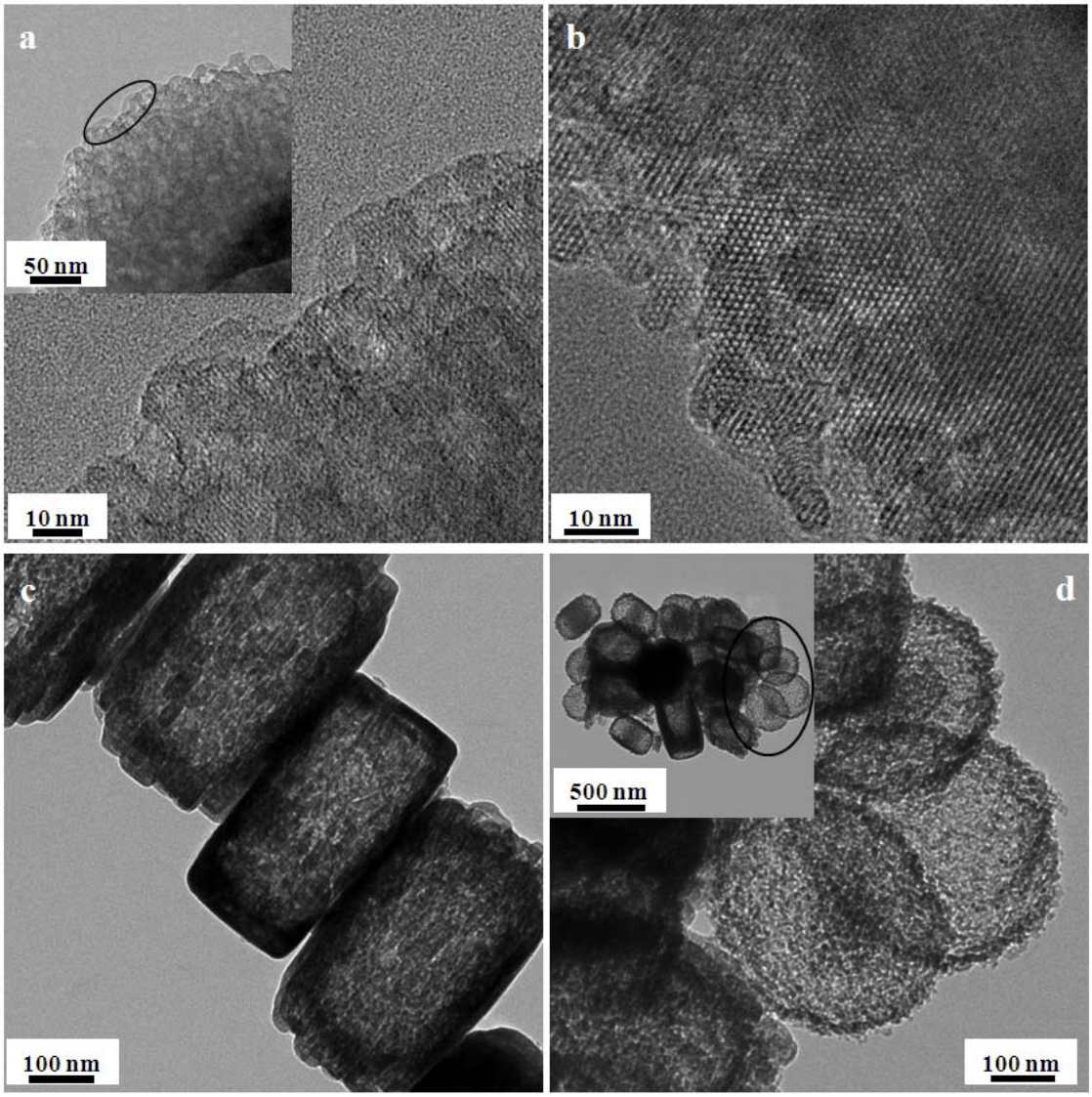

Figure 3.3 TEM images of (a and b) HZ_100_OH2_S, (c) HZ_100_OH3_NS, and (d) HZ_100_OH3_S. The images in (a) and (d) correspond to the marked regions in the insets that present a lower magnification image.

To quantify the porosity of the hydrothermally treated zeolites, nitrogen sorption measurements were carried out. BET isotherms are shown in Figure 3.4. The starting materials (ZSM-5_100 denoted as (a) in Figure 3.4) exhibit type I nitrogen sorption isotherms typical for zeolites, whereas the desilication products (denoted as (b)) and

desilication/re-assembly products (denoted as (c)) in Figure 3.4 produce type IV isotherms associated with mesoporous materials. A sharper increase of adsorption and desorption branches in the hysteresis on the desilication products (b) was observed at high relative pressures. This suggests that larger mesopores are present in the desilication products, compared to the desilication/re-assembly products.[35]

The BJH (Barrett-Joyner-Halenda) pore size distributions derived from the adsorption branches of the BET isotherms (Figure 3.5) agree with the assignment of more open structural features for the desilication products. For HZ_100_OH1.5_S/NS (Figure 3.5A) and HZ_100_OH2_S/NS (Figure 3.5B), desilication/re-assembly products (b) present higher values in the small mesopore range (usually less than 10 nm), whereas the desilication products show higher values in the large mesopore range (usually larger than 10 nm for HZ_100_OH1.5_NS/S (A) and larger than 50 nm for HZ_100_OH2_NS/S (B)). Moreover, the development of small mesopores (3–4 nm) and larger pores (ca. 10 nm) was observed in the isotherms of HZ_100_OH2_S (Figure 3.5B and D). The observation of small pores (ca. 2 nm), as those in Figure 3.5, is typical for ZSM-5 crystals, resulting from a fluid-to-crystalline like phase transition of the adsorbed phase, which depends on the Si/Al ratio and the synthetic procedures.[26]

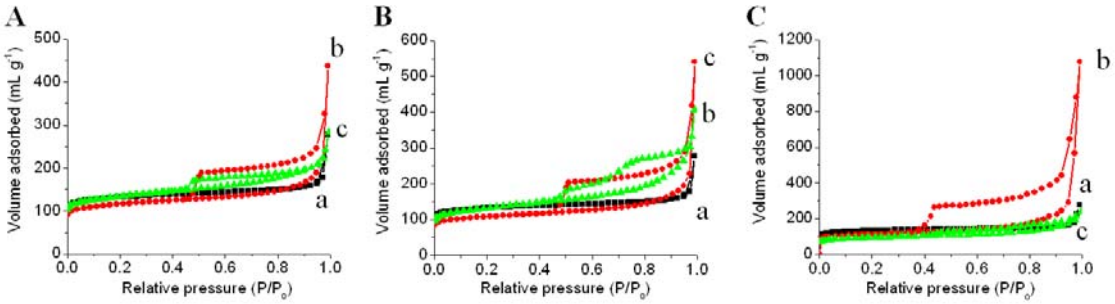

Figure 3.4 Nitrogen sorption isotherms for samples prepared using different concentrations of base (A for HZ_100_OH1.5_NS/S, B for HZ_100_OH2_NS/S, and C for HZ_100_OH3_NS/S). The parent zeolite crystal ZSM-5_100, desilication products and desilication/re-assembly products are denoted as a, b and c in all graphs, respectively.

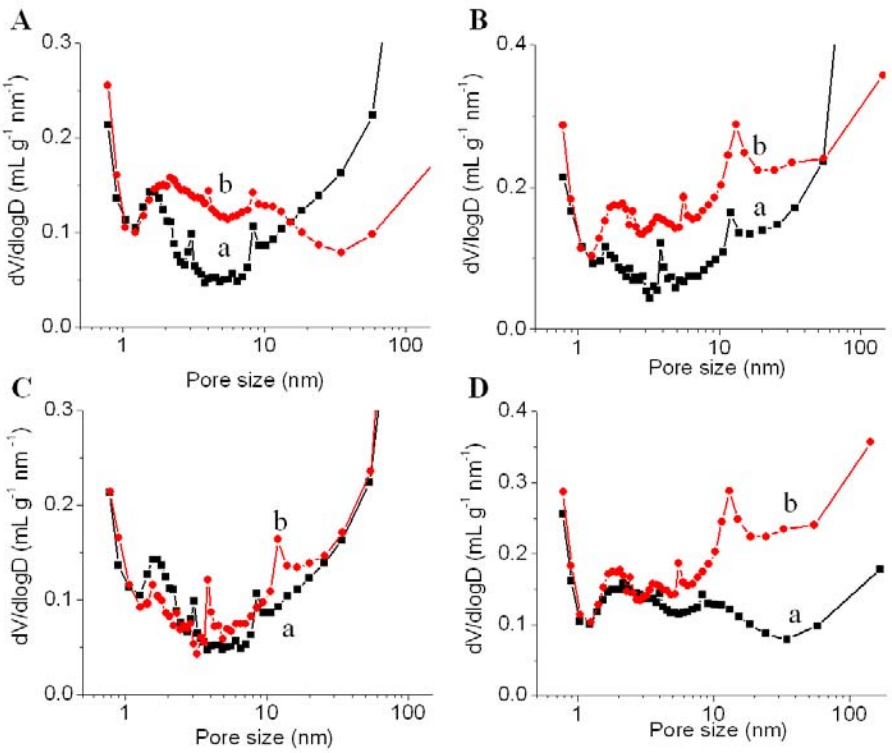

Figure 3.5 (A and B) BJH pore size distributions of samples prepared using different concentrations of base: (A) for HZ_100_OH1.5_NS (a) and HZ_100_OH1.5_S (b), and (B) for HZ_100_OH2_NS (a) and HZ_100_OH2_S (b). (C) Comparison of the pore size distributions for desilication products HZ_100_OH1.5_NS (a) and HZ_100_OH2_NS (b). (D) Comparison of the pore size distributions for desilication/re-assembly products HZ_100_OH1.5_S (a) and HZ_100_OH2_S (b).

The textural characteristics of all materials are summarized in Table 3.1. For all products, micropore surface areas and volumes were slightly lower than those of the parent materials (Figure 3.6B). It is noted that micropore volumes have often been used as an indicator for the crystallinity of MFI zeolites.[19,34] The small drops therefore show a relatively small loss in crystallinity after the hydrothermal reactions. All samples gained additional surface area (for pores > 2 nm). This gain was relatively small for the desilication products and similar for samples treated in solutions with different base concentration at a given Si/Al ratio (see Figure 3.6A). (In the discussions hereafter,

"surface area" will refer only to contributions from pore sizes with larger than 2 nm, labeled "external surface area" in Figures 3.6 and 3.10.) On the other hand, for desilication/re-assembly products, more significant increases in surface area are generally observed and depend on the concentration of base used during hydrothermal treatment (Figure 3.6A). For the materials with Si/Al ratio = 74, the sample HZ_100_OH2_S shows the highest surface area of 204 m^2 g^{-1}, i.e., a ca. 190 % increase compared to the parent sample with 107 m^2 g^{-1}. This surface area is also larger than that (118 m^2 g^{-1}) of the desilication product (HZ_100_OH2_NS).

Table 3.1 Textural characteristics of ZSM-5 crystals and meso-zeolite materials.

Sample	S_{BET} (m^2 g^{-1})			Pore volume (cm^3 g^{-1})		Crystallinity (%)
	total	> 2 nm[a]	micropore[b]	total	micropore[b]	M[c]/XRD[d]
ZSM-5_100 (Si/Al=74)[e]	388	107	282	0.428	0.157	
HZ_100_1.5_NS	345	121	233	0.678	0.127	81/78
HZ _100_1.5_S	405	165	240	0.438	0.135	86/70
HZ _100_2_NS	320	118	202	0.837	0.114	73/77
HZ _100_2_S	407	204	204	0.629	0.115	73/81
HZ _100_3_NS	333	110	223	1.668	0.126	80/67
HZ _100_3_S	284	107	177	0.369	0.1	64/63
ZSM-5_50 (Si/Al=46)[e]	407	98	310	0.565	0.174	
HZ _50_1_NS	355	149	207	0.397	0.117	67/65
HZ _50_1_S	446	223	224	0.415	0.127	73/65
HZ _50_2_NS	376	153	223	0.868	0.126	72/74
HZ _50_2_S	583	327	256	0.683	0.145	83/77
HZ _50_3_NS	344	160	183	0.691	0.104	60/53
HZ _50_3_S	336	130	207	0.41	0.117	67/52
ZSM-5_30 (Si/Al=39)[e]	303	46	257	0.221	0.144	
HZ _30_1_NS	300	120	180	0.323	0.101	
HZ _30_1_S	331	115	216	0.243	0.121	
HZ _30_2_NS	283	107	176	0.4	0.099	
HZ _30_1_S	343	125	218	0.272	0.122	
HZ _30_3_NS	340	108	233	0.518	0.131	
HZ _30_3_S	321	123	198	0.284	0.112	

[a] Data in this column refer to the difference between total surface area and micropore surface area, i.e., surface area due to mesopores, macropores, and external particle features. [b] The *t*-method was used to estimate micropore surface areas and pore volumes. [c] The ratio of the micropore volumes of the hydrothermal products compared to the parent crystals was calculated. [d] The intensity ratio of the MFI (101) peak and the internal standard (α-alumina marked with an asterisk in Figures 3.6 and 3.12) was used and compared with that of the parent crystals. [e] The Si/Al ratio was measured by ICP.

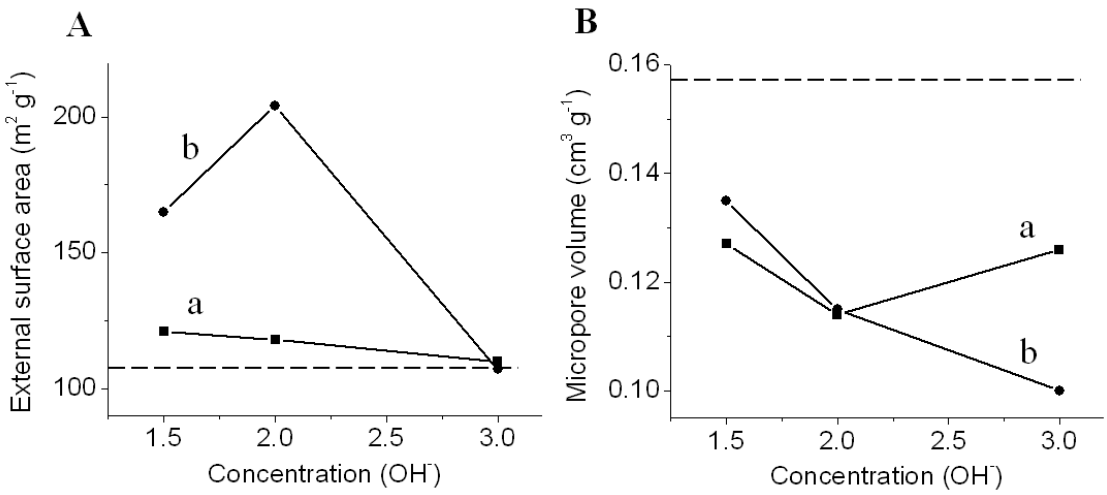

Figure 3.6 Influence of the hydroxide ion concentration and the presence of CTAB on (A) the surface area related to pores > 2 nm ("external surface area") and (B) the micropore volume. Data for the desilication products (HZ_100_OH(1.5, 2, 3)_NS) (a) and desilication/re-assembly products (HZ_100_OH(1.5, 2, 3)_S) (b) are shown in both graphs. The dashed lines represent values for the parent sample. The numbers on the concentration-axes refer to the conditions listed in the experimental section.

XRD patterns of all samples from desilication and desilication/re-assembly processes are characteristic for MFI zeolite (Figure 3.7). Using α-alumina as an internal standard, the relative intensity of the MFI (101) peak and the internal standard (the characteristic peak is marked with an asterisk in Figure 3.7) was obtained for each sample, and then those values were compared with that of the parent crystal (see Table 3.1). According to the relative intensity values, the range in relative crystallinity of the desilication/re-assembly products (63-81 %) is similar to that of the desilication products (67-78 %). Therefore, the results from both micropore volumes values by nitrogen sorption measurements and the relative intensity values by XRD measurements suggest that the desilication/re-assembly process does not significantly reduce the crystallinity of zeolite crystals, compared to products obtained by a pure desilication process.

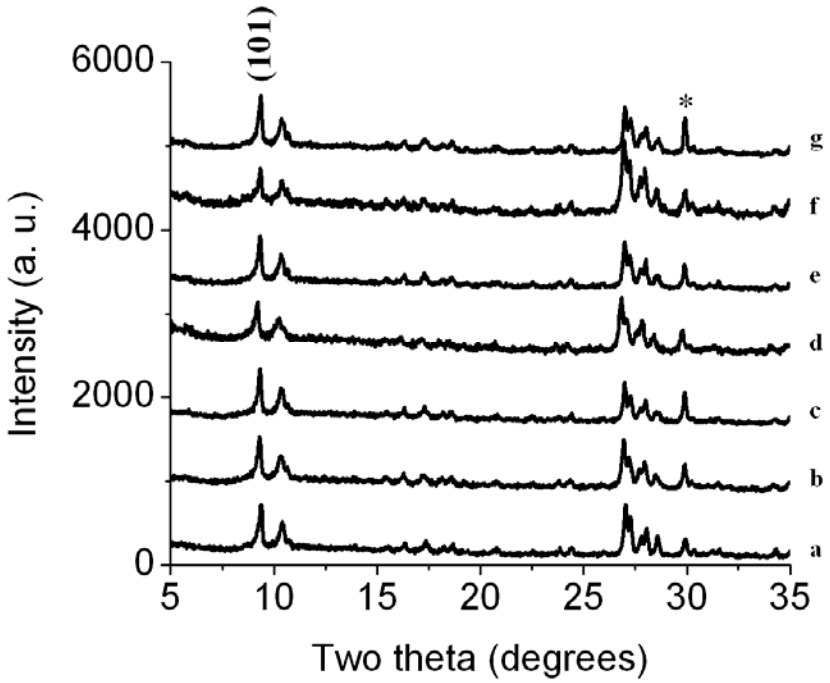

Figure 3.7 XRD patterns of (a) ZSM-5_100, (b) HZ_100_OH1.5_NS, (C) HZ_100_OH1.5_S, (d) HZ_100_OH2_NS, (e) HZ_100_OH2_S, (f) HZ_100_OH3_NS, and (g) HZ_100_OH3_S. The reflection peak marked with an asterisk (*) originates from the α-alumina used as an internal standard.

3.3.2 HZ_50 series

Parent zeolites with higher Al content (ZSM-5_50) were used to produce meso-zeolite materials under the same synthetic conditions as for the HZ_100 series. It was expected that the mesoporosity of the zeolite structure can be tailored more effectively for these materials with higher Al content. Because in alkaline media, Al atoms can preserve the zeolite frameworks, distribution of Al throughout the entire zeolite crystals can control extraction of Si atoms from the zeolite framework during the desilication process. According to papers by Pérez-Ramírez and co-workers, controlled mesoporosity can be obtained from zeolite crystals with different Si/Al ratios. When the Si/Al ratio of ZSM-5 is around 35–50, more tailored mesoporosity with ca. 10 nm mesopore diameters was obtained, leading to an surface area up to 235 m^2 g^{-1}.[26,27]

The morphology of desilication products of ZSM-5_50 was characterized by SEM. With base concentrations varying from n=1 to n=3, more open structures were observed (Figure 3.8a, c, e, and g). The hollow interior was clearly observed for the sample HZ_50_OH3_NS. On the other hand, the desilication/re-assembly products show corrugated textural features with significantly fewer visible voids. Highly corrugated textures are particularly manifest in zeolite crystals of the sample HZ_50_OH2_S.

The interior of samples HZ_50_OH2_NS/S, was examined TEM. The images of sample HZ_50_OH2_NS show features that can be interpreted as voids (Figure 3.9a) and mesopores with diameters ranging from several nanometers to tens of nanometers were observed on the hollow zeolite surface (Figure 3.9b) For sample HZ_50_OH2_S, features that may be associated with mesoscale pores throughout the entire sample and rough surface features were observed (Figure 3.9c). The edges of the sample exhibit crystalline fringes corresponding to MFI type zeolite (Figure 3.9c and d).

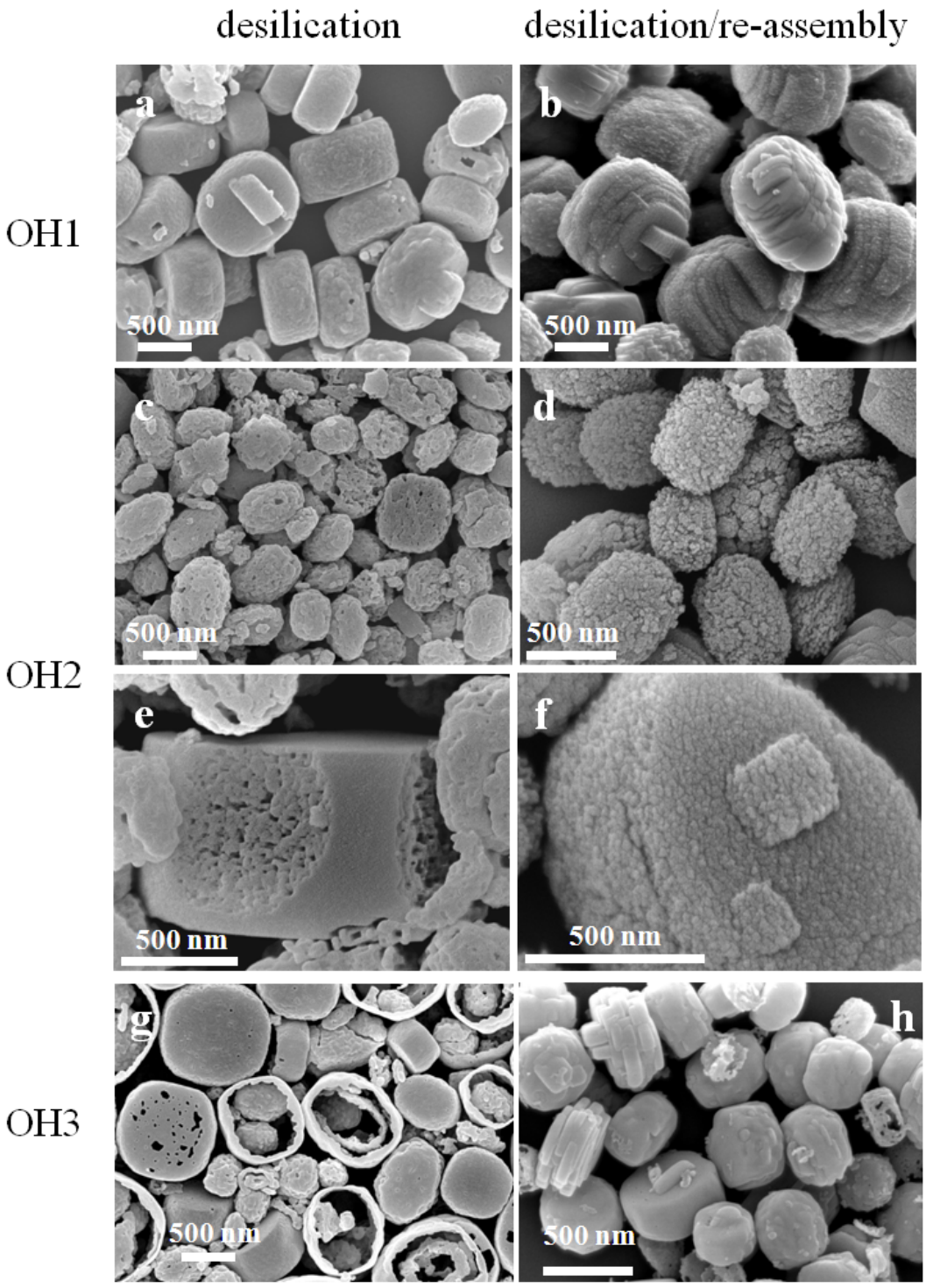

Figure 3.8 SEM images of (a) HZ_50_OH1_NS, (b) HZ_50_OH1_S, (c) HZ _50_OH2_NS, (d) HZ_50_OH2_S, (e) enlarged image of HZ _50_OH2_NS, (f) enlarged image of HZ _50_OH2_S, (g) HZ_50_OH3_NS, and (h) HZ_50_OH3_S.

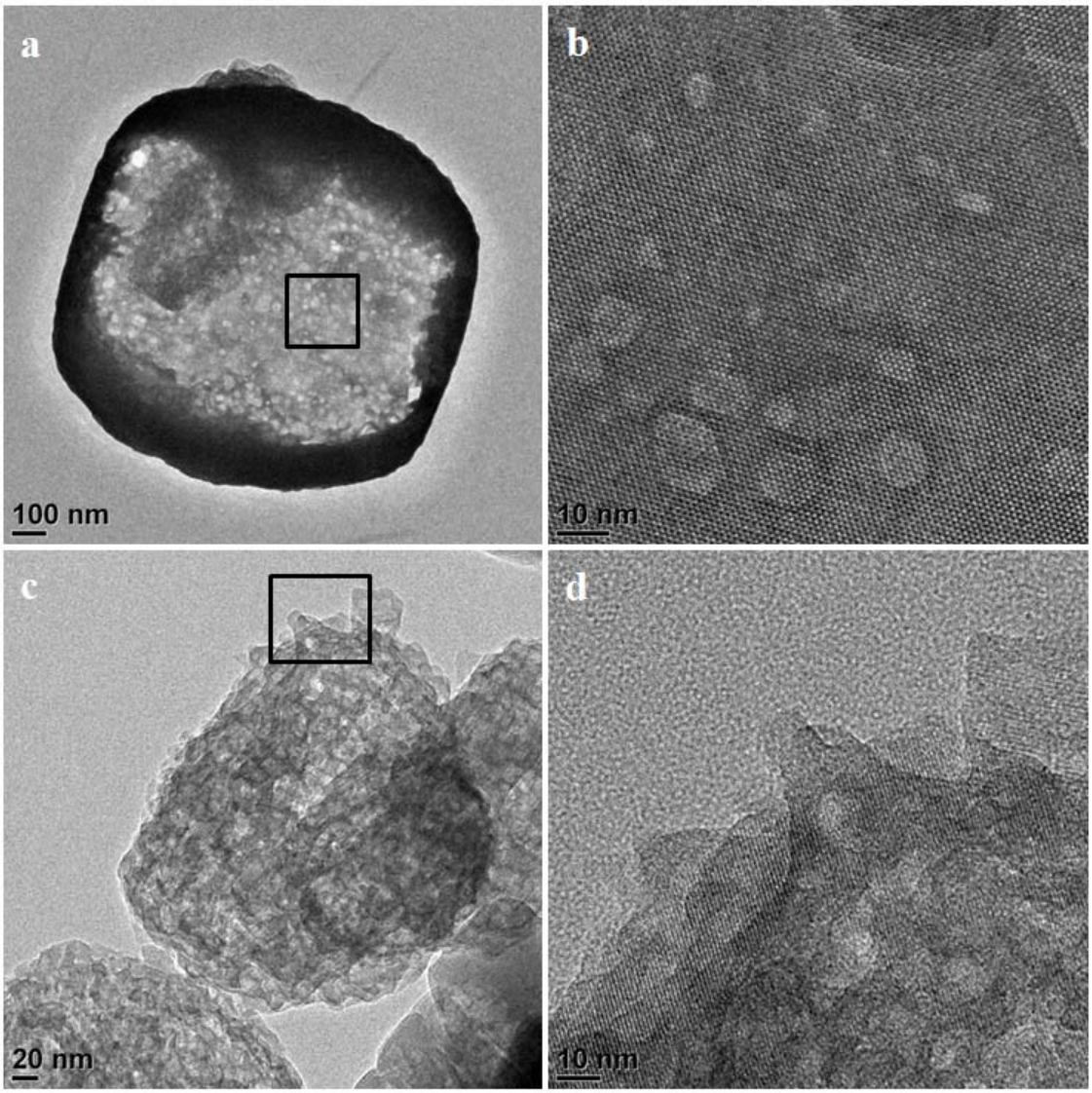

Figure 3.9 TEM images of (a) HZ_50_OH2_NS, (b) enlarged image of HZ_50_OH2_NS, (c) HZ_50_OH2_S, and (d) enlarged image of HZ_50_OH2_S. Enlargements of the squares in panels (a) and (c) are shown in (b) and (d), respectively.

Nitrogen sorption isotherms are depicted in Figure 3.10. The characteristic shapes and patterns are similar to those of HZ_100 products. For the desilication products, sharper increases in the adsorption branches and decreases in the desorption branches at

high relative pressure ranges were observed with higher concentration of base, compared to the desilication/re-assembly products with exhibited relatively smoother changes of sorption branches at high relative pressure ranges. Notably, sample HZ_50_OH2_S (Figure 3.10B) exhibited a steep increase at very low P/P_0 ranges, implying a large micropore volume (0.145 cm^3 g^{-1}) compared to HZ_50_OH2_NS (0.126 cm^3 g^{-1}).

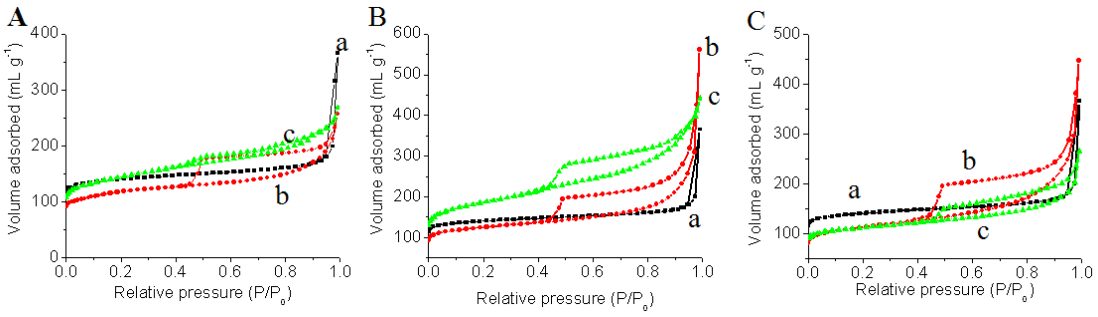

Figure 3.10 Nitrogen sorption isotherms for parent samples and samples prepared using different concentrations of base (A for HZ_50_OH1_NS/S, B for HZ_50_OH2_NS/S, and C for HZ_50_OH3_NS/S). In all graphs, the parent zeolite crystal ZSM-5_50, desilication products and desilication/re-assembly products are denoted as a, b, and c, respectively.

For the BJH pore size distribution, the graph of the desilication products shows a continuous increase in pore volume with progressively larger pore sizes, regardless of the base concentration (Figure 3.11D). In contrast, the desilication/re-assembly products generally present two different pore size ranges, one around 3 nm and one from 10–30 nm (Figure 3.11E). For example, the sample HZ_50_OH2_S (b) shows a high intensity for both mesopore sizes (ca. 3 nm and 10-30 nm), compared to the other desilication/re-assembly products (a and c). In addition, the development of both mesopore ranges of the sample HZ_50_OH2_S was monitored with different reaction times (Figure 3.11F). The intensity for both mesopore ranges was significantly increased from 13 h to 24 h of reaction time.

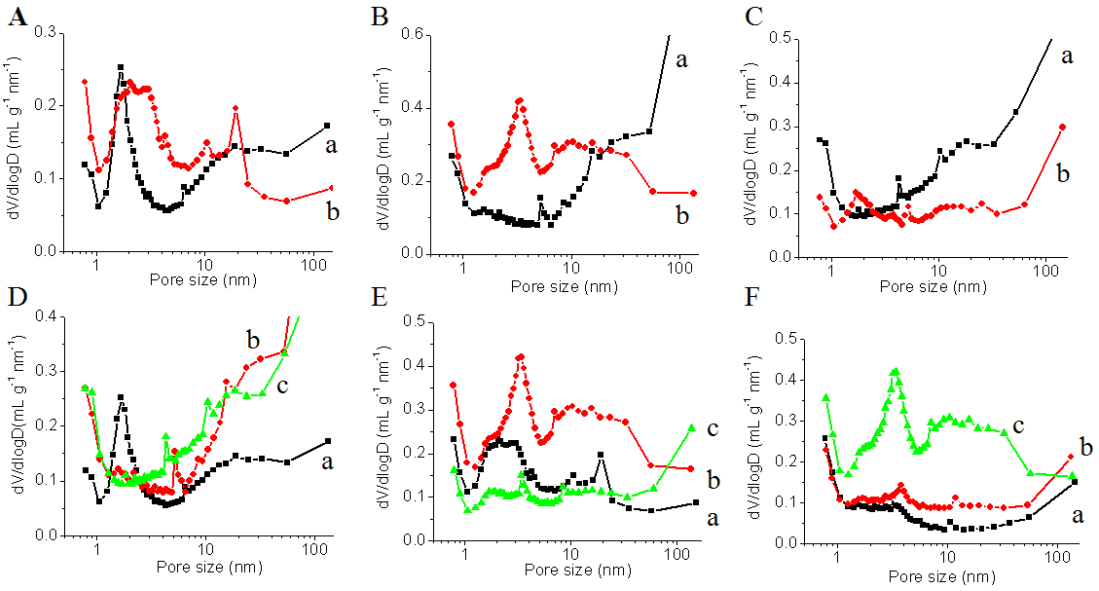

Figure 3.11 (A–C) BJH pore size distributions of samples prepared using different concentrations of base: (A) HZ_50_OH1_NS (a) and HZ_50_OH1_S (b), (B) HZ_50_OH2_NS (a) and HZ_50_OH2_S (b), (C) HZ_50_OH3_NS (a) and HZ_50_OH3_S (b). (D) Comparison of pore size distributions for desilication products HZ_50_OH1_NS (a), HZ_50_OH2_NS (b), and HZ_50_OH3_NS (c). (E) Comparison of pore size distributions for desilication/re-assembly products HZ_50_OH1_S (a), HZ_50_OH2_S (b), and HZ_50_OH3_S (c). (F) The development of the dual-pore system of HZ_50_OH2_S after reaction times of (a) 4 h, (b) 13 h, and (c) 24 h.

Changes in surface areas of desilication products are similar for all three samples treated in alkaline solutions with different base concentrations (Table 3.1 and Figure 3.12). However, the surface areas of the desilication products of ZSM5_50 are slightly higher than those of ZSM-5_100. For the desilication/re-assembly products, the surface areas for pores larger than 2 nm show a similar dependence on base concentration as for the HZ_100 series (compare Figure 3.6 with Figure 3.12), however, the values are larger (223 m^2 g^{-1} for HZ_50_OH1_S and 327 m^2 g^{-1} for HZ_50_OH2_S). The latter value represents an increase of around 330 % compared to the parent zeolite crystal. Moreover,

the crystallinity of the HZ_50_OH2_S sample is well preserved, on the basis of the large micropore volume (0.145 cm^3 g^{-1}).

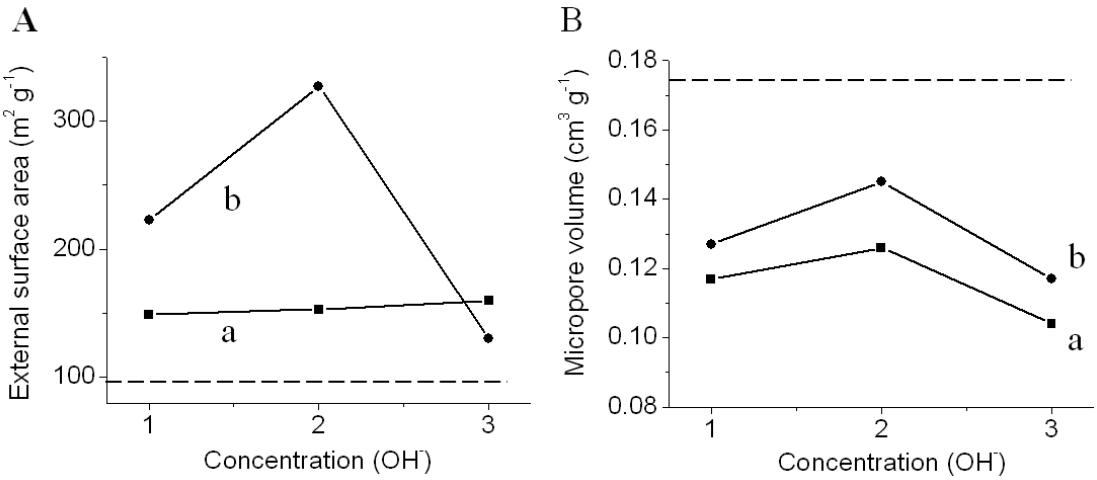

Figure 3.12 Influence of the hydroxide ion concentration and the presence of CTAB on (A) the surface area related to pores > 2 nm ("external surface area") and (B) the micropore volume. Data for the desilication products (HZ_50_OH(1, 2, 3)_NS) (a) and desilication/re-assembly products (HZ_50_OH(1, 2, 3)_S) (b) are shown in both graphs. The dashed lines represent values for the parent sample. The numbers on the concentration-axes refer to the conditions listed in the experimental section.

XRD data also confirmed that all samples from desilication and desilication/re-assembly products based on ZSM-5_50 were MFI type zeolite materials (Figure 3.13). The crystallinity values of the desilication/re-assembly products are 52–77 % and comparable to those of the desilication products (53–74 %) (Table 3.1). In particular, the sample HZ_50_OH2_S presented ca. 77 % of the parent's crystallinity.

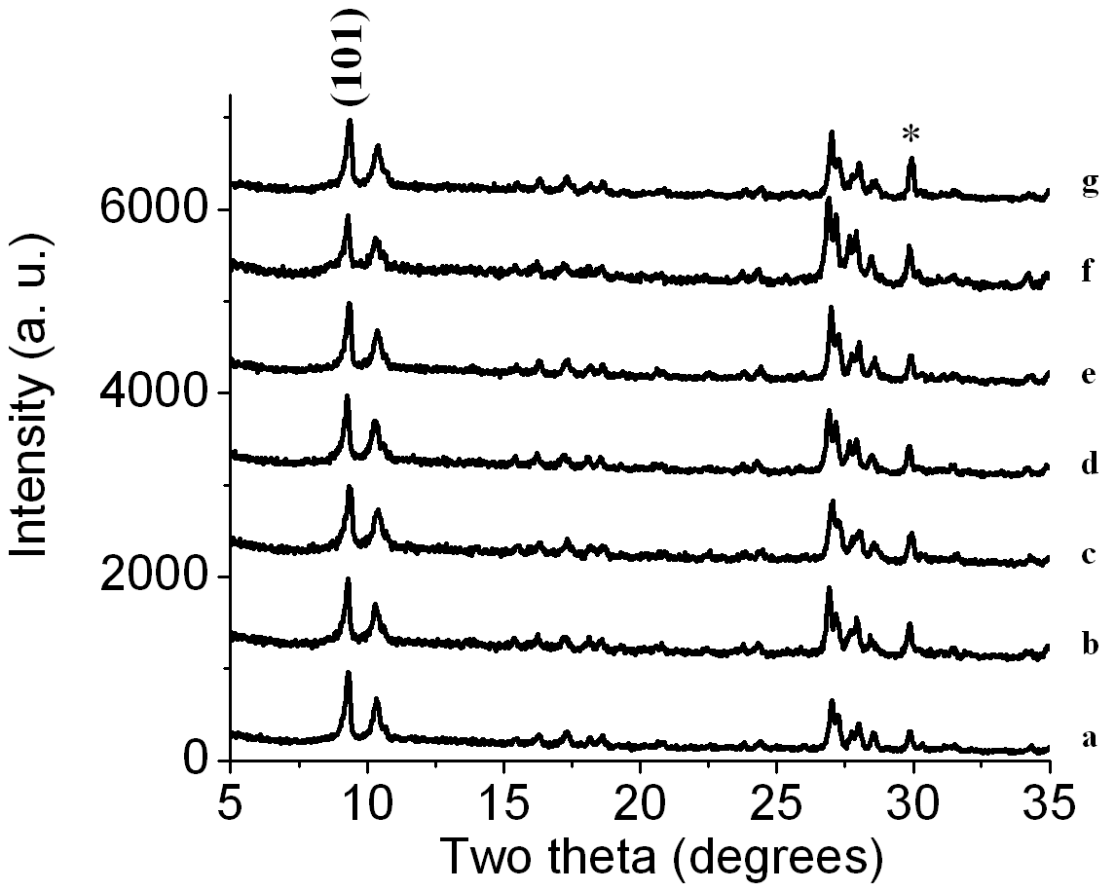

Figure 3.13 XRD patterns of (a) ZSM-5_50, (b) HZ_50_OH1_NS, (c) HZ_50_OH1_S, (d) HZ_50_OH2_NS, (e) HZ_50_OH2_S, (f) HZ_50_OH3_NS, and (g) HZ_50_OH3_S. The reflection peak marked with an asterisk (*) originates from the α-alumina used as an internal standard.

For further investigation of the desilication/re-assembly process, the ZSM-5_50 and HZ_50_OH2_NS/S samples were examined by ^{27}Al and ^{29}Si solid-state magic-angle-spinning (MAS) NMR. According to the ^{27}Al NMR spectra (Figure 3.14 left), tetrahedrally coordinated Al sites (ca. 59 ppm, 82 %) and extra-framework Al sites (ca. 17 ppm, 18 %) existed in the parent zeolite crystal (ZSM-5_50, a).[36,37] After the desilication process (HZ_50_OH2_NS, b), the amount of extra-framework Al decreased (6.5 %) and the relative proportion of tetrahedral Al sites increased (93.5 %). On the other hand, after desilication/re-assembly process, ^{27}Al NMR spectra present values

similar to those for the parent crystal, 84% tetrahedral Al and 16% extra-framework Al sites.

In addition, the ^{29}Si NMR spectra (Figure 3.14 right) show two major peaks at -110 ppm (92.3 %) and -101 ppm (7.7 %), corresponding to silicon in Q^4 and Q^3 environments, respectively.[37-40] After desilication, the Q^3 value increased to 16.5 % because weak Si sites were more affected by base (Figure 3.15 right b). On the other hand, after the desilication/re-assembly process, the values of Q^3 (8 %) and Q^4 (92 %) were similar to those of the parent crystal.

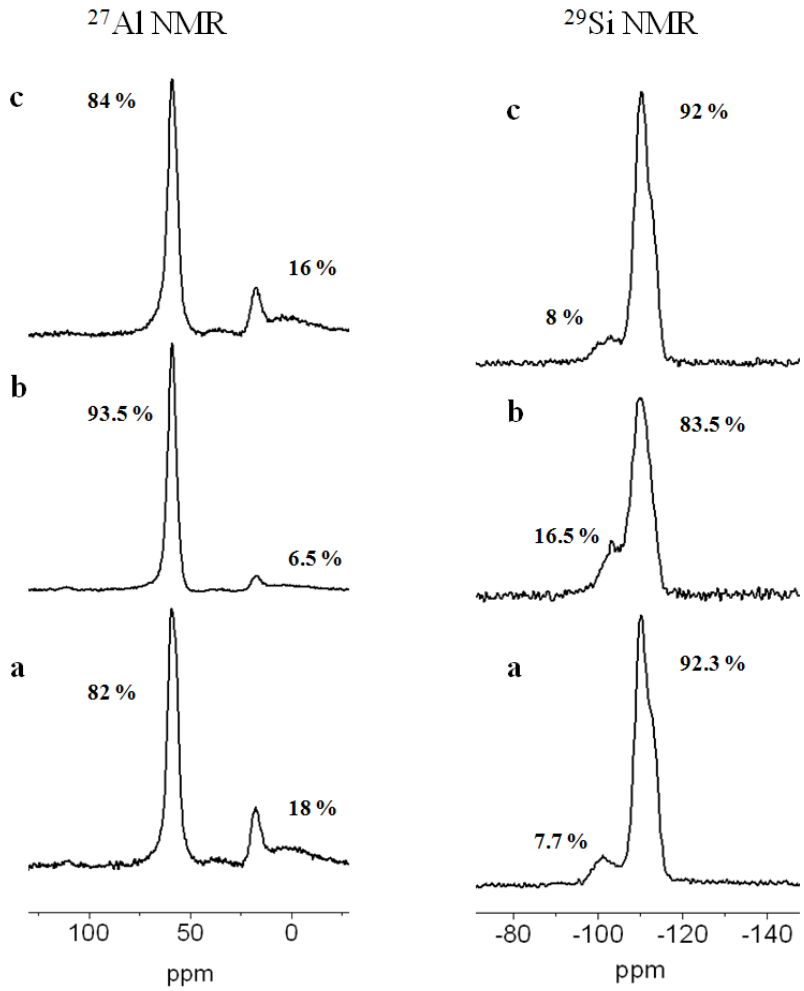

Figure 3.14 ^{27}Al (left) and ^{29}Si (right) solid-state MAS NMR spectra for (a) ZSM-5_50, (b) HZ_50_OH2_NS, and (c) HZ_50_OH2_S.

An ammonia TPD profile was acquired to determine the relative number of strong acid sites for samples ZSM-5_50_H, HZ_50_OH2_NS_H, and HZ_50_OH2_S_H (Table 3.2). For the desilication product (HZ_50_OH2_NS_H, Si/Al = 16), the number of acid sites was increased due to the higher Al content compared to the parent material (Si/Al = 46) through Si extraction from the zeolite framework.[27,41] On the other hand, the number of acid sites was similar to that of the parent crystal for the desilication/re-assembly product (HZ_50_OH2_NS_H, Si/Al = 28). This result might be attributed to the nearly unchanged fraction of tetrahedral Al sites (84 %) compared to the parent crystal (82 %) and the desilication product (93.5 %) found by solid state ^{27}Al NMR.

Table 3.2 Characteristic data for selected zeolites.

Sample	Si/Al[a]	NH_3 uptake[b] (mmol g^{-1})	S_{BET} (m^2 g^{-1})	S_{mseo}[c] (m^2 g^{-1})	V_{micro}[c] (cm^3 g^{-1})	Crystallinity (%) M[d]/XRD[e]
ZSM-5_50_H	46	0.31	407	98	0.174	100/100
HZ_50_OH2_NS_H	16	0.40	376	153	0.126	72/74
HZ_50_OH2_S_H	28	0.28	583	327	0.145	83/77

[a]Si/Al ratio measured by ICP. [b]Number of acid sites of the zeolites were measured by NH_3 TPD with temperature range of 350–540 °C. [c]The *t*-method was used to estimate micropore surface areas and pore volumes. [d]The ratio of the micropore volumes between the hydrothermal products and the parent crystals was calculated. [e]The intensity ratio of the MFI (101) peak and the internal standard (α-alumina marked with an asterisk in the Figure 3.11) was used, and compared with that of the parent crystal.

3.3.3 HZ_30 series

Hydrothermal reactions were also performed using ZSM-5_30 crystals. Both desilication and desilication/re-assembly products show only moderate increases in surface areas and pore volumes associated with pores larger than 2 nm, with surface area values in the 100–120 m^2 g^{-1} range (Table 3.1). These results suggest that the higher Al content of ZSM-5_30 crystals severely retards Si extraction.[25-27] Therefore, these samples were not analyzed further.

3.4 Discussion

3.4.1 Textural characteristics of meso-zeolites

a. Desilication products. For the desilication products (HZ_100_OH1.5_NS, HZ_100_OH2_NS, and HZ_100_OH3_NS) from ZSM-5_100, there is no significant difference in texture and morphology obtained under different basic conditions (from n=1.5 to n=3). Increases in surface area for pores larger than 2 nm are similar for all samples (Table 3.1 and Figure 3.6). In addition, textural features evident in TEM and SEM images are similar for all of these samples, which show hollow interiors and large mesopores (Figure 3.2 and 3.3). These observations would suggest that under the given reaction conditions (100 ˚C treatment for 24 h) Si atoms could be extracted from the zeolite frameworks with similar ease, regardless of the different base concentrations. In conventional desilication processes described in the literature, mild conditions, i.e., treatment of 0.2 M of NaOH for 30 min at 338 K, were employed and reaction parameters could control the mesoporosity.[25-27] For the sample of HZ_100_OH3_NS, dissolution of Si from the framework was mainly attributed from inside zeolite crystals rather than the outer surface of the crystal, which caused formation of hollow zeolite crystals (Figure 3.3c). Pérez-Ramírez and co-workers reported that the occurrence of an Al gradient across the ZSM-5 crystals from a higher content on the exterior surface to lower content on the interior core was observed.[24,26,27] After the desilication process, they observed hollow features in ZSM-5 zeolite crystals.[24] The Al-rich exterior surface remained relatively intact, so that in this region, Si extraction was retarded by the higher content of Al.

The higher Al content mitigates dissolution of Si from the framework, resulting in more controlled mesoporosity. It is therefore not unexpected that the desilication products from ZSM-5_50 present a greater increase in surface area (149-160 m^2 g^{-1}) compared to the desilication products from ZSM-5_100 (110-121 m^2 g^{-1}) (Table 3.1). In addition, when comparing pore size distributions (Figure 3.5C and Figure 3.11D), continuous increases in slopes after around 10 nm were observed for the desilication products of ZSM-5_100, but slight decreases in slopes in the 10–30 nm pore size range were

observed for desilication products of ZSM-5_50. Therefore, more controlled mesoporosity could be developed by the different Si/Al ratio under the specific conditions, which has been also reported in prior literature.[7,24,25,27]

b. Desilication/re-assembly products. On the other hand, the textural features of desilication/re-assembly products are different from those of the desilication products. The desilication/re-assembly products generally present more corrugated or "bumpy" textures on the surface, regardless of the Si/Al ratio of the parent crystals (Figure 3.2 right column and Figure 3.8 right column). In TEM images, the surfaces of the desilication/re-assembly products are also rough and the edges on the surfaces show crystalline features corresponding to MFI type zeolite (Figure 3.3 and 3.9). In addition, hollow features were observed in sample HZ_100_OH3_S. These observations imply that desilication still proceeded as the surface was changed from smooth to corrugated.

The values of increased surface area for desilication/re-assembly products with base concentrations (n=1 and 1.5 for ZSM-5_100, and n=1 and 2 for ZSM-5_50) are usually higher than those of the desilication products (Table 3.1, Figure 3.6 and 3.12). In particular, the sample of HZ_50_OH2_S presents an increase in surface area as high as 327 m^2 g^{-1}, which is rarely obtained by desilication methods.[7,24,25,27] It is reasonable that the developed dual-pore system (ca. 3 nm and 10-30 nm) for the HZ_50_OH2_S sample contributes to high surface area compared to the desilication products that usually have larger meso-/macro-pores (Figure 3.7 and 3.13).

In addition, the crystallinity of all samples was well preserved. The values of micropore volumes of all samples were slightly higher than those of the desilication products obtained under the same conditions (Table 3.1 and Figure 3.6 and 3.12). XRD data also confirm the crystalline nature of all samples. The relative intensity values of the desilication/re-assembly products show very similar values compared to those of the desilication products.

However, the samples treated in solutions with the highest content of base (HZ_100_OH3_S and HZ_50_OH3_S) presented the lowest increase in surface areas and micropore volumes, which are similar or worse than those of the parent crystals (Table

3.1). Such a high concentration of base could cause the zeolite frameworks to collapse regardless of a re-assembly process. When a very high content of base (n = 6) was applied to the reaction with a surfactant (HZ_100_OH6_S), the zeolite structures were completely destroyed (Figure 3.15).

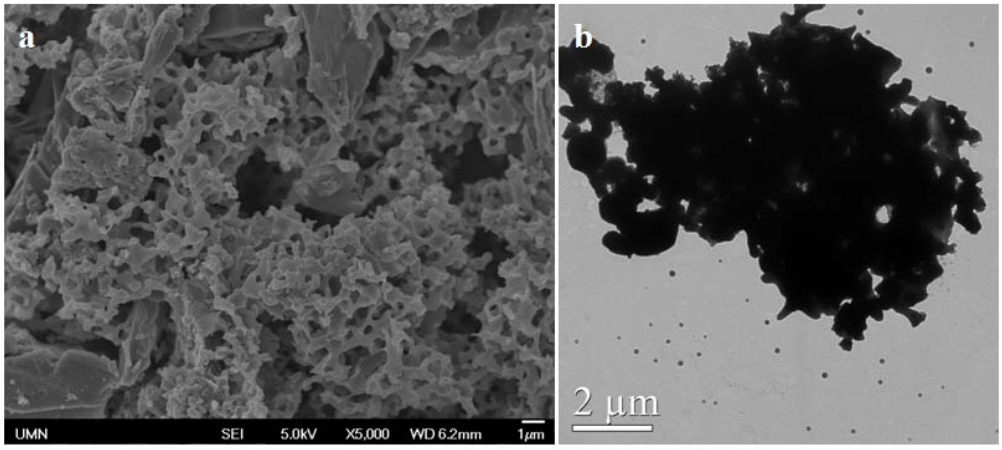

Figure 3.15 SEM (a) and TEM (b) images of the collapsed zeolite crystals after treatment in a high concentration of base (HZ_100_OH6_S).

3.4.2 Surfactant induced re-assembly of dissolved species

In extensive SEM and TEM investigations, we could not find any differently shaped structures after thorough washing steps (usually 3–5 times), which could have been produced by micelle formation of dissolved species with a surfactant to form mesoporous materials.[42] The lack of such particles strongly suggests that the 3-nm mesopores cannot be attributed to another material possibly produced in the hydrothermal reaction. These observations support the concept of re-assembly of dissolved species by the surfactant on the parent zeolite structures. This process eventually increases the surface area up to 327 m^2 g^{-1} (HZ_50_OH2_S) with well preserved crystallinity (83 % by the micropore volume and 77 % by XRD measurements, compared to the parent zeolite crystal).

In addition, solid state NMR data support re-assembly of dissolved species via micelle formation with a surfactant. For the desilication product (HZ_50_OH2_NS), the numbers of relatively weak Al sites (extra-frameworks) and Si sites (^{3}Q) were increased because the zeolite framework was dissolved by the alkaline medium (Figure 3.14). However, for the desilication/re-assembly product, the values of characteristic chemical positions for ^{27}Al and ^{29}Si NMR spectra are similar to those of the parent crystal. This implies that the loss from the zeolite crystal under basic conditions is limited. It would suggest that after partial dissolution, extended fragments of zeolite crystals remained or redeposited on the parent structure. The fragments of crystals still have chemical information that can be detected by solid state NMR. In other words, the surfactant could interact with the dissolved species via electrostatic interactions and then assemble them, so that these re-precipitate on the parent crystal under the hydrothermal conditions.

On the other hand, as a second assumption, more controlled dissolution could be possible by the presence of the surfactant that could directly interact with dissolution process to debilitate the dissolution of aluminosilicate materials. Therefore, the second assumption and other possibilities cannot be completely eliminated because there is no direct evidence. However, under the specific conditions (i.e., HZ_50_OH2_S), the amount of dissolved species, the concentration of base and the amount of the surfactant were well matched to produce the high surface areas of these meso-zeolite crystals.

3.4 Conclusions

Desilication of zeolites was carried out with and without surfactant components under various synthesis conditions. More open structures were generally developed from desilication products regardless of the Si/Al ratio (100 and 50) of the parent ZSM-5 crystals. In surfactant-induced hydrothermal reactions, the products usually exhibit additional corrugated textural features on the surface of the zeolite crystals. Furthermore, the interior of the crystals is often hollow, and the edges of the crystals show crystalline fringes corresponding to MFI. According to nitrogen sorption measurements, the increase of surface areas for desilication/re-assembly products is generally higher than those of the

desilication products under the same reaction conditions. Under specific conditions, surface areas as high as 327 m^2 g^{-1} were obtained (HZ_50_OH2_S). In addition, the crystallinity of desilication/re-assembly products was well preserved, on the basis of both micropore volume estimates from nitrogen sorption measurements and XRD intensity data. Furthermore, according to the BJH pore size distributions, two different mesopore ranges (ca. 3 nm and 10–30 nm) were developed, in which the desilication products usually exhibited meso-/macro-pores larger than 10 nm. The presence of the small mesopores (ca. 3 nm) strongly suggests that the surfactant could re-assemble the dissolved species onto the crystal frameworks. In addition, solid-state ^{27}Al and ^{29}Si MAS NMR data support the concept of re-assembly of the dissolved species onto the zeolite frameworks under hydrothermal reaction conditions. Therefore, the desilication/re-assembly method could provide high surface area and well preserved crystallinity for the ZSM-5 zeolite crystals. Furthermore, it could be possible to extend this method to other types of zeolites and to incorporate other inorganic molecules into zeolite frameworks to prepare multi-functional catalyst materials.[43]

3.5 References

(1) Snyder, M. A.; Tsapatsis, M. *Angew. Chem. Int. Ed.* **2007**, *46*, 7560-7573.

(2) Corma, A. *Chem. Rev.* **1997**, *97*, 2373-2419.

(3) Tao, Y.; Kanoh, H.; Abrams, L.; Kaneko, K. *Chem. Rev.* **2006**, *106*, 896-910.

(4) Corma, A. *J. Cat.* **2003**, *216*, 298-312.

(5) Bein, T. *Chem. Mater.* **1996**, *8*, 1636-1653.

(6) Davis, M. E. *Nature* **2002**, *417*, 813-821.

(7) Pérez-Ramírez, J.; Christensen, C. H.; Egeblad, K.; Christensen, C. H.; Groen, J. E. *Chem. Soc. Rev.* **2008**, *37*, 2530-2542.

(8) Maheshwari, S.; Jordan, E.; Kumar, S.; Bates, F. S.; Penn, R. L.; Shantz, D. F.; Tsapatsis, M. *J. Am. Chem. Soc.* **2008**, *130*, 1507-1516.

(9) Corma, A.; Fornes, V.; Pergher, S. B.; Maesen, T. L. M.; Buglass, J. G. *Nature* **1998**, *396*, 353-356.

(10) Choi, M.; Na, K.; Kim, J.; Sakamoto, Y.; Terasaki, O.; Ryoo, R. *Nature* **2009**, *461*, 246-250.

(11) Wang, H.; Pinnavaia, T. J. *Angew. Chem. Int. Ed.* **2006**, *45*, 7603-7606.

(12) Park, D. H.; Kim, S. S.; Wang, H.; Pinnavaia, T. J.; Papapetrou, M. C.; Lappas, A. A.; Triantafyllidis, K. S. *Angew. Chem. Int. Ed.* **2009**, *48*, 7645-7648.

(13) Choi, M.; Cho, H. S.; Srivastava, R.; Venkatesan, C.; Choi, D.-H.; Ryoo, R. *Nat. Mater.* **2006**, *5*, 718-723.

(14) Lee, D.-H.; Choi, M.; Yu, B.-W.; Ryoo, R. *Chem. Commun.* **2009**, 74-76.

(15) Madsen, C.; Jacobsen, C. J. H. *Chem. Commun.* **1999**, 673-674.

(16) Kim, S.-S.; Shah, J.; Pinnavaia, T. J. *Chem. Mater.* **2003**, *15*, 1664-1668.

(17) Tosheva, L.; Valtchev, V. P. *Chem. Mater.* **2005**, *17*, 2494-2513.

(18) Schmidt, I.; Madsen, C.; Jacobsen, C. J. H. *Inorg. Chem.* **2000**, *39*, 2279-2283.

(19) Holland, B. T.; Abrams, L.; Stein, A. *J. Am. Chem. Soc.* **1999**, *121*, 4308-4309.

(20) Jacobsen, C. J. H.; Madsen, C.; Houzvicka, J.; Schmidt, I.; Carlsson, A. *J. Am. Chem. Soc.* **2000**, *122*, 7116-7117.

(21) Fan, W.; Snyder, M. A.; Kumar, S.; Lee, P.-S.; Yoo, W. C.; McCormick, A. V.; Penn, R. L.; Stein, A.; Tsapatsis, M. *Nat. Mater.* **2008**, *7*, 984-991.

(22) Yoo, W. C.; Kumar, S.; Wang, Z.; Ergang, N. S.; Fan, W.; Karanikolos, G. N.; McCormick, A. V.; Penn, R. L.; Tsapatsis, M.; Stein, A. *Angew. Chem. Int. Ed.* **2008**, *47*, 9096-9099.

(23) Yoo, W. C.; Kumar, S.; Penn, R. L.; Tsapatsis, M.; Stein, A. *J. Am. Chem. Soc.* **2009**, *131*, 12377-12383.

(24) Groen, J. C.; Bach, T.; Ziese, U.; Paulaime-van Donk, A. M.; de Jong, K. P.; Moulijn, J. A.; Pérez-Ramírez, J. *J. Am. Chem. Soc.* **2005**, *127*, 10792-10793.

(25) Groen, J. C.; Moulijn, J. A.; Pérez-Ramírez, J. *J. Mater. Chem.* **2006**, *16*, 2121-2131.

(26) Groen, J. C.; Jansen, J. C.; Moulijn, J. A.; Pérez-Ramírez, J. *J. Phys. Chem. B* **2004**, *108*, 13062-13065.

(27) Groen, J. C.; Peffer, L. A. A.; Moulijn, J. A.; Pérez-Ramírez, J. *Microporous Mesoporous Mater.* **2004**, *69*, 29-34.

(28) Müller, M.; Harvey, G.; Prins, P. *Microporous Mesoporous Mater.* **2000**, *34*, 135-147.

(29) Groen, J. C.; Moulijn, J. A.; Pérez-Ramírez, J. *Microporous Mesoporous Mater.* **2005**, *87*, 153-161.

(30) Galarneau, A.; Iapichella, J.; Bonhomme, K.; Renzo, F. D.; Kooyman, P.; Terasaki, O.; Fajula, F. *Adv. Funct. Mater.* **2006**, *16*, 1657-1667.

(31) Martin, T.; Galarneau, A.; Renzo, F. D.; Fajula, F.; Plee, D. *Angew. Chem. Int. Ed.* **2002**, *41*, 2590-2592.

(32) Botella, P.; Corma, A.; Navarro, M. T. *Chem. Mater.* **2007**, *19*, 1979-1983.

(33) Yoo, W. C.; Stein, A. *Chem. Mater.* **2010**, *submitted*.

(34) Abrams, L.; Corbin, D. R. *J. Incl. Phenom. Mol. Recog.* **1995**, *21*, 1-46.

(35) Lee, J.; Sohn, K.; Hyeon, T. *J. Am. Chem. Soc.* **2001**, *123*, 5146-5147.

(36) Yu, Z.; Zheng, A.; Wang, Q.; Chen, L.; Xu, J.; Amoureux, J.-P.; Deng, F. *Angew. Chem. Int. Ed.* **2010**, *49*, 8657-8661.

(37) Fyfe, C. A.; Bretherton, J. L.; Lam, L. Y. *J. Am. Chem. Soc.* **2001**, *123*, 5285-5291.

(38) Fyfe, C. A.; Darton, R. J.; Schneider, C.; Scheffler, F. *J. Phys. Chem. C* **2008**, *112*, 80-88.

(39) Román-Leshkov, Y.; Moliner, M.; Davis, M. E. *Chem. Mater.* **2010**, *22*, 2646-2652.

(40) Archer, R. H.; Carpenter, J. R.; Hwang, S.-J.; Burton, A. W.; Chen, C.-Y.; Zones, S. I.; Davis, M. E. *Chem. Mater.* **2010**, *22*, 2563-2572.

(41) Triantafillidis, C. S.; Evmiridis, N. P.; Nalbandian, L.; Vasalos, I. A. *Ind. Eng. Chem. Res.* **1999**, *38*, 916-927.

(42) Inagaki, S.; Ogura, M.; Inami, T.; Sasaki, Y.; Kikuchi, E.; Matsukata, M. *Microporous Mesoporous Mater.* **2004**, *74*, 163-170.

(43) Choi, M.; Wu, Z.; Iglesia, E. *J. Am. Chem. Soc.* **2010**, *132*, 9129-9137.

Chapter 4

Growth Patterns and Shape Development of Zeolite Nanocrystals in Confined Syntheses

4.1 Introduction

In many applications, the properties of particles depend on particle size and dispersity,[1,2] as well as morphological features, including isotropic versus anisotropic shapes, aspect ratios,[3,4] surface regularity and surface areas.[5-7] In the case of hydrothermally prepared zeolites, for example, particle size influences the diffusion of reagents through the micropore system, the surface area impacts access to the micropore system, and particle shapes/aspect ratios affect packing of zeolite particles, e.g., when they are used as seed layers to prepare membranes by secondary growth. Ways of controlling the size and shape of zeolite particles have been investigated intensively. In the late 1980s and early 1990s much research focused on growing large single crystals of zeolites, but in more recent years attention has also turned to zeolite nanoparticles.[8,9] Larger zeolite crystals are typically prepared by the addition of nucleation suppressors,[10,11] whereas very small crystallites are synthesized by providing conditions that favor nucleation while carefully controlling the reaction stoichiometry, crystallization time and temperature.[12-15] Because particle growth has to be suppressed in nanozeolite syntheses, yields are often low.

Recently, various approaches to zeolite synthesis in confinement have been described, which can provide better control over sizes and shapes of zeolite particles than conventional hydrothermal syntheses.[12,16-26] A porous template can be used to either

define the size of zeolite particles or to introduce extra voids into the particles.[22,25] One promising approach involves syntheses in porous carbon reactors with close-packed arrays of mesopores (3DOm carbon) or macropores (3DOM carbon) that are interconnected in three dimensions. Porous carbon is chemically and thermally stable under the conditions used in hydrothermal zeolite syntheses and can be removed from the product by simple calcination in air. 3DOm carbon was recently used to prepare colloidal crystals of 10–40 nm silicalite-1 spheres by steam-assisted crystallization of a templated amorphous precursor.[25] This method enabled syntheses of uniform and isolatable nanocrystals, as well as single-crystal zeolites with ordered, imprinted mesoporosity.

Here we build on the concept of hydrothermal zeolite syntheses in the confinement of monolithic 3DOM carbon reactors and illustrate that by carrying out multiple infiltration/hydrothermal reaction (IHT) steps using specified sequences of precursor concentrations, it is possible to influence the growth pattern and shape development of zeolites and significantly enhance the control over crystal morphology. Depending on the IHT schedule, it is possible to move beyond the polycrystalline spheres including corrugated surface and hollow interior (geode like structure) and synthesize single crystalline spheres, single crystalline arrays of spheres with hierarchical pore structure, polycrystalline spheres with tunable single crystal grain sizes, small faceted zeolite particles (< 100 nm in length) in relatively high yield (i.e., virtually every reactor cage occupied with multiple crystallites), and mixed populations of zeolite particles with controllable size distributions.

The concept of scheduled multistep syntheses to control product morphology is illustrated in Figure 4.1. The syntheses studied here involve two silica precursor solutions with different nutrient concentrations. The "low concentration" precursor (L) contains a component ratio of 10 SiO_2: 2.4 tetrapropylammonium hydroxide (TPAOH) : 0.87 NaOH : 114 H_2O and the "high concentration" solution (H) a ratio of 10 SiO_2: 4.5 TPAOH : 4750 H_2O. The other parameters were the same for each set of conditions, except for the duration of each IHT cycle: 2 days for each H_n step and 4 days each L_n step to observe significant changes in a reasonable amount of time (note: the subscript *n* refers to the IHT cycle number using the corresponding precursor, H or L). Precursor H favors

nucleation, and even when crystals grow in later H steps in a sequence, additional nucleation can occur. This precursor was used during each IHT step, resulting in polycrystalline products that eventually adopted the shape of the pore space in the 3DOM carbon reactor (Figure 4.1A). When the outermost layer of the 3DOM carbon was negatively charged with PSS, corrugated and eventually aggregated polycrystalline zeolite crystals were produced. On the other hand, when positively charged 3DOM carbon (decorated with PDDA as an outermost layer) was used, due to the electrostatic attraction force between the 3DOM carbon surface and the precursor, a geode like structure with a hollow interior was found and the windows of the 3DOM carbon were eventually blocked.

When the dilute precursor, L, is used instead for each IHT cycle, nucleation is suppressed and crystal growth predominates, but at much slower rates, resulting in fewer but more regular zeolite crystals. Each of these crystals can grow through reactor windows and even through multiple adjacent macropores, forming a larger domain. (Note: In this chapter we define a "domain" as a region of interconnected solid product that can span multiple adjacent macropores and may be single crystalline or polycrystalline. We use the standard definition of a grain as an individual crystal.) Eventually, several of these relatively isotropic domains can merge together (Figure 4.1B). To increase the number of initial nuclei, the reactor may be loaded with a precursor containing a high nutrient concentration in the first IHT cycle (H_1). Subsequent L cycles produce multiple well-faceted, discrete single crystals in each macropore, whose average sizes can be increased with further L cycles until these crystals finally merge into each other and the external shape becomes dictated by the macropore wall (Figure 4.1C). Finally, the order of concentration schedules may be reversed. If an H cycle follows multiple L cycles, a new secondary population of smaller seeds is added to the existing domains, which can also be grown larger to manipulate the overall particle size distribution (Figure 4.1D). Size control and morphology control are thereby achieved through both confinement effects and precursor concentration effects.[27] These zeolite growth methods provide tools to design product morphologies tailored to specific applications. For example, when applied as building blocks for molecular sieve membranes, smaller, monodisperse and suitably shaped zeolite particles can produce a thinner and better packed seed layer for

membrane fabrication assisted by secondary growth, one of the promising methods to fabricate molecular sieve membranes.[8,28-31] Alternatively, extra empty void spaces introduced into zeolite crystals by a template (here the 3DOM carbon reactor) provide better accessibility of molecules to active sites in the zeolite particles, mitigating effects caused by diffusion limitations.[5,7,22,32-38]

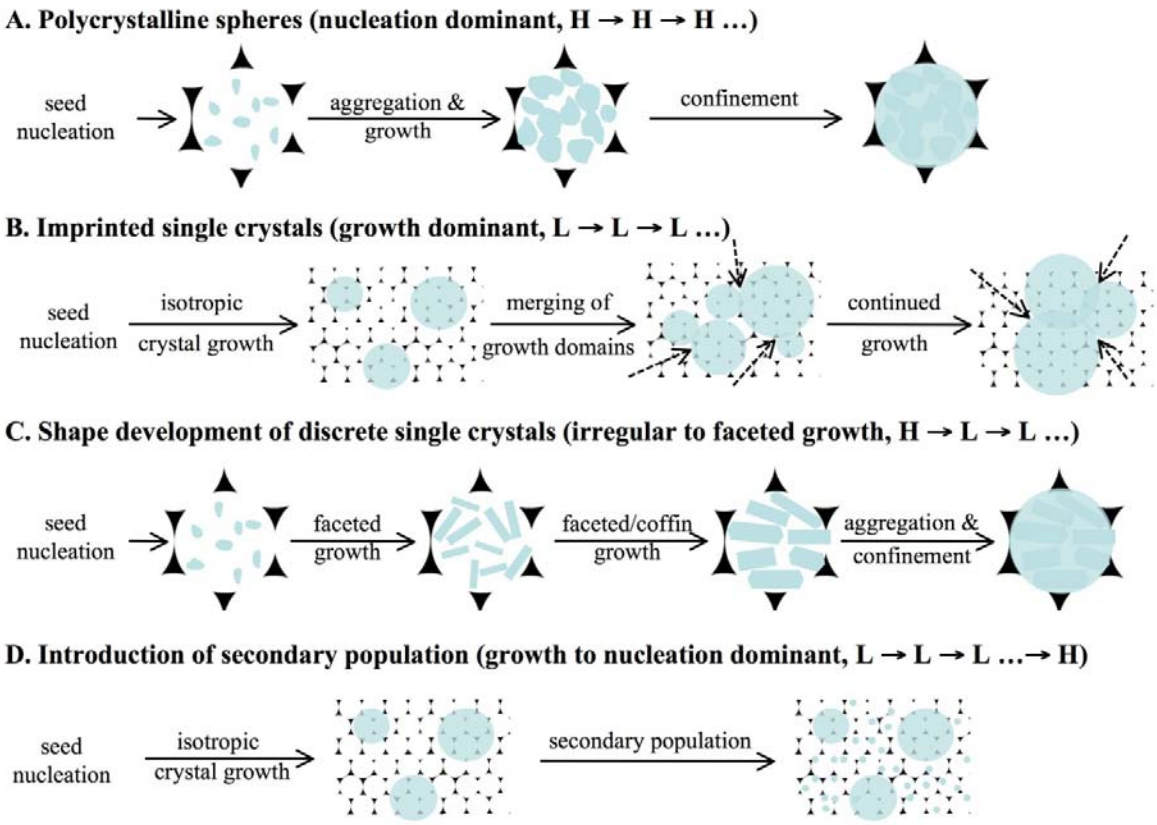

Figure 4.1 Illustration of different zeolite growth patterns obtained by programming sequences of IHT cycles with selected nutrient concentrations in the precursor that penetrates the 3DOM carbon reactor (L = low nutrient concentration, H = high nutrient concentration). (A) Growth of polycrystalline spheres in a sequence where nucleation dominates during each step. (B) Single crystal growth in a system where the low nutrient concentration favors slow growth. The circles represent single crystal domains spanning multiple macropores and the dashed black arrows indicate regions of merging domains. (C) Shape development from discrete, irregular seeds precipitated during an H step to faceted, coffin-shaped zeolite particles after changing to L steps to switch from nucleation to growth dominant conditions. (D) A secondary population of smaller zeolite particles results from a change of solutions that switch from growth to nucleation dominant conditions. The size of the templating macropores is the same in all cases.

4.2 Experimental Section

4.2.1 Reagents

The following chemicals were used without further purification. Resorcinol (99 %), polydiallyldimethylammonium chloride (PDDA, MW = 100,000~200,000, 20 wt%), sodium polystyrenesulfonate (PSS, MW = 70,000, 30 wt%), tetrapropylammonium hydroxide (TPAOH, 1.0 M in H_2O), tetraethyl orthosilicate (TEOS, 98 %) were purchased from Aldrich. Sodium hydroxide (98 %), nitric acid (68–70 %) and hydrofluoric acid (48 %) were obtained from Mallinckrodt Chemicals. Sodium carbonate (99.7 %) and silicic acid (88.04 %) were from J. T. Baker Chemical Co. Formaldehyde (37 %) was purchased from Fisher Scientific and ethanol (200 proof) from Pharmco-Aaper. Sodium hydroxide (98 %), nitric acid (68–70 %) and hydrofluoric acid (48 %) were obtained from Mallinckrodt Chemicals. Deionized water with a resistivity of 18.2 MΩ-cm was used for all reactions.

4.2.2 Preparation of 3DOM carbon and polyelectrolyte coatings

PMMA colloidal crystals prepared by emulsifier-free emulsion polymerization, as described elsewhere,[39] were used as templates for syntheses of 3DOM carbon with 354±7 nm macropores. Silica sphere colloidal crystals prepared by a Stöber synthesis [40] were employed for 3DOM carbon with 110±8 nm macropores. 3DOM carbon was prepared by polymerization and carbonization of a resorcinol-formaldehyde (RF) sol catalyzed with sodium carbonate (molar ratio of resorcinol: formaldehyde: sodium carbonate = 1: 2: 0.019).[39] The sol was infiltrated into a PMMA colloidal crystal template and cured at 85 °C for 3 days. Template removal and carbonization of the RF framework were achieved by heating the composite at 900 °C for 2 h under nitrogen using a 5 °C/min heating rate. The top surfaces of the 3DOM carbon product were polished with sand paper to product a monolith ca. 1 mm thick and several millimeters in each other dimension. To prepare 3DOM carbon for polyelectrolyte deposition, the carbon was oxidized with nitric acid at 130 °C for 15 min to increase the number of oxygen-containing functional groups and treated with NaOH (0.1 M) for 1 day to generate a negative charge on the surface after deprotonation of the carboxylic acid groups. Layers

of the positive polyelectrolyte PDDA and the negative polyelectrolyte PSS were alternatively coated on negatively charged 3DOM carbon to modify the surface charge, using 4 layers (PDDA, PSS, PDDA, PSS) for 3DOM carbon with an outermost anionic polyelectrolyte layer (measured zeta potential -46 mV at pH 7.7) or 5 layers (PDDA, PSS, PDDA, PSS, PDDA) for 3DOM carbon with an outermost cationic polyelectrolyte layer (measured zeta potential +28 to +22 mV at pH 7.4–8.2). All zeta potentials were determined in unbuffered water using finely ground samples to maximize exposure of pore surfaces.

4.2.3 Hydrothermal reactions

The silicalite-1 precursor solutions were prepared using the molar ratio 10 SiO_2 (from silicic acid): 2.4 TPAOH : 0.87 NaOH : 114 H_2O ("high nutrient concentration", H)[41] or 10 SiO_2 (from TEOS): 4.5 TPAOH : 4750 H_2O ("low nutrient concentration", L).[42] 3DOM carbon was soaked in the precursor solutions and heated at 80 °C in closed, 130 mL Teflon® bottles that were rotated for 2 days (for H) or 4 days (for L). After each seed growth step, the 3DOM carbon pieces were rinsed multiple times with deionized water, dried at room temperature and re-immersed in fresh precursor solution. To study the shape development of zeolite particles, 3DOM carbon was first infiltrated with precursor H. After one IHT reaction, the 3DOM carbon monolith was mechanically polished to remove the more developed surface regions in which aggregates had already formed due to a concentration gradient across the monolith.[26,43] The remaining fraction contained isolated seeds and was used for subsequent infiltration with precursor L.

4.2.4 Recovery of zeolite spheres and thin film preparation

After several sequential IHT cycles for each reaction condition, 3DOM carbon containing zeolite spheres was mechanically polished and treated with HF (10 wt%) for 30 min to remove unwanted zeolite particles deposited on the external 3DOM carbon surface. The composite material was heated up to 550 °C with a heating rate of 1 °C/min and a soaking time of 6 h under oxygen to remove carbon and the structure directing agent (TPAOH). The resulting opaline zeolite monolith was sonicated in ethanol for several days to break down connections between spheres and filtered to remove any

remaining larger sphere aggregates. The ethanol dispersion of zeolite spheres was dropped onto a silicon substrate and dried at room temperature.

4.2.5 Characterization

TEM images were obtained using a FEI Tecnai G2 F30 TEM operating at 300 kV and collected using a CCD camera. Samples were crushed and supported on a holey carbon-coated copper grid (Ted Pella, Inc.) for the TEM investigation. SEM images were obtained with a JEOL 6700 microscope with an accelerating voltage of 5 kV and an applied current of 20 mA. All images were obtained without coating the samples except for the calcined samples, which were coated with 5 nm Pt. X-ray diffraction (XRD) patterns were obtained using a Bruker–AXS microdiffractometer with a 2.2 kW sealed Cu K_α X-ray source (1.542 Å), a Hi–Star 2–D area detector, an operating voltage of 45 kV and a current of 40 mA. A beam size of 0.8 mm was used to focus on the core region of the 3DOM nanoreactor–zeolite composites. Zeta potential measurements were carried out on a ZetaPlus analyzer (Brookhaven Instruments).

4.3 Results and Discussion

4.3.1 Growth of polycrystalline spheres

4.3.1.1 Polycrystalline spheres with corrugated surface

Three-dimensionally ordered macroporous (3DOM) carbon matrixes can act as massively parallel reaction chambers for high-yield HT syntheses of zeolite particles with uniform sizes; the product morphology is controlled not only by the shape of the macropores but also by several parameters that can be designed into the nanoreactor structure or adjusted during HT processing. These include the charge of polyelectrolytes deposited on the surface of the porous host, the precursor concentration, the number of infiltration steps, the proximity of a pore to the monolith exterior, and the dimensions of windows that connect adjacent pores and define transport properties. Depending on these parameters, the products can be uniform solid spheres; geode-like, hollow zeolite spheres;

or colloidal crystal arrays of such spheres. The sphere surface may be smooth or corrugated.

During a HT synthesis, zeolite seeds may nucleate either heterogeneously on the surface of the reactor walls or homogeneously in the void space away from the reactor walls. As shown below, nucleation can be controlled by the charge of polyelectrolytes on the reactor walls, which affects the final product morphology. The surface of 3DOMC is nearly neutral after synthesis. After oxidation in nitric acid and neutralization, carboxylate and other oxygen-containing groups are introduced on the carbon surface, providing it with a negative charge. The charge can be altered by depositing multilayers of polyelectrolytes on the surface using layer-by-layer deposition methods.[44]

Nucleation and growth of the zeolite particles depend on precursor concentrations and reaction temperatures.[42] To allow monitoring of product growth in the nanoreactor arrays within a practical time frame, we chose a solution composition (Figure 4.1A, nucleation dominant condition) with a HT reaction temperature of 80 °C. Pieces of 3DOMC with edge lengths of several millimeters and typical thicknesses near 1 mm were immersed in this reaction mixture for two days at a time, then washed with purified water, dried for sampling, and re-immersed in the HT synthesis mixture for additional two-day infiltration steps.

Figure 4.2 shows the growth progression for polycrystalline aggregates within 3DOMC under different conditions. For 3DOMC containing a negatively charged polyelectrolyte as the top surface layer, we would expect polycrystalline particles with an intrinsic negative surface potential to be repelled by this surface, causing nucleation to occur primarily in the void space away from the wall.[45] Even though this type of nucleation is not directly apparent from the SEM image obtained after sample drying (Figure 4.2a), comparison of product morphologies formed with outermost anionic or cationic polyelectrolyte layers provides evidence that nucleation and growth indeed started away from the surface. After one infiltration/HT reaction (IHT) for two days, most cages contain a small number of isolated seeds (Figure 4.3). After a second IHT cycle, the number of particles observed in each cage increases, as does their average size (Figure 4.2b). The surface of each sphere is corrugated, and features of separate particles are visible. This carbon/silica composite produces an unambiguous XRD pattern for

silicalite (Figure 4.4), and lattice fringes from the zeolite structure are visible by TEM (Figure 4.5a). Additional IHT cycles result in more filling of the void space between particles in each cage. After four or five IHT cycles, sphere sizes are limited by confinement in the macropores, and sphere surfaces are relatively smooth (Figure 4.2c and Figures 4.3 and Figure 4.5b). The polycrystalline product is monodisperse, and nearly all macropores are filled with spheres.

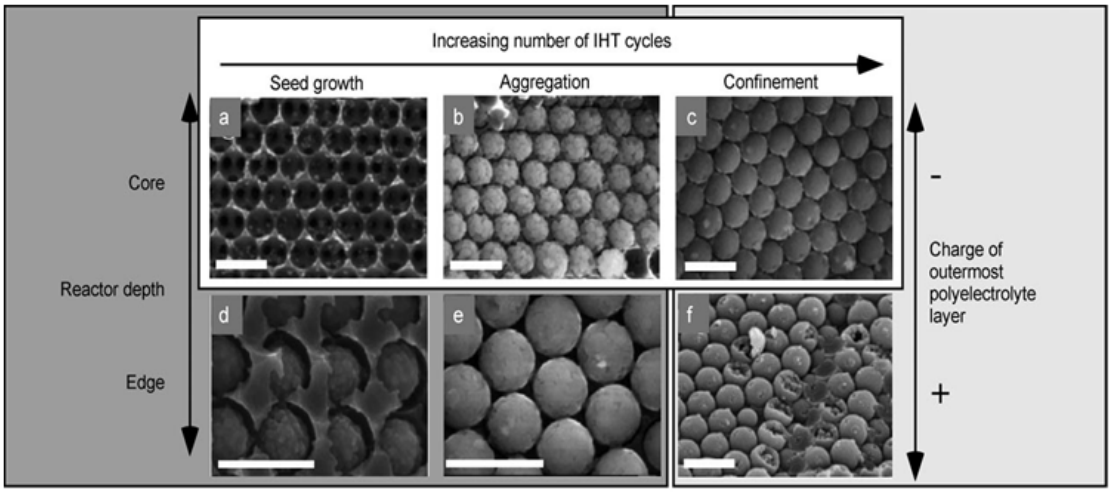

Figure 4.2 SEM images illustrating the different morphologies of silicalite products obtained after HT syntheses in 3DOM nanoreactors for varying processing conditions.

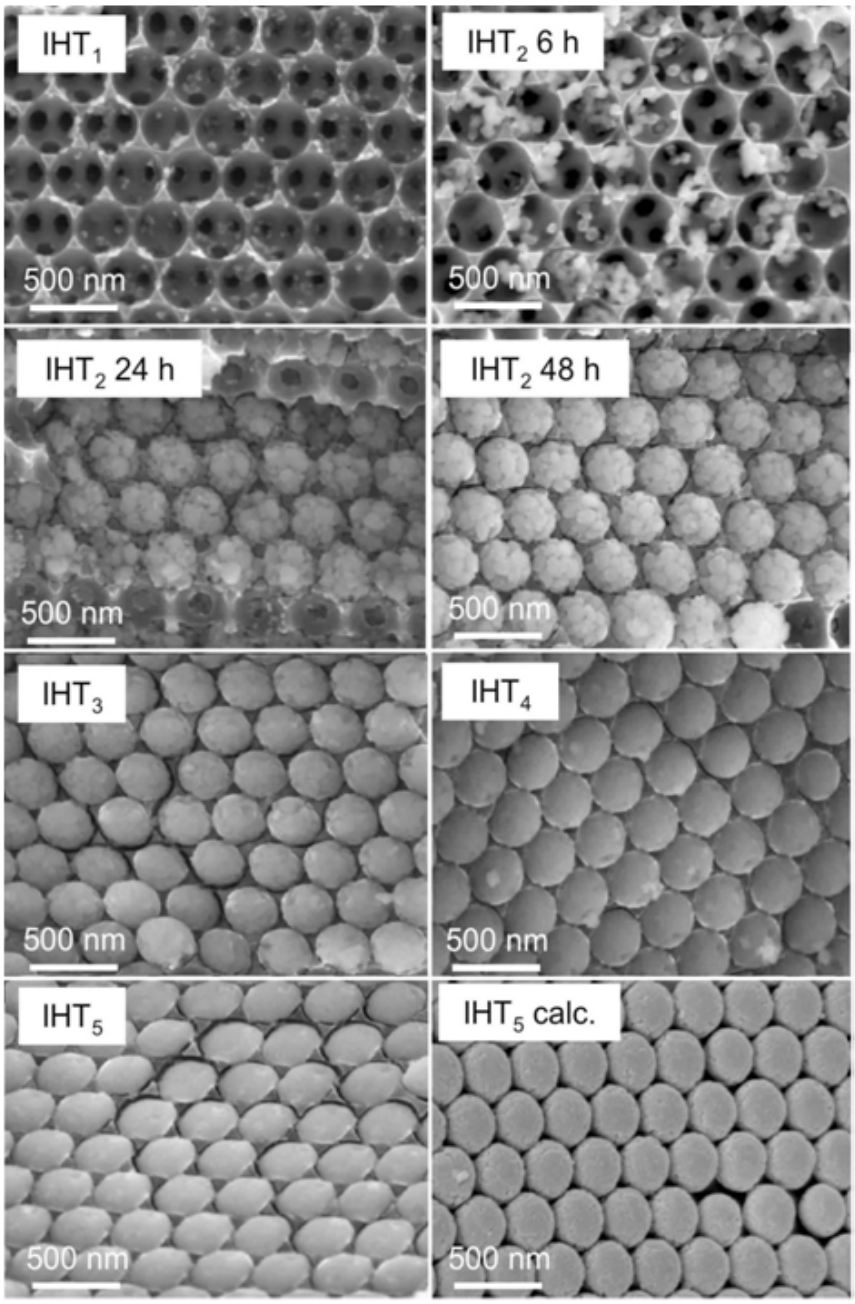

Figure 4.3 SEM images of carbon-silicalite composites after the indicated number of IHTn cycles and after calcination (calc.)

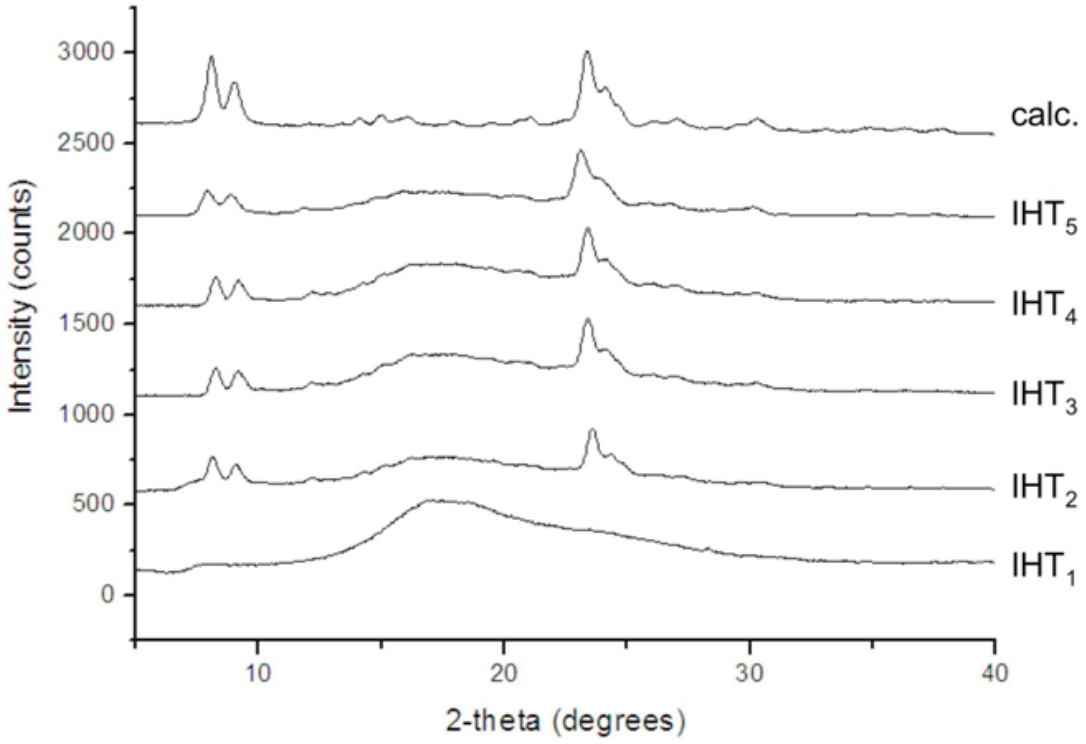

Figure 4.4 Powder X-ray diffraction (XRD) patterns of carbon-silicalite composites after the indicated number of infiltration/hydrothermal reaction (IHTn) cycles (n = cycle number) and after calcination (calc.)

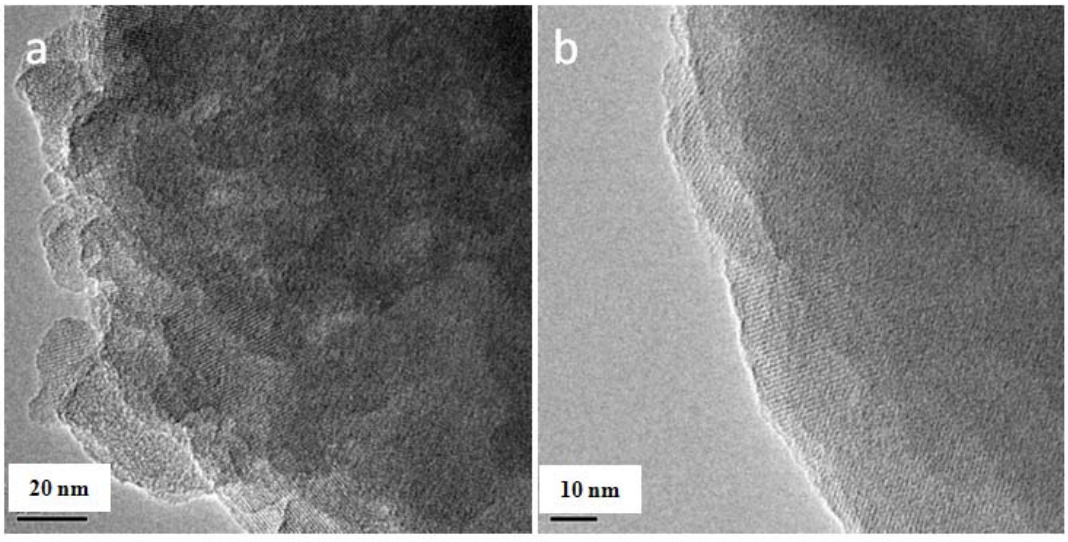

Figure 4.5 TEM images of IHT_2 (a) and IHT_5 (b).

In a 3DOM reactor, the morphology of the HT reaction product is, to some extent, diffusion-controlled. A concentration gradient across the monolith results in variation of the product morphology along the cross section, in particular during early IHT cycles (Figure 4.6). A comparison of SEM images obtained from cross sections of the monolithic composite near the edge and in the core reveals that after a single infiltration, spherical aggregates begin to form near the edge of the sample (Figure 4.2d and Figure 4.6), but much of the interior contains scattered seeds (Figure 4.2a and Figure 4.6). After the second IHT, interparticle space is filled more for near-edge particles (Figure 4.2e and Figure 4.6) than in centrally located macropores (Figure 4.2b and Figure 4.6). The observation of smoother surfaces after subsequent cycles indicates that internal pores remain accessible to nutrients for several more IHT steps. On the basis of these relationships between sample position, reagent concentration, and product morphology, it is possible to apply combinatorial approaches to study HT growth in the 3DOMnanoreactor arrays, at least during the first few IHT cycles.

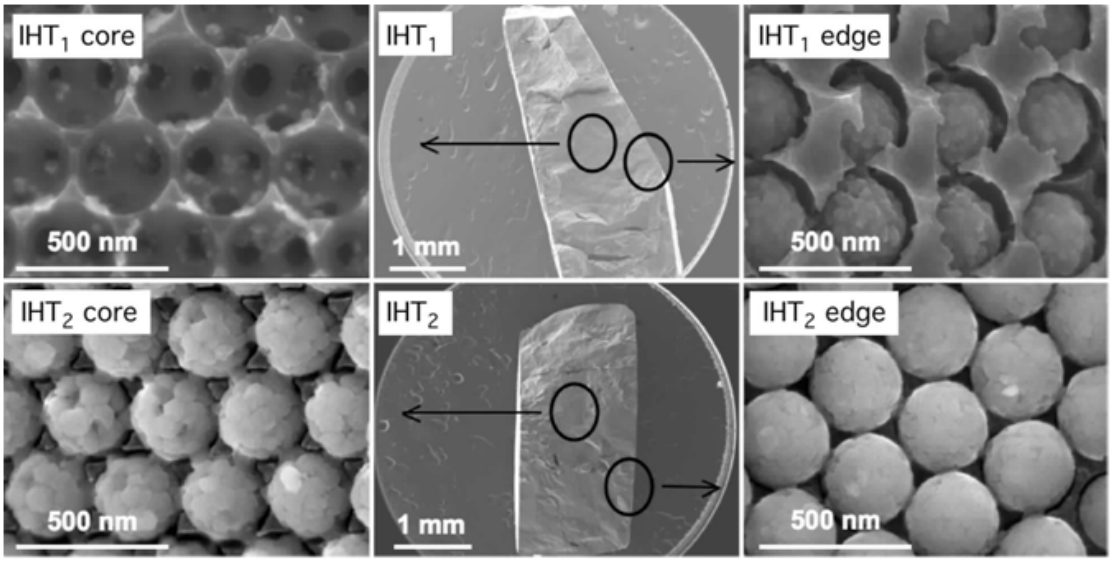

Figure 4.6 SEM images and photographs of the 3DOM carbon/silicalite composite after one and two IHT cycles (high silica concentration, outermost anionic polyelectrolyte layer). The SEM images show cross-sectional regions near the edge or near the center of the monolith. Each monolith was fractured for SEM analysis after reaction and drying of the sample.

Upon calcination of the carbon reactors in air, monolithic, opalescent-white pieces of polycrystalline spheres were obtained, which consisted of close-packed, monodisperse spheres (Figure 4.7). The opaline structure provides pathways for diffusion in interstitial spaces between silicalite spheres, creating a hierarchical pore structure with micropores within each silicalite particle, textural mesoporosity within each spherical agglomerate, and macroporosity at the level of the interstitial spaces. The 3D sphere array could also be converted into 2D layers. Through grinding and sonication of the zeolitic opal, the spheres were dispersed in solvents to form discrete particles, diads, triads, and some larger particle arrays. Reassembly on a planar silicon surface into polycrystalline close-packed layers was possible (Figure 4.7). Such monolayers of uniform zeolite particles provide a starting point for manufacturing randomly oriented molecular-sieve films by seeded growth.[8,28] The concepts described herein are, to some extent, scalable to reactor arrays with smaller pore sizes to form smaller spheres with similar morphologies (Figure 4.8).

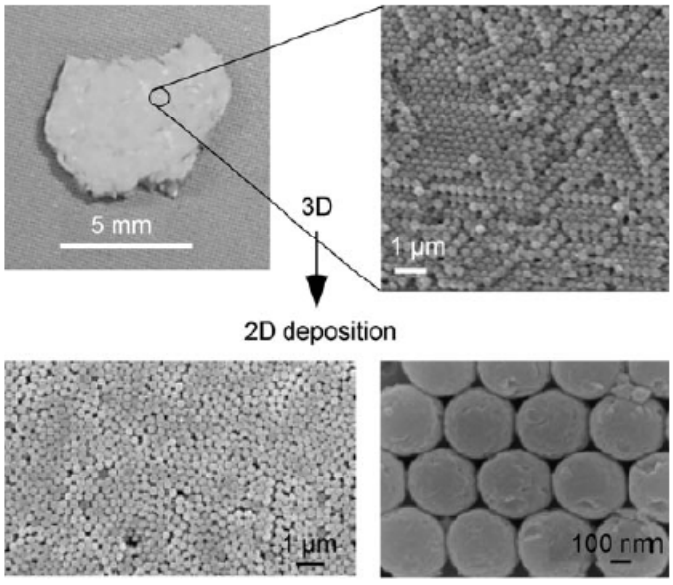

Figure 4.7 Photograph (top left) and SEM image (top right) of the calcined product consisting of a 3D array of close-packed silicalite spheres. Bottom: SEM images at different magnifications of a layer of spheres assembled on a flat silicon substrate after dispersion of the spheres in ethanol.

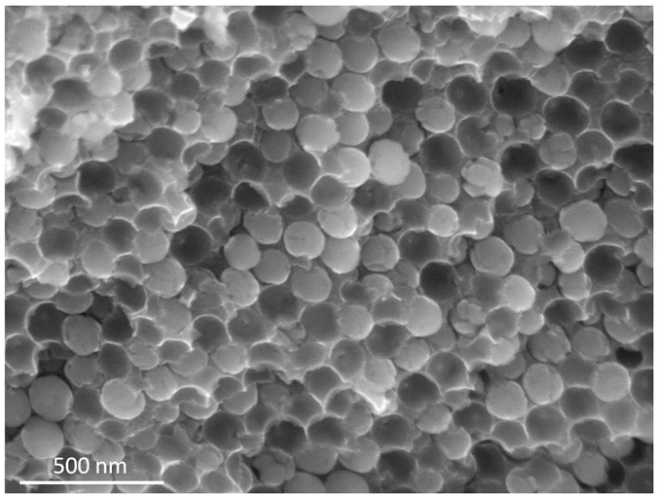

Figure 4.8 SEM image of silicalite prepared inside 3DOM C with smaller, 110 nm diameter pores (high silica concentration, outermost anionic polyelectrolyte layer). Although the nanoporous reactor is less ordered, the product morphology is similar to that obtained in the larger macropores. Some spheres with smooth surfaces and some more corrugated particle agglomerates are observed after the 3rd IHT cycle.

4.3.1.2 Polycrystalline spheres with hollow interior (geode-like structure)

Because the reactor surface/volume ratio is high in 3DOM reactors, nucleation, growth, and morphology of the HT products depend on interfacial interactions. When the outermost polyelectrolyte layer on the reactor surface is changed from anionic to cationic, silicalite particles with negative surface charge are attracted to the wall, and crystal growth on the wall is favored. After one IHT using a 3DOMC monolith with an outermost positive polyelectrolyte layer, an SEM image (not shown) reveals a small number of isolated seeds in each cage, similar to the corresponding case for the negatively charged surface. However, after several additional IHT cycles, more material coats the carbon surface to produce spherical structures with shapes dictated by the reactor walls. An SEM image of a cross section shows several cracked spheres that are hollow and resemble geodes with shells (ca. 70 nm thick) exhibiting smooth external surfaces and textured internal surfaces (Figure 4.2f and Figure 4.9). Product growth therefore must have occurred mainly starting from the reactor walls into the void space,

with seeds initially attached to the walls, in contrast with the situation for negatively charged reactor walls, where product grew from within the void space outwards to the walls. As windows between pores closed up, no additional nutrients could enter the system.

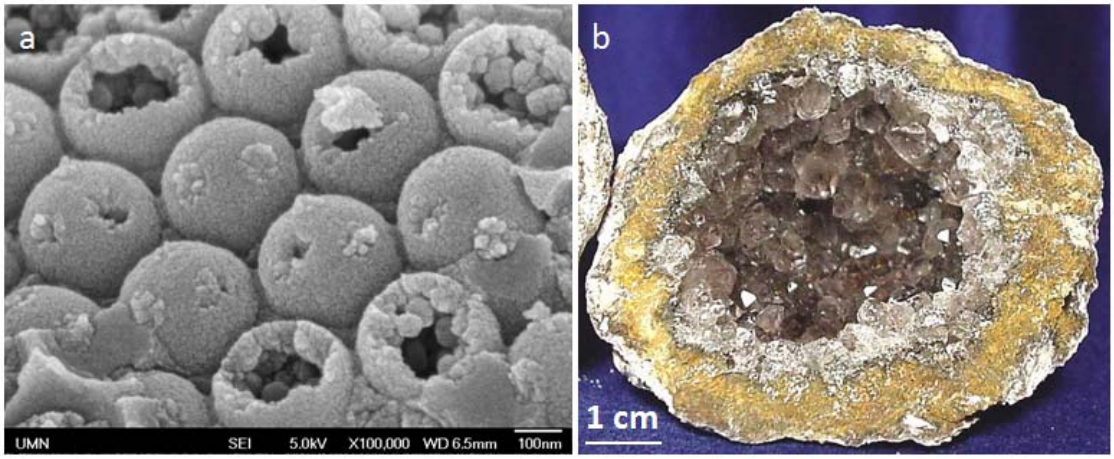

Figure 4.9 SEM image of geode-like polycrystalline zeolites (a) and photograph image of the geode structure of an amethyst (b), a larger analogue for the much smaller hollow spheres shown in panel (a).

4.3.2 Growth of imprinted single crystals

Single crystal zeolite particles with imprinted macropores were prepared using multiple L_n steps. After cycle L_2, macropores contained sets of small, discrete zeolite particles with average diameters less than ca. 10 nm (Figure 4.10A). Although these particles were attached to the carbon surfaces when they were imaged in the scanning electron microscope, they were probably detached from the walls before sample drying as a result of electrostatic repulsions between the silica particles and the negatively charged, outermost polyelectrolyte layers. After cycle L_3, domains were observed, in which a few adjacent macropores were completely filled with solid product (Figure 4.10B). These particles had smooth surfaces and overall rounded shapes. Some surface extrusions are visible where the particle had penetrated a window between neighboring macropores before the 3DOM carbon monolith was sectioned to obtain the SEM image. Cages

surrounding these solid domains were nearly empty. This contrasts with the situation after cycle L_2, when small particles were evenly distributed throughout virtually all cages (Figure 4.10A). This result is also very different when a precursor with a high nutrient concentration was used. Under those conditions, all cages remained occupied by zeolite particles, which grew and produced polycrystalline spheres in relatively few H_n cycles (see Figure 4.2 and 4.3). Eventually, their morphologies were determined by shape-confinement in the porous carbon reactor. With high nutrient concentrations, a large number of nuclei are formed, most of which can continue to grow as a result of sufficient nutrient supply throughout the 3DOM carbon reactor (see Figure 4.2 and 4.3). With low nutrient concentrations and limited nutrient supply, the number of nuclei produced during the early stages (i.e., after cycles L_1 and L_2) is smaller and a fraction of these grow into larger crystals at the expense of smaller ones by typical Ostwald ripening processes. Under these conditions, most of the additional precursor added in subsequent steps appears to be consumed by the predominant seed crystals.

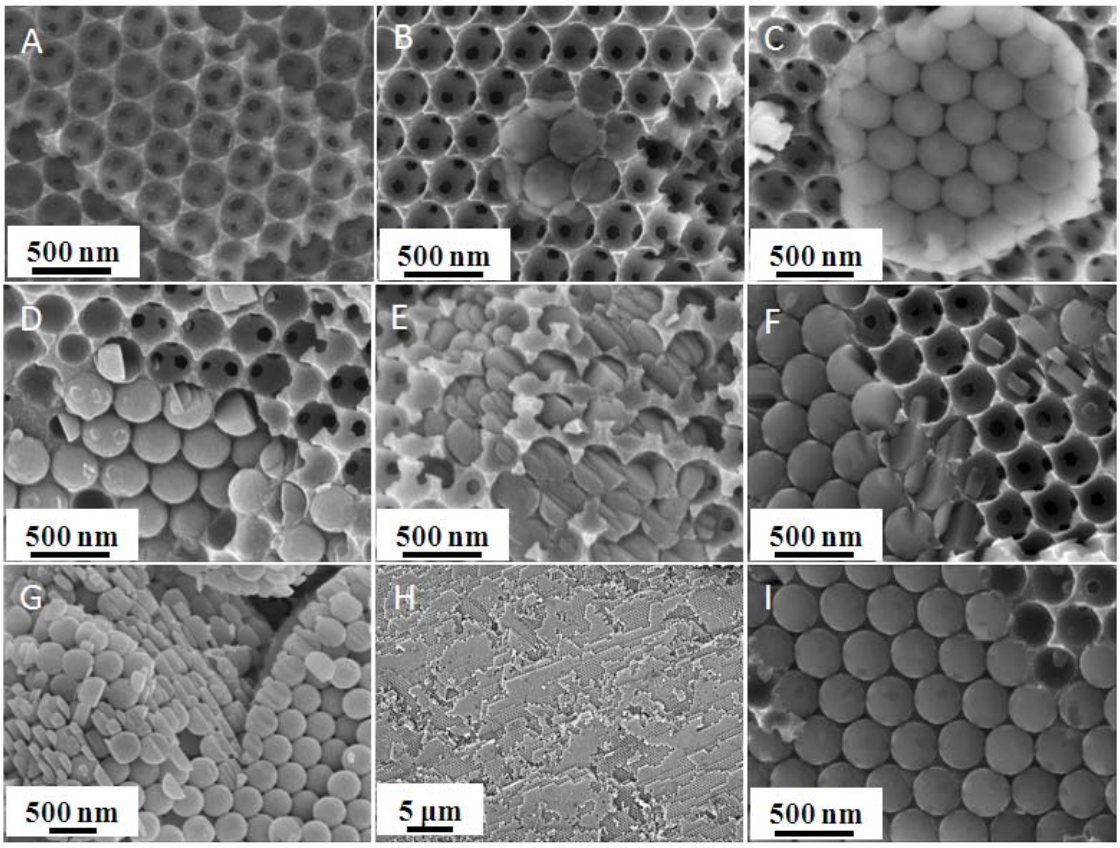

Figure 4.10 SEM images illustrating sequential single crystal growth using precursor L: (A) to (D) crystal domain growth in sequential IHT reactions after cycles L_2, L_3, L_5 and L_7, respectively, (E) different region after L_7, (F) after L_{11}, (G) calcined sample after L_{13}, (H) after L_{15}, (I) enlarged image of (H).

After L_5, larger domains of zeolite particles were observed, which were surrounded by empty macropores (Figure 4.10C). The exposed surface obtained after cross-sectioning the sample clearly shows the imprint of the 3DOM carbon template, which produced a smooth spherical morphology where the zeolite was in direct contact with the carbon walls. On the other hand, regions where the zeolite was not in direct contact with the carbon walls were frequently faceted.

In an attempt to investigate the connectivity, overall shape and crystallinity of the particle domains, the sample formed after L_5 was calcined to remove the carbon template.

Rounded, robust domains of material with an opaline morphology and diameters of several micrometers are observed, many of which are interconnected (Figures 4.11A and B). According to the selected area electron diffraction (SAED) patterns of the particle domain depicted in the TEM image (Figure 4.11B), this domain is a single crystal (Figure 4.10B-inset). Zeolite particles with this morphology may be of interest as hierarchical zeolite catalysts because they bring together the advantages of 1. short diffusion lengths within spheres molded by each macropore (e.g., 200~300 nm), 2. an open void structure that affords low mass transfer resistance, and 3. the ability to be treated from the standpoint of fluid mechanics as regular, micron-sized crystals, which offer lower pressure drop in packed beds and can be recovered from liquid mixtures or recirculated in fluidized beds.[5,7,22,32-37]

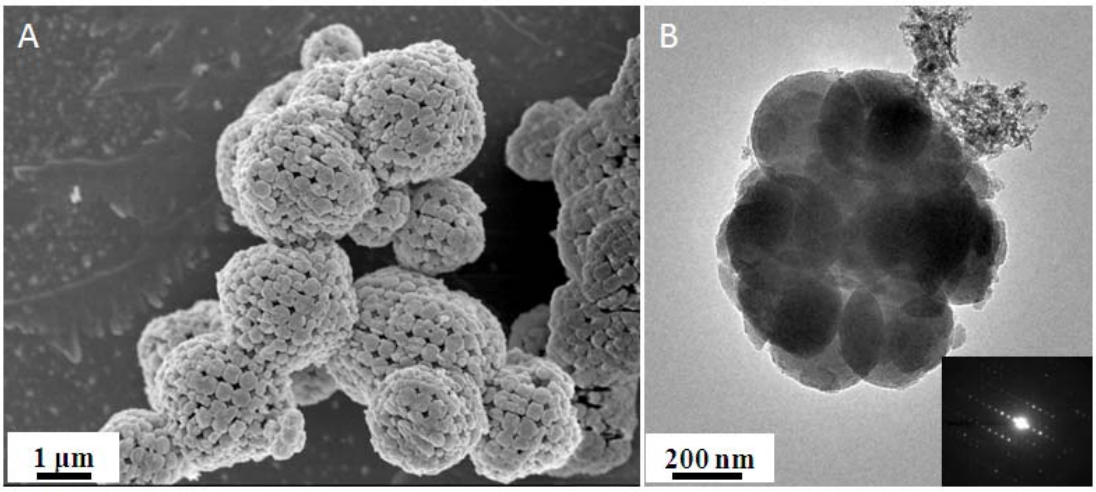

Figure 4.11 (A) SEM and (B) TEM images of the sample formed after L_5 and subsequent calcination. An SAED pattern of the particle shown in (B) is provided in the inset of (B).

Subsequent L cycles resulted in a larger crystal population and further crystal growth. However, new structural features were also observed after L_7, including facets, steps and anisotropic shapes with plate-like (Figure 4.10D and E) and needle-like appearances (Figure 4.10F, top right area of image). These features predominate in the outside regions of a domain. In the internal regions, macropores are mostly filled with solid product, giving rise to spherical particles by shape confinement. As established

above, many domains appear to be single crystals. Therefore, continued growth of such domains follows the typical growth directions of silicalite-1 crystals, as long as the domain remains isolated from other domains. The steps and plate-like shapes result from crystal faces that are exposed as the crystal grows under limited nutrient supply. If additional nutrient can reach these sites, they eventually fill in until the crystal reaches the carbon walls. If nutrient supply is cut off earlier, the steps and edges remain in the product. The needle-like structures may result from growth of the crystals through a macropore window. The SEM image of the calcined product after cycle L_{13} (Figure 4.10G) shows relatively smooth spheres in the interior of a domain, with more faceted features on the periphery. This particular image reveals the merging of two adjacent domains, which nucleated from two separate centers. In this "frustrated region", competition between crystallization and growth of the adjacent domains is likely to influence the surface features near the interface. Nearly all of the 3DOM carbon template is filled with single crystal zeolite particles after L_{15}, showing a mixture of crystal domains at various growth stages (Figure 4.10H and I).

For a detailed investigation of crystallographic features in these templated zeolite particles, the sample obtained after L_{11} was analyzed by high-resolution TEM. Figure 4.12A shows a TEM image of a particle that had filled a whole macropore and therefore took on the spherical shape of the macropore. The corresponding SAED pattern confirms that this zeolite sphere consists of a single crystal. This is in contrast to the polycrystalline spheres obtained with more concentrated silica precursors. The inset in Figure 4.12B shows another particle with a morphology that combines the characteristic hexagonal prismatic shape of silicalite-1 with more rounded edges. The longest dimension is along *c* (i.e., the preferred growth direction that is also observed in non-confined syntheses) and the particle is faceted along *a*-planes. The [101]-type planes of the usual prismatic shape have been smoothed out by confinement in the 3DOM carbon template. The sharp edge planes on both sides suggest that anisotropic growth inside macropores first produces faceted particles and eventually fills the macropores: when one macropore is not fully occupied, the anisotropic growth follows the *c*-direction until the pore is filled, and it either becomes rounded by wall confinement or continues to grow through a pore window. Not surprisingly, the major growth direction is influenced by the

internal structure in each crystal, not by the 3DOM carbon template. For example, the images in Figures 4.10F and Figure 4.12C and D show finger-like outgrowths from spheres that are not perpendicular to the sphere surface (i.e., the window direction), but instead follow the *c*-growth direction. Crystal growth clearly occurred through a window in these cases, but the direction of fastest growth was not changed by the carbon walls. This observation is in contrast to a recent report of crystal orientation of glycine inside nanoporous polystyrene-poly(dimethyl acrylamide), where the crystal size was comparable to the 20 nm diameter of the one-dimensional pores of the polymer template and the fastest growth direction was parallel to the axis of the cylindrical mesopores.[46] In our case, the pores are larger and 3D interconnected.

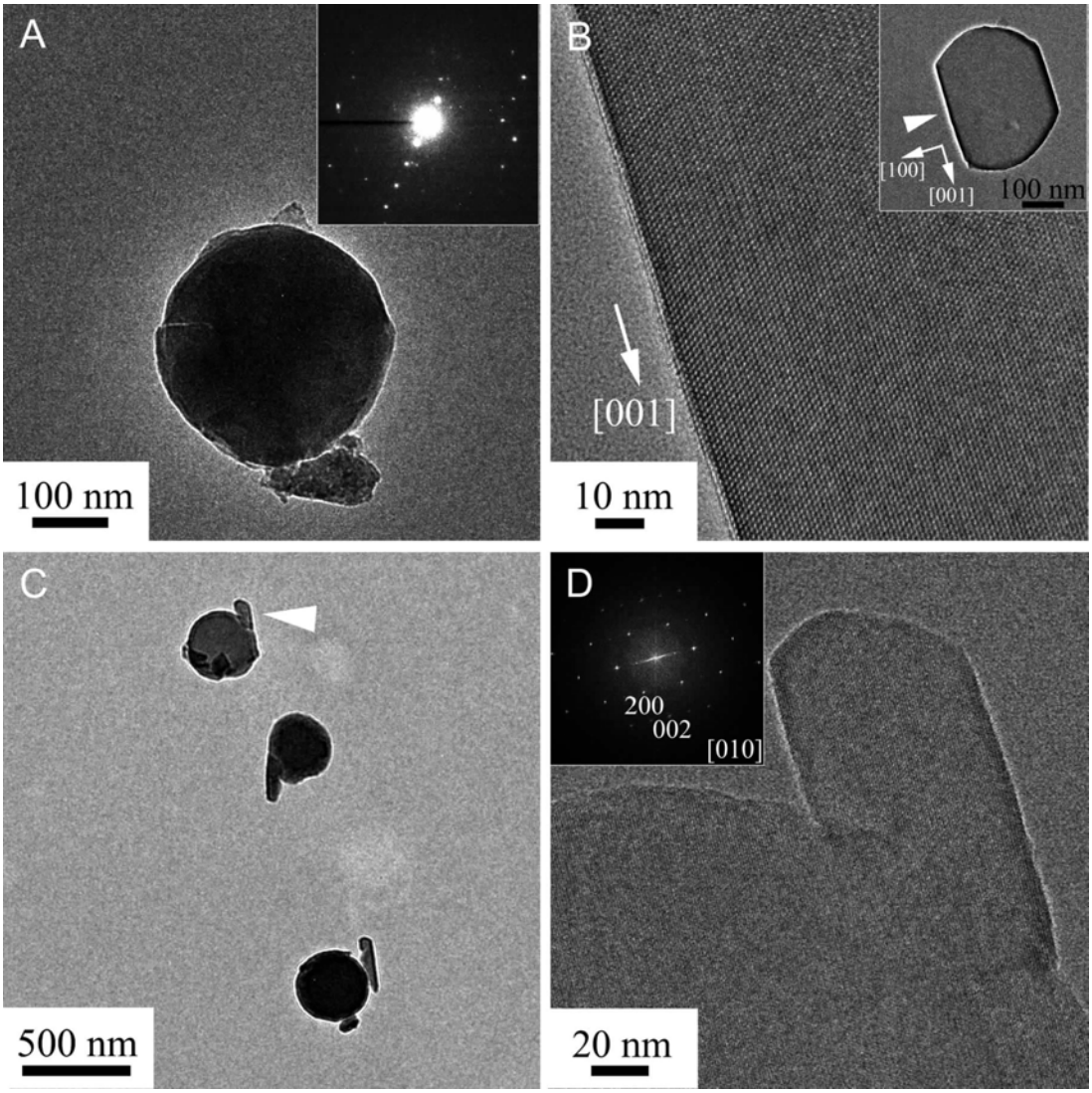

Figure 4.12 TEM images of various shaped zeolite crystals after cycle L_{11}: (A) A sphere templated by one macropore. The inset shows the corresponding selected area electron diffraction (SAED) pattern, confirming that the sphere is a single silicalite-1 crystal. (B) A representative crystal showing the influence of confinement on the characteristic coffin-like morphology of silicalite-1. The crystal is faceted along the *a*-planes. The facet marked by the white arrowhead is enlarged in the high resolution TEM image. (C) Three spheres with outgrowths. (D) High resolution image of the area marked by the white arrowhead in panel (C). The outgrowth follows the *c*-direction and its width is close to the size of windows in 3DOM carbon. The inset shows the corresponding SAED pattern. A similar particle can be seen in the center of the SEM image shown in Figure 1F.

4.3.3 Shape development of discrete zeolite particles

When we employed only precursor H, a large number of seeds was produced in the initial IHT step and grew into irregular particles and then polycrystalline spheres after multiple cycles. In contrast, using a sequence of an initial H_1 step and subsequent L cycles made it possible to produce small, well faceted zeolite crystals. Reaction conditions favored nucleation during cycle H_1 and produced irregular zeolite particles ca. 10–40 nm in length (average length 24.5 ± 5.4 nm) throughout most of the 3DOM carbon monolith (Figure 4.13A). Outermost layers of the monolith containing more completely filled macropores were removed by mechanical polishing before continuing with L_n cycles continued. The new conditions favored crystal growth from the original nuclei. During cycles H_1L_1 and H_1L_2, continuous growth produced highly crystalline, well-faceted, discrete zeolite particles whose average sizes increased with each cycle (Figures 4.13B, C and Figure 4.14). A distribution of sizes resulted, which could be attributed partly to the size variation of the parent seeds produced during cycle H_1. After H_1L_1, most of the smaller crystallites appeared to be brick-shaped (see Figure 4.14A and C), whereas the fraction of coffin-shaped particles (a common morphology for an MFI-type zeolite, Figure 4.14D) increased after H_1L_2 (Figure 4.14B). We also observed several twinned structures (indicated by black arrows in Figures 4.13C and 4.14B). The morphological development of zeolite particles from irregular to well faceted is a consequence of the lower precursor concentration, which introduces fewer seed particles and instead provides a low level of nutrients for slow hydrothermal crystal growth. Rectangular and coffin-shaped zeolite particles with lengths less than 100 nm have recently been reported as products of conventional hydrothermal reactions.[12] Lee et al. prepared faceted silicalite-1 nanocrystals ca. 100 nm × 40 nm × 200 nm in size using anionic microemulsions as a soft template, but they noted that different morphologies resulted from strong interactions between zeolite particle and the surfactant, not from the confinement provided by the microemulsion.[47] The thickness of the faceted zeolite particles produced here is much smaller than 100 nm, so that these well faceted zeolite particles may be suitable as building blocks for seed layers of molecular sieve membranes prepared by secondary growth methods.[8,28-31]

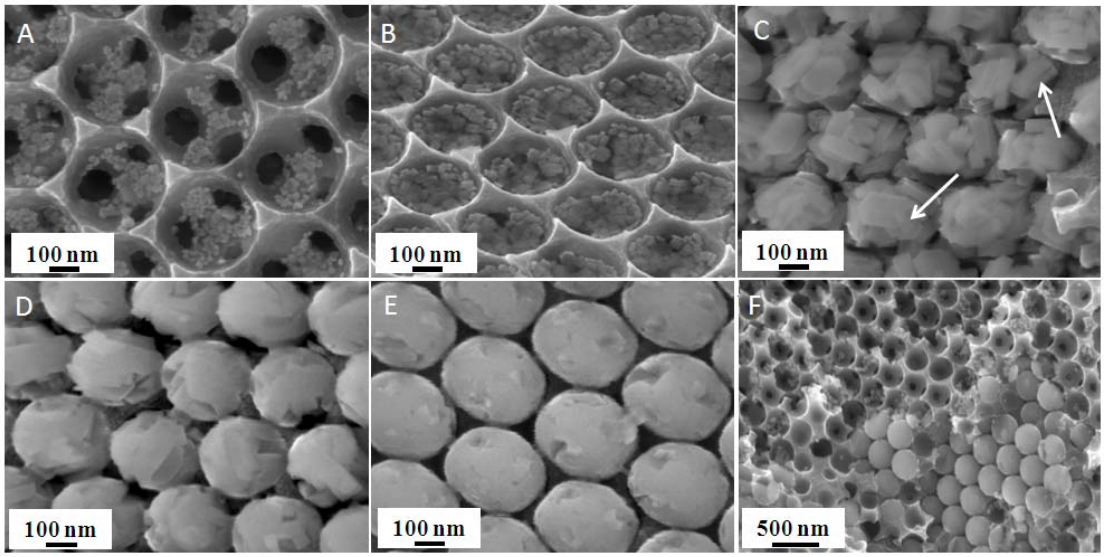

Figure 4.13 SEM images illustrating the shape development of zeolite particles during programmed growth with multiple concentration schedules: (A) Product obtained after H_1. (B) Product obtained after a H_1L_1. (C) Product after H_1L_2, clearly showing faceted, coffin-like crystals. The white arrows point at twinned crystals. (D) Product after H_1L_3 and (E) product after H_1L_4. At these stages, crystals aggregate and growth becomes limited by confinement inside the 3DOM carbon monolith. (F) A secondary population of irregular zeolite particles is produced after applying precursor H following six L cycles (L_6H_1).

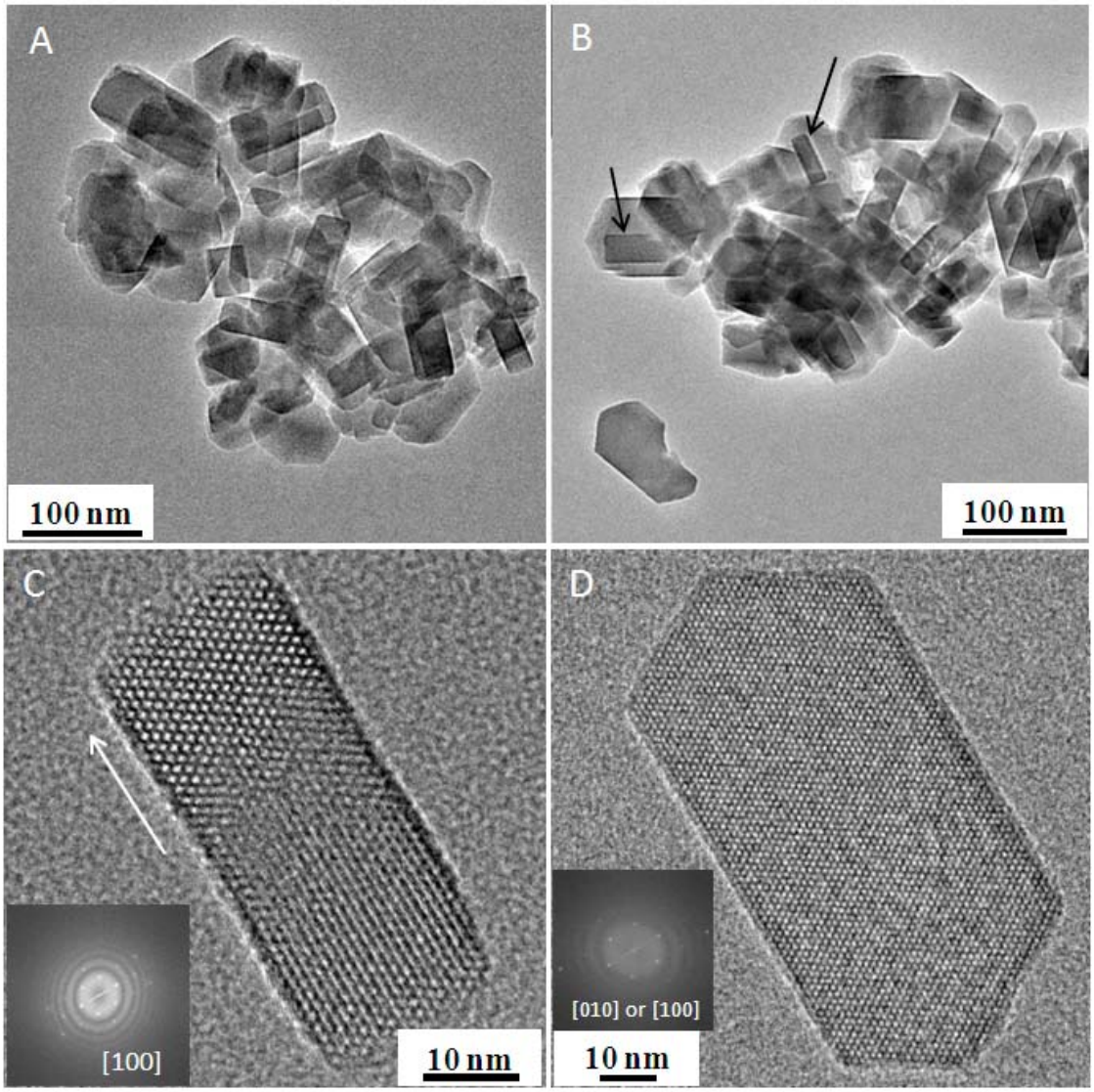

Figure 4.14 TEM images illustrating the shapes, pore structures and crystallinity of the faceted, coffin-like products shown in Figures 4B and 4C: (A) and (B) low magnification images of the products obtained after cycles H_1L_1 and H_1L_2, respectively, (C) and (D) higher magnification images of crystals obtained after cycle H_1L_1. The black arrows in (B) indicate twinned structures and the white arrow in the (C) indicates the *c*-orientation. FFT patterns of the TEM images in (C) and (D) are presented in the insets.

After additional L cycles, faceted zeolite particles grew into each other, especially in the periphery region of the 3DOM carbon monolith (Figure 4.13D, after H_1L_3).

Eventually, intergrowth of these crystals and confinement by the carbon walls produced rounded particles with relatively smooth surfaces (Figure 4.13E, after H_1L_4). These merging and confinement effects are similar to polycrystalline growth of zeolite spheres under confinement in 3DOM carbon (when a precursor with high nutrient concentration was used throughout all IHT cycles), although in the present case, the spheres contain fewer and larger crystal grains.

4.3.4 Secondary population growth

By altering the sequence of H and L cycles, it is also possible to produce multiple populations of zeolite particles with different size distributions. As we have seen, introduction of precursor solution H favors nucleation of new seeds. We have already demonstrated this when the high concentration precursor was used in the first IHT cycle. However, the nucleation effect is also observed when a precursor H is used at a later cycle, following a series of L cycles (i.e., growth-dominant conditions). Figure 4.13F and Figure 4.15 show an SEM image of a product obtained after six L cycles and one subsequent H cycle (L_6H_1). Because of the nucleation dominant conditions created by the high nutrient content in solution, a second population of small, irregular zeolite particles formed in the available spaces between larger domains. This behavior shows that even in the presence of crystals in the 3DOM carbon reactor, the H mixture nucleates fast enough to start a new population. The effect may be attributed to the presence of the 3DOM carbon matrix which slows down diffusion of dissolved species and small nanoparticles, while eliminating diffusion of the existing zeolite crystals and hence, creating isolated regions with conditions very similar to those in H mixtures without preexisting crystals. Thus, judicious scheduling of IHT cycles with conditions that favor either nucleation or growth, permits some control over particle size distribution in the zeolite product. Controlled mixtures of particle sizes would be of interest for preparing densely packed seed layers for zeolite membranes.

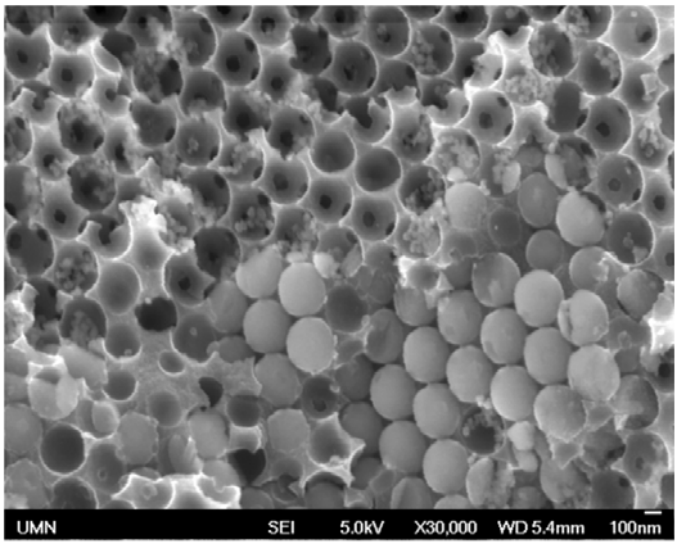

Figure 4.15 SEM image showing that a secondary population of irregular zeolite particles is produced after cycle L_6H_1. This is the same image as Figure 4.13F.

4.4 Conclusions

We have demonstrated that varying the sequence of precursor concentrations in multistep hydrothermal reactions under confinement permits control over morphology, grain size, density of grain boundaries and particle size of the hydrothermal products, specifically the zeolite silicalite-1. Depending on the relative magnitudes of nucleation and growth rates, development of the crystal grain shape from irregular to faceted is possible and controlled syntheses of single crystal or polycrystalline zeolite particles can be achieved.

When HT growth occurs homogeneously and seeds are detached from the reactor walls through repulsive electrostatic interactions, solid spherical agglomerates of zeolite particles are formed, whose corrugated walls can be smoothed out by filling interparticle spaces with more nutrients. 3D arrays of discrete, monodisperse zeolite spheres are produced after calcination. Uniform hollow spheres can be recovered with heterogeneous growth from seeds that are electrostatically attached to the reactor walls.

If, on the other hand, the crystals are permitted to grow without additional nucleation, they can extend through the windows of multiple reactor cages and are

eventually shaped by the host (the 3DOM carbon reactor) to form spheres or close-packed sphere arrays. The domains can be isolated by calcination, producing single crystalline zeolite particles with hierarchical porosity, created by the structure-directing agent (micropores) and by the reactor walls that act as a hard template (mesopores/macropores). These particles combine features of nanoparticles and macroscopic objects. Although similar single crystalline hierarchical zeolites have previously been prepared in much smaller, 10–40 nm, mesopores,[25] a very different reaction, steam-assisted crystallization, was employed in that case. It is therefore notable that single crystallinity is maintained through multiple sets of much larger, 350 nm pores of the 3DOM carbon reactors when hydrothermal reactions are used. A secondary population with smaller particle sizes could be introduced to existing zeolite crystals by application of a nucleation step following multiple growth steps.

Depending on their morphologies, the products from these reactions are interesting for different applications. 3DOM carbon-imprinted zeolite particles may be used as a hierarchical zeolite catalyst, and well faceted, coffin-shaped zeolite particles with average lengths less than 100 nm are suitable as seed layers for syntheses of molecular sieve membranes. The concept of scheduling nucleation and growth-dominant cycles in multistep hydrothermal reactions using confinement may also be extended to other hydrothermal reactions in future research.

4.5 References

(1) Peng, X.; Wickham, J.; Alivisatos, A. P. *J. Am. Chem. Soc.* **1998**, *120*, 5343-5344.

(2) Yin, Y.; Alivisatos, A. P. *Nature* **2005**, *437*, 664-670.

(3) Jun, Y.-W.; Choi, J.-S.; Cheon, J. *Angew. Chem. Int. Ed.* **2006**, *45*, 3414-3439.

(4) Xia, Y.; Xiong, Y.; Lim, B.; Skrabalak, S. E. *Angew. Chem. Int. Ed.* **2009**, *48*, 60-103.

(5) Tao, Y.; Kanoh, H.; Abrams, L.; Kaneko, K. *Chem. Rev.* **2006**, *106*, 896-910.

(6) Corma, A. *Chem. Rev.* **1997**, *97*, 2373-2419.

(7) Pérez-Ramírez, J.; Christensen, C. H.; Egeblad, K.; Christensen, C. H.; Groen, J. C. *Chem. Soc. Rev.* **2008**, *37*, 2530-2542.

(8) Snyder, M. A.; Tsapatsis, M. *Angew. Chem. Int. Ed.* **2007**, *46*, 7560-7573.

(9) Drews, T. O.; Tsaptsis, M. *Current Opin. Colloid Interface Sci.* **2005**, *10*, 233-238.

(10) Qiu, S.; Yu, J.; Zhu, G.; Terasaki, O.; Nozue, Y.; Pang, W.; Xu, R. *Microporous Mesoporous Mater.* **1998**, *21*, 245-251.

(11) Lethbridge, Z. A. D.; Williams, J. J.; Walton, R. I.; Evans, K. E.; Smith, C. W. *Microporous Mesoporous Mater.* **2005**, *79*, 339-352.

(12) Tosheva, L.; Valtchev, V. P. *Chem. Mater.* **2005**, *17*, 2494-2513.

(13) Schoeman, B. J.; Sterte, J.; Otterstedt, J.-E. *Zeolites* **1994**, *14*, 110-116.

(14) Yamamura, M.; Chaki, K.; Wakatsuki, T.; Okado, H. *Zeolites* **1994**, *14*, 643-649.

(15) Mintova, S.; Bein, T. *Adv. Mater.* **2001**, *13*, 1880-1883.

(16) Holland, B. T.; Abrams, L.; Stein, A. *J. Am. Chem. Soc.* **1999**, *121*, 4308-4309.

(17) Madsen, C.; Jacobsen, C. J. H. *Chem. Commun.* **1999**, 673-674.

(18) Zhang, B.; Davis, S. A.; Mendelson, N. H.; Mann, S. *Chem. Commun.* **2000**, 781-782.

(19) Schmidt, I.; Madsen, C.; Jacobsen, C. J. H. *Inorg. Chem.* **2000**, *39*, 2279-2283.

(20) Jacobsen, C. J. H.; Madsen, C.; Janssens, T. V. W.; Jakobsen, H. J.; Skibsted, J. *Microporous Mesoporous Mater.* **2000**, *39*, 393-401.

(21) Dong, A.; Wang, Y.; Tang, Y.; Zhang, Y.; Ren, N.; Gao, Z. *Adv. Mater.* **2002**, *14*, 1506-1510.

(22) Kim, S.-S.; Shah, J.; Pinnavaia, T. J. *Chem. Mater.* **2003**, *15*, 1664-1668.

(23) Chem, Z.; Li, S.; Yan, Y. *Chem. Mater.* **2005**, *17*, 2262-2266.

(24) Wang, J.; Vinu, A.; Coppens, M.-O. *J. Mater. Chem.* **2007**, *17*, 4265-4273.

(25) Fan, W.; Snyder, M. A.; Kumar, S.; Lee, P.-S.; Yoo, W. C.; McCormick, A. V.; Penn, R. L.; Stein, A.; Tsapatsis, M. *Nat. Mater.* **2008**, *7*, 984-991.

(26) Yoo, W. C.; Kumar, S.; Wang, Z.; Ergang, N. S.; Fan, W.; Karanikolos, G. N.; McCormick, A. V.; Penn, R. L.; Tsapatsis, M.; Stein, A. *Angew. Chem. Int. Ed.* **2008**, *47*, 9096-9099.

(27) Barton, J. E.; Odom, T. W. *Nano Lett.* **2004**, *4*, 1525-1528.

(28) Lai, Z.; Bonilla, G.; Diaz, I.; Nery, J. G.; Sujaoti, K.; Amat, M. A.; Kokkoli, E.; Terasaki, O.; Thompson, R. W.; Tsapatsis, M.; Vlachos, D. G. *Science* **2003**, *300*, 456-460.

(29) Yoon, K. B. *Acc. Chem. Res.* **2007**, *40*, 29-40.

(30) Choi, J.; Ghosh, S.; Lai, Z.; Tsapatsis, M. *Angew. Chem. Int. Ed.* **2006**, *45*, 1154-1158.

(31) Gouzinis, A.; Tsapatsis, M. *Chem. Mater.* **1998**, *10*, 2497-2504.

(32) Jacobsen, C. J. H.; Madsen, C.; Houzvicka, J.; Schmidt, I.; Carlsson, A. *J. Am. Chem. Soc.* **2000**, *122*, 7116-7117.

(33) Janssen, A. H.; Schmidt, I.; Jacobsen, C. J. H.; Koster, A. J.; Jong, K. P. d. *Microporous Mesoporous Mater.* **2003**, *65*, 59-75.

(34) Tao, Y.; Kanoh, H.; Kaneko, K. *J. Am. Chem. Soc.* **2003**, *125*, 6044-6045.

(35) Groen, J. C.; Bach, T.; Ziese, U.; Donk, A. M. P.-v.; de Jong, k. P.; Moulijn, J. A.; Pérez-Ramírez, J. *J. Am. Chem. Soc.* **2005**, *127*, 10792-10793.

(36) Choi, M.; Cho, H. S.; Srivastava, R.; Venkatesan, C.; Choi, D.-H.; Ryoo, R. *Nat. Mater.* **2006**, *5*, 718-723.

(37) Egeblad, K.; Christensen, C. H.; Kustova, M.; Christensen, C. H. *Chem. Mater.* **2008**, *20*, 946-960.

(38) Christensen, C. H.; Johannsen, K.; Schmidt, I.; Christensen, C. H. *J. Am. Chem. Soc.* **2003**, *125*, 13370-13371.

(39) Wang, Z.; Ergang, N. S.; Al-Daous, M. A.; Stein, A. *Chem. Mater.* **2005**, *17*, 6805-6813.

(40) Stöber, W.; Fink, A.; Bohn, E. *J. Colloid Interface Sci.* **1968**, *26*, 62-69.

(41) de Moor, P.-P. E. A.; Beelen, T. P. M.; Santen, R. A. v. *J. Phys. Chem. B* **1999**, *103*, 1639-1650.

(42) Davis, T. M.; Drews, T. O.; Ramanan, H.; He, C.; Dong, J.; Schnablegger, H.; A.Katsoulakis, M.; Kokkoli, E.; McCormick, A. V.; Penn, R. L.; Tsapatsis, M. *Nat. Mater.* **2006**, *5*, 400-408.

(43) Lee, K. T.; Lytle, J. C.; Ergang, N. S.; Oh, S. M.; Stein, A. *Adv. Funct. Mater.* **2005**, *15*, 547-556.

(44) Decher, G. *Science* **1997**, *277*, 1232-1237.

(45) Nikolakis, V.; Tsapatsis, M.; Vlachos, D. G. *Langmuir* **2003**, *19*, 4619-4626.

(46) Hamilton, B. D.; Weissbuch, I.; Lahav, M.; Hillmyer, M. A.; Ward, M. D. *J. Am. Chem. Soc.* **2009**, *131*, 2588-2596.

(47) Lee, S.; Carr, C. S.; Shantz, D. F. *Langmuir* **2005**, *21*, 12031-12036.

Chapter 5

High Performance Randomly Oriented Zeolite Membranes Using Brittle Seeds and Rapid Thermal Processing

5.1 Introduction

Intergrown zeolite films prepared by secondary hydrothermal growth of seeded layers are of great interest for size-selective, energy-efficient membrane separations, microelectronic low-dielectric devices, and ion-exchange sensors.[1-3] The task of preparing molecular sieve membranes with high fluxes and separation efficiencies has been addressed through the optimization of growth conditions to obtain preferred crystallographic orientations of zeolite films,[4-6] but this approach usually demands complex procedures.

Since Lai et al. reported a high-performance zeolite membrane in which the preferred *b*-orientation of zeolite grains (i.e., the direction of straight channels perpendicular to the plane of the membrane) was obtained through the use of crystal shape-modifying,[7,8] structure-directing agents (SDAs),[5] significant effort has been expended on fabricating oriented membranes by various approaches.[9-15] Although kinetically favorable orientations (*c*- or *hoh*-oriented MFI type zeolite membranes) can be easily achieved by manipulating the secondary growth crystallization temperature, the performance of the resulting intergrown membranes is poor due to grain boundary defects and microcracks that form during SDA removal by calcination.[16,17] Several methods have been explored to deposit oriented MFI seeds on porous supports and to subsequently grow oriented zeolite films, but none have produced zeolite films with sufficiently high permeation, for example, for xylene isomer separation, to be viable in industrial processes.[9,12,14,15,18,19] In order to improve the efficiency of membranes, it is necessary to prepare thinner membrane layers that permit higher permeate fluxes while limiting the

formation of debilitating defects and cracks during calcination to maintain high separation factors. A fundamental understanding of zeolite growth from seed particles and of defect formation during calcination would facilitate fabrication of thinner, more efficient membranes for various applications. The use of nanoparticle seeds (< 100 nm) and a small filler layer between seeds during secondary growth could be expected to limit crack propagation. Hedlund et al. reported thin, high-flux, zeolite membranes (ca. 500 nm in thickness), but size-selective properties of these MFI-type membranes were limited and separation factors for xylene isomer separation remained moderate.[20,21]

Recently, Choi et al. demonstrated that grain boundary defects could be eliminated through rapid thermal processing (RTP), a calcination technique which was postulated to strengthen grain bonding through the condensation of terminal silanol groups (Si-OH) present in zeolite grains. A dramatic improvement in *p*-/o-xylene isomer separation was realized for RTP-treated columnar *c*-oriented MFI membranes grown on porous α-alumina discs and stainless steel tubes.[22] However, because the membranes were several micrometers thick, a second (conventional or RTP) calcination step was necessary to completely eliminate SDAs.

In addition, for more practical applications of zeolite membranes in industrial processes, robust zeolite membranes are needed that can operate under high flux, pressure and temperature.[2-4,6,23,24] So far, research endeavor has focused on evaluation of intrinsic size-selective properties of zeolite membranes on porous supports (e.g., α-alumina) that are usually less practical for industrial applications.[5,16,20] An understanding of fundamental issues, e.g., crack or defect generation during calcination, different selectivity depending on crystallographic orientations of zeolite films, efficient seed layer deposition techniques with controllable orientation of seed layers and various film growth methods including secondary hydrothermal growth, provides insight for fabrication of zeolite membranes for more practical applications.[5,6,10,12-14,16-22,24-40]

In this chapter, we present a facile method to fabricate MFI zeolite membranes (zeolite membranes with 100 °C and 12 h condition) with high flux (ca. 2.6×10^{-7} mol m^{-2} s^{-1} Pa^{-1}) and high separation factors (SF, 123–139 and in one case as high as 335) for xylene isomer separation by optimizing seed deposition and calcination processes. Zeolite nanoparticles prepared by confined syntheses[41,42] were deposited as randomly

oriented seed layers on porous supports by rubbing and leveling methods to obtain zeolite films. The film thickness of zeolite films grown by secondary hydrothermal growth at 100 °C for 12 h is typically between 400-500 nm. Films grown by secondary hydrothermal growth at 175 °C for only 1 h tend to be thicker with typical thickness between 800-1000 nm. In addition, xylene isomer separation was achieved to investigate the intrinsic size-selective property of both types of zeolite films. Both types of zeolite membranes were calcined via conventional calcination and rapid thermal processing (RTP) to remove SDAs. Furthermore the influence of RTP for both film qualities was tested. RTP as a single calcination step to completely remove SDAs was applied to the zeolite films grown under low temperature conditions (100 °C for 12 h), which presented dramatically reduced processing times and energy-usage and improved the separation efficiency of the membranes. In addition, for the zeolite membrane grown on the stainless steel tube support, multiple seeding was achieved using the rubbing and leveling methods, and conventional calcination or RTP was applied to remove SDAs.

5.2 Experimental Section

5.2.1 Reagents

Tetrapropylammonium hydroxide (TPAOH, 1.0 M in H_2O), tetraethyl orthosilicate (TEOS, 98 %) and polyethyleneimine (PEI, branched) were purchased from Aldrich. Deionized water with a resistivity of 18.2 MΩ-cm was used for all reactions.

5.2.2 Preparation of seed particles

The preparation of the polycrystalline spherical silicalite-1 aggregates followed the same synthetic process introduced in Chapter 4. Using a precursor solution of the composition 10 SiO_2/2.4 TPAOH/0.87 NaOH/114 H_2O, polycrystalline spherical silicalite-1 with ca. 300 nm in size was produced inside a 3DOM carbon reactor after five infiltration/hydrothermal treatment cycles.[42] The 3DOM/zeolite composite was treated with concentrated nitric acid for 10 min at 130 ˚C and washed with DI water several times and dried at 100 °C for overnight. The 3DOM carbon was removed by combustion with a heating rate of 1 °C/min up to 550 °C where it was maintained for 6 h and cooled

down at a rate of 1 °C/min to room temperature in oxygen atmosphere to isolate the zeolitic material. The polycrystalline aggregate monolith was sonicated in ethanol for 2–3 days to break the connections between particles. Monodisperse spherical silicalite-1 aggregates were isolated by centrifugation and then dried before being used as seed particles.

5.2.3 Seed deposition (rubbing and leveling methods)

A rubbing method was applied to deposit zeolite seed particles on a home-made, 22-mm diameter, porous α-alumina support.[9,43] A 10 wt% solution of polyethyleneimine (PEI, branched, Aldrich) in ethanol was spin-coated on the support at 3000 rpm for 30 s. A small amount of zeolite particles (usually less than 5 mg) was rubbed onto the support for 1 min, using a latex glove. Subsequently, the seed layer was leveled on a rigid and flat substrate while applying a circularly traversing downward force on the support with the gloved finger for 5 s. The PEI layer was removed by calcination at 450 ˚C for 3 h under flowing air.

5.2.4 Zeolite membrane growth (secondary hydrothermal growth)

To fill the spaces between seed particles, the seed layer was exposed to secondary hydrothermal growth. The support coated with the seed layer was aligned vertically in a 25-mL Teflon-lined autoclave and immersed in a precursor for secondary hydrothermal growth (composition 40 SiO_2/9 TPAOH/9500 H_2O or 0.6 g TEOS/0.67 g TPAOH/12.1 g H_2O; aged for one day). The hydrothermal reactions were conducted at 100 ˚C for 12 h and 175 C for 1 h. The zeolite membranes on the stainless steel tube support (Pall Corp.) were fabricated using the rubbing and leveling methods. For the multiple seeding method, seed particles produced by confined synthesis were used and rubbed on the support several times, followed by leveling to cover the larger pores (1-10 μm). For two-step seeding method, big MFI crystals (5-6 μm) were firstly used as a seed layer and then polycrystalline aggregates were used as another seed layer on the first seed layer. The hydrothermal reactions were conducted at 175 ˚C for 4 h. The resulting zeolite films were rinsed several times with deionized water.

SDA molecules were removed either by conventional calcination (CC) or by rapid thermal processing (RTP). CC was performed with a heating rate of 1 ˚C /min to 480 ˚C, maintaining that temperature for 6 h and cooling down to room temperature at a rate of 1 ˚C /min. For RTP treatment, an infrared chamber (E4-10 from Research Inc.) controlled by a Eurotherm temperature controller (Model 2404) was used to heat the supported membranes with a nominal heating rate of 700 ˚C /min, holding at 700 ˚C for 60 s and cooling down to room temperature by water circulation at a nominal cooling rate of 700 ˚C/min using a water-to-air heat exchanger (C100-1 from Research Inc.).

5.2.5 Permeation test

The xylene isomer vapor experiments were conducted in Wicke-Kallenbach mode with a stainless steel permeation cell, using an equimolar *p*-xylene/*o*-xylene feed as previously reported (Figure 5.1).[9,17] The equilibration time at each temperature (25 ˚C to 250 ˚C) was at least four hours. On-line sampling of the permeate stream composition was carried out with an HP 5890 gas chromatograph equipped with a flame ionization detector (FID) and an Alltech, EconoCap EC-WAX capillary column for xylene isomer detection. The permeation fluxes of the xylene isomer were estimated by the molar fraction at the time of sampling, the helium sweep stream volumetric flow-rate and the available membrane area in the stainless steel permeation cell. The separation factors were defined as the ratio of the aforementioned fluxes.

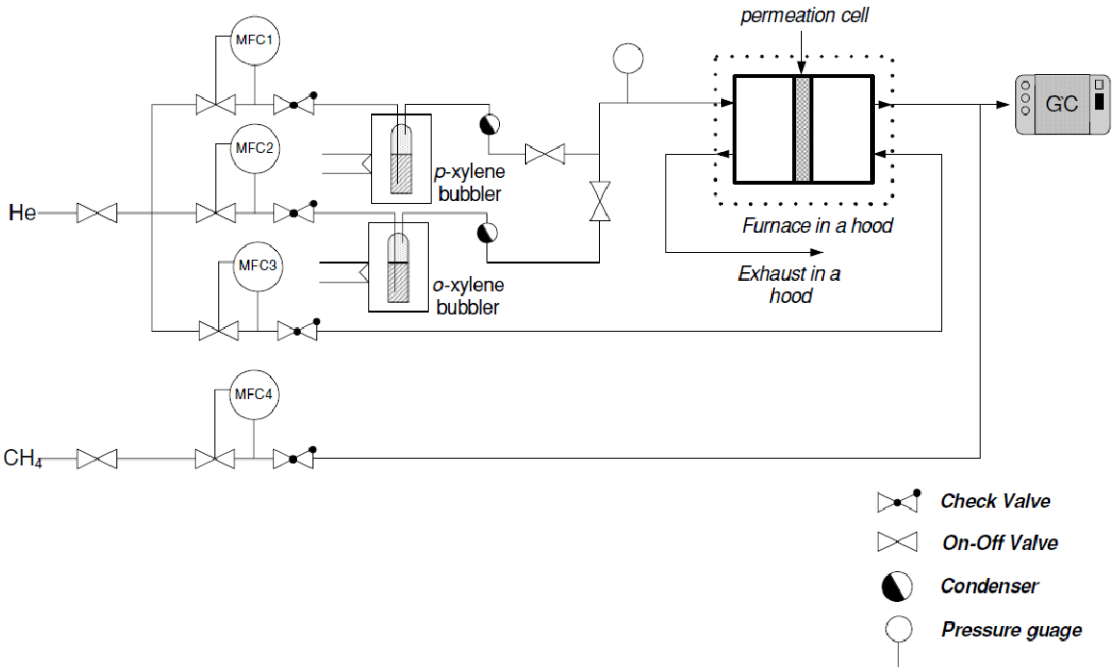

Figure 5.1 Permeation setup for xylene isomer separation.[9]

5.2.6 Characterization

Membranes (zeolite membranes grown on the porous alumina supports) were characterized by scanning electron microscopy (SEM) with a JEOL 6700 microscope operating at an accelerating voltage of 5 kV and an applied current of 20 mA. The images of zeolite membrane grown on the porous alumina supports were obtained with samples coated with 5 nm of Pt. The zeolite membranes on the stainless steel tubes were characterized by a JEOL 6500 SEM at an accelerating voltage of kV and an applied current of 200 μA, and without coating. X-ray photoelectron spectroscopy (XPS) was acquired for analyzing the surface of zeolite membranes. A hemispherical sector electron energy analyzer and a resistive anode detector equipped SSX-100 system of Surface Science Lab. Inc. was used with a monochromated Al K_α X-ray source with a spot size of 1 mm. Elemental analyses were carried out for a precursor solution including a bare α-alumina support on a Thermo Scientific iCAP 6500 duo view ICP-OES (inductively coupled plasma optical emission spectrometer). The XRD patterns were acquired using a

PANalytical X-Pert PRO MPD X-ray diffractometer equipped with a Co source (Co-Kα, λ= 1.790 Å) and an X-Celerator detector, which was used for all samples except the Figure 5.5. The XRD pattern in the Figure 5.6 was acquired using a Bruker-AXS D5005 diffractometer with a 2.2 kW sealed Cu source (Cu-Kα, λ= 1.544 Å).

5.3 Results and Discussion

5.3.1 Zeolite membranes on α-alumina supports (100 °C for 12 h)

The facile fabrication of zeolite membranes exhibiting high flux and high separation efficiency is described using zeolite nanocrystal seed particles with well-controlled morphology obtained by confined synthesis (Figure 5.2). Polycrystalline spherical aggregates (ca. 300 nm in diameter, Figure 5.3) of zeolite seeds were directly deposited on home-made porous α-alumina supports using a rubbing method.[43] The seed particles were broken down into smaller grains (50–100 nm in diameter) and deposited in the pores of the support by the applied rubbing process. Subsequently, unbroken polycrystalline aggregates remaining on the support were pushed down deeper into the pores of the support or broken down further by a leveling process. This seed-deposition process could be completed in approximately one minute compared to conventional multi-step seeding methods that usually require several hours. Starting with the resulting high-quality seed layer, thin zeolite membranes (400–500 nm) were grown hydrothermally (100 °C for 12 h) with good reproducibility. With such thin membranes, SDA removal to open the MFI pores was possible by a single RTP step that was completed in minutes, eliminating the need for slower and more energy-intensive, conventional calcination. As shown below, the RTP step also improved the performance of the zeolite membranes.

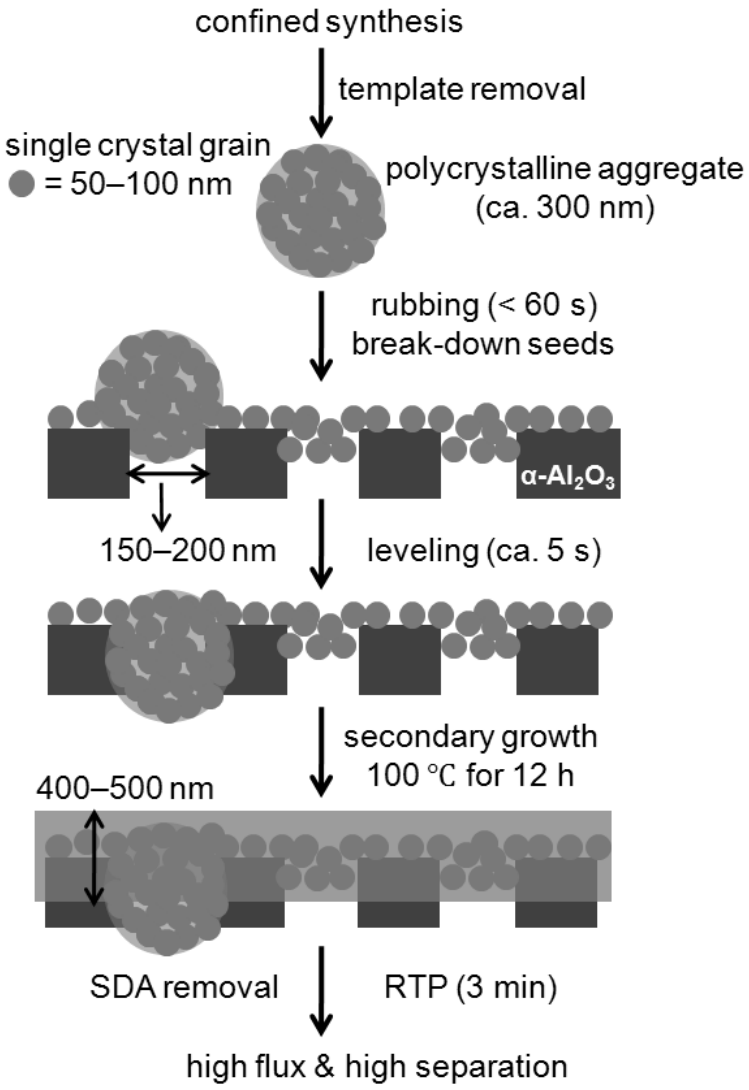

Figure 5.2 Fabricating the high-performance zeolite membrane. Polycrystalline spherical aggregates of silicalite-1 (300 nm in diameter) were prepared by confined synthesis in 3DOM carbon[42]. These aggregates were broken down into single crystal grains (50–100 nm) by rubbing them directly onto a home-made α-alumina support to form a seed layer. Any remaining aggregates were either pushed down deeper into pores of the support or broken down further by a leveling process. The high-quality seed layer was used to prepare well-intergrown and very thin (400–500 nm) zeolite membranes with appropriate secondary growth conditions. The thin zeolite membranes were thermally treated to remove SDA molecules by conventional calcination (CC) or a rapid thermal processing (RTP) step.

Confined syntheses have been of great interest for producing hierarchical zeolite catalysts and shape- and size-controlled seed particles for membrane applications.[41,42,44-51] 3DOM carbon with interconnected pores was used to elucidate the mechanism of zeolite nanocrystal growth in confinement.[41,42] The growth patterns and the development of zeolite nanocrystal shapes in the confinement were described in chapter 4. For use of these polycrystalline particles, the isolation of the zeolites from the 3DOM carbon was achieved by calcination, which resulted in concurrent removal of the SDAs (Figure 5.3a). For this step, oxidation of the 3DOM carbon/zeolite composite by treatment with nitric acid prior to calcination facilitated a more complete removal of the carbon phase, providing suitable seed particles for deposition on a porous support.

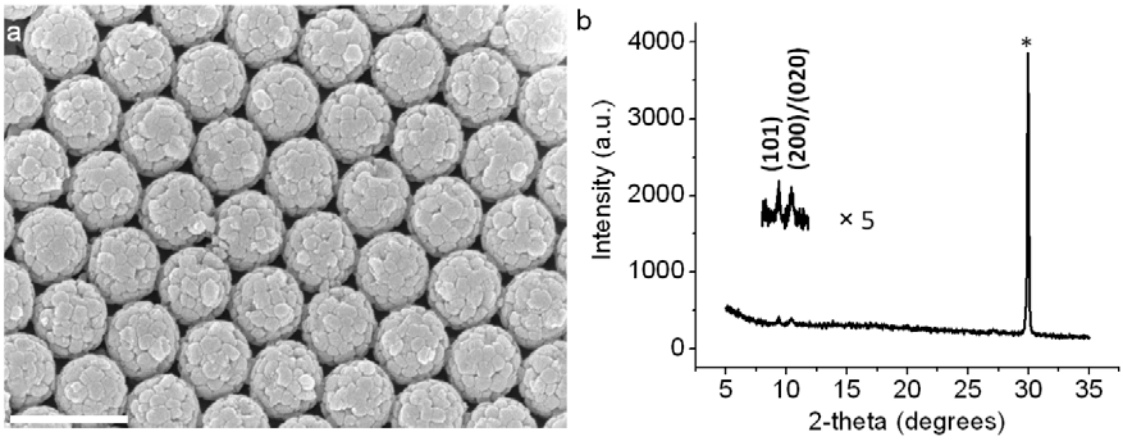

Figure 5.3 SEM image of polycrystalline spherical aggregates produced by five IHT cycles (a) and XRD patterns of a seed layer prepared by the rubbing and leveling methods on the porous alumina disc after removal of a PEI layer (b). The two indexed peaks in the right image (b) are characteristic for silicalite-1. The scale bar in (a) is 500 nm and the reflection peak marked with an asterisk (*) originates from the α-alumina support (b).

Yoon and co-workers reported that simply rubbing zeolite particles on large areas of smooth supports produced high-quality monolayers suitable as seed layers for membrane fabrication.[43,52] If the interaction between the support and an initial particle layer is stronger than the interaction between the first layer and subsequent layers,

rubbing of the particles on the support removes excess material and yields a high-quality monolayer. This rubbing method was applied to deposit the zeolite seed particles produced in the confined synthesis. To enhance the interaction between the first layer and the support, polyethyleneimine (PEI, 10 wt% in ethanol) was spin-coated on the α-alumina support (3000 rpm for 30 s) to provide a more hydrophilic surface. Polycrystalline aggregate spheres were directly rubbed on the α-alumina support. During rubbing, the polycrystalline aggregates broke down into individual silicalite-1 grains which entered the pores of the support as a consequence of the applied rubbing pressure (Figure 5.4a and b). During this process the silicalite-1 structure was retained as illustrated in the XRD pattern of the seed layer in Figure 5.3b. However, alteration of the surface structure cannot be excluded. The 50–100 nm-sized zeolite grains fit easily into the 150–200 nm pores at the top layer of the α-alumina support. Due to the sticky PEI layer and the tortuosity of the pores in the support, the seed particles did not enter deeper into the support (not shown here). A mesoporous silica interlayer, which was previously reported to smoothen the support for seed deposition[5,6,9,12,16,17,22], was not needed.

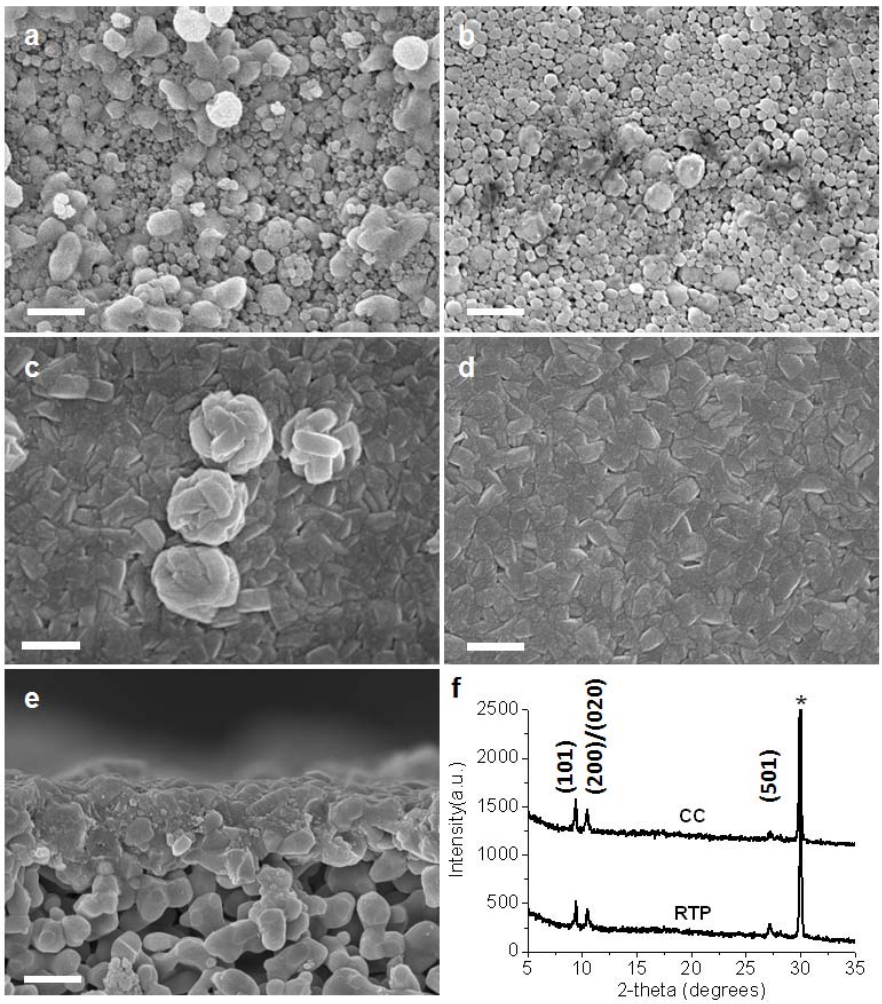

Figure 5.4 Development of the membrane. a-e, SEM images of seed layers and silicalite-1 seeded membranes on a porous α-alumina support at various stages of the fabrication process. **a,** Top view of a seed layer after the rubbing step and **b,** after rubbing and leveling. After secondary hydrothermal growth, intergrown MFI-zeolite layers are formed. **c,** In membranes prepared without leveling (denoted as R-membranes), several protrusions remain after secondary growth, but **d,** they are not prominent in membranes grown from the leveled seed layers shown in **b** (denoted as RL-membranes). **e,** The cross-sectional view of the RL-membrane after secondary growth shows an ultrathin MFI-zeolite layer on top of the α-alumina support. All scale bars correspond to 500 nm. **f,** X-ray diffraction patterns of zeolite films treated by conventional calcination (CC) and rapid thermal processing (RTP). The reflection peak marked with an asterisk (*) originates from the α-alumina support.

While many of the polycrystalline sphere aggregates had broken up into individual grains after the rubbing procedure, numerous unbroken aggregates remained on the support (Figures 5.4a and 5.5a). In order to obtain a more uniform seed layer, the remaining aggregates were pushed down deeper into the pores of the support by a separate leveling process, which could also break down the aggregates further. A gentle circular force was applied to the seed layer on a flat and rigid substrate, rendering the surface of the seed layer smoother in a time frame of less than 5 s (Figures 5.4b and 5.5b). This simple leveling process successfully reduced the surface roughness and improved the uniformity of the membrane thickness.

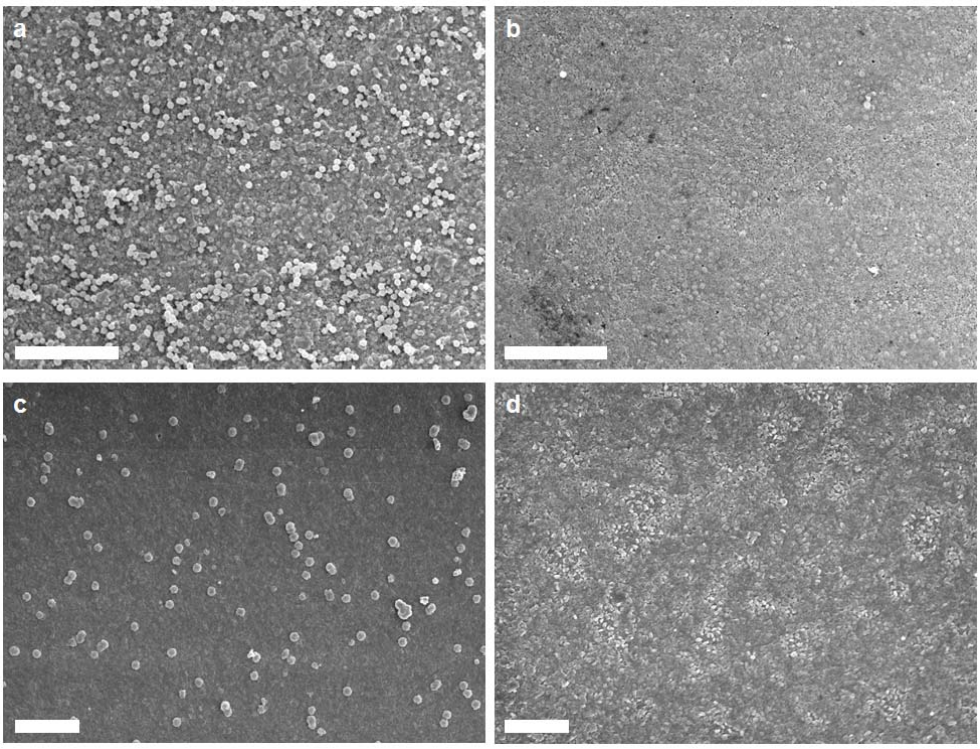

Figure 5.5 Development of the membrane. Low magnification SEM images of seed layers (**a** and **b**) and zeolite membranes after secondary growth (**c** and **d**). **a,** The seed layer prepared by the rubbing process. **b,** The seed layer after rubbing and leveling processes. **c,** The zeolite membrane (R-membrane) prepared from **a** via secondary growth shows numerous protrusions. **d,** Most of these are absent in the zeolite membrane prepared from **b** after secondary growth (RL-membrane). The scale bar corresponds to 5 μm in all images.

Interstitial spaces between seeds were closed by immersing the coated membranes in a nutrient solution that promotes further zeolite growth during a secondary hydrothermal reaction. Preferential film orientations influence the permeation of molecules through the membrane and depend on the specific conditions of the hydrothermal reaction. The *c*-orientation is favored by high temperature hydrothermal treatment (e.g., 175 ˚C), whereas *hoh*-out-of-plane orientations are preferentially obtained at lower temperatures (e.g., 100 ˚C)[16,17,27,53]. In this section, lower temperature treatments at 100 ˚C for 12 h were used to minimize the zeolite film thickness. Figure 5.4 shows SEM images of samples obtained after secondary growth, starting with seed layers prepared by (denoted as R-membrane, Figure 5.4c) or rubbing and leveling (denoted as RL-membrane, Figure 5.4d). In both cases, fully intergrown zeolite films were generated after secondary growth, typically 400–500 nm thick (Figure Figure 5.4e), which corresponds to some of the thinnest zeolite membranes reported so far.[20,21] The surface morphologies, however, differed for the two membranes. The R-membrane shows several surface protrusions in addition to a well-intergrown surface layer comprised of small grains several hundred nanometers in dimensions (Figures 5.4c and 5.5c). The protrusions originate from polycrystalline sphere aggregates that remained on the support after the rubbing procedure and grew only slightly bigger during secondary hydrothermal growth, from ca. 300 nm to ca. 500 nm. As indicated from permeation measurements (see below), the surface roughness in these zeolite films generated more stress-induced grain boundary defects during subsequent thermal treatment. On the other hand, SEM images of the RL-membrane prepared from the higher-quality seed layer reveal a more uniform surface, albeit with similar grain sizes as found in the R-membrane (Figures 5.4d and 5.5d).

Both types of membranes were thermally treated to remove SDAs by conventional calcination (CC, heated at 1 ˚C /min to 480 ˚C, held for 6 h and cooled at 1 ˚C/min to room temperature). The X-ray diffraction (XRD) patterns of the products revealed a characteristic MFI-type diffraction pattern, but there was no evidence for a preferred crystallographic orientation (Figure 5.4f). However, when the secondary growth time was extended, e.g. to 20 h, keeping other conditions the same, patterns characteristic for preferred *hoh*-orientation appeared (Figure 5.6), consistent with previous reports

involving secondary growth at relatively low temperatures (ca. 90–140 ˚C).[5,16,17,27,53] In addition, rapid thermal processing (RTP, heating at 700 °C/min to 700 °C and holding for 60 s) was evaluated as a method to remove SDA molecules occluded in the porous MFI crystals. In an initial report, RTP was considered as a pre-treatment step before conventional calcination in order to strengthen grain boundaries via condensation of terminal Si-OH groups located at the grain boundaries.[22] This pre-treatment changed the nature of defect/crack formation to lateral propagation instead of vertical propagation from the surface of the membrane to its support.[22] The MFI membranes studied by Choi et al. required a subsequent conventional or RTP calcination step to completely open the pore structure in RTP-treated zeolite membranes.[22] However, because the membranes described herein are an order of magnitude thinner, complete pore opening of the membranes was possible by using only one RTP treatment without any additional calcination. The XRD pattern of the product showed that membranes that had undergone only RTP treatment were structurally equivalent to those obtained by conventional calcination (Figure 5.4f).

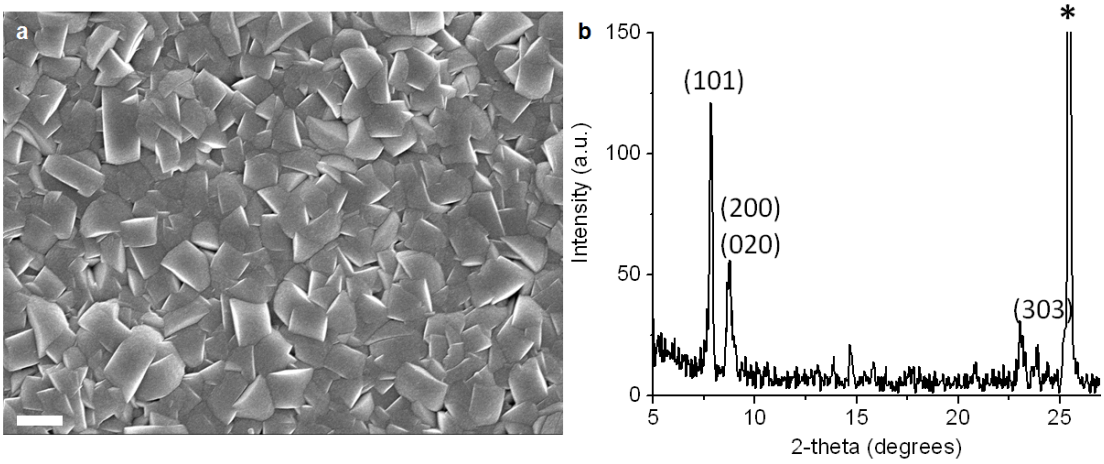

Figure 5.6 MFI-zeolite membrane prepared by extended secondary hydrothermal growth (100 ˚C for 20 h). **a,** An SEM image showing a top view of the membrane after calcination. The scale bar corresponds to 1 μm. **b,** The XRD pattern shows features characteristic for preferred *hoh*-out-of-plane orientation of the crystallites. The asterisk marks a reflection originating from the α-alumina support.

To evaluate the membrane quality, permeation measurements involving the separation of *p*-xylene/*o*-xylene isomers were conducted. These measurements are based on the intrinsic capability of zeolite membranes for size-selective molecular separations. Separation factors (SF) improved significantly if a leveling step was employed during the membrane fabrication and if SDAs were removed by RTP rather than conventional calcination. As shown in Figures 5.4d and 5.5d, leveling leads to smoother seed layers, which favor the formation of smoother, highly intergrown films, while in the absence of leveling, overgrowths, like the ones shown in Figures 5.4c and 5.5c, are common. Such overgrowths have been associated with poor separation performance in the past, either because of poor intergrowth or due to stress-induced defects formed during calcinations.[25] RTP-treated R-membranes exhibited increased separation factors (ca. 17) compared to ca. 8 for CC-treated R-membranes (Figure 5.7a and b). Furthermore, RTP-treated RL-membranes exhibited separation factors in the range from 123 to 139 and in one case as high as 335, compared to CC-treated RL-membranes with SF values of ca. 28 (Figure 5.7c and d). Separation factors of more than 100 for the separation of *p*-/*o*-xylene isomers have rarely been reported for such thin films.[19-21,54] In addition, all membranes generally permitted very high fluxes of *p*-xylene due to the reduced membrane thickness. For example, the permeation flux of *p*-xylene through RTP-treated RL-membranes was ca. 2.6×10^{-7} mol m^{-2} s^{-1} Pa^{-1} (Figure 5.7d), with a limiting permeation flux of ca. 4.0×10^{-7} mol m^{-2} s^{-1} Pa^{-1} imposed by the home-made α-alumina support. Among zeolite membranes with SF values higher than 100, a permeation flux of *p*-xylene as high as 2.6×10^{-7} mol m^{-2} s^{-1} Pa^{-1} is rarely achieved (Table 5.1). Although these data indicate a high quality membrane and the absence of significant contributions to permeation by defects, there are still issues regarding the practical use of such membranes at the industrially relevant high pressure of xylenes and high temperatures, as indicated by the findings of reference of 21.

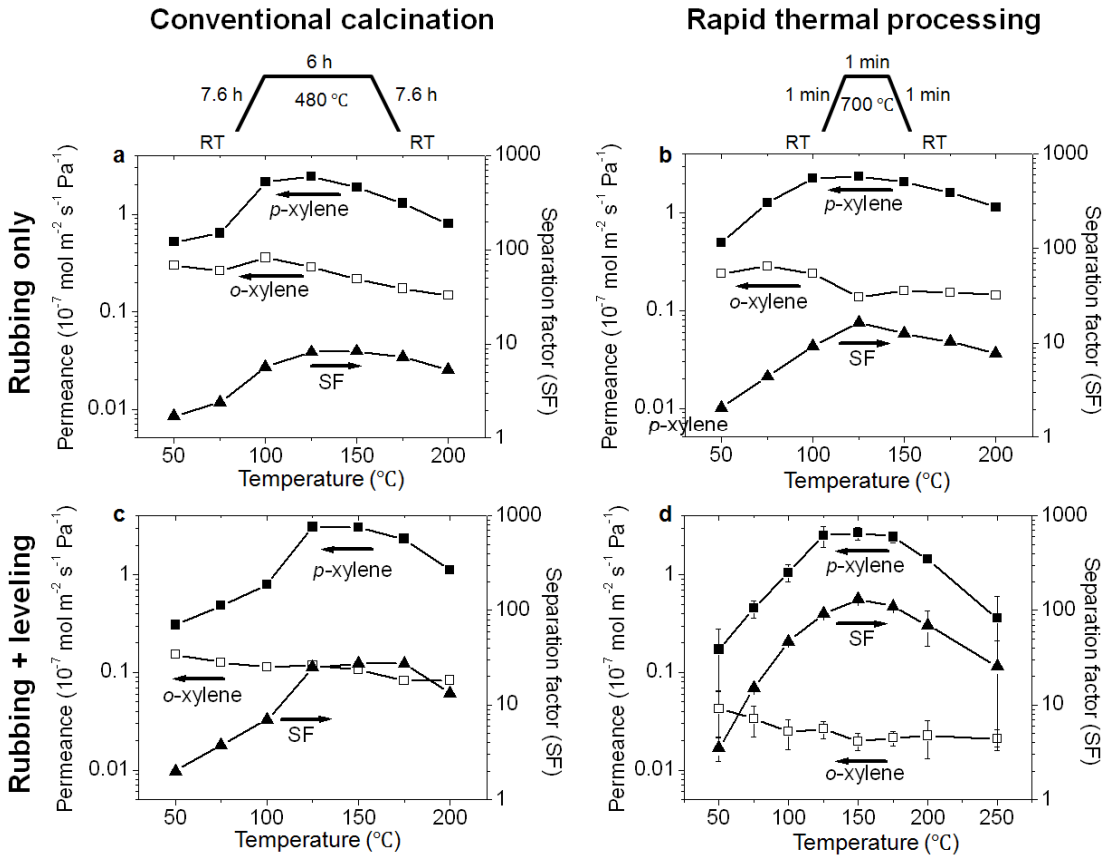

Figure 5.7 Permeation data and *p*-/*o*-xylene separation factors for nanocrystal-seeded membranes thermally-treated by conventional calcination or rapid thermal processing. Graphs **a** and **b** correspond to R-membranes prepared without a leveling step and thermally treated by CC and RTP, respectively. Graphs **c** and **d** correspond to RL-membranes from preparations in which a leveling step was used and membranes were thermally treated by CC and RTP, respectively. Data points and error bars in graph **d** correspond to the three RL-membranes with separation factors in the range from 123 to 139.

Table 5.1 Comparison of xylene isomer separation factors, permeation data and membrane structure for MFI-zeolite membranes from the present work and from select references.

	calcination type	separation factor (SF)[c]	permeance (10^{-7} mol m^{-2} s^{-1} Pa^{-1})	thickness (μm)	orientation	temperature (°C) [d]
R-membrane[a]	CC	ca. 8	ca. 2.0	0.4–0.5	random/*hoh*	150
	RTP	ca. 17	ca. 2.4	0.4–0.5	random/*hoh*	125
RL-membrane[b]	CC	ca. 28	ca. 3.0	0.4–0.5	random/*hoh*	150-175
	RTP	123–139, 335	2.6±0.4	0.4–0.5	random/*hoh*	150
ref.[22]	RTP + CC	126	0.48	ca. 10	*c*	125
ref.[5]	CC	483	1.96	2	*b*	200
ref.[21]	CC	3	6.0	0.5	random	100

[a] Membranes denoted as R-membrane were fabricated using a seed layer deposited on the α-alumina support by the rubbing method.
[b] Membranes denoted as RL-membrane were fabricated using a seed layer deposited on the α-alumina support by the rubbing and leveling methods. 123–139 is the range found for three membranes and 335 is the value for the highest performing membrane that was synthesized, all using the same conditions.
[c] The separation factor is defined as the ratio of the permeances of *p*-xylene/*o*-xylene that passed through the membrane.
[d] This temperature corresponds to the temperature at which the highest separation factor was obtained (SF value shown).

The thermal stability of RTP-treated RL-membrane was tested (Figure 5.8). After saturation the membrane with xylene vapor at 100 °C for 12 h, the temperature was increased to 175 °C and thermal stability of the membrane was performed. After 3 h, SF was ca. 87 with *p*-xylene flux of 1.5×10^{-7} mol m^2 s^{-1} Pa^{-1}. The SF value was increased to ca. 110 after 5 h of permeation test with *p*-xylene flux of 1.0×10^{-7} mol m^2 s^{-1} Pa^{-1}. However, 12 h later from the starting point, the flux was rapidly decreased, causing the decrease of the SF. Then, the decreasing slopes of the SF and *p*-xylene flux were stiffer after 12 h, and eventually the separation ability of the zeolite membrane was finished after 24 h of permeation test. This suggests that coke formation catalyzed by aluminum content in the support blocks the micropores of the zeolite membranes.

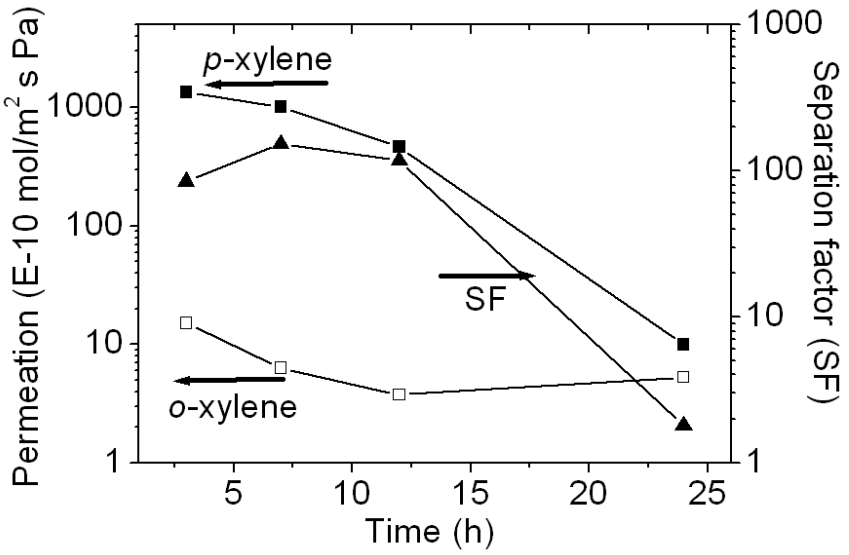

Figure 5.8 Thermal stability test of RTP-treated RL-membrane. The zeolite membrane was maintained at 100 °C for 12 h to fully adsorb xylene vapor. The stability test was profiled at 175 °C. The x-axis presents the permeation test time at 175 °C after staying at 100 °C for 12 h.

To identify Al leaching from the support during secondary growth hydrothermal reaction, XPS data was acquired (Figure 5.9). In the XPS data, Al (oxidation state is +3) was definitely identified. Triplicate runs using a beam spot size of 1 mm were performed and all results indicated that the surface of the zeolite membrane contained Al within the probe depth of 10 nm.

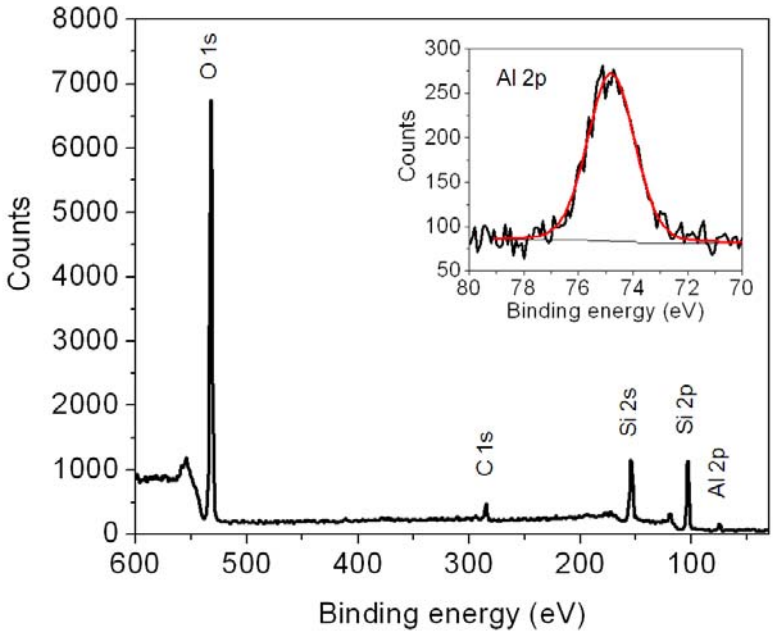

Figure 5.9 X-ray photoelectron spectra. Al on the surface of the RTP treated RL-membrane was identified.

In attempt to identify Al leaching from secondary hydrothermal growth, elemental analysis using ICP was performed. The Teflon-lined autoclave containing a precursor solution with α-alumina support was placed in the oven at 100 °C for 12 h, which corresponds to the same synthetic conditions as for the fabrication of the RTP-treated RL-membrane except for the seed layer on the support. The Al content was determined by ICP, yielding a Si/Al ratio of ca. 1300. The Si/Al ratio is very large, but such a small portion of Al content inside the zeolite membrane could contribute to coke formation.

5.3.2 Zeolite membranes on α-alumina supports (175 °C for 1 h)

Zeolite membranes were also fabricated using different conditions (175 °C for 1 h) during secondary hydrothermal growth. Zeolite membranes with the kinetically preferred orientation (*c*-orientation) of MFI crystals are expected if the crystals are grown from a randomly oriented seed layer at the higher temperature hydrothaml reaction. Rubbing and leveling methods were implemented to deposit continuous and smooth seed particles on the porous α-alumina support without a mesoporous silica layer in between the seed

particles and the support. Because of the higher temperature during secondary hydrothermal growth, faster crystal growth was observed. After 50 min of hydrothermal reaction, a zeolite membrane with a smooth surface was observed by SEM (not shown here). However, there was no selective permeation for xylene isomer, which suggests a possibility of unfilled voids in between crystal grains. On the other hand, after 1 h hydrothermal reaction, the zeolite film was fully developed (Figure 5.9) and a permeation test was performed.

According to the SEM image in Figure 5.10, the surface to the zeolite membrane is well covered with columnar crystals (a) and the thickness was usually 800-1000 nm. According to XRD measurements, this MFI film does not exhibit significant preferred orientation (Figure 5.11). It is likely that the secondary growth time was too short to permit growth of *c*-oriented crystals. However, at high temperature with sufficient secondary growth time, *c*-oriented growth from randomly oriented seed layer has been well known and described by the van der Drift's theory that is about the dominancy of the faster growth direction (*c*-axis for MFI).[16] For example, the same reaction condition with prolonged reaction time, such as 12 h, c-oriented preference was observed byXRD (not shown here).

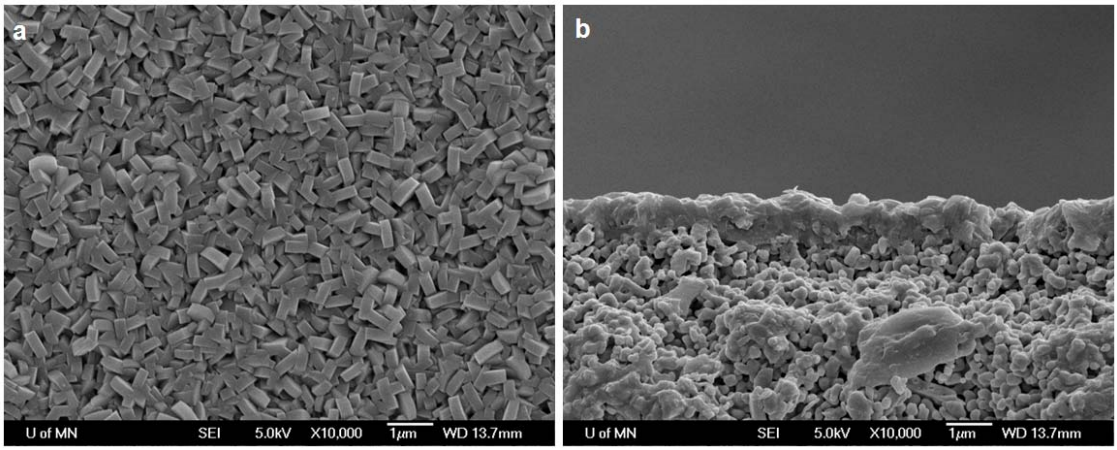

Figure 5.10 SEM images of the RL-membrane prepared at 175 °C for 1h hydrothermal reaction and after conventional calcination to remove SDAs: (a) The plain view of the zeolite membrane. (b) The cross-sectional view of the zeolite membrane.

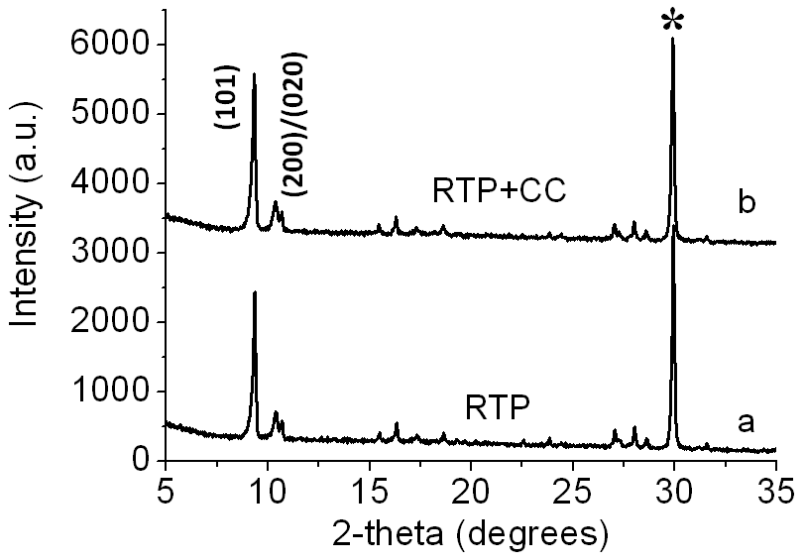

Figure 5.11 XRD patterns of the RL-membrane prepared at 175 °C for 1h hydrothermal reaction: (a) after RTP treatment (b) after RTP and conventional calcination (CC) treatment.

After RTP treatment to remove SDAs from the zeolite membrane, MFI zeolite type patterns were observed (Figure 5.11a). However, there was no separation of xylene isomer. Therefore, we subsequently performed conventional calcination (CC) after RTP treatment. A ca. 10 % increase in intensities of X-ray reflection peaks was observed from the RTP-treated membrane (Figure 5.10b). This suggests that RTP condition (heating rate of 700 °C/min, 1 min at 700 °C, and cooling rate of 700 °C/min) was not enough to completely remove SDAs from the 800-1000 nm thick zeolite membranes.

Xylene isomer separation was performed using two different zeolite membranes: a CC-treated RL-membrane (Figure 5.12a) and a RTP-CC-treated RL-membrane (Figure 5.12b). For the CC-treated RL-membrane, a separation factor of ca. 3.5 was observed, a typical value for *c*-oriented MFI membranes.[16,17,25] On the other hand, the RTP-CC-treated RL-membrane presents a separation factor of ca. 42. The increase of SF from the RTP-CC-treated RL-membrane also supports the idea that RTP treatment improves the quality of zeolite membranes by strengthening grain boundaries.

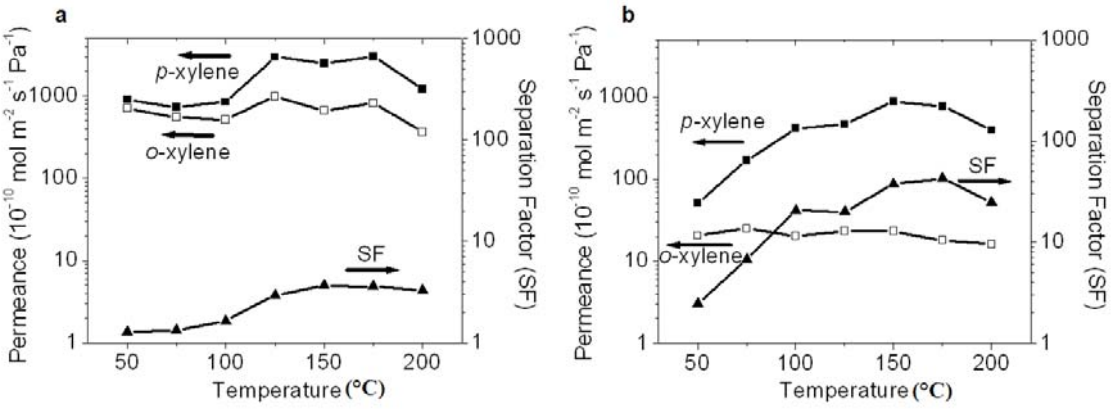

Figure 5.12 Permeation data and *p*-/*o*-xylene separation factors for a CC-treated RL-membrane (a) and a RTP-CC-treated RL-membrane (b).

5.3.3 Zeolite membranes on stainless steel tube supports

As alternatives for conventional separation processes, such as distillation and crystallization, zeolite membranes should satisfy the industrial demands, e.g., physical and chemical robustness under high temperatures and pressures.[2,3,6,23,24] So far, much effort has focused on evaluating the intrinsic size-selective properties of zeolite membranes that have been usually fabricated on the less practical porous supports, e.g., porous alumina support.[2,5,6,9,14,17,21,22,24] Therefore, the need of practical zeolite membranes has been addressed, which should combine the technical know-how from the aforementioned pilot systems. In the initial step to design practical zeolite membranes, the use of a robust support should be accomplished. For example, stainless steel tubes with 1-10 μm pores and with capability to connect metallic tubing, gauges and valves can be good candidates for industrial demands. However, huge differences of thermal expansion coefficients of zeolite films and the support, and lack of methods to deposit seed layer on such a large pore have limited the use of stainless steel tubes as zeolite membrane supports. For example, because one cannot form a continuous mesoporous silica layer on the very large pores of stainless steel tubes, the advantage of use of large pores that increases maximum flux of system cannot be established.

According to our previous experience, the rubbing method was applied to directly deposit seed particles onto the porous support. A PEI polymer layer was used to prevent particle layers from disloading from the supports. Inspired by our previous experience, we employed the rubbing and leveling methods to directly deposit small zeolite crystals (compared to the pores of the stainless steel tube) on the stainless steel tube support after dip coating of a PEI polymer layer in between the particles and the support (Figure 5.13). Two different strategies were implemented: multiple deposition of polycrystalline aggregates (called multiple-seeding method, Figure 5.14a) and a two-step approach in which big MFI crystals are covered on the support and then polycrystalline aggregates are deposited as a second layer (called two-step seeding method, Figure 5.14b). After seeding, secondary hydrothermal reactions were performed. RTP and CC were also applied to remove SDAs.

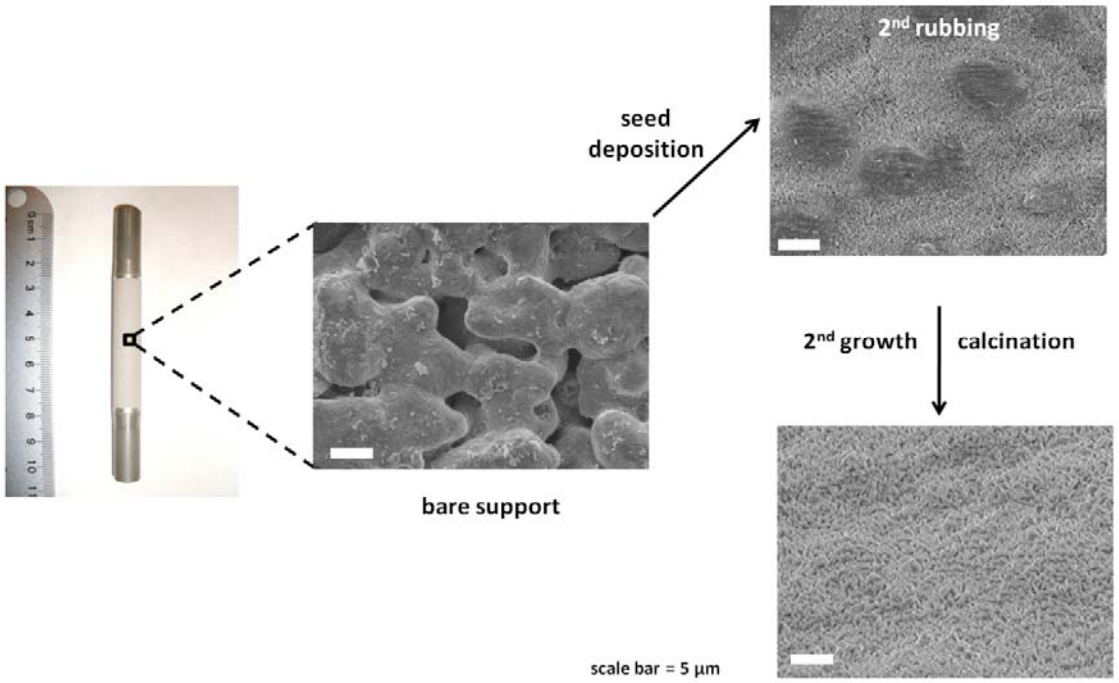

Figure 5.13 Schematic illustration of zeolite membrane fabrication on the stainless steel tube. After two times of seed deposition of polycrystalline aggregates (right top), secondary hydrothermal growth was performed and the zeolite membrane was calcined by conventional calcination (right bottom).

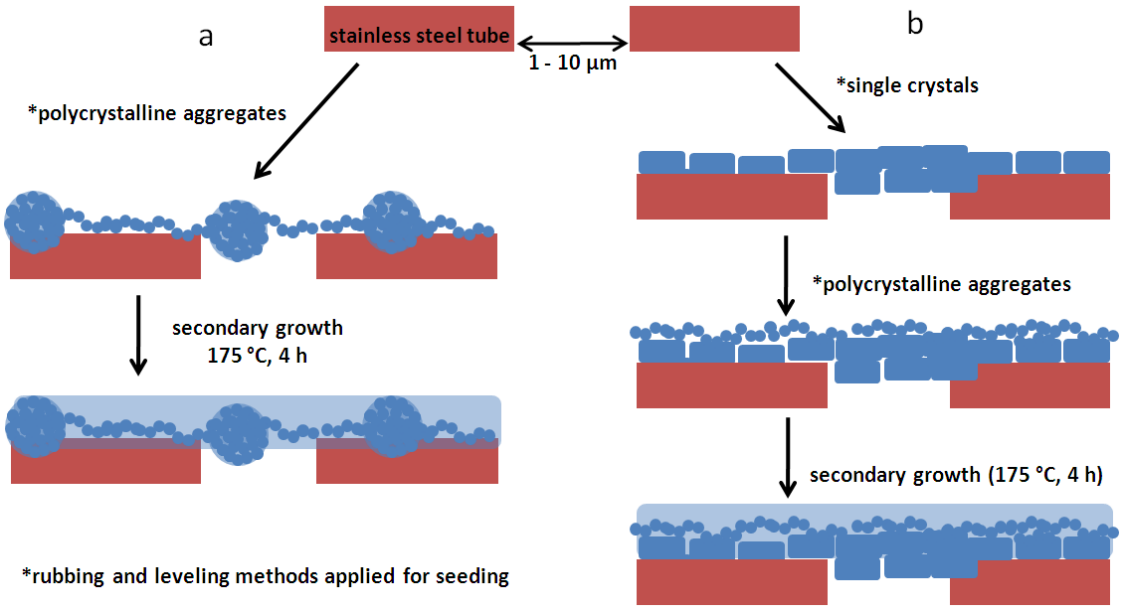

Figure 5.14 Two different strategies to fabricate zeolite membranes on the stainless steel tube support: (a) multiple-seeding of polycrystalline aggregates by the rubbing and leveling methods, and secondary growth for filling in the spaces between seed particles, and (b) deposition of big MFI crystals on the support and subsequent seeding of polycrystalline aggregates on the first seed layer, and secondary growth followed for zeolite membrane fabrication.

For the multiple-seeding method, 2-3 times of seeding of polycrystalline aggregates were applied to cover the support (Figure 5.15b). Each step was followed by a leveling step to produce a smooth top layer for the next rubbing process. After multiple applications of seed particles, secondary hydrothermal growth (175 °C for 4 h) was performed. For removing SDAs, conventional calcination (Figure 5.15c) and RTP treatment (Figure 5.15d) were carried out. According to SEM images (Figure 5.15c and d), the zeolite films do not form cracks during calcination.

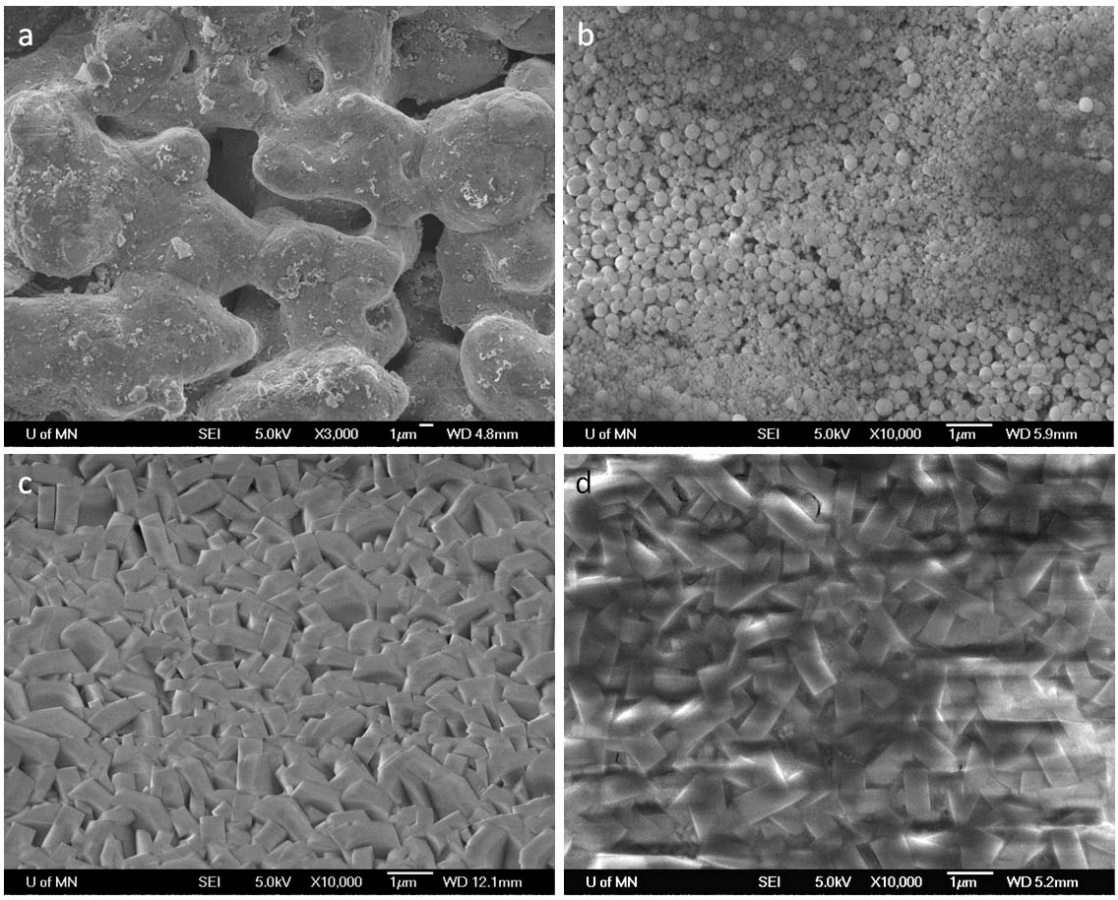

Figure 5.15 SEM images of the surface of the stainless steel tube (a), a seed layer after multiple-seeding of polycrystalline aggregates by the rubbing and leveling methods (b), the surface of zeolite membrane after CC treatment (c), and the zeolite membrane after RTP treatment (d). The PEI polymer layer was removed by calcination (450 °C for 3 h) after each deposition process. SEM measurements were accomplished without coating for all samples.

For the two-step seeding method, big MFI crystals (5-6 μm long) were first used to cover the support (Figure 5.16a). On the first layer, polycrystalline aggregates were deposited multiple times to fully cover the surface (Figure 5.16b). Each step was followed by a leveling step to produce a smooth top layer for the next rubbing process. After employing the two-step seeding method, secondary hydrothermal growth (175 °C for 4 h) was performed. SDAs were removed by CC (Figure 5.16c) and RTP treatments

(Figure 5.16d). According to SEM images (Figure 5.16c and d), no cracks formed on the zeolite membranes after calcination.

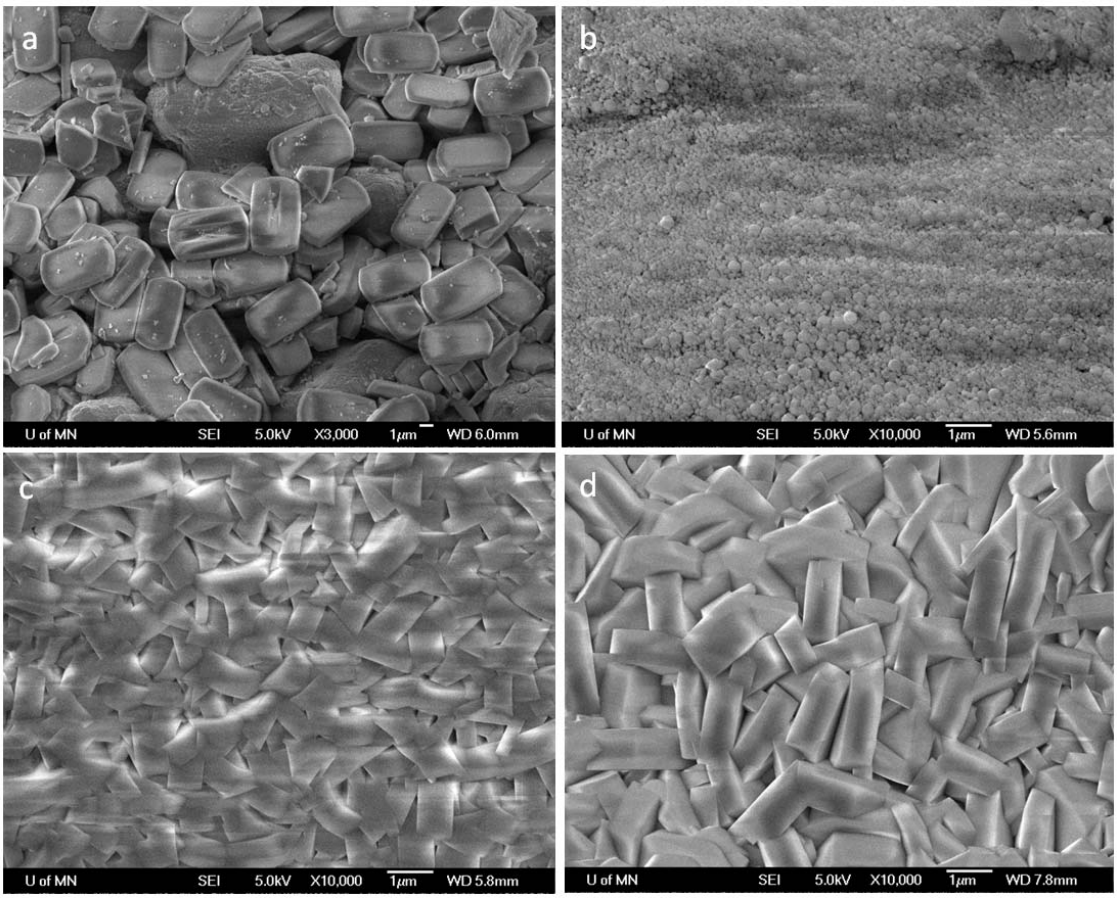

Figure 5.16 SEM images of the surface of the big MFI seed layer (a), a seed layer after multiple-seeding of polycrystalline aggregates (b), the surface of the zeolite membrane after CC treatment (c), and the zeolite membrane after RTP treatment (d). Big MFI seeding and polycrystalline aggregate seeding were accomplished by the rubbing and leveling methods. The PEI polymer layer was removed by calcination (450 °C for 3 h) after each deposition process. SEM images were obtained without coating for all samples.

The permeation test of xylene isomers will be carried out under high pressure and high temperature conditions for identifying intrinsic size-selective properties of zeolite membranes.

5.4 Conclusions

This study demonstrated that brittle, polycrystalline zeolite particles prepared by confined growth can produce seeds with suitable morphology for direct deposition onto a porous support by rubbing and leveling methods. Even though the resulting high-quality seed layers are initially randomly oriented, the zeolite membranes with a synthetic condition (100 °C for 12 h) can be converted to very thin (400–500 nm), well-intergrown zeolite films that exhibit high flux and excellent xylene isomer separation. Using an RTP step not only shortened the processing time and reduced energy usage, but also improved the membrane performance. Although the separation performance values of the reported membranes are not too different from the *b*-oriented membranes of reference of 5, the synthesis procedure reported here may be more attractive because it does not require the use of specially designed SDAs. The fact that seed layer formation and calcination steps could be completed in only a few minutes, significantly shortened the overall membrane fabrication process compared to conventional methods that involve complementary interactions between support and seed particles, as well as slow calcination.[22] In addition, for the zeolite membranes prepared under 175 C for 1 h, RTP treatment also improved the quality of the zeolite films compared to RTP-CC-treated RL-membrane. Finally, the seeding method was applied to grow zeolite membranes on stainless steel tube supports. Similar processes of optimizing the deposition and calcination steps to obtain high flux membranes with high separation should be applicable to the nanofabrication of thin films with other compositions.

5.5 References

(1) Davis, M. E. *Nature* **2002**, *417*, 813-821.

(2) Caro, J.; Noack, M. *Microporous Mesoporous Mater.* **2008**, *115*, 215-233.

(3) McLeary, E. E.; Jansen, J. C.; Kapteijn, F. *Microporous Mesoporous Mater.* **2006**, *90*, 198-220.

(4) Coronas, J. *Chem. Eng. J.* **2010**, *156*, 236-242.

(5) Lai, Z.; Bonilla, G.; Diaz, I.; Nery, J. G.; Sujaoti, K.; Amat, M. A.; Kokkoli, E.; Terasaki, O.; Thompson, R. W.; Tsapatsis, M.; Vlachos, D. G. *Science* **2003**, *300*, 456-460.

(6) Snyder, M. A.; Tsapatsis, M. *Angew. Chem. Int. Ed.* **2007**, *46*, 7560-7573.

(7) Bonilla, G.; Díaz, I.; Tsapatsis, M.; Jeong, H.-K.; Lee, Y.; Vlachos, D. G. *Chem. Mater.* **2004**, *16*, 5697-5705.

(8) Díaz, I.; Kokkoli, E.; Terasaki, O.; Tsapatsis, M. *Chem. Mater.* **2004**, *16*, 5226-5232.

(9) Choi, J.; Ghosh, S.; King, L.; Tsapatsis, M. *Adsorption* **2006**, *12*, 339-160.

(10) Lee, J. S.; Lee, Y.-J.; Tae, E. L.; Park, Y. S.; Yoon, K. B. *Science* **2003**, *301*, 818-821.

(11) Yoon, K. B. *Acc. Chem. Res.* **2007**, *40*, 29-40.

(12) Choi, J.; Ghosh, S.; Lai, Z.; Tsapatsis, M. *Angew. Chem. Int. Ed.* **2006**, *45*, 1154-1158.

(13) Liu, Y.; Li, Y.; Yang, W. *Chem. Commun.* **2009**, 1520-1522.

(14) Liu, Y.; Li, Y.; Yang, W. *J. Am. Chem. Soc.* **2010**, *132*, 1768-1769.

(15) Lee, I.; Buday, J. L.; Jeong, H.-K. *Microporous Mesoporous Mater.* **2009**, *122*, 288-293.

(16) Gouzinis, A.; Tsapatsis, M. *Chem. Mater.* **1998**, *10*, 2497-2504.

(17) Xomeritakis, G.; Lai, Z.; Tsapatsis, M. *Ind. Eng. Chem. Res.* **2001**, *40*, 544-552.

(18) Gump, C. J.; Tuan, V. A.; Noble, R. D.; Falconer, J. L. *Ind. Eng. Chem. Res.* **2001**, *40*, 565-577.

(19) Yuan, W.; Lin, Y. S.; Yang, W. *J. Am. Chem. Soc.* **2004**, *126*, 4776-4777.

(20) Hedlund, J.; Jareman, F.; Bons, A.-J.; Anthonis, M. *J. Membr. Sci.* **2003**, *222*, 163-179.

(21) Hedlund, J.; Sterte, J.; Anthonis, M.; Bons, A.-J.; Carstensen, B.; Corcoran, N.; Cox, D.; Deckman, H.; Gijnst, W. D.; Moor, P.-P. d.; Lai, F.; McHenry, J.; Mortier, W.; Reinoso, J.; Peters, J. *Microporous Mesoporous Mater.* **2002**, *52*, 179-189.

(22) Choi, J.; Jeong, H.-K.; Snyder, M. A.; Stoeger, J. A.; Masel, R. I.; Tsapatsis, M. *Science* **2009**, *325*, 590-593.

(23) Tarditi, A. M.; Irusta, S.; Lombardo, E. A. *Chem. Eng. J.* **2006**, *122*, 167-174.

(24) Bein, T. *Chem. Mater.* **1996**, *8*, 1636-1653.

(25) Xomeritakis, G.; Gouzinis, A.; Nair, S.; Okubo, T.; He, M.; Overney, R. M.; Tsapatsis, M. *Chem. Eng. Sci.* **1999**, *54*, 3521-3531.

(26) Lai, Z.; Tsapatsis, M. *Ind. Eng. Chem. Res.* **2004**, *43*, 3000-3007.

(27) Bons, A.-J.; Bons, P. D. *Microporous Mesoporous Mater.* **2003**, *62*, 9-16.

(28) Snyder, M. A.; Lai, Z.; Tsapatsis, M.; Vlachos, D. G. *Microporous Mesoporous Mater.* **2004**, *76*, 29-33.

(29) Snyder, M. A.; Vlachos, D. G.; Nikolakis, V. *J. Membr. Sci.* **2007**, *290*, 1-18.

(30) Mintova, S.; Mo, S.; Bein, T. *Chem. Mater.* **1998**, *10*, 4030-4036.

(31) Chaikittisilp, W.; Davis, M. E.; Okubo, T. *Chem. Mater.* **2007**, *19*, 4120-4122.

(32) Yan, Y.; Davis, M. E.; Gavalas, G. R. *Ind. Eng. Chem. Res.* **1995**, *34*, 1652-1661.

(33) Li, X.; Yan, Y.; Wang, Z. *Ind. Eng. Chem. Res.* **2010**, *49*, 5933-5938.

(34) Liu, X.; Liu, W.; Li, J.; Zhang, Y.; Lang, L.; Ma, L.; Zhang, B. *Ind. Eng. Chem. Res.* **2010**, *49*, 8826-8831.

(35) Wang, Z.; Ge, Q.; Shao, J.; Yan, Y. *J. Am. Chem. Soc.* **2009**, *131*, 6910-6911.

(36) Hunt, H. K.; Lew, C. M.; Sun, M.; Yan, Y.; Davis, M. E. *Microporous Mesoporous Mater.* **2010**, *128*, 12-18.

(37) Huang, A.; Caro, J. *Chem. Mater.* **2010**, *22*, 4353-4355.

(38) Jeong, H.-K.; Krohn, J.; Sujaoti, K.; Tsapatsis, M. *J. Am. Chem. Soc.* **2001**, *124*, 12966-12968.

(39) Berenguer-Murcia, Á.; Morallón, E.; Cazorla-Amorós, E.; Linares-Solano, Á. *Microporous Mesoporous Mater.* **2003**, *66*, 331-340.

(40) Jiang, Y.-B.; Xomeritakis, G.; Chen, Z.; Dunphy, D.; Kissel, D. J.; Cecchi, J. L.; Brinker, C. J. *J. Am. Chem. Soc.* **2007**, *129*, 15446-15447.

(41) Yoo, W. C.; Kumar, S.; Penn, R. L.; Tsapatsis, M.; Stein, A. *J. Am. Chem. Soc.* **2009**, *131*, 12377-12383.

(42) Yoo, W. C.; Kumar, S.; Wang, Z.; Ergang, N. S.; Fan, W.; Karanikolos, G. N.; McCormick, A. V.; Penn, R. L.; Tsapatsis, M.; Stein, A. *Angew. Chem. Int. Ed.* **2008**, *47*, 9096-9099.

(43) Lee, J. S.; Kim, J. H.; Lee, Y. J.; Jeong, N. C.; Yoon, K. B. *Angew. Chem. Int. Ed.* **2007**, *46*, 3087-3090.

(44) Fan, W.; Snyder, M. A.; Kumar, S.; Lee, P.-S.; Yoo, W. C.; McCormick, A. V.; Penn, R. L.; Stein, A.; Tsapatsis, M. *Nat. Mater.* **2008**, *7*, 984-991.

(45) Holland, B. T.; Abrams, L.; Stein, A. *J. Am. Chem. Soc.* **1999**, *121*, 4308-4309.

(46) Jacobsen, C. J. H.; Madsen, C.; Janssens, T. V. W.; Jakobsen, H. J.; Skibsted, J. *Microporous Mesoporous Mater.* **2000**, *39*, 393-401.

(47) Kim, S.-S.; Shah, J.; Pinnavaia, T. J. *Chem. Mater.* **2003**, *15*, 1664-1668.

(48) Madsen, C.; Jacobsen, C. J. H. *Chem. Commun.* **1999**, 673-674.

(49) Schmidt, I.; Madsen, C.; Jacobsen, C. J. H. *Inorg. Chem.* **2000**, *39*, 2279-2283.

(50) Tosheva, L.; Valtchev, V. P. *Chem. Mater.* **2005**, *17*, 2494-2513.

(51) Wang, J.; Vinu, A.; Coppens, M.-O. *J. Mater. Chem.* **2007**, *17*, 4265-4273.

(52) Khanh, N. N.; Yoon, K. B. *J. Am. Chem. Soc.* **2009**, *131*, 14228-14230.

(53) Bonilla, G.; Vlachos, D. G.; Tsapatsis, M. *Microporous Mesoporous Mater.* **2001**, *42*, 191-203.

(54) Miachon, S.; Ciavarella, P.; van Dyk, L.; Kumakiri, I.; Fiaty, K.; Schuurman, Y.; Dalmon, J.-A. *J. Membr. Sci.* **2007**, *298*, 71-79.

Chapter 6

Summary and Outlook

6.1 Summary

6.1.1 Surfactant-induced re-assembly of dissolved species

Simultaneous dissolution and surfactant-induced re-assembly via micelle formation with dissolved species were performed to introduce mesoporosity in the amorphous silica spheres and zeolite crystals. The different dissolution rate imposed by the different degree of condensation of amorphous silica spheres allowed one to control the textural features from corrugated to smooth mesoporous silica spheres. The *in-situ* investigation for identifying the incorporation of surfactant-induced re-assembly into the amorphous silica spheres was carried out by carbon nanocasting, resulting in hollow-core@mesopore-shell carbon spheres.

In addition, meso-zeolite catalysts were fabricated via the simultaneous dissolution and surfactant-induced re-assembly of dissolved crystal fragments of the zeolites. The final meso-zeolites exhibited well preserved crystallinity and increased surface area in the specific conditions. The ease of this process and the capability of extending to other types of zeolites can attractive for rational design of meso-zeolite catalysts.

6.1.2 Morphology control of zeolite nanocrystals using confined synthesis

Using 3DOM carbon as a massively parallel nanoreactor, growth patterns and shape developments of zeolite crystals were studied. Depending on the reaction parameters, i.e., the concentration of precursor solution to define nucleation or growth dominant condition, sequential infiltration hydrothermal reaction (ITH), the surface charge of the reactor controlled by layer-by-layer deposition of polyelectrolytes and the size of the nanoreactor, not only various shapes of zeolite crystals but also growth pattern

and shape development of zeolite crystals were investigated. Geode like crystals with hollow interior, 100-300 nm sized crystals with corrugated or smooth surfaces, needle shapes and nanosized coffin structures of zeolite crystals were grown. In addition, growth dominant (low nutrient content) and nucleation dominant (high nutrient content) conditions were controlled to produce 3DOM imprinted single crystals and polycrystalline aggregates. Furthermore, the shape development from irregular to faceted or secondary population of zeolite crystals was controlled by nutrient concentrations. This confined growth mechanism provides interesting morphologies of zeolite crystals that can be used for seed particles for zeolite membrane fabrication and zeolite catalysts.

6.1.3 Fabrication of high performance zeolite membranes using brittle seed particles

Facile fabrication of zeolite membranes with high performance (high SF and fast flux) was established using brittle seed particles produced by the confined synthesis. Polycrystalline aggregates (ca. 300 in diameter) comprising of small gains (50-100 nm) were implemented as seed particles for fabrication of zeolite membranes by the secondary hydrothermal growth. The rubbing and leveling methods were applied as seed deposition techniques to provide a high quality of a smooth monolayer on the porous alumina supports. Due to the high quality of the seed layer, the intergrown zeolite films could be kept very thin (400-500 nm) under specific synthetic conditions, which permits a high flux of target molecules. Furthermore, rapid thermal processing (RTP) that improves the quality of the zeoltie membranes via strengthening grain boundaries was applied as a single calcinaton step, which reduced the whole processing time significantly and improved the quality of the zeolite membranes. In addition, this novel seeding method was applied to stainless steel tube supports that are more suitable for industrial demands, e.g., high pressure and temperature.

6.2 Outlook

6.2.1 Design of dual/multi-component catalysts

Dual/multi-component catalysts could be designed by confined synthesis. For example, careful control of the growth conditions can provide a catalyst inside each confined space where it still has room for growth of another catalyst. Using the nucleation dominant conditions, one can incorporate several different catalysts into one confined space (macropore). After removal of the template and SDAs, dual/multi-component catalysts can be obtained (Figure 6.1). In addition, after deposition of one or two catalysts using the nucleation dominant condition, one can apply the growth dominant condition, producing dual/multi-component 3DOM-imprinted zeolite catalysts (Figure 6.2). Furthermore, interesting metallic nanoparticles with a catalytic function can be incorporated into the 3DOM carbon template (Figure 6.3). Vacuum infiltration of a metal nanoparticle solution can deposit them on the confinement wall through electrostatic interactions between the particle and the surface of the 3DOM carbon template (Figure 6.4). Metal nanoparticle-decorated 3DOM carbon templates can be used for growing other catalysts via either nucleation or growth dominant conditions inside confinement.

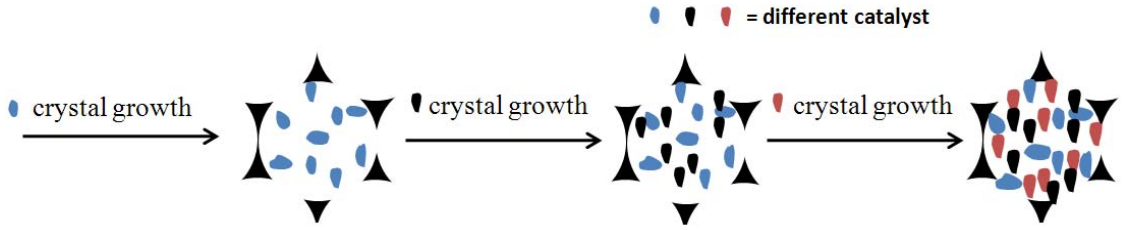

Figure 6.1 An illustration for fabrication of dual/multi-component polycrystalline catalysts via nucleation dominant conditions.

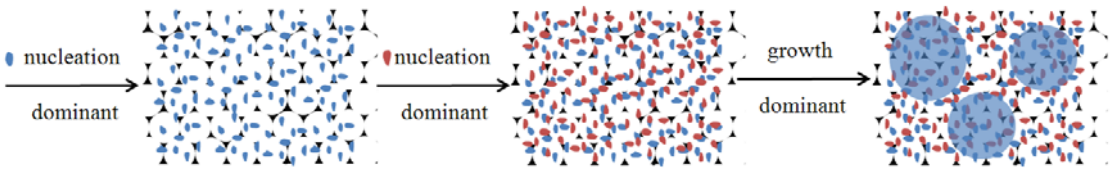

Figure 6.2 An illustration for 3DOM-imprinted dual/multi-component catalysts.

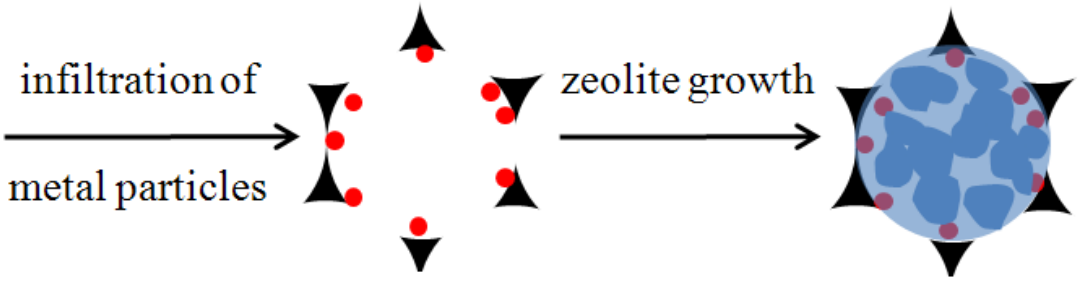

Figure 6.3 An illustration of a metal-nanoparticle/zeolite composite catalyst.

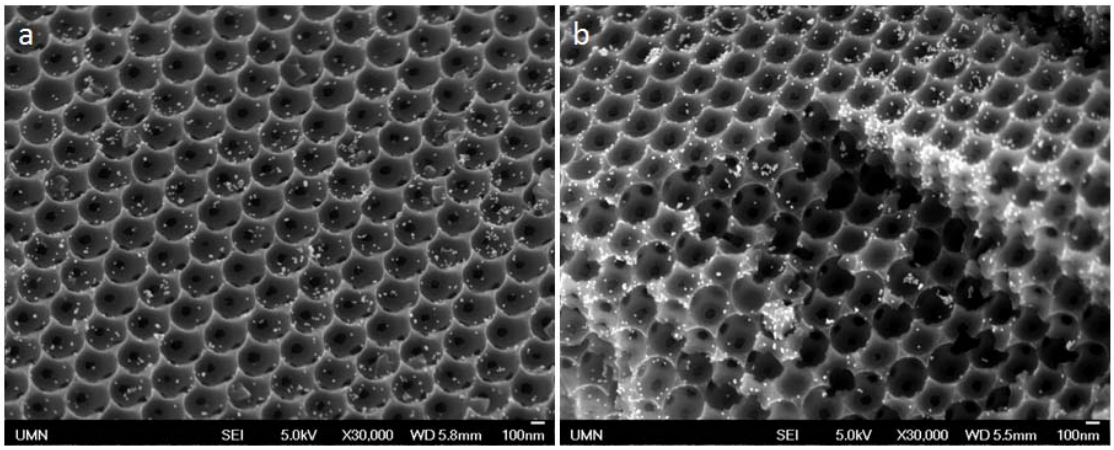

Figure 6.4 SEM images of Au nanoparticles inside 3DOM carbon: (a) the plain view and (b) the cross sectional view. The negatively charged Au nanoparticles were located inside positively charged 3DOM carbon by vacuum infiltration of an Au nanoparticle solution.

6.2.2 Metal ion impregnated meso-zeolite catalysts

Transition metal ions could be involved in the surfactant-induced re-assembly process (Figure 6.5). During the re-assembly process, metal ions can be impregnated in the zeolite frameworks via chemical bonding between metal ions and the dangling bonds of the frameworks, which could specify the oxidation state of metal atom. So far, impregnation of metal ions into zeolite frameworks has been accomplished by ion exchange, but it is usually difficult to define the oxidation state of the impregnated metal

atoms. Furthermore, aggregation or formation of small metallic nanoparticles decreases the catalytic performance.[1] Therefore, difined and stable chemical structure of metal ions in the zeolite frameworks could be produced by the re-assembly process, which allows one to design a tailored catalyst for specific catalysis reactions.

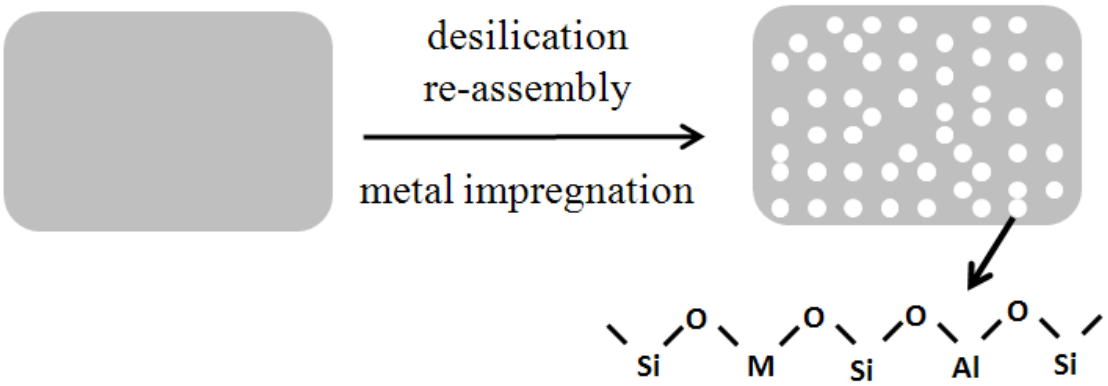

Figure 6.5 An illustration of impregnation of metal ions into zeolite frameworks through the surfactant-induced re-assembly process.

6.2.3 Thin *b*-oriented MFI membranes

Fabrication of a thin *b*-oriented MFI membrane can be possible. The *b*-oriented MFI membrane has shown the best performance in terms of separation of xylene isomer. However, the thickness of *b*-oriented MFI films is still several micrometers because of lack of methods to produce nanosized and coffin-shaped MFI crystals by conventional hydrothermal methods in which the coffin-shaped crystal should be used as a seed particle for the *b*-oriented MFI film.[2,3] On the other hand, the confined synthesis can produce nanosized coffin structures ca. 100 nm long (Figure 6.6) through careful choice of IHT cycles with different nutrient concentrations: one cycle of nucleation dominant condition (high nutrient content, H) and subsequent use of growth dominant condition (low nutrient content, L). After IHT cycles of H_1L_2, nanosized coffin-shaped MFI crystals were obtained after removal of the 3DOM carbon template. The rubbing and

leveling methods can be used to deposit a seed layer on the alumina support and using a crystal-shape modifier,[4] a very thin *b*-oriented MFI membrane can be fabricated.

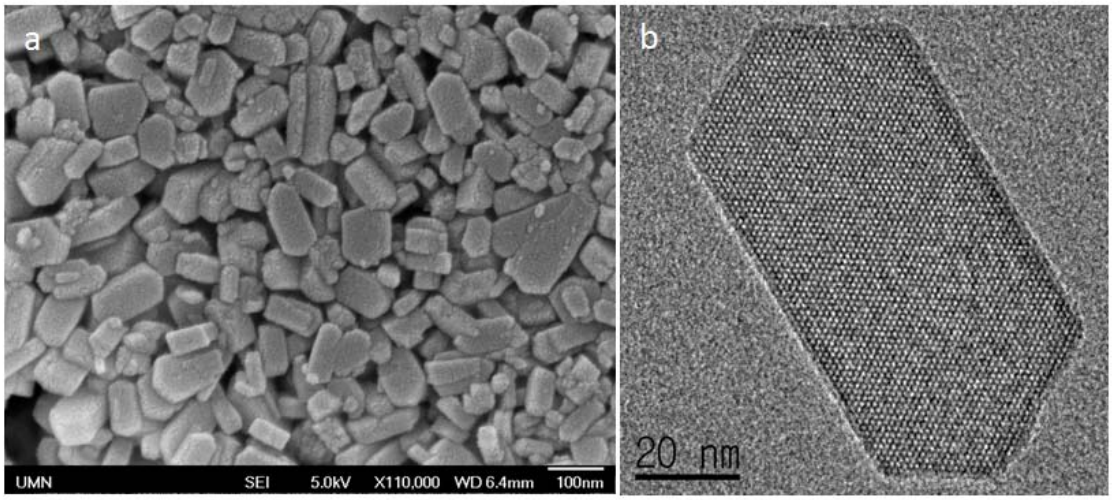

Figure 6.6 Nanosized and coffin-shaped MFI zeolites after several infiltration hydrothermal reaction cycles of H_1L_2. SEM image (a) of MFI nanocrystals after calcination and the corresponding TEM image (b).

6.3 References

(1) Choi, M.; Lee, D.-H.; Na, K.; Yu, B.-W.; Ryoo, R. *Angew. Chem. Int. Ed.* **2009**, *48*, 3673-3676.

(2) Lee, S.; Carr, C. S.; Shantz, D. F. *Langmuir* **2005**, *21*, 12031-12036.

(3) Snyder, M. A.; Tsapatsis, M. *Angew. Chem. Int. Ed.* **2007**, *46*, 7560-7573.

(4) Lai, Z.; Bonilla, G.; Diaz, I.; Nery, J. G.; Sujaoti, K.; Amat, M. A.; Kokkoli, E.; Terasaki, O.; Thompson, R. W.; Tsapatsis, M.; Vlachos, D. G. *Science* **2003**, 300, 456-460.

Bibliography

http://en.wikipedia.org/wiki/Zeolite.

IUPAC Mannual of Symbols and Terminology, Appendix 2, Part 1, Colloidal and Surface Chemistry Pure Appl. Chem. 1972, 31, 578.

Abrams, L.; Corbin, D. R. *J. Incl. Phenom. Mol. Recog.* 1995, *21*, 1-46.

Al-Muhtaseb, S. A.; Ritter, J. A. *Adv. Mater.* **2003**, *15*, 101-114.

Archer, R. H.; Carpenter, J. R.; Hwang, S.-J.; Burton, A. W.; Chen, C.-Y.; Zones, S. I.; Davis, M. E. *Chem. Mater.* **2010**, *22*, 2563-2572.

Armatas, G. S.; Kanatzidis, M. G. *Natue* **2006**, *441*, 1122-1125.

Artaki, I.; Zerda, T. W.; Jonas, J. *J. Non-Cryst. Solids* **1986**, *81*, 381-395.

Attard, G. S.; Bartlett, P. N.; Coleman, N. R. B.; Elliott, J. M.; Owen, J. R.; Wang, J. H. *Science* **1997**, *278*, 838-840.

Baerlocher, C.; Meier, W. M.; Olson, D. H., Atlas of Zeolite Framework Types, 5th Ed. 2001, The Structure Commission of the International Zeolite Associaiton, Elsevier.

Bansal, R. C.; Goyal, M. *Activated Carbon Adsorption.*, CRC Press:Boca Raton, 2005; p 497.

Bárcia, P. S.; Ferreira, A.; Gascon, J.; Aguado, S.; Silva, J. A. C.; Rodrigues, A. E.; Kapteijn, F. *Microporous Mesoporous Mater.* **2010**, *128*, 194-202.

Barton, J. E.; Odom, T. W. *Nano Lett.* **2004**, *4*, 1525-1528.

Beck, J. S.; Vartuli, J. C.; Roth, W. J.; Leonowicz, M. E.; Kresge, C. T.; Schmitt, K. D.; Chu, C. T.-W.; Olson, D. H.; Sheppard, E. W.; McCullen, S. B.; Higgins, J. B.; Schlenker, J. L. *J. Am. Chem. Soc.* **1992**, *114*, 10834-10843.

Bein, T. *Chem. Mater.* **1996**, *8*, 1636-1653.

Berenguer-Murcia, Á.; Morallón, E.; Cazorla-Amorós, E.; Linares-Solano, Á. *Microporous Mesoporous Mater.* **2003**, *66*, 331-340.

Bonilla, G.; Díaz, I.; Tsapatsis, M.; Jeong, H.-K.; Lee, Y.; Vlachos, D. G. *Chem. Mater.* **2004**, *16*, 5697-5705.

Bonilla, G.; Tsapatsis, M.; Vlachos, D. G.; Xomeritakis, G. *J. Membr. Sci.* **2001**, *182*, 103-109.

Bonilla, G.; Vlachos, D. G.; Tsapatsis, M. *Microporous Mesoporous Mater.* **2001**, *42*, 191-203.

Bons, A.-J.; Bons, P. D. *Microporous Mesoporous Mater.* **2003**, *62*, 9-16.

Botella, P.; Corma, A.; Navarro, M. T. *Chem. Mater.* **2007**, *19*, 1979-1983.

Braun, P. V.; Osenar, P.; Stupp, S. I. *Nature* **1996**, *380*, 325-328.

Büchel, G.; Unger, K. K.; Matsumoto, A.; Tsutsumi, K. *Adv. Mater.* **1998**, *10*, 1036-1038.

Burkett, S. L.; Davis, M. E. *Chem. Mater.* **1995**, *7*, 1453-1463.

Calzaferri, G.; Huber, S.; Maas, H.; Minkowski, C. *Angew. Chem. Int. Ed.* **2003**, *42*, 3732-3758.

Caro, J.; Noack, M. *Microporous Mesoporous Mater.* **2008**, *115*, 215-233.

Caruso, F. *Adv. Mater.* **2001**, *13*, 11-22.

Chaikittisilp, W.; Davis, M. E.; Okubo, T. *Chem. Mater.* **2007**, *19*, 4120-4122.

Che, S.; Liu, Z.; Ohsuna, T.; Sakamoto, K.; Terasaki, O.; Tatsumi, T. *Nature* **2004**, *429*, 281-284.

Chem, Z.; Li, S.; Yan, Y. *Chem. Mater.* **2005**, *17*, 2262-2266.

Chen, H.; Hu, T.; Zhang, X.; Huo, K.; Chu, P. K.; He, J. *Langmuir* **2010**, *26*, 13556-13563.

Chen, H.-T.; Huh, S.; Wiench, J. W.; Pruski, M.; Lin, V. S.-Y. *J. Am. Chem. Soc.* **2005**, *127*, 13305-13311.

Chirico, R. D.; Steele, W. V. *J. Chem. Eng. Data* **1997**, *42*, 784.

Choi, J.; Ghosh, S.; King, L.; Tsapatsis, M. *Adsorption* **2006**, *12*, 339-160.

Choi, J.; Ghosh, S.; Lai, Z.; Tsapatsis, M. *Angew. Chem. Int. Ed.* **2006**, *45*, 1154-1158.

Choi, J.; Jeong, H.-K.; Snyder, M. A.; Stoeger, J. A.; Masel, R. I.; Tsapatsis, M. *Science* **2009**, *325*, 590-593.

Choi, J.; Tsapatsis, M. *J. Am. Chem. Soc.* **2010**, *132*, 448-449.

Choi, M.; Cho, H. S.; Srivastava, R.; Venkatesan, C.; Choi, D.-H.; Ryoo, R. *Nat. Mater.* **2006**, *5*, 718-723.

Choi, M.; Lee, D.-H.; Na, K.; Yu, B.-W.; Ryoo, R. *Angew. Chem. Int. Ed.* **2009**, *48*, 3673-3676.

Choi, M.; Na, K.; Kim, J.; Sakamoto, Y.; Terasaki, O.; Ryoo, R. *Nature* **2009**, *461*, 246-250.

Choi, M.; Wu, Z.; Iglesia, E. *J. Am. Chem. Soc.* **2010**, *132*, 9129-9137.

Christensen, C. H.; Johannsen, K.; Schmidt, I.; Christensen, C. H. *J. Am. Chem. Soc.* **2003**, *125*, 13370-13371.

Corma, A. *Chem. Rev.* **1997**, *97*, 2373-2419.

Corma, A. *J. Cat.* **2003**, *216*, 298-312.

Corma, A. *Nature* **2009**, *461*, 182-183.

Corma, A.; Davis, M. E. *ChemPhysChem* **2004**, *5*, 304-313.

Corma, A.; Fornes, V.; Pergher, S. B.; Maesen, T. L. M.; Buglass, J. G. *Nature* **1998**, *396*, 353-356.

Coronas, J. *Chem. Eng. J.* **2010**, *156*, 236-242.

Davis, M. E. *Nature* **2002**, *417*, 813-821.

Davis, M. E.; Saldarriaga, C.; Montes, C.; Garces, J.; Crowder, C. *Nature* **1998**, *331*, 698-699.

Davis, T. M.; Drews, T. O.; Ramanan, H.; He, C.; Dong, J.; Schnablegger, H.; A.Katsoulakis, M.; Kokkoli, E.; McCormick, A. V.; Penn, R. L.; Tsapatsis, M. *Nat. Mater.* **2006**, *5*, 400-408.

de Moor, P.-P. E. A.; Beelen, T. P. M.; Komanschek, B. U.; Beck, L. W.; Wagner, P.; Davis, M. E.; van Santen, R. A. *Chem. Eur. J.* **1999**, *5*, 2083-2088.

de Moor, P.-P. E. A.; Beelen, T. P. M.; Santen, R. A. v. *J. Phys. Chem. B* **1999**, *103*, 1639-1650.

Decher, G. *Science* **1997**, *277*, 1232-1237.

Deng, Y.; Qi, D.; Deng, C.; Zhang, X.; Zhao, D. *J. Am. Chem. Soc.* **2008**, *130*, 28-29.

Díaz, I.; Kokkoli, E.; Terasaki, O.; Tsapatsis, M. *Chem. Mater.* **2004**, *16*, 5226-5232.

Dong, A.; Wang, Y.; Tang, Y.; Zhang, Y.; Ren, N.; Gao, Z. *Adv. Mater.* **2002**, *14*, 1506-1510.

Drews, T. O.; Tsaptsis, M. *Current Opin. Colloid Interface Sci.* **2005**, *10*, 233-238.

Egeblad, K.; Christensen, C. H.; Kustova, M.; Christensen, C. H. *Chem. Mater.* **2008**, *20*, 946-960.

Fan, W.; Snyder, M. A.; Kumar, S.; Lee, P.-S.; Yoo, W. C.; McCormick, A. V.; Penn, R. L.; Stein, A.; Tsapatsis, M. *Nat. Mater.* **2008**, *7*, 984-991.

Firouzi, A.; Kumar, D.; Bull, L. M.; Besier, T.; Sieger, P.; Huo, Q.; Walker, S. A.; Zasadzinski, J. A.; Glinka, C.; Nicol, J.; Margolese, D.; Stucky, G. D.; Chmelka, B. F. *Science* **1995**, *267*, 1138-1143.

Fyfe, C. A.; Bretherton, J. L.; Lam, L. Y. *J. Am. Chem. Soc.* **2001**, *123*, 5285-5291.

Fyfe, C. A.; Darton, R. J.; Schneider, C.; Scheffler, F. *J. Phys. Chem. C* **2008**, *112*, 80-88.

Galarneau, A.; Iapichella, J.; Bonhomme, K.; Renzo, F. D.; Kooyman, P.; Terasaki, O.; Fajula, F. *Adv. Funct. Mater.* **2006**, *16*, 1657-1667.

Ganguly, A.; Ahmad, T.; Ganguli, A. K. *Langmuir* **2010**, *26*, 14901-14908.

Gavalas, G. R. *Ind. Eng. Chem. Res.* **2008**, *47*, 5797-5811.

Gouzinis, A.; Tsapatsis, M. *Chem. Mater.* **1998**, *10*, 2497-2504.

Graph, G. *Purchasing Magazine* **2003**, June 19.

Groen, J. C.; Bach, T.; Ziese, U.; Paulaime-van Donk, A. M.; de Jong, K. P.; Moulijn, J. A.; Pérez-Ramírez, J. *J. Am. Chem. Soc.* **2005**, *127*, 10792-10793.

Groen, J. C.; Jansen, J. C.; Moulijn, J. A.; Pérez-Ramírez, J. *J. Phys. Chem. B* **2004**, *108*, 13062-13065.

Groen, J. C.; Moulijn, J. A.; Pérez-Ramírez, J. *Microporous Mesoporous Mater.* **2005**, *87*, 153-161.

Groen, J. C.; Moulijn, J. A.; Pérez-Ramírez, J. *J. Mater. Chem.* **2006**, *16*, 2121-2131.

Groen, J. C.; Peffer, L. A. A.; Moulijn, J. A.; Pérez-Ramírez, J. *Microporous Mesoporous Mater.* **2004**, *69*, 29-34.

Grün, M.; Lauer, I.; Unger, K. K. *Adv. Mater.* **1997**, *9*, 254-257.

Grün, M.; Unger, K. K.; Matsumoto, A.; Tsutsumi, K. *Microporous Mesoporous Mater.* **1999**, *27*, 207-216.

Gump, C. J.; Tuan, V. A.; Noble, R. D.; Falconer, J. L. *Ind. Eng. Chem. Res.* **2001**, *40*, 565-577.

Hamilton, B. D.; Weissbuch, I.; Lahav, M.; Hillmyer, M. A.; Ward, M. D. *J. Am. Chem. Soc.* **2009**, *131*, 2588-2596.

Han, Y.; Lee, S. S.; Ying, J. Y. *Chem. Mater.* **2007**, *19*, 2292-2298.

Hayward, R. C.; Saville, D. A.; Aksay, I. A. *Nature* **2000**, *404*, 56-59.

Hedlund, J.; Jareman, F.; Bons, A.-J.; Anthonis, M. *J. Membr. Sci.* **2003**, *222*, 163-179.

Hedlund, J.; Sterte, J.; Anthonis, M.; Bons, A.-J.; Carstensen, B.; Corcoran, N.; Cox, D.; Deckman, H.; Gijnst, W. D.; de Moor, P.-P.; Lai, F.; McHenry, J.; Mortier, W.; Reinoso, J.; Peters, J. *Microporous Mesoporous Mater.* **2002**, *52*, 179-189.

Holland, B. T.; Abrams, L.; Stein, A. *J. Am. Chem. Soc.* **1999**, *121*, 4308-4309.

Holland, B. T.; Blanford, C. F.; Stein, A. *Science* **1998**, *281*, 538-540.

Huang, A.; Bux, H.; Steinbach, F.; Caro, J. *Angew. Chem. Int. Ed.* **2010**, *49*.

Huang, A.; Caro, J. *Chem. Mater.* **2010**, *22*, 4353-4355.

Hunt, H. K.; Lew, C. M.; Sun, M.; Yan, Y.; Davis, M. E. *Microporous Mesoporous Mater.* **2010**, *128*, 12-18.

Huo, Q.; Margolese, D. I.; Ciesla, U.; Feng, P.; Gier, T. E.; Sieger, P.; Leon, R.; Petroff, P. M.; Schüth, F.; Stucky, G. D. *Nature* **1994**, *368*, 317-321.

Inagaki, S.; Ogura, M.; Inami, T.; Sasaki, Y.; Kikuchi, E.; Matsukata, M. *Microporous Mesoporous Mater.* **2004**, *74*, 163-170.

Jacobsen, C. J. H.; Madsen, C.; Houzvicka, J.; Schmidt, I.; Carlsson, A. *J. Am. Chem. Soc.* **2000**, *122*, 7116-7117.

Jacobsen, C. J. H.; Madsen, C.; Janssens, T. V. W.; Jakobsen, H. J.; Skibsted, J. *Microporous Mesoporous Mater.* **2000**, *39*, 393-401.

Janssen, A. H.; Schmidt, I.; Jacobsen, C. J. H.; Koster, A. J.; de Jong, K. P. *Microporous Mesoporous Mater.* **2003**, *65*, 59-75.

Jeong, H.-K.; Krohn, J.; Sujaoti, K.; Tsapatsis, M. *J. Am. Chem. Soc.* **2001**, *124*, 12966-12968.

Jeong, H.-K.; Lai, Z.; Tsapatsis, M.; Hanson, J. C. *Microporous Mesoporous Mater.* **2005**, *84*, 332-337.

Jiang, Y.-B.; Xomeritakis, G.; Chen, Z.; Dunphy, D.; Kissel, D. J.; Cecchi, J. L.; Brinker, C. J. *J. Am. Chem. Soc.* **2007**, *129*, 15446-15447.

Jun, Y.-W.; Choi, J.-S.; Cheon, J. *Angew. Chem. Int. Ed.* **2006**, *45*, 3414-3439.

Khanh, N. N.; Yoon, K. B. *J. Am. Chem. Soc.* **2009**, *131*, 14228-14230.

Kim, J. H.; Yoon, S. B.; Kim, J.-Y.; Chae, Y. B.; Yu, J.-S. *Colloids and Surfaces A: Physicochem. Eng. Aspects* **2008**, *313-314*, 77-81.

Kim, S.-S.; Shah, J.; Pinnavaia, T. J. *Chem. Mater.* **2003**, *15*, 1664-1668.

Kim, T.-W.; Chung, P.-W.; Lin, V. S.-Y. *Chem. Mater.* **2010**, *22*, 5093-5104.

Kirkland, J. J.; Truszkowski, F. A.; Dilks, C. H.; Engel, G. S. *J. Chromatogr. A* **2000**, *890*, 3-13.

Kresge, C. T.; Leonowicz, M. E.; Roth, W. J.; Vartuli, J. C.; Beck, J. S. *Nature* **1992**, *359*, 710-712.

Kroschwitz, J. I.; in *Kirk-Othmer Encyclopedia of Chemical Technology, Wiley, New York,* **1998**, p.831.

Kustova, M.; Egeblad, K.; Zhu, K.; Christensen, C. H. *Chem. Mater.* **2007**, *19*, 2915-2917.

Lai, C.-Y.; Trewyn, B. G.; Jeftinija, D. M.; Jeftinija, K.; Xu, S.; Jeftinija, S.; Lin, V. S.-Y. *J. Am. Chem. Soc.* **2003**, *125*, 4451-4459.

Lai, Z.; Bonilla, G.; Diaz, I.; Nery, J. G.; Sujaoti, K.; Amat, M. A.; Kokkoli, E.; Terasaki, O.; Thompson, R. W.; Tsapatsis, M.; Vlachos, D. G. *Science* **2003**, *300*, 456-460.

Lai, Z.; Tsapatsis, M. *Ind. Eng. Chem. Res.* **2004**, *43*, 3000-3007.

Lai, Z.; Tsapatsis, M.; Nicolich, J. P. *Adv. Funct. Mater.* **2004**, *14*, 716-729.

Lee, D.-H.; Choi, M.; Yu, B.-W.; Ryoo, R. *Chem. Commun.* **2009**, 74-76.

Lee, I.; Buday, J. L.; Jeong, H.-K. *Microporous Mesoporous Mater.* **2009**, *122*, 288-293.

Lee, J.; Sohn, K.; Hyeon, T. *J. Am. Chem. Soc.* **2001**, *123*, 5146-5147.

Lee, J. S.; Kim, J. H.; Lee, Y. J.; Jeong, N. C.; Yoon, K. B. *Angew. Chem. Int. Ed.* **2007**, *46*, 3087-3090.

Lee, J. S.; Lee, Y.-J.; Tae, E. L.; Park, Y. S.; Yoon, K. B. *Science* **2003**, *301*, 818-821.

Lee, J. Y.; Farha, O. K.; Roberts, J.; Scheidt, K. A.; Nguyen, S. T.; Hupp, J. T. *Chem. Soc. Rev.* **2009**, *38*, 1450-1459.

Lee, K. T.; Lytle, J. C.; Ergang, N. S.; Oh, S. M.; Stein, A. *Adv. Funct. Mater.* **2005**, *15*, 547-556.

Lee, S.; Carr, C. S.; Shantz, D. F. *Langmuir* **2005**, *21*, 12031-12036.

Lethbridge, Z. A. D.; Williams, J. J.; Walton, R. I.; Evans, K. E.; Smith, C. W. *Microporous Mesoporous Mater.* **2005**, *79*, 339-352.

Lew, C. M.; Cai, R.; Yan, Y. *Acc. Chem. Res.* **2010**, *43*, 210-219.

Li, X.; Yan, Y.; Wang, Z. *Ind. Eng. Chem. Res.* **2010**, *49*, 5933-5938.

Liang, C.; Li, Z.; Dai, S. *Angew. Chem. Int. Ed.* **2008**, *47*, 3639-3717.

Lim, S.; Ranade, A.; Du, G.; Pfefferle, L. D.; Haller, G. L. *Chem. Mater.* **2006**, *18*, 5584-5590.

Lin, H.-P.; Mou, C.-Y. *Acc. Chem. Res.* **2002**, *35*, 927-935.

Liu, X.; Liu, W.; Li, J.; Zhang, Y.; Lang, L.; Ma, L.; Zhang, B. *Ind. Eng. Chem. Res.* **2010**, *49*, 8826-8831.

Liu, Y.; Li, Y.; Yang, W. *Chem. Commun.* **2009**, 1520-1522.

Liu, Y.; Li, Y.; Yang, W. *J. Am. Chem. Soc.* **2010**, *132*, 1768-1769.

Long, J. R.; Yaghi, O. M. *Chem. Soc. Rev.* **2009**, *38*, 1213-1214.

Lu, A.-H.; Schüth, F. *C. R. Chimie* **2005**, *8*, 609-620.

Lu, J.; Liong, M.; Zink, J. I.; Tamanoi, F. *Small* **2007**, *3*, 1341-1346.

Lu, Y.; Fan, H.; Stump, A.; Ward, T. L.; Rieker, T.; Brinker, C. J. *Nature* **1999**, *398*, 223-226.

Lu, Y.; Ganguli, R.; Drewien, C. A.; Anderson, M. T.; Brinker, C. J.; Gong, W.; Guo, Y.; Soyes, H.; Dunn, B.; Huang, M. H.; Zink, J. I. *Nature* **1997**, *389*, 364-368.

Madsen, C.; Jacobsen, C. J. H. *Chem. Commun.* **1999**, 673-674.

Maheshwari, S.; Jordan, E.; Kumar, S.; Bates, F. S.; Penn, R. L.; Shantz, D. F.; Tsapatsis, M. *J. Am. Chem. Soc.* **2008**, *130*, 1507-1516.

Martin, T.; Galarneau, A.; Renzo, F. D.; Brunel, D.; Fajula, F.; Heinisch, S.; Crétier, G.; Rocca, J.-L. *Chem. Mater.* **2004**, *16*, 1725-1731.

Martin, T.; Galarneau, A.; Renzo, F. D.; Fajula, F.; Plee, D. *Angew. Chem. Int. Ed.* **2002**, *41*, 2590-2592.

McLeary, E. E.; Jansen, J. C.; Kapteijn, F. *Microporous Mesoporous Mater.* **2006**, *90*, 198-220.

Megelski, S.; Calzaferri, G. *Adv. Funct. Mater.* **2001**, *11*, 277-286.

Meng, Y.; Gu, D.; Zhang, F.; Shi, Y.; Cheng, L.; Feng, D.; Wu, Z.; Chen, Z.; Wan, Y.; Stein, A.; Zhao, D. *Chem. Mater.* **2006**, *18*, 4447-4464.

Miachon, S.; Ciavarella, P.; van Dyk, L.; Kumakiri, I.; Fiaty, K.; Schuurman, Y.; Dalmon, J.-A. *J. Membr. Sci.* **2007**, *298*, 71-79.

Mihi, A.; Ocaña, M.; Míguez, H. *Adv. Mater.* **2006**, *18*, 2244-2249.

Mintova, S.; Bein, T. *Adv. Mater.* **2001**, *13*, 1880-1883.

Mintova, S.; Mo, S.; Bein, T. *Chem. Mater.* **1998**, *10*, 4030-4036.

Moliner, m.; Román-Leshkov, Y.; Davis, M. E. *Proc. Natl. Acad. Sci. USA* **2010**, *107*, 6144-6168.

Möller, K.; Kobler, J.; Bein, T. *Adv. Funct. Mater.* **2007**, *17*, 605-612.

Müller, M.; Harvey, G.; Prins, P. *Microporous Mesoporous Mater.* **2000**, *34*, 135-147.

Murray, L. J.; Dincă, M.; Long, J. R. *Chem. Soc. Rev.* **2009**, *38*, 1294-1314.

Nikolakis, V.; Tsapatsis, M.; Vlachos, D. G. *Langmuir* **2003**, *19*, 4619-4626.

Nooney, R. I.; Thirunavukkarasu, D.; Chen, Y.; Josephs, R.; Ostafin, A. E. *Chem. Mater.* **2002**, *14*, 4721-4728.

Norris, D. J.; Arlinghaus, E. G.; Meng, L.; Heiny, R.; Scriven, L. E. *Adv. Mater.* **2004**, *16*, 1393-1399.

Park, D. H.; Kim, S. S.; Wang, H.; Pinnavaia, T. J.; Papapetrou, M. C.; Lappas, A. A.; Triantafyllidis, K. S. *Angew. Chem. Int. Ed.* **2009**, *48*, 7645-7648.

Pauwels, B.; Tendeloo, G. V.; Thoelen, C.; Rhijn, W. V.; Jacobs, P. A. *Adv. Mater.* **2001**, *13*, 1317-1320.

Peng, X.; Wickham, J.; Alivisatos, A. P. *J. Am. Chem. Soc.* **1998**, *120*, 5343-5344.

Pérez-Ramírez, J.; Christensen, C. H.; Egeblad, K.; Christensen, C. H.; Groen, J. E. *Chem. Soc. Rev.* **2008**, *37*, 2530-2542.

Qiu, S.; Yu, J.; Zhu, G.; Terasaki, O.; Nozue, Y.; Pang, W.; Xu, R. *Microporous Mesoporous Mater.* **1998**, *21*, 245-251.

Román-Leshkov, Y.; Moliner, M.; Davis, M. E. *Chem. Mater.* **2010**, *22*, 2646-2652.

Ryoo, R.; Joo, S. H.; Jun, S. *J. Phys. Chem. B* **1999**, *103*, 7743-7746.

Schmidt, I.; Madsen, C.; Jacobsen, C. J. H. *Inorg. Chem.* **2000**, *39*, 2279-2283.

Schoeman, B. J.; Sterte, J.; Otterstedt, J.-E. *Zeolites* **1994**, *14*, 110-116.

Shokouhimehr, M.; Piao, Y.; Kim, J.; Jang, Y.; Hyeon, T. *Angew. Chem. Int. Ed.* **2007**, *46*, 7039-7043.

Snyder, M. A.; Lai, Z.; Tsapatsis, M.; Vlachos, D. G. *Microporous Mesoporous Mater.* **2004**, *76*, 29-33.

Snyder, M. A.; Tsapatsis, M. *Angew. Chem. Int. Ed.* **2007**, *46*, 7560-7573.

Snyder, M. A.; Vlachos, D. G.; Nikolakis, V. *J. Membr. Sci.* **2007**, *290*, 1-18.

Stein, A.; Li, F.; Denny, N. R. *Chem. Mater.* **2008**, *20*, 649-666.

Stein, A.; Melde, B. J.; Schroden, R. C. *Adv. Mater.* **2000**, *12*, 1403-1419.

Stein, A.; Wang, Z.; Fierke, M. A. *Adv. Mater.* **2009**, *21*, 265-293.

Stöber, W.; Fink, A.; Bohn, E. *J. Colloid Interface Sci.* **1968**, *26*, 62-69.

Sun, D.; Riley, A. E.; Cadby, A. J.; Richman, E. K.; Korlann, S. D.; Tolbert, S. H. *Nature* **2006**, *441*, 1126-1130.

Sun, J.; Bonneau, C.; Cantim, A.; Corma, A.; Diaz-Cabanas, M. J.; Moliner, M.; Zhang, D.; Li, M.; Zou, X. *Nature* **2009**, *458*, 1154-1158.

Tan, B.; Lehmler, H.-J.; Vyas, S. M.; Knutson, B. L.; Rankin, S. E. *Adv. Mater.* **2005**, *17*, 2368-2371.

Tan, B.; Rankin, S. E. *J. Phys. Chem. B* **2004**, *108*, 20122-20129.

Tao, Y.; Kanoh, H.; Abrams, L.; Kaneko, K. *Chem. Rev.* **2006**, *106*, 896-910.

Tao, Y.; Kanoh, H.; Kaneko, K. *J. Am. Chem. Soc.* **2003**, *125*, 6044-6045.

Tarditi, A. M.; Irusta, S.; Lombardo, E. A. *Chem. Eng. J.* **2006**, *122*, 167-174.

Tendeloo, G. V.; Lebedev, O. I.; Collart, O.; Cool, P.; Vansant, E. F. *J. Phys.:Condens. Matter* **2003**, *15*, S3037-S3046.

Tosheva, L.; Valtchev, V. P. *Chem. Mater.* **2005**, *17*, 2494-2513.

Tranchemontagne, D. J.; Mendoza-Cortés, J. L.; O'Keeffe, M.; Yaghi, O. M. *Chem. Soc. Rev.* **2009**, *2009*, 1257-1283.

Triantafillidis, C. S.; Evmiridis, N. P.; Nalbandian, L.; Vasalos, I. A. *Ind. Eng. Chem. Res.* **1999**, *38*, 916-927.

Tullo, A. H. *Chem. Eng. News* **2001**, *79(35)*, 28.

Walcarius, A.; Sibottier, E.; Etienne, M.; Ghanbaja, J. *Nat. Mater.* **2007**, *6*, 602-608.

Wan, Y.; Yang, H.; Zhao, D. *Acc. Chem. Res.* **2006**, *39*, 423-432.

Wan, Y.; Zhao, D. *Chem. Rev.* **2007**, *107*, 2821-2860.

Wang, D.; Zhang, Y.; Dong, A.; Tang, Y.; Wang, Y.; Xia, J.; Ren, N. *Adv. Funct. Mater.* **2003**, *13*, 563-567.

Wang, H.; Pinnavaia, T. J. *Angew. Chem. Int. Ed.* **2006**, *45*, 7603-7606.

Wang, J.; Vinu, A.; Coppens, M.-O. *J. Mater. Chem.* **2007**, *17*, 4265-4273.

Wang, Y.; Caruso, F. *Chem. Mater.* **2005**, *17*, 953-961.

Wang, Y.; Caruso, F. *Adv. Mater.* **2006**, *18*, 795-800.

Wang, Y.; Yu, A.; Caruso, F. *Angew. Chem. Int. Ed.* **2005**, *44*, 2888-2892.

Wang, Z.; Ergang, N. S.; Al-Daous, M. A.; Stein, A. *Chem. Mater.* **2005**, *17*, 6805-6813.

Wang, Z.; Ge, Q.; Shao, J.; Yan, Y. *J. Am. Chem. Soc.* **2009**, *131*, 6910-6911.

Wang, Z.; Li, F.; Ergang, N. S.; Stein, A. *Chem. Mater.* **2006**, *18*, 5543-5553.

Wucher, B.; Yue, W.; Kulak, A. N.; Meldrum, F. C. *Chem. Mater.* **2007**, *19*, 1111-1119.

Xia, Y.; Xiong, Y.; Lim, B.; Skrabalak, S. E. *Angew. Chem. Int. Ed.* **2009**, *48*, 60-103.

Xomeritakis, G.; Gouzinis, A.; Nair, S.; Okubo, T.; He, M.; Overney, R. M.; Tsapatsis, M. *Chem. Eng. Sci.* **1999**, *54*, 3521-3531.

Xomeritakis, G.; Lai, Z.; Tsapatsis, M. *Ind. Eng. Chem. Res.* **2001**, *40*, 544-552.

Yamamura, M.; Chaki, K.; Wakatsuki, T.; Okado, H. *Zeolites* **1994**, *14*, 643-649.

Yan, Y.; Davis, M. E.; Gavalas, G. R. *Ind. Eng. Chem. Res.* **1995**, *34*, 1652-1661.

Yang, H.; Zhao, D. *J. Mater. Chem.* **2005**, *15*, 1217-1231.

Yang, P.; Zhao, D.; Margolese, D. I.; Chmelka, B. F.; Stucky, G. D. *Nature* **1998**, *396*, 152-155.

Yin, Y.; Alivisatos, A. P. *Nature* **2005**, *437*, 664-670.

Yoo, W. C.; Kumar, S.; Penn, R. L.; Tsapatsis, M.; Stein, A. *J. Am. Chem. Soc.* **2009**, *131*, 12377-12383.

Yoo, W. C.; Kumar, S.; Wang, Z.; Ergang, N. S.; Fan, W.; Karanikolos, G. N.; McCormick, A. V.; Penn, R. L.; Tsapatsis, M.; Stein, A. *Angew. Chem. Int. Ed.* **2008**, *47*, 9096-9099.

Yoo, W. C.; Stein, A. *Chem. Mater.* **2010**, *submitted*.

Yoo, W. C.; Stoeger, J. A.; Lee, P.-S.; Tsapatsis, M.; Stein, A. *Angew. Chem. Int. Ed.* **2010**, *49*, 8699-8703.

Yoo, W. C.; Zhang, X.; Tsapatsis, M.; Stein, A. *manuscript in preparation.* **2010**.

Yoon, K. B. *Acc. Chem. Res.* **2007**, *40*, 29-40.

Yoon, S. B.; Kim, J.-Y.; Kim, J. H.; Park, Y. J.; Yoon, K. R.; Park, S.-K.; Yu, J.-S. *J. Mater. Chem.* **2007**, *17*, 1758-1761.

Yoon, S. B.; Sohn, K.; Kim, J. Y.; Shin, C.-H.; Yu, J.-S.; Hyeon, T. *Adv. Mater.* **2002**, *14*, 19-21.

Yu, Z.; Zheng, A.; Wang, Q.; Chen, L.; Xu, J.; Amoureux, J.-P.; Deng, F. *Angew. Chem. Int. Ed.* **2010**, *49*, 8657-8661.

Yuan, W.; Lin, Y. S.; Yang, W. *J. Am. Chem. Soc.* **2004**, *126*, 4776-4777.

Zalusky, A. S.; Olayo-Valles, R.; Wolf, J. H.; Hillmyer, M. A. *J. Am. Chem. Soc.* **2002**, *124*, 12761-12773.

Zhang, B.; Davis, S. A.; Mendelson, N. H.; Mann, S. *Chem. Commun.* **2000**, 781-782.

Zhang, Q.; Lee, I.; Ge, J.; Zaera, F.; Yin, Y. *Adv. Funct. Mater.* **2010**, *20*, 2201-2214.

Zhang, Q.; Lee, I.; Ge, J.; Zaera, F.; Yin, Y. *Adv. Funct. Mater.* **2010**, *20*, 2201-2214.

Zhao, D.; Feng, J.; Huo, Q.; Melosh, N.; Fredrickson, G. H.; Chmelka, B. F.; Stucky, G. D. *Science* **1998**, *279*, 548-552.

Zhao, D.; Huo, Q.; Feng, J.; Chmelka, B. F.; Stucky, G. D. *J. Am. Chem. Soc.* **1998**, *120*, 6024-6036.

Zhu, Y.; Shi, J.; Shen, W.; Dong, X.; Feng, J.; Ruan, M.; Li, Y. *Angew. Chem. Int. Ed.* **2005**, *44*, 5083-5087.